

**The Effects of Driving Forces and Reversed Bending  
Fatigue of Concrete-Filled FRP Circular Tubes for Piles  
and Other Applications**

by

**Karim Helmi**

A Dissertation Submitted to the Faculty of Graduate Studies of  
The University of Manitoba  
In Partial Fulfillment of the Requirements of the Degree of

**Doctor of Philosophy**

Structural Engineering Division  
Department of Civil Engineering  
The University of Manitoba  
Winnipeg, Manitoba, Canada

Copyright © 2006 by Karim Helmi

**THE UNIVERSITY OF MANITOBA**  
**FACULTY OF GRADUATE STUDIES**  
\*\*\*\*\*  
**COPYRIGHT PERMISSION**

**The Effects of Driving Forces and Reversed Bending Fatigue of Concrete-Filled FRP Circular  
Tubes for Piles and Other Applications**

**By**

**Karim Helmi**

**A Thesis/Practicum submitted to the Faculty of Graduate Studies of The University of**

**Manitoba in partial fulfillment of the requirement of the degree**

**Of**

**Doctor of Philosophy**

**Karim Helmi © 2006**

**Permission has been granted to the Library of the University of Manitoba to lend or sell copies of this thesis/practicum, to the National Library of Canada to microfilm this thesis and to lend or sell copies of the film, and to University Microfilms Inc. to publish an abstract of this thesis/practicum.**

**This reproduction or copy of this thesis has been made available by authority of the copyright owner solely for the purpose of private study and research, and may only be reproduced and copied as permitted by copyright laws or with express written authorization from the copyright owner.**

## **Abstract**

Concrete filled Fiber Reinforced Polymer (FRP) tubes (CFFTs) provide a non-corrosive alternative to conventional materials in many applications. Studies performed on CFFT in the past have mostly been focused on characterizing their short-term monotonic behavior, leaving areas in need of further investigation. In this thesis, a research program was conducted to address three of these areas namely, the effects of driving forces on CFFT piles, a splicing system for CFFTs, and the fatigue behavior of CFFTs under reversed cyclic bending.

To study the effects of the driving forces, four 367 mm diameter CFFT piles, one of which was with a splice, were driven into the ground and then extracted. The piles were cut into 6.0 m and 0.3 m long sections that were used for beam tests, tensile and compression coupon tests, tension-tension fatigue tests, and push-off bond tests. Test results were compared to those of control specimens, which were not subjected to driving forces. The study showed that driving forces had insignificant effect on the CFFTs or the GFRP tubes. The mechanical splice used in this study showed adequate behavior and a slightly higher moment capacity than that of the CFFT pile it self, and therefore is considered successful.

To study the fatigue behavior of CFFT beams three full-scale 4.0 m long specimens were tested under reversed cyclic bending. Eighty on GFRP coupons, cut from the tubes, were also tested. Several parameters were varied including the type of coupon, loading frequency, and the type of test whether tension-tension or tension-compression. It was shown that some stiffness degradation behavior occurs, and that CFFTs seem to have a relatively short fatigue life under bending moments of about 40% and higher of their

ultimate static bending moment capacities. However, a fatigue life of one million cycles or more could be achieved if the maximum bending moments is limited to 25-30% of the ultimate static bending moment and lower. The coupon tests showed that fatigue life will vary significantly with varying coupon type, loading frequency and including a compression component. The results also showed that the empirical equation suggested by Epaarachchi and Clausen (2003) could be used to represent fatigue life of FRP coupons, which could then be used to predict the fatigue life of full-scale CFFT specimens.

An analytical study was also conducted to model the behavior of CFFT beams under reversed cyclic bending. The results of this analytical modeling were compared to experimental results of CFFTs tested under reversed cyclic bending, showing reasonable agreement. A parametric study conducted using this model showed that both the concrete and FRP time-dependant properties have a significant contribution to the behavior of CFFT members subjected to reversed cyclic bending. The study also showed that the FRP tube diameter-to-wall thickness ratio have insignificant effect on fatigue life of CFFT flexural members.



## **Acknowledgments**

I would like to express my sincere appreciation and profound gratitude to my advisor Dr. Aftab Mufti for his guidance, support and patience throughout my thesis.

I would also like to express my appreciation to my co-advisor Dr. Amir Fam of Queens University for his guidance and valuable assistance.

Deepest appreciations are due to Dr. Dimos Polyzois, and Dr. Douglas Thomson for serving on my Ph.D. advisory committee, and to Dr. Khaled Soudki from the University of Waterloo for acting as my external examiner.

Many thanks are due to Mr. Moray McVey and Mr. Grant Whiteside of the McQuade Structures lab, and Mr. Scott Sparrow form for their help with the experimental program.

I would also like to thank Lancaster Composites and Ameron International for providing the tubes, to LaFarge Canada for casting them and to Agra Foundation for driving and extracting the tubes.

I would also like to thank the staff of ISIS Canada, especially Ms. Nancy Fehr for her efforts in preparing for the defense exam.

Last but not least I would like to express my deepest appreciation to my family for their support and encouragement during my graduate studies.

## **Table of Contents**

<b>Abstract.....</b>	<b>ii</b>
<b>Acknowledgments .....</b>	<b>iv</b>
<b>Table of Contents .....</b>	<b>v</b>
<b>List of Tables .....</b>	<b>xii</b>
<b>List of Figures.....</b>	<b>xiii</b>
<b>Notation.....</b>	<b>xxvi</b>
<b>Chapter 1 Introduction.....</b>	<b>1</b>
1.1 General .....	1
1.2 Concrete Filled FRP Tubes .....	2
1.3 Research Objectives .....	3
1.3.1 The effect of the driving forces on CFFT .....	3
1.3.2 Splicing of CFFT members .....	4
1.3.3 Reversed bending fatigue behavior of CFFT members.....	4
1.4 Research Significance .....	5
1.4.1 Effect of driving forces on CFFT piles.....	5
1.4.2 Splicing of CFFT piles.....	5
1.4.3 Fatigue behavior of CFFT .....	6
1.5 Research Methodology.....	6
1.5.1 Experimental study on the effect of driving forces and splicing of full scale CFFT piles.....	6
1.5.2 Experimental and analytical investigations of the fatigue behavior of CFFT members .....	7

---

1.6	Thesis Outline.....	7
<b>Chapter 2</b>	<b>Literature Review .....</b>	<b>11</b>
2.1	Introduction .....	11
2.2	Behavior of Axially Loaded CFFTs .....	11
2.2.1	Short CFFT columns.....	11
2.2.1.1	Confinement models.....	13
2.2.1.1.1	Design oriented models .....	13
2.2.1.1.2	Analysis oriented models.....	15
2.2.1.2	Factors affecting FRP confined concrete .....	16
2.2.1.2.1	Effect of loading the FRP jacket.....	16
2.2.1.2.2	Presence of a hole in the concrete core.....	17
2.2.1.2.3	Effect of concrete strength.....	17
2.2.2	Slender CFFT columns .....	19
2.3	Behavior of Flexural and Axial-Flexural CFFT Members.....	20
2.4	Behavior of CFFT in Shear .....	23
2.5	Creep Behavior of CFFT Members.....	24
2.6	Bond issues in CFFT Members .....	25
2.7	Cyclic and Fatigue Behavior of CFFT Members .....	26
2.8	Reinforced and Prestressed CFFTs .....	30
2.9	Drivability and the Effect of Driving Forces on CFFT Piles .....	34
2.10	Durability and Environmental Effects.....	37
2.11	Connections and Splices of CFFT Members.....	39

<b>Chapter 3 The Effects of Driving Forces and Mechanical Splicing of CFFT .....</b>	<b>53</b>
3.1 Introduction .....	53
3.2 Materials .....	53
3.2.1 GFRP tubes .....	53
3.2.2 Concrete .....	54
3.2.3 Splices .....	55
3.3 Mechanical Properties of the Tubes .....	55
3.3.1 Tension properties in the longitudinal direction .....	56
3.3.1.1 Coupon specimens .....	57
3.3.1.2 Coupon monotonic testing .....	57
3.3.1.3 Stress-strain response based on monotonic tension tests .....	58
3.3.1.4 Failure modes based on monotonic tension tests .....	58
3.3.2 Compression properties in the longitudinal direction .....	59
3.3.3 Tension properties in the circumferential direction .....	59
3.4 Description of CFFT Pile Specimens and the Fabrication Process .....	60
3.5 Driving, Splicing and Extraction of CFFT Piles .....	60
3.6 Description of Test Specimens Extracted from the Piles .....	61
3.6.1 CFFT beam specimens .....	61
3.6.2 CFFT push-off specimens .....	62
3.6.3 GFRP tension, compression and tension-tension fatigue coupon specimens .....	62
3.7 Test Setups and Instrumentation .....	63
3.7.1 Beam tests .....	63

3.7.2 Push-off tests .....	64
3.7.3 GFRP coupon tests .....	65
3.8 Test Results and Discussion .....	65
3.8.1 CFFT beam tests .....	65
3.8.1.1 Load-deflection behavior.....	65
3.8.1.2 Load-slip behavior.....	67
3.8.1.3 Load-strain behavior.....	68
3.8.1.4 Failure modes .....	69
3.8.2 CFFT push-off tests .....	69
3.8.3 GFRP tension, compression and tension-tension fatigue coupon tests .....	70
<b>Chapter 4 Experimental Investigation of the Fatigue Behavior of CFFT Members under Reversed Bending .....</b>	<b>99</b>
4.1 Introduction .....	99
4.2 Description of Test Specimens.....	99
4.2.1 Full-scale CFFT beam specimens.....	99
4.2.2 GFRP coupon specimens.....	100
4.3 Test Setups and Instrumentations.....	101
4.3.1 Full-scale CFFT beam test setup and instrumentation .....	101
4.3.2 Coupon tests setup and instrumentation .....	102
4.4 Testing Procedures .....	103
4.4.1 Full-scale CFFT beam specimens.....	103
4.4.2 Coupon tests.....	104
4.5 Test Results .....	105

4.5.1 Full-scale CFFT beam test results .....	105
4.5.1.1 Deflection behavior .....	105
4.5.1.2 Slip behavior.....	106
4.5.1.3 Strain behavior.....	107
4.5.1.4 Failure mode and total number of cycles .....	107
4.5.2 Coupon test results .....	108
4.5.2.1 Failure modes of coupon specimens.....	108
4.5.2.2 Effect of coupon type .....	109
4.5.2.3 Effect of loading frequency .....	109
4.5.2.4 Effect of tension-tension and tension-compression fatigue.....	109
4.5.2.5 Stiffness degradation behavior .....	110
4.5.2.6 Fatigue life modeling of GFRP coupons .....	110
4.5.2.6.1 The effectiveness of the empirical method.....	112
4.5.2.6.2 Estimating fatigue life of full-scale CFFT specimens using empirical method .....	113
4.5.2.7 Modeling stiffness degradation .....	115
<b>Chapter 5 Analytical Modeling of CFFT under Reversed Bending Fatigue.....</b>	<b>142</b>
5.1 Introduction .....	142
5.2 Static Analysis .....	142
5.2.1 Constitutive models .....	143
5.2.1.1 Concrete in compression .....	143
5.2.1.2 Concrete in tension .....	144
5.2.1.3 FRP tube .....	145

---

5.2.2 Modeling procedure.....	145
5.2.3 Verification of the model.....	146
5.3 Cyclic Loading Analysis .....	147
5.3.1 Constitutive models .....	147
5.3.1.1 Fatigue and creep model for concrete under compression .....	147
5.3.1.2 ..... Application of concrete fatigue and creep models in reversed bending conditions .....	150
5.3.1.3 GFRP creep model .....	151
5.3.1.4 GFRP stiffness degradation model.....	152
5.3.1.5 ..... Application of the GFRP stiffness degradation and creep models in a reversed bending condition.....	153
5.3.1.6 Estimation of fatigue life .....	155
5.3.2 Modeling procedure.....	156
5.3.3 Verification of the model.....	159
5.4 Parametric Study .....	160
5.4.1 Results of the parametric studies .....	161
5.4.1.1 Effect of time dependant properties of materials .....	161
5.4.1.2 Effect of loading frequency and load level.....	162
5.4.1.3 Effect of tube diameter (i.e. FRP reinforcement ratio).....	163
<b>Chapter 6 Summary, Conclusions, Recommendations for Future Study, and Design Recommendations and Limitations.....</b>	<b>183</b>
6.1 Summary.....	183
6.2 Conclusions .....	184

6.2.1 Effect of driving forces and splicing of CFFT.....	184
6.2.2 Reversed cyclic bending behavior of CFFT members .....	186
6.3 Recommendations for Future Study.....	188
6.4 Design Recommendations and Limitations.....	189
<b>References .....</b>	<b>191</b>
<b>Appendix A.....</b>	<b>205</b>
<b>Appendix B .....</b>	<b>234</b>



**List of Tables**

Table 3-1 Details of concrete mix used to fill the tubes .....72

Table 3-2 Mechanical properties of the GFRP tubes as provided by the manufacturer  
(Lancaster Composite, Inc.).....72

Table 3-3 Summary of tension coupon test results.....73

Table 3-4 Description of beam specimens.....73

Table 3-5 Results of push-off tests .....74

Table 3-6 Results of TC1 type monotonic tension coupon tests .....75

Table 3-7 Results of TC5 type monotonic tension coupon tests .....76

Table 3-8 Results of monotonic compression coupon tests.....77

Table 3-9 Results of tension-tension fatigue tests .....78

Table 4-1 Summary of full-scale Fatigue CFFT beam test program .....117

Table 4-2 Fatigue coupon test matrix .....117

Table 4-3 Coupon test results .....118

Table 4-4  $R^2$  values under different conditions .....120

Table 4-5 Calculation of Nf for CFFT beams.....120

Table 4-6 Fatigue life predictions for full-scale CFFT specimens using coupon test results  
.....120

Table 5-1 Fatigue life predictions compared to experimental results.....164

Table 5-2 Summary of the parametric study.....165

Table 5-3 Fatigue life predictions of parametric study.....166

**List of Figures**

Figure 1-1 CFFTs in marine pile application (Lancaster Composite, Inc.) .....9

Figure 1-2 CFFTs in Route 40 Bridge pier, Virginia (Fam et al., 2003b) .....9

Figure 1-3 Connection between CFFT piles and pier cap beam (Fam et al., 2003b) .....10

Figure 1-4 CFFT beams in Kings Stormwater Channel Bridge, San Diego, California (Seible et al. 1999) .....10

Figure 1-5 CFFTs subjected to reversed cyclic bending loads .....10

Figure 2-1 Comparison between the behavior of GFRP-confined concrete and steel-confined concrete (Fam and Rizkalla, 2001a) .....45

Figure 2-2 Effect of the bi-axial loading conditions on the strength of FRP tube (Fam and Rizkalla, 2001a) .....45

Figure 2-3 Effect of central void on confinement effectiveness (Fam and Rizkalla, 2001b) .....46

Figure 2-4 Effect of unconfined concrete strength on confinement effectiveness (Mandal et al., 2005) .....46

Figure 2-5 Biaxial stress-strain curves for slender CFFT columns (Mirmiran et al., 2001)47

Figure 2-6 Test setup of CFFT in bending (Fam and Rizkalla, 2002).....47

Figure 2-7 Effect of wall thickness and laminate structure of CFFT on the balanced reinforcement ratio (Fam and Rizkalla, 2002).....48

Figure 2-8 Test setup and results of CFFT in combined bending and axial loads (Flisak 2004) .....48

Figure 2-9 Effect of reinforcement on shear behavior of CFFT .....49

Figure 2-10 Typical hysteretic response of different types of CFFT beam columns (a) W series (b) Y series (Shao and Mirmiran, 2004) .....	49
Figure 2-11 Three girder beam and slab assembly (Karbhari et al., 2000 ) .....	50
Figure 2-12 Effect of prestressing on CFFT (Fam and Mandal, 2006) .....	50
Figure 2-13 Behavior of steel reinforced CFFT compared to regular steel reinforced concrete members (Cole and Fam, 2006) .....	51
Figure 2-14 Lateral load test using Statnamic test setup (Fam et al., 2003).....	51
Figure 2-15 Summary of results of the freeze-thaw study on CFFT by Knog (2005).....	51
Figure 2-16 Types of end anchorage for splicing CFFT (Karbhari et al., 2000).....	52
Figure 2-17 CFFT column-pier cap assembly (Zhu et al., 2004) .....	52
Figure 3-1 GFRP tubes .....	79
Figure 3-2 components of the mechanical splices .....	79
Figure 3-3 Tension coupons configurations .....	80
Figure 3-4 Tension coupons test setup.....	80
Figure 3-5 Typical Stress-strain relations for various monotonic tension coupons.....	81
Figure 3-6 Failure modes of tension coupons.....	81
Figure 3-7 A typical monotonic compression coupon Stress-strain relation.....	82
Figure 3-8 Split disk test.....	82
Figure 3-9 Tube and plugs to prepare for casting .....	83
Figure 3-10 Pumping of concrete into tubes.....	83
Figure 3-11 Pile driving and splicing process.....	84
Figure 3-12 Drilling around piles for extraction.....	85
Figure 3-13 Cutting of various specimens from the CFFT piles .....	85

---

Figure 3-14 Test specimens extracted from CFFT piles.....	86
Figure 3-15 Unspliced monotonic beam test setup.....	87
Figure 3-16 Spliced monotonic beam test setup.....	87
Figure 3-17 General view of test setup for BP2L.....	87
Figure 3-18 Strain gauge locations at midspan of monotonic beam specimens.....	88
Figure 3-19 LVDT locations.....	88
Figure 3-20 Push-off test setup.....	88
Figure 3-21 Load-deflection behavior (unspliced CFFT beams).....	89
Figure 3-22 Load-deflection behavior (spliced CFFT beams).....	89
Figure 3-23 Load-slip behavior of BC2.....	90
Figure 3-24 Load-slip behavior of BP2U.....	90
Figure 3-25 Load-slip behavior of BP2L.....	91
Figure 3-26 Load-slip behavior of SCx.....	91
Figure 3-27 Load-slip behavior of SC+.....	92
Figure 3-28 Load-slip behavior of SP3Ux.....	92
Figure 3-29 Load-tube strain (unspliced CFFT beams).....	93
Figure 3-30 Load-tube strain (spliced CFFT beams)(Average of two strain gauges).....	93
Figure 3-31 Load-bottom key strains in specimens SCx and SP3Ux.....	94
Figure 3-32 Load-bottom key strain in specimen SC+.....	94
Figure 3-33 Failure mode of unspliced beams.....	95
Figure 3-34 Failure mode of spliced beams.....	95
Figure 3-35 Load-slip behavior of control push-off specimens.....	96
Figure 3-36 Load-slip behavior of push-off specimens from driven pile P1.....	96

Figure 3-37 Load-slip behavior of push-off specimens from driven pile P2.....97

Figure 3-38 Load-slip behavior of push-off specimens from driven pile P3.....97

Figure 3-39 Load-slip behavior of push-off specimens from driven pile P4-I.....98

Figure 3-40 Load-slip behavior of push-off specimens from driven pile P4-II.....98

Figure 4-1 Schematic of full-scale CFFT beam test setup.....121

Figure 4-2 Schematic of support system to take reaction of push and pull loading .....121

Figure 4-3 View of support system and loading point.....122

Figure 4-4 Coupon test setup in the 25 kN machine.....122

Figure 4-5 Loading history of test specimens.....123

Figure 4-6 Mid-span deflection vs. number of cycles for specimen BFC3 .....123

Figure 4-7 Load-deflection behavior for specimen BFC3 at different number of cycles124

Figure 4-8 Mid-span deflection vs. number of cycles for specimen BFP1U.....124

Figure 4-9 Load-deflection behavior for specimen BFP1U at different number of cycles ...  
.....125

Figure 4-10 Mid-span deflection vs. number of cycles for specimen BFC1 .....125

Figure 4-11 Load-deflection behavior for specimen BFC1 ( $M_{max}/M_{ult}=0.25$ ).....126

Figure 4-12 Load-deflection behavior for specimen BFC1 ( $M_{max}/M_{ult}=0.375$ ).....126

Figure 4-13 End slip history of specimen BFC3 .....127

Figure 4-14 End slip history of specimen BFP1U .....127

Figure 4-15 End slip history of specimen BFC1 .....128

Figure 4-16 Mid-height strain history of specimen BFC3.....128

Figure 4-17 Mid-height strain history of specimen BFP1U .....129

Figure 4-18 Mid-height strain history of specimen BFC1 .....129

Figure 4-19 PI gauge readings of specimen BFP1U.....130

Figure 4-20 PI gauge readings of specimen BFC1 .....130

Figure 4-21 Failure of specimen BFC3 .....131

Figure 4-22 Failure of specimen BFP1U.....131

Figure 4-23 Failure of specimen BFC1 .....132

Figure 4-24 Cracks in specimen BFC1 after removing the GFRP tube .....132

Figure 4-25 Effect of coupon type on fatigue life in terms of ( $\sigma_{max}/\sigma_{ult}$ ) ratio.....133

Figure 4-26 Effect of coupon type on fatigue life in terms of  $\sigma_{max}$  .....133

Figure 4-27 Effect of loading frequency on fatigue life of tension-tension coupons ( $R = 0.1$ ) .....134

Figure 4-28 Effect of loading frequency on fatigue life of tension-compression coupons ( $R = -0.25$ ).....134

Figure 4-29 Effect of tension-tension and tension-compression loading on fatigue life of specimens with  $f = 5$  Hz .....135

Figure 4-30 Effect of tension-tension and tension-compression loading on fatigue life of specimens with  $f = 1$  Hz .....135

Figure 4-31 Stiffness degradation history ( $R = -0.25$ ,  $f = 1$  Hz and  $\sigma/\sigma_{max} = 0.4$ ) .....136

Figure 4-32 Stiffness degradation history ( $R = -0.25$ ,  $f = 5$  Hz and  $\sigma/\sigma_{max} = 0.5$ ) .....136

Figure 4-33 Stiffness degradation history ( $R = 0.1$ ) .....137

Figure 4-34 Stress-strain hysteretic ( $R = -0.25$ ,  $f = 1$  Hz and  $\sigma_{max}/\sigma_{lt} = 0.4$ ).....137

Figure 4-35 Stress-strain hysteretic ( $R=0.1$ ,  $f = 1$  Hz, and  $\sigma_{max}/\sigma_{ult} =0.5$ ).....138

Figure 4-36 Estimating the  $\alpha$  and  $\beta$  parameters using results from all 25 mm TC5 specimens.....138

Figure 4-37 Formula predictions for coupons tested at  $R = 0.1$  and  $f = 5$  Hz .....139

Figure 4-38 Formula predictions for coupons tested at  $R = 0.1$  and  $f = 1$  Hz .....139

Figure 4-39 Formula predictions for coupons tested at  $R = -0.25$  and  $f = 5$  Hz.....140

Figure 4-40 Formula predictions for coupons tested at  $R = -0.25$  and  $f = 1$  Hz.....140

Figure 4-41 Comparison of predicted ad experimental fatigue lives of full scale CFFT beam specimens .....141

Figure 4-42 Estimating  $A$  and  $n$  constants for stiffness degradation models .....141

Figure 5-1 Schematic of CFFT model parameters in flexure .....167

Figure 5-2 Predicted concrete stress-strain relation for CFFT members in compression using model by Fam and Rizkalla (2001b).....168

Figure 5-3 Predicted versus experimental load-deflection behavior of CFFT under monotonic static bending .....168

Figure 5-4 Predicted versus experimental load-strain behavior of CFFT under monotonic static bending .....169

Figure 5-5 CFFT sections subjected to reversed bending.....169

Figure 5-6 Predicted neutral axis depth verses static bending moment for CFFT specimen BC2 .....170

Figure 5-7 Strain versus time for concrete layers in a CFFT member.....170

Figure 5-8 Calibration of Findley's (1960) creep model using FRP tube test data .....171

Figure 5-9 Schematic of FRP creep behavior (Mallick, 1998).....171

Figure 5-10 Creep and stiffness degradation models for FRP in tension and compression (Based on Deskovic, 1993).....172

Figure 5-11 Comparison of deflection behavior for specimen BFC1.....173

Figure 5-12 Comparison of strain behavior for specimen BFC1 .....173

Figure 5-13 Comparison of deflection behavior for specimen BFP1U .....174

Figure 5-14 Comparison of strain behavior for specimen BFP1U .....174

Figure 5-15 Comparison of deflection behavior for specimen BFC3.....175

Figure 5-16 Comparison of strain behavior for specimen BFC3.....175

Figure 5-17 Comparison of predicted and experimental fatigue lives.....176

Figure 5-18 Effect of the time dependant properties of the materials on the strain behavior  
(Dt =256 - Mmax/Mult = 50% - f = 1Hz).....176

Figure 5-19 Effect of the time dependant properties of the materials on the depth of the  
neutral axis (Dt =367 - Mmax/Mult = 50% - f = 5Hz) .....177

Figure 5-20 Effect of the time dependant properties of the materials on the midspan  
deflection (Dt =456 - Mmax/Mult = 50% - f = 1Hz).....177

Figure 5-21Effect of the time dependant properties of the materials on the strain behavior  
(Dt =456 - Mmax/Mult = 25% - f = 5Hz).....178

Figure 5-22 Effect of the time dependant properties of the materials on the depth of the  
neutral axis (Dt =367 - Mmax/Mult = 25% - f = 1Hz) .....178

Figure 5-23 Effect of the time dependant properties of the materials on the midspan  
deflection (Dt =256 - Mmax/Mult = 25% - f = 5Hz).....179

Figure 5-24 Effect of loading frequency and load level on bottom strain behavior (Dt =  
256 mm).....179

Figure 5-25 Effect of loading frequency and load level on top strain behavior (Dt = 367  
mm).....180



Figure 5-26 Effect of loading frequency and load level on deflection behavior ( $Dt = 456$ mm).....	180
Figure 5-27 Effect of the tube diameter on bottom strain behavior ( $M_{max}/M_{ult} = 50\% - f = 1\text{Hz}$ ) .....	181
Figure 5-28 Effect of the tube diameter on top strain behavior ( $M_{max}/M_{ult} = 25\% - f = 5\text{Hz}$ ).....	181
Figure 5-29 Effect of the tube diameter on deflection behavior ( $M_{max} /M_{ult} = 50\% - f = 5\text{Hz}$ ).....	182
Figure 5-30 Effect of FRP reinforcement ration on fatigue life .....	182
Figure A-1 Effect of the time dependant properties of the materials on the strain behavior ( $Dt = 256 - M_{max}/M_{ult} = 50\% - f = 1\text{Hz}$ ) .....	205
Figure A-2 Effect of the time dependant properties of the materials on the depth of the neutral axis ( $Dt = 256 - M_{max}/M_{ult} = 50\% - f = 1\text{Hz}$ ) .....	206
Figure A-3 Effect of the time dependant properties of the materials on the midspan deflection ( $Dt = 256 - M_{max}/M_{ult} = 50\% - f = 1\text{Hz}$ ).....	206
Figure A-4 Effect of the time dependant properties of the materials on the strain behavior ( $Dt = 256 - M_{max}/M_{ult} = 50\% - f = 5\text{Hz}$ ).....	207
Figure A-5 Effect of the time dependant properties of the materials on the depth of the neutral axis ( $Dt = 256 - M_{max}/M_{ult} = 50\% - f = 5\text{Hz}$ ) .....	207
Figure A-6 Effect of the time dependant properties of the materials on the midspan deflection ( $Dt = 256 - M_{max}/M_{ult} = 50\% - f = 5\text{Hz}$ ).....	208
Figure A-7 Effect of the time dependant properties of the materials on the strain behavior ( $Dt = 256 - M_{max}/M_{ult} = 25\% - f = 1\text{Hz}$ ).....	208

Figure A-8 Effect of the time dependant properties of the materials on the depth of the neutral axis ( $Dt = 256 - M_{max}/M_{ult} = 25\% - f = 1\text{Hz}$ ) .....209

Figure A-9 Effect of the time dependant properties of the materials on the midspan deflection ( $Dt = 256 - M_{max}/M_{ult} = 25\% - f = 1\text{Hz}$ ).....209

Figure A-10 Effect of the time dependant properties of the materials on the strain behavior ( $Dt = 256 - M_{max}/M_{ult} = 25\% - f = 5\text{Hz}$ ).....210

Figure A-11 Effect of the time dependant properties of the materials on the depth of the neutral axis ( $Dt = 256 - M_{max}/M_{ult} = 25\% - f = 5\text{Hz}$ ) .....210

Figure A-12 Effect of the time dependant properties of the materials on the midspan deflection ( $Dt = 256 - M_{max}/M_{ult} = 25\% - f = 5\text{Hz}$ ).....211

Figure A-13 Effect of the time dependant properties of the materials on the strain behavior ( $Dt = 367 - M_{max}/M_{ult} = 50\% - f = 1\text{Hz}$ ).....211

Figure A-14 Effect of the time dependant properties of the materials on the depth of the neutral axis ( $Dt = 367 - M_{max}/M_{ult} = 50\% - f = 1\text{Hz}$ ) .....212

Figure A-15 Effect of the time dependant properties of the materials on the midspan deflection ( $Dt = 367 - M_{max}/M_{ult} = 50\% - f = 1\text{Hz}$ ).....212

Figure A-16 Effect of the time dependant properties of the materials on the strain behavior ( $Dt = 367 - M_{max}/M_{ult} = 50\% - f = 5\text{Hz}$ ).....213

Figure A-17 Effect of the time dependant properties of the materials on the depth of the neutral axis ( $Dt = 367 - M_{max}/M_{ult} = 50\% - f = 5\text{Hz}$ ) .....213

Figure A-18 Effect of the time dependant properties of the materials on the midspan deflection ( $Dt = 367 - M_{max}/M_{ult} = 50\% - f = 5\text{Hz}$ ).....214

Figure A-19 Effect of the time dependant properties of the materials on the strain behavior ( $Dt = 367$  -  $M_{max}/M_{ult} = 25\%$  -  $f = 1\text{Hz}$ ).....214

Figure A-20 Effect of the time dependant properties of the materials on the depth of the neutral axis ( $Dt = 367$  -  $M_{max}/M_{ult} = 25\%$  -  $f = 1\text{Hz}$ ) .....215

Figure A-21 Effect of the time dependant properties of the materials on the midspan deflection ( $Dt = 367$  -  $M_{max}/M_{ult} = 25\%$  -  $f = 1\text{Hz}$ ).....215

Figure A-22 Effect of the time dependant properties of the materials on the strain behavior ( $Dt = 367$  -  $M_{max}/M_{ult} = 25\%$  -  $f = 5\text{Hz}$ ).....216

Figure A-23 Effect of the time dependant properties of the materials on the depth of the neutral axis ( $Dt = 367$  -  $M_{max}/M_{ult} = 25\%$  -  $f = 1\text{Hz}$ ) .....216

Figure A-24 Effect of the time dependant properties of the materials on the midspan deflection ( $Dt = 367$  -  $M_{max}/M_{ult} = 25\%$  -  $f = 1\text{Hz}$ ).....217

Figure A-25 Effect of the time dependant properties of the materials on the strain behavior ( $Dt = 456$  -  $M_{max}/M_{ult} = 50\%$  -  $f = 1\text{Hz}$ ).....217

Figure A-26 Effect of the time dependant properties of the materials on the depth of the neutral axis ( $Dt = 456$  -  $M_{max}/M_{ult} = 50\%$  -  $f = 1\text{Hz}$ ) .....218

Figure A-27 Effect of the time dependant properties of the materials on the midspan deflection ( $Dt = 456$  -  $M_{max}/M_{ult} = 50\%$  -  $f = 1\text{Hz}$ ).....218

Figure A-28 Effect of the time dependant properties of the materials on the strain behavior ( $Dt = 456$  -  $M_{max}/M_{ult} = 50\%$  -  $f = 5\text{Hz}$ ).....219

Figure A-29 Effect of the time dependant properties of the materials on the depth of the neutral axis ( $Dt = 456$  -  $M_{max}/M_{ult} = 50\%$  -  $f = 5\text{Hz}$ ) .....219

Figure A-30 Effect of the time dependant properties of the materials on the midspan deflection (Dt =456 - Mmax/Mult = 50% - f = 5Hz).....220

Figure A-31 Effect of the time dependant properties of the materials on the strain behavior (Dt =456 - Mmax/Mult = 25% - f = 1Hz).....220

Figure A-32 Effect of the time dependant properties of the materials on the depth of the neutral axis (Dt =456 - Mmax/Mult = 25% - f = 1Hz) .....221

Figure A-33 Effect of the time dependant properties of the materials on the midspan deflection (Dt =456 - Mmax/Mult = 25% - f = 1Hz).....221

Figure A-34 Effect of the time dependant properties of the materials on the strain behavior (Dt =456 - Mmax/Mult = 25% - f = 5Hz).....222

Figure A-35 Effect of the time dependant properties of the materials on the depth of the neutral axis (Dt =456 - Mmax/Mult = 25% - f = 5Hz) .....222

Figure A-36 Effect of the time dependant properties of the materials on the midspan deflection (Dt =456 - Mmax/Mult = 25% - f = 5Hz).....223

Figure A-37 Effect of the loading frequency and load level on the bottom strain behavior (Dt = 256).....223

Figure A-38 Effect of the loading frequency and load level on the top strain behavior (Dt = 256) .....224

Figure A-39 Effect of the loading frequency and load level on the deflection behavior (Dt = 256).....224

Figure A-40 Effect of the loading frequency and load level on the bottom strain behavior (Dt = 367).....225

Figure A-41 Effect of the loading frequency and load level on the top strain behavior ( $Dt = 367$ ) .....225

Figure A-42 Effect of the loading frequency and load level on the deflection behavior ( $Dt = 367$ ) .....226

Figure A-43 Effect of the loading frequency and load level on the bottom strain behavior ( $Dt = 456$ ).....226

Figure A-44 Effect of the loading frequency and load level on the top strain behavior ( $Dt = 456$ ) .....227

Figure A-45 Effect of the loading frequency and load level on the deflection behavior ( $Dt = 456$ ).....227

Figure A-46 Effect of the tube diameter on the bottom strain behavior ( $M_{max}/M_{ult} = 50\% - f = 1\text{Hz}$ ) .....228

Figure A-47 Effect of the tube diameter on the top strain behavior ( $M_{max}/M_{ult} = 50\% - f = 1\text{Hz}$ ) .....228

Figure A-48 Effect of the tube diameter on the deflection behavior ( $M_{max}/M_{ult} = 50\% - f = 1\text{Hz}$ ).....229

Figure A-49 Effect of the tube diameter on the bottom strain behavior ( $M_{max}/M_{ult} = 50\% - f = 5\text{Hz}$ ) .....229

Figure A-50 Effect of the tube diameter on the top strain behavior ( $M_{max}/M_{ult} = 50\% - f = 5\text{Hz}$ ) .....230

Figure A-51 Effect of the tube diameter on the deflection behavior ( $M_{max}/M_{ult} = 50\% - f = 5\text{Hz}$ ).....230

Figure A-52 Effect of the tube diameter on the bottom strain behavior ( $M_{max}/M_{ult} = 25\%$  -  $f = 1\text{Hz}$ ) .....231

Figure A-53 Effect of the tube diameter on the top strain behavior ( $M_{max}/M_{ult} = 25\%$  -  $f = 1\text{Hz}$ ) .....231

Figure A-54 Effect of the tube diameter on the deflection behavior ( $M_{max}/M_{ult} = 25\%$  -  $f = 1\text{Hz}$ ).....232

Figure A-55 Effect of the tube diameter on the bottom strain behavior ( $M_{max}/M_{ult} = 25\%$  -  $f = 5\text{Hz}$ ) .....232

Figure A-56 Effect of the tube diameter on the top strain behavior ( $M_{max}/M_{ult} = 25\%$  -  $f = 5\text{Hz}$ ) .....233

Figure A-57 Effect of the tube diameter on the deflection behavior ( $M_{max}/M_{ult} = 25\%$  -  $f = 5\text{Hz}$ ).....233

## Notation

$f^2(t)$	The stress at any given time.
$f'_c$	The unconfined strength of concrete.
$f'_{cc}$	The confined strength of concrete.
$\varepsilon'_c$	The strain in concrete at maximum stress $f'_c$ .
$\sigma'$	Calculated stress in iteration process.
$A$	Material constant for the stiffness degradation equation by Ogin et al.
$C$	The depth of the neutral axis.
$D$	Function in the equation by Epaarachchi and Clausen.
$D_f$	Diameter at fiber mid-thickness of FRP tube.
$D_i$	Internal diameter of the FRP tube.
$DMG_k$	The damage at time step $k$ .
$D_t$	Total diameter of the FRP tube.
$E$	The secant modulus of FRP.
$E_{co}$	The tangent modulus of concrete.
$E_{fcN}$	The modulus of elasticity for FRP in compression after $N$ cycles.
$E_{fco}$	The initial modulus of elasticity for FRP in compression.
$E_{ftN}$	The modulus of elasticity for FRP in tension after $N$ cycles.
$E_{fto}$	The initial modulus of elasticity for FRP in tension.
$E_o$	Uncracked elastic modulus of FRP.
$f$	Frequency of the applied load.
$h$	Height of pushoff specimen.

$L_p$	The complimentary probability.
$m$	Material dependant parameter for Findley's equation.
$M_j$	Bending moment at section $j$ .
$M_{max}$	Maximum applied bending moment.
$M_t$	Bending moment at constant moment zone.
$M_{ult}$	Ultimate bending moment.
$N$	The number of load cycles.
$n$	Number of layers.
$nc$	Material dependant parameter for Findley's equation.
$N_f$	The total number of cycles to failure.
$N_{f(k)}$	The number of cycles to failure calculated at step $k$ .
$ng$	Material constant for the stiffness degradation equation by Ogin et al.
$N_k$	The number of cycles at time step $k$ .
$ns$	Number of sections.
$P$	applied load.
$p$	The probability of failure.
$R$	Ratio of minimum stress to maximum stress.
$R^2$	The goodness of fit parameter.
$s$	Slip.
$S_c$	The characteristic stress level or sum of the mean stress level and the root mean square value (RMS).
$S_{cc}$	The characteristic stress level for concrete.
$S_{cf}$	The characteristic stress level for FRP.



$S_{max}$	The ratio of the applied maximum stress level $\sigma_{max}$ to the confined concrete strength $f'_c$ .
$S_{min}$	The ratio of the applied minimum stress level $\sigma_{min}$ to the confined concrete strength $f'_c$ .
$t$	Time.
$T_o$	The entire duration of time.
$\alpha$	Curve fitting parameters for the equation by Epaarachchi and Clausen.
$\alpha_1$	A factor accounting for the bond characteristics of the reinforcement in the Vecchio and Collins equation.
$\alpha_2$	A factor accounting for the nature of loading in the Vecchio and Collins equation.
$\beta$	Curve fitting parameters for the equation by Epaarachchi and Clausen.
$\varepsilon$	Strain.
$\varepsilon_b$	Bottom strain
$\varepsilon_{cr}$	The creep strain.
$\varepsilon_{crc}$	The cracking strain of concrete.
$\varepsilon_{crne}$	The net creep strain.
$\varepsilon_e$	The endurance strain.
$\varepsilon_o$	Instantaneous strain.
$\varepsilon_o$	The maximum total strain in the first load cycle.
$\varepsilon_{tot}$	Total strain.
$\theta$	The smallest angle of fibers between the loading direction and the fiber direction.

$\sigma$	Stress.
$\sigma_{cr}$	The cracking stress of concrete.
$\sigma_{max}$	Maximum applied stress.
$\varphi(\sigma_{max}, N)$	Stiffness reduction function.
$\psi$	Curvature.

## **Chapter 1**

### **Introduction**

#### **1.1 General**

Various problems could be associated with traditional construction materials, including deterioration of concrete and corrosion of steel members and rebar in concrete structures. Untreated timber structures also suffer from attack by marine borers and other types of organisms, and if chemically treated, they may pose environmental hazards when there is a need to dispose of them. A recent survey on highway bridges in the United States estimated that nearly 36% of the bridges are structurally deficient, primarily due to corrosion of steel members or steel reinforcement. The direct annual cost of corrosion repair for highway bridges is estimated as \$8.93 billion consisting of \$2.93 billion for maintenance of the superstructure alone (Koch et al., 2001). In another study, it has been estimated that the repair and replacement of marine piling systems in the United States costs \$2 billion a year (Lampo, 1996). Therefore, a need exists for innovative solutions to strengthen and/or extend the life span of current infrastructure and to find alternative construction materials and systems that are more durable and require less maintenance.

Fiber reinforced polymers (FRPs) were introduced into the construction industry, long after being established in the aerospace, marine and automobile industries, with excellent track records. Fiber reinforced polymers have a much higher strength-to-weight and stiffness-to-weight ratios than conventional materials. Additionally, they are not susceptible to corrosion or attack by different organisms. Furthermore, FRPs have the flexibility to be manufactured in different shapes and configurations to meet very specific requirements. The vast majority of FRPs used in structural engineering applications to

date are in the strengthening and rehabilitation areas of existing structures. This is because, in addition to the mentioned advantages of FRPs, their application in most cases of rehabilitation is easier than conventional techniques and requires less equipment and time. The use of FRPs in new structures, however, is still somewhat limited, mainly because of their relatively higher initial cost, lack of design codes in some areas, and the lack of long term track records in civil engineering applications.

## **1.2 Concrete Filled FRP Tubes**

The concept of Concrete-Filled FRP Tubes (CFFTs) combines both FRP and concrete in an effective way that takes full advantage of both materials. CFFTs are constructed by simply filling prefabricated FRP tubes with concrete. The FRP tube can take several shapes and could be manufactured using different types of fibers and matrices. The concrete core could be solid or hollow for reduced dead weight. This thesis mainly focuses on CFFTs made of circular Glass Fiber Reinforced Polymer (GFRP) tubes, completely filled with concrete.

Concrete filled FRP tubes do not require form work for construction, and therefore labor costs are reduced. The light weight FRP materials make transporting and handling of the tubes prior to casting easier and faster. The FRP tubes also protect the concrete core from aggressive environments and at the same time act as the sole reinforcement system. Fibers oriented in the circumferential direction confine the concrete, enhancing its strength and ductility, and also provide the shear reinforcement, whereas fibers oriented in the longitudinal direction provide the flexural strength and stiffness. The concrete core adds to the strength and stiffness of the member and prevents the premature local buckling of the FRP tube, allowing the achievement of its full material strength. This also

allows the use of thinner tubes, which reduces the cost of CFFTs. Concrete filled FRP tubes have been extensively studied in the past decade and have been used in marine piles (Parvathaneni et al., 1996 and Fam et al., 2003a), bridge piers (Fam et al., 2003b), and bridge girders (Zhao et al., 2000). They also have a great potential for use in monopole applications and overhead sign structures. Figures 1.1 to 1.5 show samples of CFFT actual and potential applications. The studies conducted on CFFTs, however, have mostly focused on characterizing the short-term monotonic behavior of CFFT piles in bending, shear and under axial loads. Although some research has been conducted in some other areas it has been quite limited, leaving research gaps in need of further investigation as discussed next.

### **1.3 Research Objectives**

The objective of this thesis is to address three areas of research needs for CFFTs, namely: (a) the effects of driving forces on CFFT piles, (b) splicing of precast CFFT members, and (c) fatigue behaviour of CFFT members under reversed cyclic bending. The following sections present a detailed description of these objectives.

#### **1.3.1 The effect of the driving forces on CFFT**

When CFFTs are used as piles they are driven into the ground using hammers, subjecting them to impact forces which could potentially cause some damage to these piles. The objective of this study is to examine the effects of the driving forces on:

- i. The overall behavior and strength of CFFT piles, represented by monotonic bending tests.
- ii. Bond strength at the interface between the FRP tube and the concrete core.

- iii. Mechanical properties of the FRP tube, including the tensile and compressive strengths and the fatigue life.

### **1.3.2 Splicing of CFFT members**

The development of reliable splices for CFFT piles is particularly important since FRP tubes have limited lengths due to manufacturing and transportation constraints. Furthermore, pile driving equipment may provide additional restrictions on the length of piles they can accommodate. The objective of this study is to examine the following:

- i. The structural performance and adequacy of a splicing system, in which splicing could be performed during the driving process.
- ii. The effect of driving stresses on this type of splices.

### **1.3.3 Reversed bending fatigue behavior of CFFT members**

Structural members are generally subjected to repeated loads, which cause cumulative damage and may result in continuous degradation of the properties of the members, potentially leading to premature fatigue failure. The objective of this research program is to:

- i. Examine the fatigue behavior of CFFT members under fully reversed cyclic bending moments.
- ii. Examine the effects of various loading conditions on the fatigue life of coupons cut from the GFRP tubes, including the type of coupons used in fatigue testing, frequency of the applied load, and the nature of loading including both, tension-tension and tension-compression loadings.
- iii. Examine the stiffness degradation behavior of the FRP tube material.

- iv. Develop analytical models for predicting fatigue life and stiffness degradation of the FRP tube materials, calibrated using data based on the coupon tests.
- v. Develop an analytical procedure to predict the behavior and fatigue life of CFFT's under reversed bending, using the models calibrated from the data obtained from coupon tests.

## **1.4 Research Significance**

### **1.4.1 Effect of driving forces on CFFT piles**

Studies in this area have mainly focussed on the drivability of CFFT piles. Ashford and Jakrapiyanum (2001) and Iskander et al. (2001) conducted purely analytical studies, while Mirmiran et al. (2002) and Fam et al. (2003b) studied the drivability of CFFT piles in the field by monitoring the driving process. In all these studies, the issue of damage that may result from the process, in the form of strength or stiffness reduction of the pile has not been adequately addressed. In this thesis, full scale CFFT piles were driven into the ground and then extracted and the damage caused by the driving process was evaluated through laboratory testing.

### **1.4.2 Splicing of CFFT piles**

A number of attempts to splice CFFT piles were reported in literature. However, in all of these studies, the splicing had to be performed before filling the tubes with concrete (Parvathaneni et al., 1996) or required the use of adhesives or grouting which require time to set (Mirmiran et al., 2002 and Zhu, 2004). In any case, the splicing of CFFT piles using these systems can not be practically done during the driving process, if there is a need to drive piles to depths larger than the length the driving equipment can

accommodate. In this thesis, a splicing system, in which splicing of precast units could be performed during the driving process was examined.

### **1.4.3 Fatigue behavior of CFFT**

Shao and Mirimran (2004) studied low cycle fatigue behavior of CFFTs under seismic-like loads, while Ahmad (2004) studied their unidirectional high cycle bending fatigue behavior. In real life, however, CFFTs used in applications such as mono poles, overhead sign structures, and some marine structures are usually subjected to reversed bending loading, as shown in Figure 1.5. This loading configuration has not been addressed in the literature. Additionally, the study by Ahmad (2004) did not examine the effect of different loading conditions, such as the frequency of the applied loads, on the fatigue life of CFFTs. Furthermore the study did not provide a model for fatigue life prediction. In this thesis, full-scale CFFT specimens were subjected to reversed bending moments using push and pull forces. Extensive tests were also conducted on coupons to study the effects of various parameters on the fatigue life of the tube material. Models were also developed to predict the fatigue life and behavior of CFFTs based on the coupon tests.

## **1.5 Research Methodology**

### **1.5.1 Experimental study on the effect of driving forces and splicing of full scale CFFT piles**

Four, 367 mm diameter and 13.7 m long CFFT piles, one of which was spliced, were driven into the ground and then extracted, the piles were then cut into 6 m and 0.3 m long segments. The 6 m segments were tested under monotonic and cyclic bending. The 0.3 m segments were used for tension and compression coupon tests, tension-tension coupon



fatigue tests and push-off bond tests. Test results were compared to those of control specimens, which were not subjected to driving forces. Some of the beam tests conducted on the 6 m long segments were used to evaluate the structural performance of the splices.

### **1.5.2 Experimental and analytical investigations of the fatigue behavior of CFFT members**

The experimental work included testing of three large-scale CFFT beam specimens under fully reversed cyclic bending. The experimental work also included testing of 81 coupons cut from the GFRP tubes, under tension-tension and tension-compression fatigue. This was intended to establish the fatigue and stiffness degradation properties of the tube materials, and to study the effect of various parameters, including stress ratio, the type of coupon and the frequency on the fatigue life of the tube material. The analytical work included adapting the procedure developed by Deskovic (1993) to predict the cyclic behavior of hybrid FRP/concrete beams to predict the fatigue behavior and fatigue life of CFFT members subjected to fully reversed cyclic bending.

## **1.6 Thesis Outline**

This thesis consists of six chapters. Chapter 1 (this chapter) presents the problem statement, objectives, significance, and methodology of the research presented in this thesis. Chapter 2 presents a literature review of the research conducted on CFFTs to date. Although the main focus of this study is on totally filled GFRP circular tubes, references are made in Chapter 2 to other types of CFFTs and to FRP-wrapped concrete members when the research is relevant to this study. Chapter 3 presents the details and results of the experimental program that was conducted to study the effect of driving forces on

CFFT piles, and the adequacy of the proposed splicing system in both control and driven specimens. Chapter 4 presents the details and results of the experimental program that was conducted to study the behaviour of CFFTs under reversed bending fatigue, including both full scale beam tests and coupon tests. This chapter also presents the analysis conducted on the results obtained from the coupon tests, to establish the fatigue life prediction and stiffness degradation models for the GFRP tube material. Chapter 5 presents the analytical model adapted to predict the behavior of the CFFT system under reversed bending fatigue. It also includes the model verification and the parametric study conducted to study the effect of several factors on the fatigue behavior of CFFT members. Chapter 6 presents a summary of the work done in this thesis, conclusions drawn from the experimental and analytical studies, recommendations for future research, and recommendations for design and limitations.

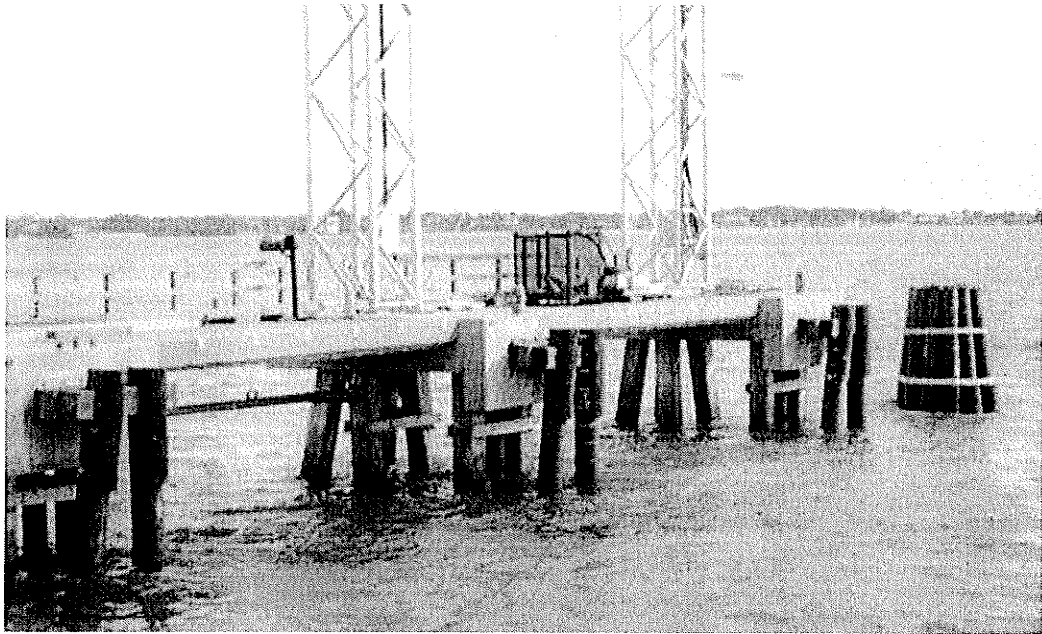


Figure 1-1 CFRTs in marine pile application (Lancaster Composite, Inc.)



Figure 1-2 CFRTs in Route 40 Bridge pier, Virginia (Fam et al., 2003b)

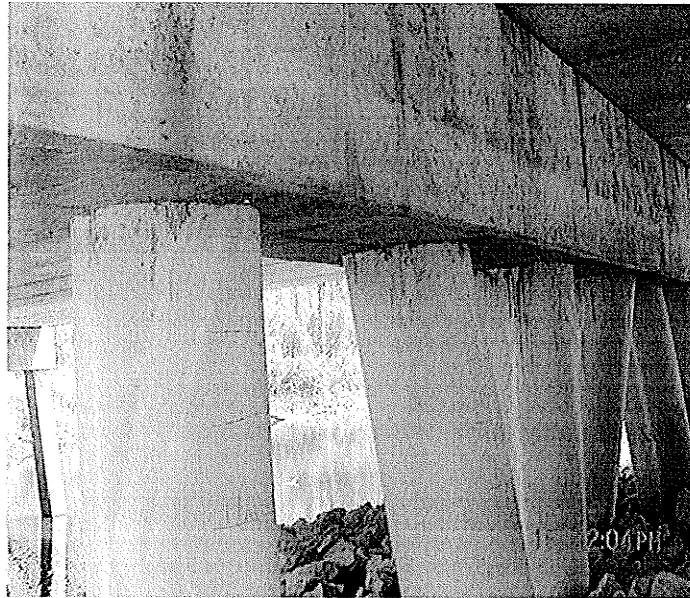
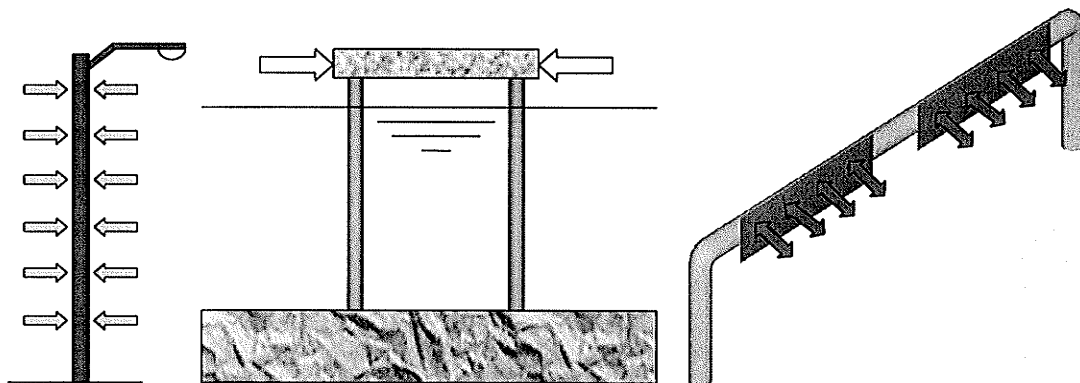


Figure 1-3 Connection between CFPT piles and pier cap beam (Fam et al., 2003b)



Figure 1-4 CFPT beams in Kings Stormwater Channel Bridge, San Diego, California (Seible et al. 1999)



(a) Monopoles

(b) Marine piles

(c) Overhead sign structures

Figure 1-5 CFPTs subjected to reversed cyclic bending loads

## **Chapter 2**

### **Literature Review**

#### **2.1 Introduction**

One of the first attempts to encase concrete in a non-metallic shell, using commercially available PVC and ABS pipes, was reported by Kurt (1978). Later, Fardis and Khalili (1981) tested concrete confined with an FRP jacket made of resin impregnated fiber glass cloth but the authors suggested using the filament winding process to produce the FRP jackets. Concrete filled FRP tubes have been extensively studied since the mid 1990's, and have been used in the field as in marine piles (Parvathaneni et al., 1996 and Fam et al., 2003a), bridge girders (Zhao et al., 2000), and bridge piers (Fam et al., 2003b). This chapter presents a summary of the various research programs conducted on CFFTs.

#### **2.2 Behavior of Axially Loaded CFFTs**

##### **2.2.1 Short CFFT columns**

Unconfined short concrete columns subjected to pure axial load typically have an initial Poisson's ratio ranging between 0.15 and 0.22 and experience a volumetric strain reduction or compaction up to about 90% of the peak stress. Thereafter, the concrete shows a volumetric expansion or dilation due to unstable micro crack growth in the concrete, leading to failure (Teng and Lam, 2004). If the concrete is subjected to an active lateral pressure, the onset of the unstable dilation is delayed and becomes less pronounced and consequently the strength and ductility of the concrete are enhanced. The degree of this enhancement depends on the amount of active pressure. Concrete passively confined by a steel jacket exhibits an increase in strength as the passive confinement

pressure increases until the steel jacket yields. At this point, the confinement pressure remains constant and the concrete behaves as if it were actively confined. Concrete passively confined by an FRP jacket, on the other hand, exhibits a continuous increase in strength due to the continuously increasing confinement pressure resulting from the linear elastic characteristics of the FRP jacket (Fam, 2000). Figure 2.1 shows a comparison between a concrete filled steel tube and a concrete filled GFRP tube, in terms of axial stress-strain response (Fam, 2000).

Most tests conducted on concrete confined with FRP jackets resulted in an almost bi-linear stress-strain relationship with a curved transition zone. At the beginning of the test, the behavior is similar to that of plain concrete, due to the low level of confinement pressure, resulting from the insignificant lateral expansion of the concrete core and the low elastic modulus of the FRP jackets. The stress-strain relationship at this stage is more or less elastic. Once the axial stress reaches the vicinity of the peak unconfined concrete stress, extensive micro cracking occurs and the lateral expansion of the concrete increases and so does the confining pressure as the FRP jacket becomes gradually activated. This zone of gradual activation of the FRP jacket is represented by a curve in the stress-strain relationship. Once the FRP jacket is fully activated, the confining pressure increases as the lateral expansion increases and the stress-strain behavior becomes linear once again (Li et al., 2005). Failure finally occurs when the FRP jacket reaches its ultimate tensile strength in the circumferential direction and ruptures with the concrete core failing almost instantaneously. Extensive experimental results have shown that the measured tensile strength in the hoop direction of FRP jackets at failure is smaller than that obtained from coupon or ring tests conducted on the jacket material. While several researchers

suggested using certain ratios of the ultimate strength obtained from material tests or limiting the tensile strain at failure to a certain value (Teng and Lam, 2004), Fam and Rizkalla (2001a) suggested explanations and analytical procedures to account for the reduced failure strength due to the biaxial state of stress in the jacket.

The amount of strength enhancement depends on the stiffness of the FRP jacket in the circumferential direction. Increasing the stiffness in the circumferential direction could be achieved by increasing the amount of fibers in the circumferential direction or by using fibers with higher modulus of elasticity. In some cases, where pultruded tubes were used, the lack of fibers in the circumferential direction caused splitting of the FRP shell at the onset of the excessive expansion of the concrete core (Kanathrana and Lu, 1998; Fam and Rizkalla, 2001a).

#### **2.2.1.1 Confinement models**

Teng and Lam (2004) classified the existing models in literature into two categories; design-oriented models where the stress-strain relationship is represented in a closed form solution, and analysis-oriented models where the stress-strain relationship is predicted using an incremental and/or iterative numerical procedures.

##### **2.2.1.1.1 Design oriented models**

Nanni and Bradford (1995) suggested a strictly bi-linear stress-strain relationship with the transition point being at a stress equal to the unconfined compressive strength and a strain of 0.003. Similar bi-linear models were suggested by Karbhari and Gao (1997) and Xiao and Wu (2000). A trilinear model was suggested by Chaallal et al. (2003).

Toutanji (1999), Saafi et al. (1999), Jin et al.(2003), Miyauchi et al.(1997), and Lillistone and Jolly (2000) used either Sargin's (1971) general expression, which is given in Equation 2.1, or the special case of the expression known as Hognestad's (1951) parabola which is given in equation 2.2 to represent the first portion of the stress-strain relations prior to the extensive cracking and activation of the FRP jacket in confinement. Toutanji (1999) and Saafi et al. (1999) used separate equations for axial stress and strain, based on the lateral strain  $\varepsilon_r$ , to represent the second portion. Jin et al. (2003) suggested using a linear relation for the second part of the curve which may be ascending or descending. Miyauchi et al. (1997), and Lillistone and Jolly (2000) suggested using a linear relation for the second part of the curve.

$$\frac{\sigma_c}{f'_{co}} = \frac{\frac{A\varepsilon_c}{\varepsilon_{co}} + (D-1)\left(\frac{\varepsilon_c}{\varepsilon_{co}}\right)^2}{1 + (A-2)\frac{\varepsilon_c}{\varepsilon_{co}} + \left(\frac{\varepsilon_c}{\varepsilon_{co}}\right)^2} \quad (2.1)$$

$$\frac{\sigma_c}{f'_{co}} = \frac{2\varepsilon_c}{\varepsilon_{co}} - \left(\frac{\varepsilon_c}{\varepsilon_{co}}\right)^2 \quad (2.2)$$

where;

$\sigma_c$  is the stress in concrete

$f'_{co}$  is the maximum unconfined stress of the concrete

$\varepsilon_c$  is the strain in the concrete

$\varepsilon_{co}$  is the strain in concrete at  $f'_{co}$  (usually taken as 0.002)

$A$  is a constant controlling the initial slope of the stress-strain curve

$D$  is a constant controlling the descending path of the stress-strain curve



Samaan et al. (1998), Arduini et al. (1999), Yu (2001), Cheng et al. (2002), Moran and Pantelides (2002) and Xiao and Wu (2003) used Richard and Abbot's (1975) four parameter curve used for modeling strain hardening, as the basis for their models.

$$\sigma = \frac{(E_1 - E_2)\varepsilon}{\left\{1 + \left|\frac{(E_1 - E_2)}{f_o}\right|^n\right\}^{1/n}} + E_2\varepsilon \quad (2.3)$$

where;

$\sigma$  is the stress in concrete

$\varepsilon$  is the strain in the concrete

$E_1$  is the initial modulus

$E_2$  is the plastic modulus

$f_o$  is the reference stress

$n$  is a shape parameter controlling the transition from the first part to the second part of the curve

#### 2.2.1.1.2 Analysis oriented models

The models of Mirmiran and Shahawy (1996), Spoelstra and Monti (1999), Fam and Rizkalla (2001b), Chun and Park (2002) and Harris and Kharel (2002) are based on the assumption that the axial stress and axial strain of concrete confined by FRP, at any given lateral strain, are the same as those of the same concrete actively confined with a constant confining pressure equal to that provided by the FRP jacket, at this loading level. The stress-strain curve, therefore, crosses a series of stress-strain curves for the same concrete with different levels of confining. All the previously mentioned models adopted the model by Mander et al. (1988) for actively confined concrete. The lateral strain was

determined by different means. Mirmiran and Shahawy (1996), and Chun and Park (2002) used the cubic polynomial equation by Elwi and Murray (1979). Spoelstra and Monti (1999) used a simple constitutive model proposed by Pantazopoulou and Mills (1995). Fam and Rizkalla (2001b) used an equation representing the change of secant Poisson's ratio with confining pressure based on the results of Gardener (1969). Harris and Kharel (2002) based the lateral strain of their model on the test results of FRP confined concrete.

Harmon et al. (1998) developed a model for FRP confined concrete based on the concept of crack slip and separation of concrete, while Becque et al. (2003) proposed a model based on Gerstle's (1981a, b) octahedral stress-strain models, with some modifications.

### **2.2.1.2 Factors affecting FRP confined concrete**

#### **2.2.1.2.1 Effect of loading the FRP jacket**

If both the FRP jacket and the concrete core are loaded simultaneously, the FRP jacket will expand outwards and may tend to separate from the concrete, which reduces the confinement effect. The amount of confinement depends on the difference between the Poisson's ratios of the concrete and the FRP jacket. If the FRP jacket has a larger Poisson's ratio than concrete, no confinement will occur and the behavior will be similar to that of an unconfined concrete. This was reported in cases where  $\pm 35^\circ$  and  $\pm 45^\circ$  angle ply FRP tubes were used (Fam et al., 2002 and Howie and Karbhari, 1995). Additionally, loading the FRP jacket axially produces a state of biaxial stress on the FRP jacket which results in a reduced FRP strength in the circumferential direction as shown in Figure 2.2. Tests conducted by Zhu (2004) comparing loaded and unloaded tubes, however, did not show any significant difference in the strength. The author attributed this to the ample

friction between the FRP tube and the concrete core, which allows stress transfer to the tube. Additionally, the area of the FRP tube in this case was very small compared to the area of the concrete and the elastic modulus of the FRP in the longitudinal direction of the tube was smaller than the elastic modulus of the concrete, consequently the FRP tube carried only a small percentage of the applied load.

#### **2.2.1.2.2 Presence of a hole in the concrete core**

The presence of a hole in the concrete core to reduce the self weight of the member reduces the strength enhancement provided by the FRP jacket (Fam and Rizkalla, 2001a), as shown in Figure 2.3. This is because while the concrete is confined in the outwards direction, it is able to expand inwards in this case, and therefore the effectiveness of the FRP jacket is reduced. By providing another inner FRP tube this inward expansion is reduced and the confinement is increased.

#### **2.2.1.2.3 Effect of concrete strength**

Mandal et al. (2005) studied the effect of the unconfined compressive strength of the concrete ( $f'_c$ ) on the behavior of FRP confined concrete. The experimental program included testing two GFRP tubes filled with two concrete mixes of 26 and 67 MPa compressive strength  $f'_c$ . The researchers also tested 20 concrete cylinders with  $f'_c$  ranging from 31 to 81 MPa wrapped with one or two layers of GFRP or one layer of carbon FRP (CFRP). The study also compared the experimental results to four models available in literature (Samman et al., 1998; Spoelstra and Monti, 1999; Toutanji, 1999; and Fam and Rizkalla, 2001b). The researchers made the following observations and conclusions:

- For low to medium strength concrete (26-55 MPa) the stress-strain curves showed a typical bilinear trend with a large increase in ductility. For medium to high strength concrete (67-80 MPa), as the concrete strength increases, the second part of the curve gradually shifts from strain hardening to a flat plateau, and eventually to a sudden strain softening with a drastically reduced ductility.
- Confinement effectiveness with regard to enhancing strength and ductility of the concrete reduces with increasing the unconfined concrete strength as shown in Figure 2.4.
- For low to medium strength concrete the confinement effectiveness increases with increasing the jacket's hoop modulus, thickness and tensile strength while these effects are insignificant in high strength concrete.
- The models examined were able to predict the stress-strain curves for low to medium strength concrete and were able to capture some influence of the concrete strength on the behavior. The models, however, failed to predict the behavior of confined high strength concrete as they grossly overestimated the ultimate axial strain.

The researchers proposed a simple model to predict the strength of FRP confined concrete and the corresponding strain for concrete of various compressive strengths. They also observed that taking the biaxial state of stress of the FRP jacket at failure into account increases the accuracy of the predictions.

Tests by Li et al. (2005), on E-glass/vinylester tubes with fibers oriented at  $\pm 54^\circ$ , filled with 35, 49, and 82 MPa concrete also concluded that the confinement effectiveness with regard to enhancing the strength and the ductility of the concrete reduces with increasing

the unconfined concrete strength. For example the tubes filled with 49 MPa concrete failed at a stress of 175.5 MPa while the ones filled with 82 MPa concrete failed at a stress of 180.2 MPa. The researchers also observed that the transition zone in the bilinear relation becomes smaller with the increase in the unconfined concrete strength.

### 2.2.2 Slender CFFT columns

Mirmiran et al. (1998) reported test results on the effect of column length on the compressive capacity of concrete-filled GFRP tubes. The specimens used were similar to the ones used in the tests conducted by Mirmiran and Shahawy (1997), except that four different lengths were used. The height-to-diameter ratio of the specimens used were 2:1, 3:1, 4:1, and 5:1. The authors observed that the length-to-diameter ratios within the tested range did not have any significant effect on either strength or ductility of the members. Later, Mirmiran et al. (2001) tested seven concrete-filled GFRP tubular columns of a wider range of slenderness. The specimens were filament wound with the fibers oriented at  $\pm 75^\circ$ . The inner diameter of the tubes was 147.3 mm and the wall thickness was 3.68 mm. The specimens ranged in length from 813 mm to 2743 mm, leading to slenderness ratios of 4 to 36. Three 305 mm long (i.e. short) specimens were also tested. The authors observed that as the slenderness ratio increased from 11 to 36, the strength dropped from about 75% of the equivalent short column to less than 30%, as shown in Figure 2.5. The authors also observed that for slenderness ratio of 11, the axial and hoop strains were 69% and 84%, respectively, of the equivalent short column, while axial and hoop strains were about 15% and 13%, respectively, of the equivalent short column for a slenderness ratio of 36. This indicated that the effect of slenderness on ductility is significantly more than its effect on strength.

### 2.3 Behavior of Flexural and Axial-Flexural CFFT Members

Fam and Rizkalla (2002) studied the flexural behavior of hollow and concrete filled FRP tubes ranging from 89 to 942 mm in diameter, with span lengths ranging from 1.07 to 10.40 m. The study included the effect of total concrete filling, partial filling, and laminate structure of the tubes. The specimens were tested in four point bending, as shown in Figure 2.6, creating a constant moment zone. Concrete filling was shown to prevent local buckling of the tube and increase its strength and stiffness. The load-deflection behavior of concrete filled tubes was almost bi-linear with the cracking load significantly smaller than the ultimate load. The post cracking stiffness is controlled by the laminate structure and the diameter-to-thickness ratio of the tube. The filament-wound tubes were shown to be superior to pultruded tubes, as the latter failed prematurely in horizontal shear. Higher strength-to-weight ratios were achieved by providing a central hole inside the tube. The study showed that excessive slip between concrete and the tube could reduce both strength and stiffness. The study also indicated that the balanced reinforcement ratio of concrete filled FRP tubes depends on the laminate structure of the tube, and is generally smaller for tubes with higher stiffness in the axial direction, as shown in Figure 2.7.

Mirmiran et al. (2000) tested 16 concrete filled FRP tubes under different combinations of axial loads and bending moments. The tests included two types of tubes. Type I tubes were 348 mm in diameter spun cast GFRP tubes with a total wall thickness of 14 mm. Type II GFRP tubes were 356 mm filament wound with a total wall thickness of 6.6 mm. Type I tubes had a total of 40 layers with a symmetric lay-up consisting of  $0^\circ$  and  $\pm 45^\circ$  degrees laminate. Type II tubes had a total of 17 layers with an asymmetric lay-up

consisting of  $\pm 55^\circ$  degrees lamina. The specimens were tested under a constant axial load and an increasing lateral load to produce a bending moment. Type I specimens failed in compression with crumbling and wrinkling of the tube near the mid span region and in some cases longitudinal split rupture of the tube near the support. Type II specimens failed mainly by tube fracture along its main winding angle. At lower levels of axial load, failure of type II specimens was generally controlled by tension, while under large axial loads, concrete crushed in compression. The authors compared the behavior of these specimens to prestressed concrete sections and found that type I specimens compared to 584 mm diameter sections with 20 grade 1862 MPa strands, and type II specimens compared to 460 mm square sections with eight strands of the same grade.

Flisak (2004) tested 15 specimens under axial loads, bending and combined axial loads and bending. Two types of filament wound tubes were used in this investigation. Type I tubes were 326 mm diameter E-glass/epoxy with a thickness of 6.4 mm. Type II tubes were 320 mm diameter E-glass/polyester with a thickness of 5.96 mm. The stacking sequence for type I tubes was  $-88^\circ/+3^\circ/-88^\circ/-88^\circ/+3^\circ/-88^\circ/+3^\circ/-88^\circ/+3^\circ/-88^\circ$  and the stacking sequence for type II tubes was  $+34^\circ/+34^\circ/+80^\circ/+34^\circ/-34^\circ$ . The specimens were tested under pure axial load, pure bending as beams, and under eccentric axial loads [Figure 2.8(a)]. The beam specimens failed by rupture of the fibers in the tension side. The column specimens failed by fracture of the tube under a state of biaxial stress including axial compressive and hoop tensile stresses. Type II column specimen showed minor local buckling which suggests some separation between the tube and the core. This was caused by the high Poisson's ratio of the tubes. The beam-column specimens with large eccentricities failed in the same manner as the beam specimens, whereas the

specimens with lower eccentricities failed by crushing of the tubes in the compression side. The interaction diagram for both types of tubes resembled that of reinforced concrete sections, where by increasing the axial load the ultimate bending moment increases and failure is controlled by tension up to a point of balanced failure, after which, increasing the axial load decreases the ultimate bending moment capacity and failure is controlled by compression, as shown in Figure 2.8(b).

Li et al. (2005) tested E-glass/vinyl ester tubes with fibers oriented at  $\pm 54^\circ$ , filled with 35, 49, and 82 MPa concrete. All specimens were tested in four point bending. The GFRP tubes had an inner diameter of 101.6 mm and a thickness of 5 mm. It was observed that all CFFT specimens had the same ultimate load with the CFFT filled with 35 MPa concrete showing a slightly lower load. The CFFT filled with 82 MPa concrete showed the largest stiffness while the one filled with 49 MPa concrete showed the largest deflection. The authors suggested that this was due to the fact that the 49 MPa concrete had the highest interfacial bond and therefore was able to undergo large deflection prior to failure.

Davol (1998) and Burgueno (1999) tested two 343 mm (inside diameter) CFFT specimens under four point loading. Two types of CFRP tubes were used, tube #1 had a thickness of 9.65 mm and a  $[90^\circ, \pm 10^\circ_2, 90^\circ, \pm 10^\circ_2, 90^\circ]_{\text{sym}}$  layup. This specimen failed in compression due to local buckling at a longitudinal strain of 0.55%. Tube # 2 was designed with additional hoop fibers on the outside of the shell to prevent this buckling failure. The layup for tube # 2 was  $[90^\circ_2, \pm 10^\circ_2, 90^\circ_2, \pm 10^\circ_2, 90^\circ_2, \pm 10^\circ_2, 90^\circ_2, \pm 10^\circ_2, 90^\circ_3]$  yielding a total thickness of 8.89 mm. The specimen failed in compression at a strain of 0.83%.



## 2.4 Behavior of CFFT in Shear

Burgueno and Bhide (2004) presented an analytical approach for predicting the shear response of CFFT with either full or non composite interaction. The behavior was modeled using the modified compression field theory in combination with a smeared shear modulus for cracked concrete. The classical lamination theory was used to model the FRP tube. The approach was based on a sectional layered analysis with an iterative algorithm to achieve equilibrium and compatibility conditions of the composite system, including the cracked behavior of the FRP confined concrete, until first-ply-failure of the FRP tube occurs. The model assumes linear strain distribution across the depth, and resolves the shear stress distribution from the first order mechanics. The analytical response was found to be in satisfactory agreement when compared with experimental data from small-scale and large scale tests conducted by Davol (1998) and Burgueno (1999), although none of these tests failed in shear. The study showed that the concrete in full composite action increases both the stiffness and the shear load carrying capacity of the section and that the concrete carries more than half of the vertical shear force. The ability of the model to accurately predict shear failure, however, could not be assessed since the tests used for comparison were designed to fail in flexure as indicated earlier.

Ahmad et al. (2005) tested five deep CFFT beams with a shear span-to-diameter ratio ( $a/D$ ) of about 1. All specimens exhibited a linear response until initiation of cracking in the concrete, followed by a reduction in stiffness, slippage between the concrete and the tube, and then a nonlinear response until failure. The degree of nonlinearity depended on the fiber architecture, where beams fabricated with angle ply laminates exhibited a more nonlinear behavior than CFFT with fibers close to the  $[0^\circ/90^\circ]$  directions. All specimens

failed in flexure. After the tests were concluded, the tubes were removed and the crack patterns were examined as shown in Figure 2.9 (a). The specimens with low GFRP reinforcement ratio had two major flexural cracks formed under the load point. Beams with high reinforcement ratio, on the other hand, showed additional few fine web-shear and flexure-shear cracks as well. A strut and tie model for deep CFFT beams was also developed. The model showed good agreement with the experimental results. A parametric study concluded that shear failure will be critical only for beams where the  $(a/D)$  ratio is less than one.

Cole (2005) tested CFFT short beams with internal longitudinal steel and FRP rebars, using various  $a/D$  ratios. The study showed that shear failure could happen in this case for  $a/D$  ratios less than 2, as shown in Figure 2.9 (b), due to the presence of longitudinal reinforcement which increases the flexural strength and reduces slip.

## 2.5 Creep Behavior of CFFT Members

Naguib and Mirmiran (2002) investigated the long-term behavior of FRP-confined concrete columns. Shrinkage, interface bond, creep, creep recovery, static and reserve strength of a number of CFFT and fiber-wrapped concrete columns were measured. The study showed that the concrete shrinkage in CFFT columns is quite small and by subtracting the plastic shrinkage of the first day from the experimental values, the drying shrinkage would be rendered negligible. The authors therefore, concluded that it is safe to consider the concrete core of CFFT as sealed or partially sealed with only autogeneous shrinkage to account for. The study also showed that the bond strength at the interface of the concrete core and FRP tube is lower than that in steel tubes. However, the authors concluded based on shrinkage strain and bond strength measurements that for columns

with length-to-diameter ratio of 4:1 or greater the tube could effectively curtail the shrinkage of concrete in the axial direction. The effect of tube confinement on the creep of the concrete core was found not to be as significant as sealing of the concrete core and the stress redistribution that takes place between the concrete and the FRP tube in the axial direction. As the stiffness of the tube increases relative to that of the concrete core, larger stress redistribution can occur over time, yielding a lower creep coefficient. The ACI 209 model (ACI, 1992) was shown to over estimate the creep of FRP-confined concrete. The creep coefficients for CFFT were found to be as low as 22% of those recommended by ACI 209 for an equivalent sealed concrete. The difference between ACI 209 predictions and test results for FRP wrapped columns, however, were not as significant. While no strength degradation was observed for the FRP wrapped specimens, the FRP tube specimens showed approximately 30% strength degradation when tested to failure after being subjected to creep.

## **2.6 Bond issues in CFFT Members**

Naguib and Mirmiran (2002) conducted push out tests on CFFT specimens. The specimens had a maximum bond strength of 0.18 MPa. Once the bond was broken the load dropped but eventually stabilized around an asymptotic value representing the dynamic friction between the FRP and the concrete.

Li et al. (2005) performed push-out tests on GFRP tubes filled with 35, 49, and 82 MPa concrete. The specimens filled with 35 and 82 MPa concrete had a bond strength of 0.42 MPa while the specimens filled with 49 MPa concrete had a bond strength of 0.62 MPa. The researches identified three factors affecting the bond strength, namely chemical bond, dry shrinkage and Poisson's ratio effect. The specimens filled with 82 MPa

concrete would have the highest chemical bond and drying shrinkage due to the high cement content, while having the smallest Poisson's ratio effect due to the small lateral displacement. The opposite would be true about the specimens filled with 35 MPa concrete. The authors suggested that due to the moderate effect of each of the mentioned factors the specimens filled with 49 MPa concrete had the highest bond strength while the other specimens had almost equal strength.

Karbhari et al. (2000) reported push out tests on concrete filled CFRP tubes, where transverse ribs were provided on the inside of the shell. After the attainment of maximum shear strength, the stresses dropped to a residual level of bond strength due to friction or crushing of concrete. Two failure modes could be distinguished. The first one is due to delamination in the tube and shearing off of the ribs. The second one is due to crushing of concrete between the ribs. Both failure types showed a non-brittle behavior and a residual strength close to the maximum strength.

## 2.7 Cyclic and Fatigue Behavior of CFFT Members

Shao and Mirmiran (2004) studied the non linear cyclic response of CFFT beam column specimens under seismic-like loading. Six specimens were tested under constant axial loading and reversed lateral loading in four-point flexure. Three of the GFRP tubes (W series) were fabricated using centrifuge (spin) casting with a total wall thickness of 12.7 mm. The structural wall thickness of these tubes was 7.6 mm and consisted of 40 plies in the form of  $[0^\circ/0^\circ/+45^\circ/-45^\circ]_{10}$  symmetric lay-up. The other three GFRP tubes (Y series) were filament wound with a 5 mm wall thickness and a  $\pm 55^\circ$  fiber orientation. All tubes were made of E-glass and epoxy resin. In each series, one specimen was fabricated with no internal reinforcement, while the other two specimens incorporated approximately

1.7% and 2.5% longitudinal steel reinforcement ratios. The two groups of specimens represented two potential failure modes; a brittle compression failure for the W series and a ductile tension failure for the Y series. Loading was applied in displacement control mode with reversed motion from  $\pm 6.4$  mm up to  $\pm 127$  mm. The hysteretic response curves indicated little energy dissipation for the W series, while a ductile behavior was apparent in the Y series as shown in Figure 2.10. The internal steel reinforcement improved the response of both types of tubes, but the effect was more pronounced in the Y series. Moreover, the study showed that any internal steel reinforcement ratio in excess of 1 to 2% may lead to premature crushing of the tubes. The authors also tested GFRP coupons in order to obtain the hysteretic response characteristics of the tubes. For each type of tube four series of coupon testing were carried out, including monotonic tension, monotonic compression, cyclic tension and cyclic compression. Additional tests were carried out on the Y series with reversed cyclic loading in tension and compression.

The study also included analytical modeling of the CFFT specimens using the fiber element model that was initially developed by Aval et al. (2002) for concrete filled steel tubes. The fiber element is a two dimensional three-node combined element with 13 degrees of freedom, including five at each end node and three at the middle one. The generalized element consists of two frame elements for the concrete core and FRP tube. The fiber element model was incorporated into a general purpose nonlinear finite element program FEAP (Taylor, 1998). The analytical model showed good agreement with the experimental results.

Ahmad (2004) tested eight CFFT specimens under unidirectional bending fatigue. The author also conducted coupon tests to evaluate the creep and fatigue properties of the

tubes. The parameters studied were fiber architecture, load range, reinforcement index and end restraint condition. Four types of tubes were used to manufacture the specimens. The specimens were tested at a certain load level for one million cycles and if failure did not occur, the load was increased. The author made the following observations;

- The rates of stiffness degradation, deflection or damage accumulation of CFFT beam are all significantly higher for the beam with relatively low reinforcement index.
- The rates of deflection growth and stiffness degradation are higher for specimens subjected to the higher load range, even with the same maximum load.
- End restraints prevented the relative slippage between the GFRP tube and the concrete, thereby maintaining the composite action and reducing the rate of stiffness degradation, deflection and damage accumulation which increases the fatigue life of the CFFT specimen.
- The specimen with a  $\pm 34^\circ$  fiber architecture with respect to the axial direction showed a better fatigue performance as compared to the specimen with a  $\pm 55^\circ$  fiber architecture. It also had higher stiffness and lower initial deflection, which resulted in less relative slippage, thereby maintaining a higher degree of composite action between the tube and the concrete core. The specimens with a  $\pm 55^\circ$  fiber architecture experienced matrix cracking and delamination within the first 1,500 cycles, whereas the specimen with a  $\pm 34^\circ$  fiber architecture did not show any delamination even after one million cycles.

The author also made the following conclusions;

- Fatigue life of a CFFT beam without end restraints is related to the amount of stiffness degradation that takes place during its life time, regardless of the variation of the load range and concrete properties. A CFFT beam is expected to fail when its flexural stiffness reaches 40% to 50% of its initial stiffness. For beams with end restraint this value is expected to be lower but this could not be established due to the insufficient amount of experimental data.
- Slippage is probably the single most important factor that dominates the fatigue behavior and fatigue life of CFFT beams. Fatigue life is directly related to the amount of slippage that occurs between the concrete core and the FRP tube. The load range clearly impacts the slippage. The higher the load range, the higher the slippage. Hence, it is important to preserve the composite action between the concrete core and the FRP tube.

An analytical model for the fatigue behavior of CFFT was also presented by the author. The model is adapted from the model developed by Deskovic (1993) for the analysis of hybrid FRP/concrete beams. The model uses layered sectional analysis, while accounting for time-dependent behavior by introducing time-dependent changes in the stress-strain relationships of the materials. The model by Samaan et al. (1998) was used for the confined concrete, while a linear elastic relationship was used to model the FRP tube. The stiffness degradation and creep models developed by Holmen (1982) for unconfined concrete were used to model the cyclic behavior of the concrete, while substituting unconfined concrete strength  $f'_c$  with the confined concrete strength  $f'_{cc}$ . The models by Ogin et al. (1985) for stiffness reduction and Findley (1960) for creep were used to model the cyclic behavior of the FRP tubes.

Karbhari et al. (2000) conducted fatigue testing on Three-Girder/Slab Assemblies consisting of three longitudinal CFFT girders with an integral advanced composite deck made of pultruded E-glass section, as shown in Figure 2.11. Static stiffness characterization tests were conducted to provide a baseline evaluation, before initiation of the fatigue loading of the structure and characterization of the load distribution to the girders by the deck system. The assembly was subjected to two million cycles of fatigue service loading, duplicating the shear force demand on the prototype bridge at the girder-deck interface under full service loads. Analysis of the data indicated that the structure suffered no structural degradation during fatigue loading. This conclusion was further validated as the stiffness characterization static tests were repeated after completion of the 2 million fatigue cycles without any noticeable change in structural response.

## 2.8 Reinforced and Prestressed CFFTs

Parvathaneni et al. (1996) constructed a prestressed CFFT mooring pile. Three 35 mm diameter prestressing DYWIDAG bars were used for to produce a 31.5 MPa prestress level. The unconfined strength of the concrete used was 35 MPa. The high prestressing level (90% of the unconfined concrete strength), referred to as “Super prestressing,” was chosen taking into account the strength enhancement resulting from the confinement effect of the FRP tube.

Fam and Mandal (2006) tested five prestressed CFFT specimens. Two types of GFRP tubes were used. The ratio of the fibers oriented in the axial direction to the fibers oriented in the hoop direction for tube type I used for specimens PCFFT1 and PCFFT2 was 1.73:1, whereas this ratio was 1:1.55 in tube type II used for specimen PCFFT3. The effective prestress level in the concrete was 11, 4.8, and 5.8 MPa for specimens PCFFT1,



PCFFT2, and PCFFT3, respectively. Specimens PCFFT4 was post-tensioned and specimen PCFFT5 was identical to one of the other tests to establish reliability of test results. Specimens PCFFT1 and PCFFT2 failed by splitting of the fibers in the hoop direction on the compression side. PCFFT3 on the other hand failed by rupture of the axial fibers on the tension side. This difference in the mode of failure is attributed to the different fiber architecture of the tubes used. All specimens exhibited large ductility and high initial stiffness, compared to non-prestressed CFFT beams as shown in Figure 2.12. The authors also developed an analytical model to describe the behavior of prestressed CFFT members and develop the full axial load-moment interaction curve.

Cole and Fam (2006), tested seven specimens including five CFFT specimens reinforced with steel, GFRP, and CFRP bars. The other two specimens were conventional circular reinforced concrete sections, one of which was reinforced with steel spirals designed to give the same confinement effect as the GFRP tube and the other had no transverse reinforcement. The tubes used in this study consisted of an eight-layer asymmetric  $[+5^\circ/-88^\circ]$  laminate, with the ratio of fibers oriented at  $5^\circ$  relative to the longitudinal direction, to fibers oriented at  $2^\circ$  relative to the hoop direction being 1:2. The specimens with steel reinforcement failed progressively, exhibiting large pseudo ductility as shown in Figure 2.13, with the tension steel yielding, followed by rupture of the GFRP fibers of the tube in tension associated with a load drop of about 30%. The load started to increase again, due to the continued contribution of the intact compression side of the GFRP tube, until it reached an ultimate strain of 0.022 and crushed at that point in compression. This was also accompanied by a 20% load drop. At this point, the GFRP tube lost continuity in the longitudinal direction and ceased to contribute as longitudinal reinforcement. However,

as the fibers in the hoop direction were fully intact, the tube confined the concrete core. This was associated with the development of hoop tensile stresses to accommodate the internal pressure induced by the expanding and highly compressed concrete core, which would have otherwise crushed and spalled. Eventually, the GFRP tube ruptured in the hoop direction. Once confinement was lost, the concrete core crushed and the load dropped to a level almost identical to that of the control reinforced concrete specimen without a tube. The specimens reinforced with GFRP and CFRP bars failed by rupture of the bottom fibers of the tubes, followed almost instantaneously by rupture of the bottom layer of the bars, while exhibiting little ductility. The researchers also developed an analytical model for reinforced CFFT members capable of predicting the progressive failure of steel reinforced CFFT. The model predictions were in reasonable agreement with the experimental results.

Yu et al., (2006) tested a hybrid FRP-concrete-steel member in flexure. The hybrid member is in the form of a double-skin tube, composed of a steel inner tube and an FRP outer tube with a concrete infill between the two tubes. Fourteen Double-skin Tube Beams (DSTBs) were tested using 4-point bending configuration. The members had an outer diameter of 152.5 mm, and a 69 mm void. The parameters examined were, the concrete strength, the presence of FRP reinforcement bars, the eccentricity of the steel tube and the thicknesses of the steel tube and the FRP tube, respectively. A simple theoretical model based on the plane section assumption and the fiber element approach was also developed and employed to predict the responses of the test beams. The following conclusions were made by the authors;

- The hybrid DSTBs possess a very ductile response. The FRP tube confines the concrete and provides additional shear resistance. The steel tube provides ductile longitudinal reinforcement.
- A DSTB with an eccentric steel tube benefits more significantly from the outer FRP tube than a corresponding DSTB with a concentric steel tube because in the former a larger amount of concrete is in the compression zone.
- Significant slips between the concrete and the two tubes, particularly the steel tube, and associated load fluctuations may occur. Improvements to the bond resistance at both interfaces are desirable.
- The flexural response of a DSTB, including the flexural stiffness, the ultimate load, and cracking, can be substantially improved by shifting the inner steel tube toward the tension region or providing FRP bars as additional longitudinal reinforcement.
- The effect of FRP confinement on concrete in beam specimens is less significant than that in column specimens of identical sections, because of the existence of a strain gradient and a relatively small concrete compression zone.
- The predictions from the theoretical model are in reasonably close agreement with the test results. Differences arise from factors not considered in the theoretical model, including the concentrations of cracks and the slip between the concrete and the two tubes. The development of a more accurate model should take these factors into account and use a more accurate stress-strain model for the confined concrete in DSTBs. Furthermore, a method for predicting the ultimate strain for the stress-strain equation needs to be established.

## 2.9 Drivability and the Effect of Driving Forces on CFFT Piles

Ashford and Jakrapiyanum (2001) studied the drivability of composite piling analytically. Their study included six types of piles; two conventional piles, and four composite piles. The conventional piles included a precast prestressed concrete pile and a hollow steel pipe pile. The composite piles were a plastic encased steel pile, two filament-wound tubes, one of which filled with concrete, while the other was empty, and a tube manufactured using the resin transfer molding process. All piles were assumed to be 12.2 m long. The pile driving was analyzed using the wave equation as coded in the computer program WEAP87 (Goble and Rausche, 1987). Three single acting diesel hammers with different sizes were used in the analysis.

The authors concluded that the composite piles compared favorably with conventional steel and precast prestressed concrete piles and that they are capable of being driven to a 400 kN design capacity with a moderate size hammer. They also concluded that the ultimate capacity of piles composed solely of GFRP material at refusal are 65-75% of the other piles analyzed. This is attributed to their significantly lower impedance, which is the product of the mass density, the cross sectional area, and the compression wave velocity, since the amount of force that can be transferred through the pile to the soil is a function of the impedance.

Iskander et al. (2001) also studied the drivability of FRP composite piles analytically. Their study included three types of piles; reinforced plastic, steel core with plastic casing and concrete filled GFRP tubular piles. The soil profile used for the study was for a typical Manhattan waterfront site. The study was conducted using the computer program GRLWEAP (PDI, 1998) with adjusted input parameters using available driving records.

The study included low capacity short piles, to represent typical fender piles, and high capacity long piles to represent typical load bearing piles. The low capacity short piles were compared to timber piles and the high capacity long piles were compared to steel pipe piles. The authors recommended incorporating residual stress analysis and reduced values of the elastic modulus to account for the polymer's nonlinear behavior, and the use of high damping ratios in analyzing FRP piles. They concluded that composite piling could be driven to reasonable capacities for load bearing piles, and that the drivability of polymeric materials depends on the specific weight and the elastic modulus of the composite section, while the drivability of stiffer materials depends mostly on soil conditions.

Mirmiran et al. (2002) conducted field driving tests on four GFRP tubular piles and a conventional concrete pile. The GFRP tubes were fabricated centrifugally using E-glass and epoxy resin. Two of the GFRP tubes were filled with concrete and two were empty. Of each type, one pile was a single unit and one was spliced. The male and female units of the spliced piles had an overlap of 600 mm, within which the wall thickness was machined to one half of the thickness. The overlap regions were wetted with epoxy in the field before fitting. The empty tubes were fitted with steel cone tips. All piles were instrumented with strain gauges and accelerometers. The single unit concrete filled pile was driven with no problems and suffered no visible damage or separation between the concrete and the tube. The spliced concrete filled pile suffered from buckling at the splice due to lack of proper fit, however, the pile was driven to refusal despite buckling at the splice. The empty piles suffered damage at the top ends during the driving of the piles in sand. The authors also performed an analytical study on the piles using the computer

program Microwave (LL. Lowery, 1993). The parametric study included three types of hammers; light, medium and heavy, and three types of soils; clay, sand and silt. Two different types of soil profiles were studied. In the first profile, 90% of the capacity is provided by end bearing while in the second only 10% of the capacity is provided by end bearing. The study concluded that;

- There is no significant difference between the drivability of empty FRP tubular piles in different soil profiles
- The difference between the drivability of FRP tubular tubes in different soil profiles becomes more pronounced under heavier hammers.
- There is no difference in the drivability of CFFTs and prestressed concrete piles of the same cross sectional area and concrete strength.

Fam et al. (2003b) conducted a test pile program at the site of Route 40 Bridge in Virginia, USA. Two types of piles were tested, a 625 mm diameter circular CFFT pile, and a 500 mm square prestressed pile. Both piles were instrumented with strain gauges in the axial direction at three levels along the length of the piles. Each pile was also instrumented with eight lateral motion sensors to measure the lateral displacement profile of the pile during the lateral load test. Both piles were driven to the refusal depth using a hydraulic impact hammer. After driving, both piles were subjected to axial loads using the Statnamic testing system. This system applies the load to the pile by launching a heavy reaction mass upwards at close to 20g an equal and opposite reaction force acts on the test pile in a gradually increasing manner with a typical duration of 0.2 to 0.3 seconds. Each pile was subjected to three loading cycles with an increasing magnitude of the applied load. The behavior during the last cycle in both piles showed that the

geotechnical capacity of the piles was fully mobilized. The equivalent static load of the prestressed and CFFT piles at failure were 4190 and 4359 kN, respectively. Following the axial load tests lateral load tests were conducted on both piles using the same test setup but placed horizontally as shown in Figure 2.14. Each pile was subjected to four loading cycles with increasing magnitude of the load. The behavior of the piles was similar to that of similar piles statically tested in the lab. For the last two cycles of loading the deflection profiles of both piles were almost bilinear with a sudden change of slope occurring at a depth of about 4.8 m, suggesting that failure have occurred at the location of the change in slope.

## **2.10 Durability and Environmental Effects**

Toutanji and Saafi (2001) investigated the durability of concrete columns encased in PVC-FRP tubes. These tubes are commercially available PVC tubes, externally reinforced with impregnated continuous fibers in the form of hoops at different spacing. Three types of fibers were used, Glass, aramid and carbon. The specimens were subjected to 200 and 400 freeze/thaw and wet/dry cycles. The specimens were then tested under uniaxial compression. The results were compared to those of unexposed specimens. After 200 freeze thaw cycles, the PVC-GFRP tubes exhibited a loss of strength ranging from 4% to 7%, while the PVC-AFRP specimens showed no losses. The PVC-CFRP specimens exhibited an increase in strength ranging from 3% to 9%. The exposure did not affect the bilinear stress strain behavior. After 400 freeze thaw cycles, the PVC-GFRP tubes exhibited a significant loss of strength of up to 18%, while the PVC-AFRP tubes exhibited a loss of strength of about 10%. The PVC-CFRP specimens did not exhibit any loss of strength. The PVC-GFRP and PVC-AFRP specimen tended to reach a

maximum load, and then the capacity decreases very slightly and stabilizes while the axial strain increases until failure, which occurred in a brittle manner.

After 200 wet/dry cycles, the PVC-GFRP specimens exhibited a small reduction in strength of up to 3%, while the PVC-AFRP and PVC-CFRP showed no sign of deterioration. There was also no change in the stress strain behavior or any major loss of ductility in any of the specimens. After 400 wet/dry cycles, the PVC-GFRP tubes exhibited a significant loss of strength of 9-15%, while the he PVC-AFRP tubes exhibited a loss of strength ranging from 6% to 11%. The PVC-CFRP specimens did not exhibit any loss of strength. The stress strain behavior of PVC-GFRP and PVC-AFRP specimens changed from bilinear to almost linear behavior to failure. The stress strain behavior of PVC-CFRP specimens remained bilinear, however, with a reduced ductility.

Pando et al. (2001) outlined a project to study the effect of moisture exposure on CFFT piles. Baseline mechanical properties were evaluated in the axial and hoop directions via tension coupon and split disk tests. Specimens were immersed in water tanks at different temperatures (22° C, 35° C, 45° C, 55° C, 65° C, and 80° C) to obtain the moisture absorption iso-thermal curves and determine the diffusion coefficient. The equilibrium moisture for the studied FRP laminate immersed in 22° C water was estimated to be about 0.43% by weight. Axial tension tests were conducted on specimens immersed in 22° C water for 4, 10, 26, 66 and 185 days. The specimens showed no loss of strength and in some cases even an increase of strength of about 20%. A model was proposed for the moisture diffusion and the relation between the moisture concentration and the strength of the FRP. A method to estimate the loss of strength of the CFFT piles, as a



whole, based on the results of the proposed durability study on FRP coupons was also proposed.

Dutta and Piyush (2002) tested several composite piles including two CFFT piles, designated as specimens A and E under four point bending at  $-30^{\circ}$  C temperature. Subjecting these specimens to low temperature resulted in a slight protrusion (6-12 mm) of the concrete resulting from the mismatch in the thermal coefficients. In addition, a longitudinal crack appeared on one of the tubes of Group E. Specimen A failed in a more brittle manner as compared to a similar specimen type tested at room temperature. Specimen E did not fail under the full capacity of the loading frame (445 kN), and exhibited a large increase in stiffness, compared to a similar specimen tested at room temperature.

In a recent study by Kong (2005) CFFT short columns were subjected to 300 freeze-thaw cycles with and without sustained axial compression loads. All specimens survived the exposure with no major negative effect on the axial strength. Some of the specimens that were subjected to sustained load showed an increase in the axial strength due to the restrained expansion in the longitudinal direction under the freeze-thaw action. Figure 2.15 shows a summary of the test findings.

### **2.11 Connections and Splices of CFFT Members**

Parvathaneni et al (1996) produced a 13.7 m long CFFT pile using three 4.6 m long units, spliced using a 0.6 m long steel tubing matching the inside diameter of the GFRP tubes. Mirmiran et al (2002) constructed a splice by machining the wall thicknesses of the two FRP tube units to half the thickness, forming a 0.6 m long male-female splice. The overlap regions were wetted with epoxy in the field before fitting. It should be noted that

in these cases splicing was done before filling the tubes with concrete and before driving the piles.

Wernli and Seible (1998) performed pull-out tests on rectangular CFRP pultruded bars. Three different types of rod surface treatment and end geometry, shown in Figure 2.16, were chosen to improve the bond behavior at the end of the rods. In the first type, the rod was sand blasted, painted with epoxy and dipped in sand. The surface treatment of the second type was identical to the first type except that two slots were cut along the sides at the end of the rods and the sides were widened so that the ends had a lens shape. The third type also had an identical surface treatment to the first type but with seven longitudinal cuts being made at the end and splayed apart. Tests showed that the bond behavior can be tailored by choosing a certain geometry and surface treatment of the anchorage. It was also shown that by combining the three anchorage types described above, a nearly elastic-plastic resistance during pullout could be produced, which comes close to the elastic plastic behavior of steel during yielding. This behavior, however, could be achieved only in one direction and is irreversible. A splice connecting two CFRP tubes together using CFRP reinforcement cage was also tested. The splice reinforcement thereby consisted of rods having combined sanded and splayed anchor type ends. The spliced tube was filled with concrete and tested in four-point bending. In spite of the brittle nature of FRP, the force-displacement response indicated that failure of the joint was gradual.

Zhu (2004) tested four types of joints for CFFT systems, including GFRP and steel grouted dowels, post-tensioned threaded rods and epoxy glued FRP socket splice. The steel and GFRP grouted dowel splices were constructed by providing ducts in the

concrete during casting, in which the dowels were later inserted and grouted. For the post-tensioned threaded rod splice, threaded rods were inserted in similar ducts and tightened to the desired prestressing level. The epoxy glued FRP socket splice included the concept of male-female joint with tapered ends, which corresponded to the standard joining method in the FRP pipe industry. All splice systems were tested under four point bending and compared to that of an unspliced specimen. The post tensioned specimen showed higher initial stiffness due to the prestressing force. The specimen later underwent continuous softening and experienced significant stiffness loss after the threaded rods yielded. The strain measurements of FRP tube along the span at both top and bottom were quite low, indicating negligible participation of the FRP tube in load transfer, mainly due to the discontinuity of the tube at the joint. On the other hand, hoop strain in FRP tube at the joint showed a certain level of confinement in the concrete core under the post-tensioning force. The specimens with steel and GFFP dowels behaved similarly with the steel dowel specimen having higher stiffness. In both specimens, slip occurred in the dowels and excessive joint opening followed. The strain measurements at the tube revealed that the precast CFFT units did not undergo much bending, but rather deflected as rigid bodies with the mid-span joint opening. However, hoop strain measurement near the joint showed a localized confining effect of the tube on the concrete core in the compression zone. For the FRP socket specimen the behavior was linear elastic before the epoxy started to crack at the bottom of the joint and the load dropped. Further epoxy cracking caused additional load redistributions and an increase of the joint opening was observed with each cracking of epoxy. The specimen failed when the epoxy between the socket and the FRP tube was completely sheared off. In general,

all specimens failed at the joint location and showed an inferior behavior as compared to the unspliced specimen. The author suggested that the use of better quality grouting could improve the behavior of the dowel splices.

Zhu (2004) also tested CFFT column to reinforced concrete footing assemblies. Test matrix for this study included three CFFT columns and a control RC column, all with similar RC footings. The three CFFT specimens included a cast-in-place CFFT column with starter bars from its RC footing, a precast CFFT column with starter bars from its RC footing and grouted ducts, and a precast CFFT column post-tensioned to its RC footing. The author also conducted an analytical study on CFFT using the nonlinear structural analysis software OpenSees. The following conclusions were made;

- Practices of the precast industry can be easily and effectively implemented for the CFFT column construction.
- In comparison to each other, the various CFFT-RC joints performed quite similarly, as long as the FRP tube was properly embedded or implanted into the footing. These joints were proved to be feasible, constructible, and functional for load transfer between a CFFT column and its foundation, even at high levels of lateral drift.
- In comparison with traditional RC columns, all CFFT systems performed much better in terms of strength and ductility as well as energy absorption capacity, under both hysteretic static load and major earthquake records.
- The better performance of CFFT systems was mainly attributed to the confinement effect of the FRP tube, which prevented spalling of concrete. Additionally the embedment of the tube into the footing further improved the

performance significantly, as the tube participated effectively in the axial direction.

- Post-tensioning at the levels provided in the experiments did not particularly improve system performance, compared to the reinforced joint. However, it did reduce the amount of permanent residual deformations.
- Modeling of CFFT columns is quite possible using available analytical tools for traditional RC structures.
- Fiber architecture of the FRP tube has a great influence on system performance, and could be optimized for strength and ductility.
- The parametric study indicates that internal steel reinforcement is necessary to provide adequate ductility and system integrity under seismic loads.
- A minimum thickness of FRP tube (or a maximum diameter-to-thickness ratio) is necessary to achieve composite action in the longitudinal direction.

Zhu et al. (2004) tested two pre-fabricated modular CFFT-RC pier frame specimens at 1/6 scale of a prototype bridge pier system, as shown in Figure 2.17. Each frame consisted of one RC footing, two CFFT columns, two CFFT beam-column T-units, and one CFFT interior beam. Three different types of connections were considered: male-female, dowel reinforced with or without embedment in the footing, and post-tensioned. After testing of the two frames in negative and positive bending, the cap beams were cut from the frames and tested to failure in four point bending.

The authors made the following observations and conclusions;

- The post-tensioned joints exhibited the most robust and ductile behavior, and proved to be one of the preferred method of joining CFFT members.

- The male-female joints, even with dowel bars, lacked the necessary structural integrity in the pier frames, however, better surface preparation for FRP units and higher quality of grouting may improve the response.
- The stiffness of the joint depends largely on the stiffness of the grout and the quality of its placement and that embedment of the CFFT into the footing provides additional benefit for the connection.
- Internal reinforcement might not be necessary for the CFFT members outside of the connection area.
- It is important to maintain tolerances in male-female connections for CFFT joints and embedment for CFFT-RC joints. Therefore, match casting of the precast units may be necessary in field applications.
- The overall feasibility of the precast modular system was demonstrated.

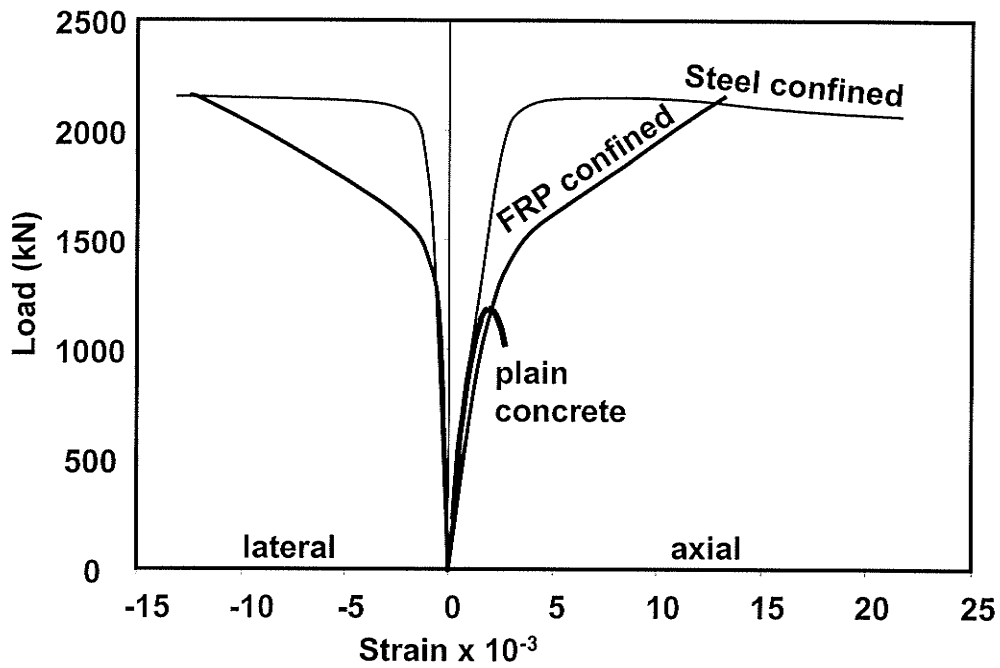


Figure 2-1 Comparison between the behavior of GFRP-confined concrete and steel-confined concrete (Fam and Rizkalla, 2001a)

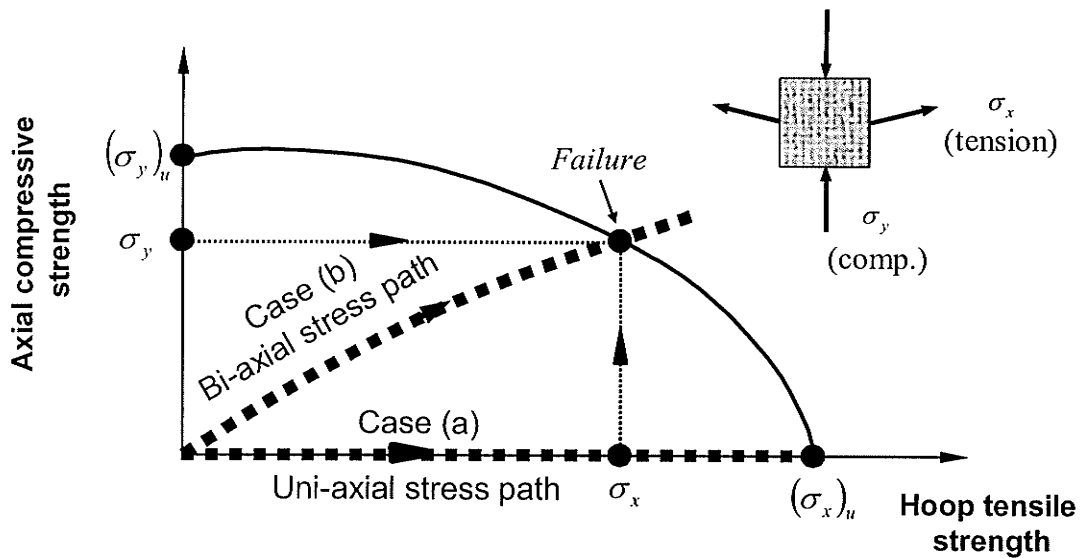


Figure 2-2 Effect of the bi-axial loading conditions on the strength of FRP tube (Fam and Rizkalla, 2001a)

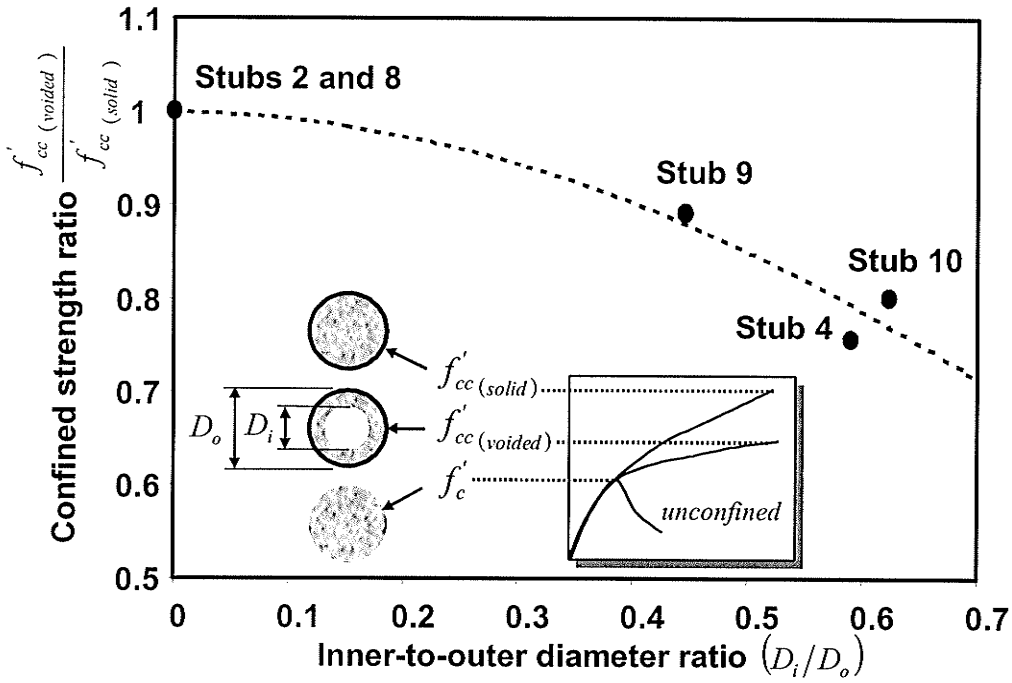


Figure 2-3 Effect of central void on confinement effectiveness (Fam and Rizkalla, 2001b)

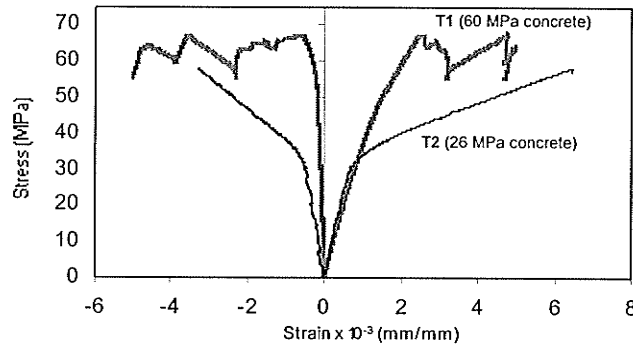


Figure 2-4 Effect of unconfined concrete strength on confinement effectiveness (Mandal et al., 2005)



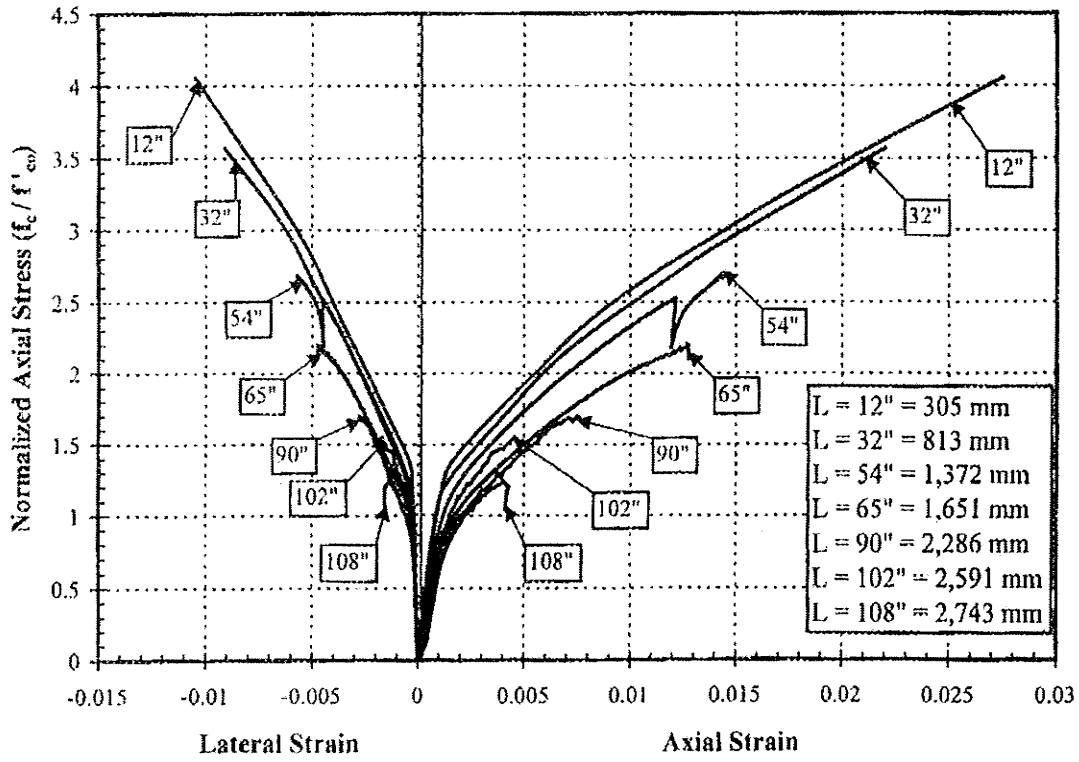


Figure 2-5 Biaxial stress-strain curves for slender CFFT columns (Mirmiran et al., 2001)

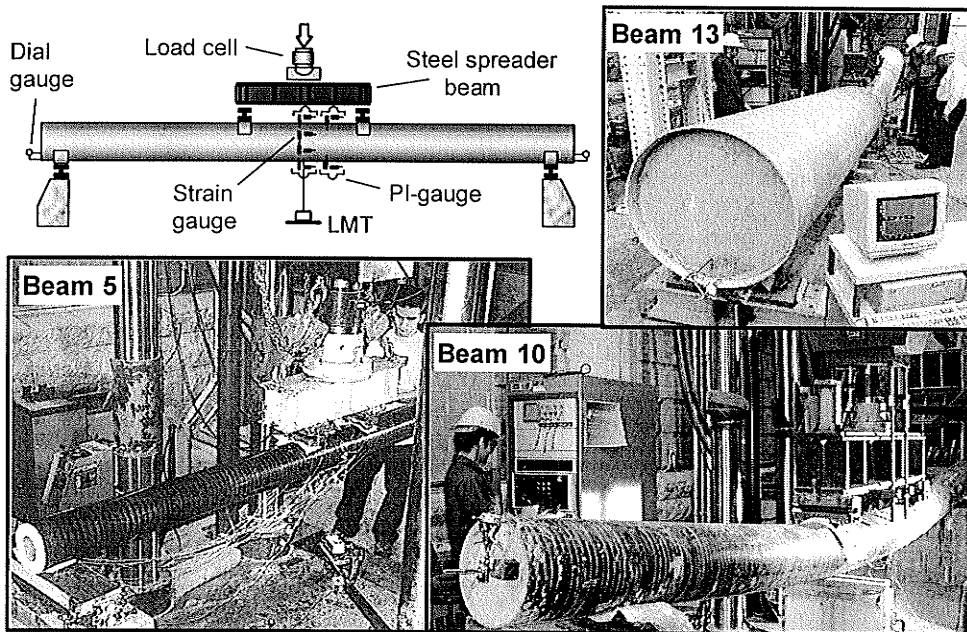


Figure 2-6 Test setup of CFFT in bending (Fam and Rizkalla, 2002)

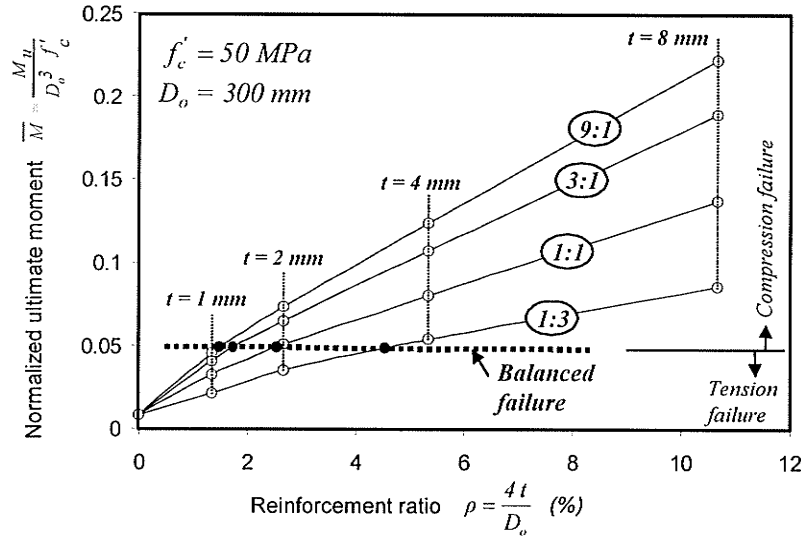


Figure 2-7 Effect of wall thickness and laminate structure of CFFT on the balanced reinforcement ratio (Fam and Rizkalla, 2002)

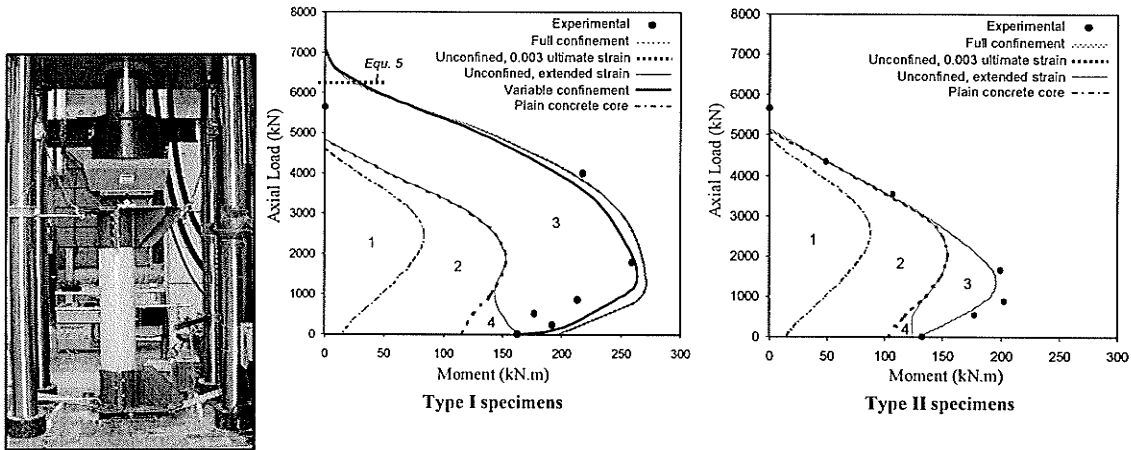


Figure 2-8 Test setup and results of CFFT in combined bending and axial loads (Flisak 2004)

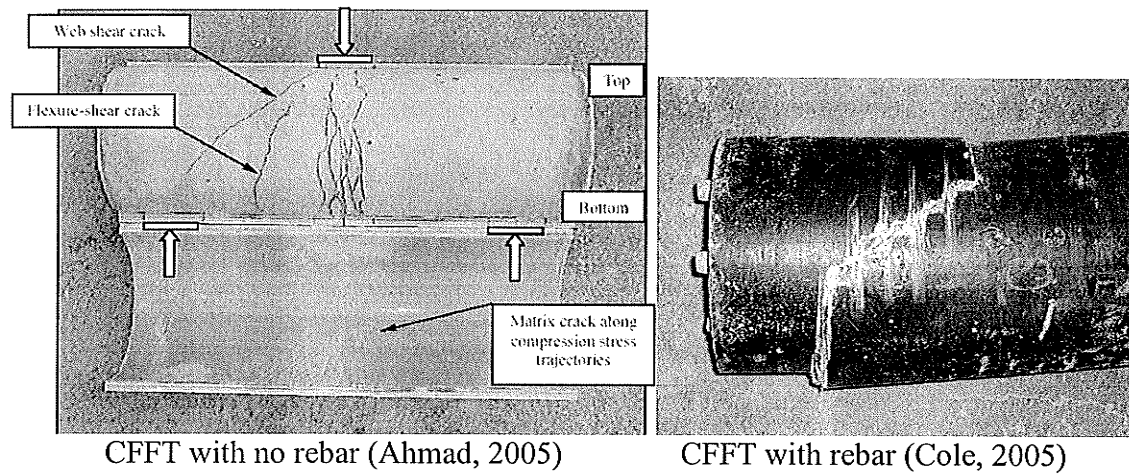


Figure 2-9 Effect of reinforcement on shear behavior of CFFT

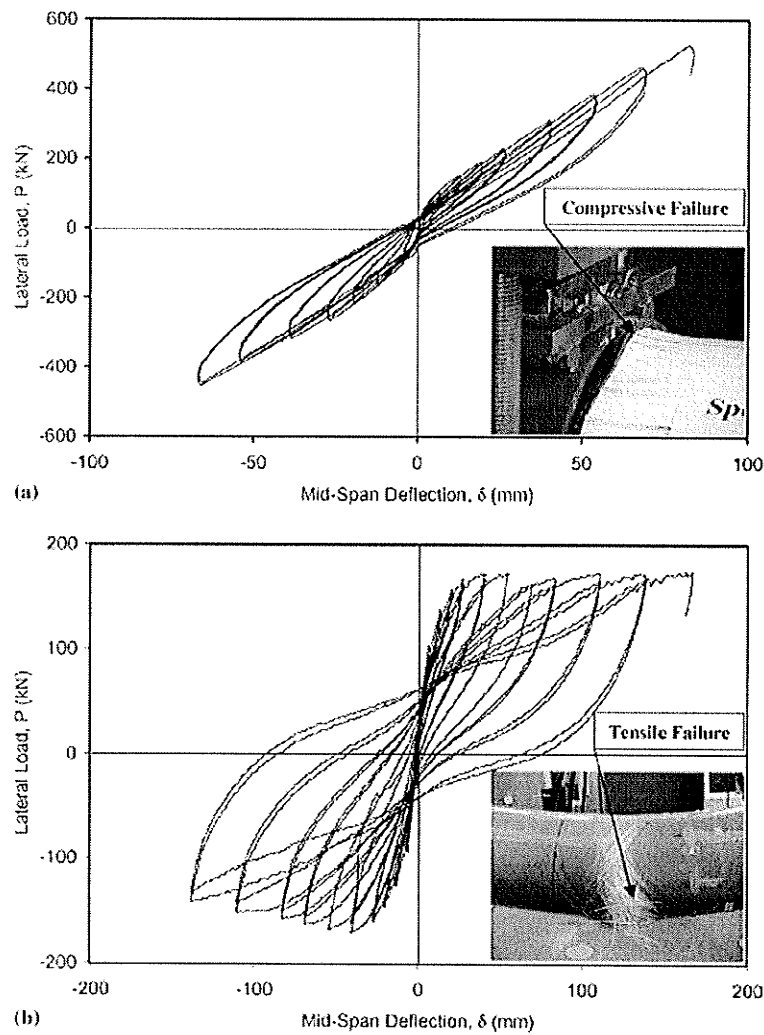
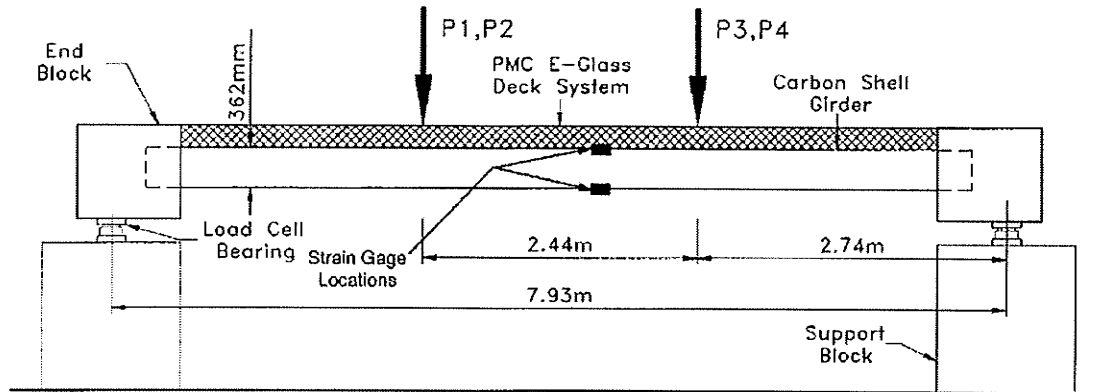
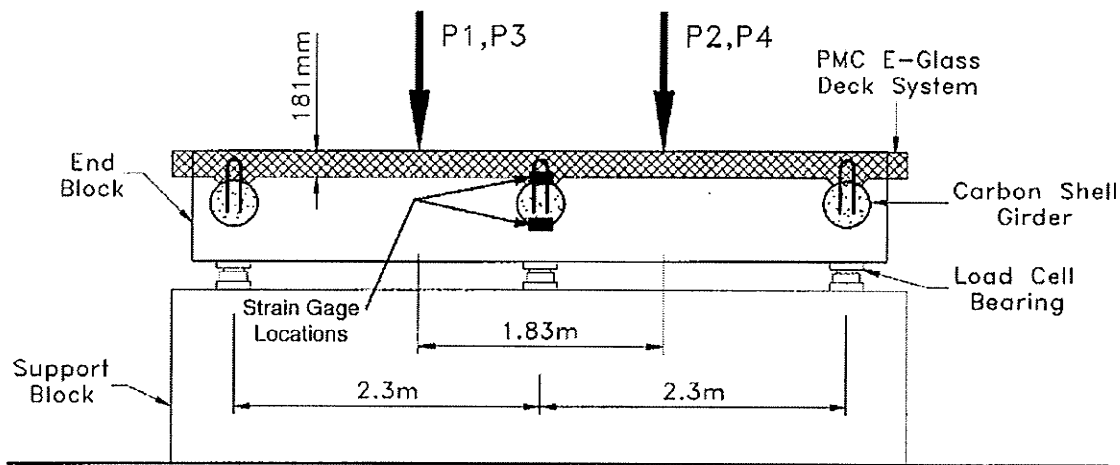


Figure 2-10 Typical hysteretic response of different types of CFFT beam columns (a) W series (b) Y series (Shao and Mirmiran, 2004)



a) Side View



b) Cross Section

Figure 2-11 Three girder beam and slab assembly (Karbhari et al., 2000)

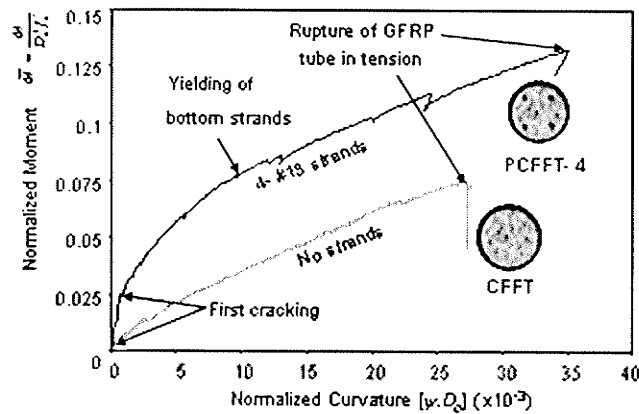


Figure 2-12 Effect of prestressing on CFFT (Fam and Mandal, 2006)

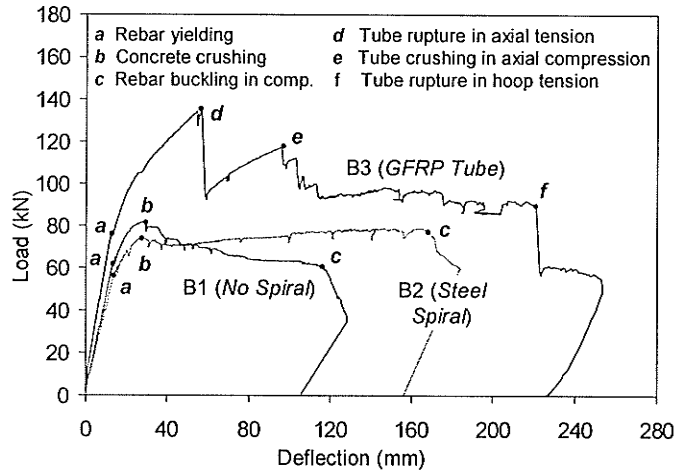


Figure 2-13 Behavior of steel reinforced CFFT compared to regular steel reinforced concrete members (Cole and Fam, 2006)

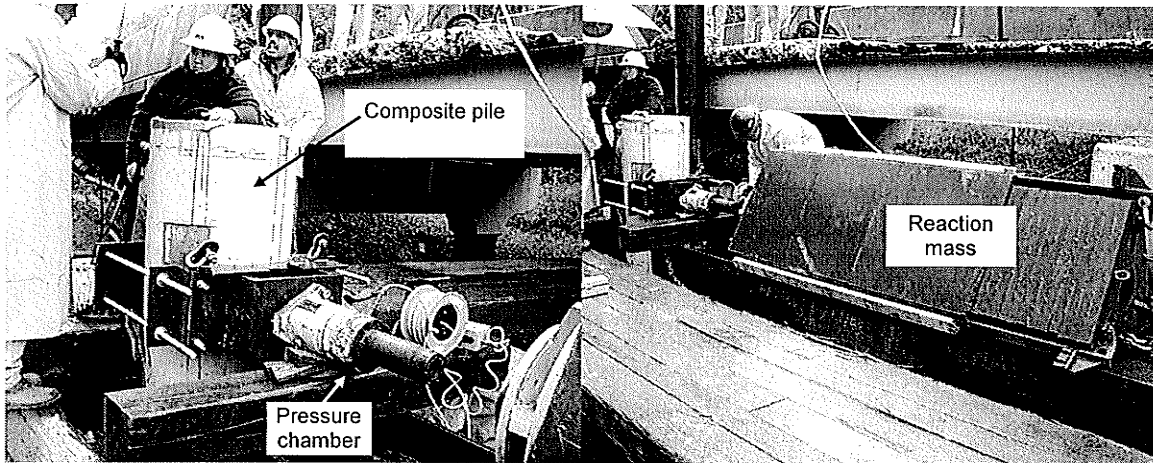


Figure 2-14 Lateral load test using Statnamic test setup (Fam et al., 2003)

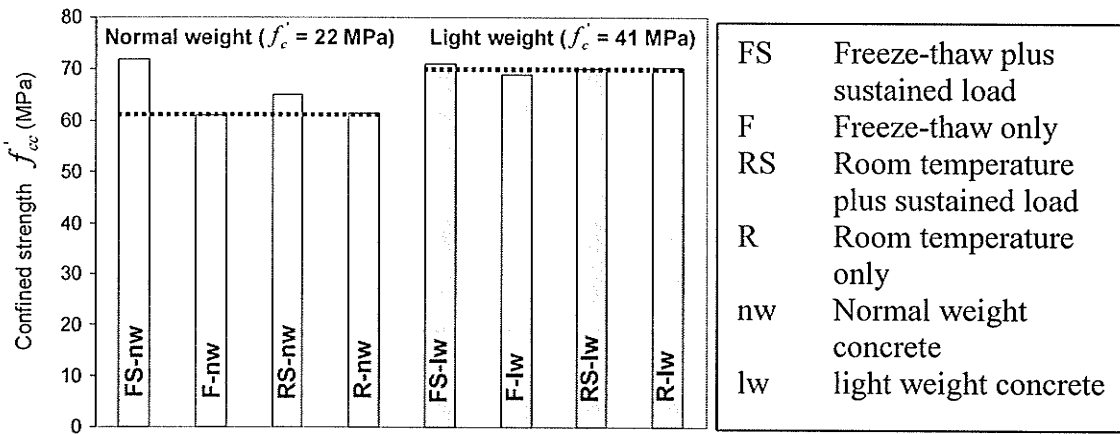


Figure 2-15 Summary of results of the freeze-thaw study on CFFT by Knog (2005)

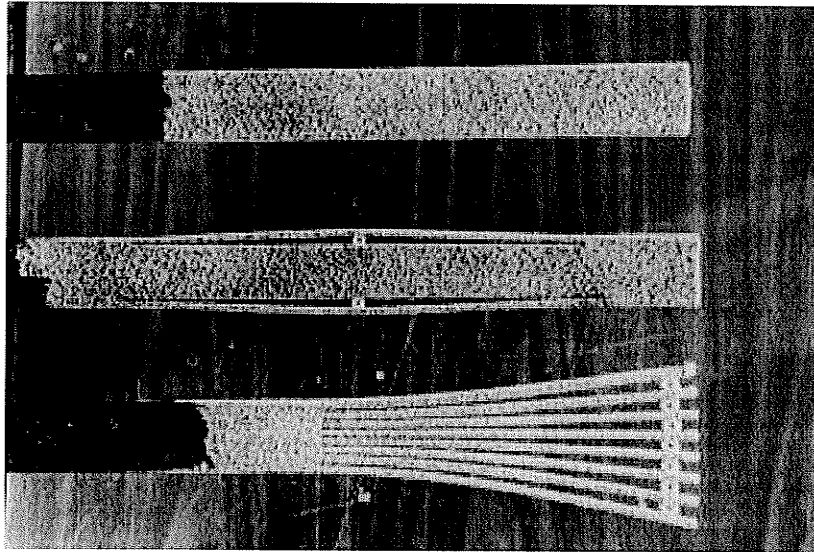


Figure 2-16 Types of end anchorage for splicing CFFT (Karbhari et al., 2000)

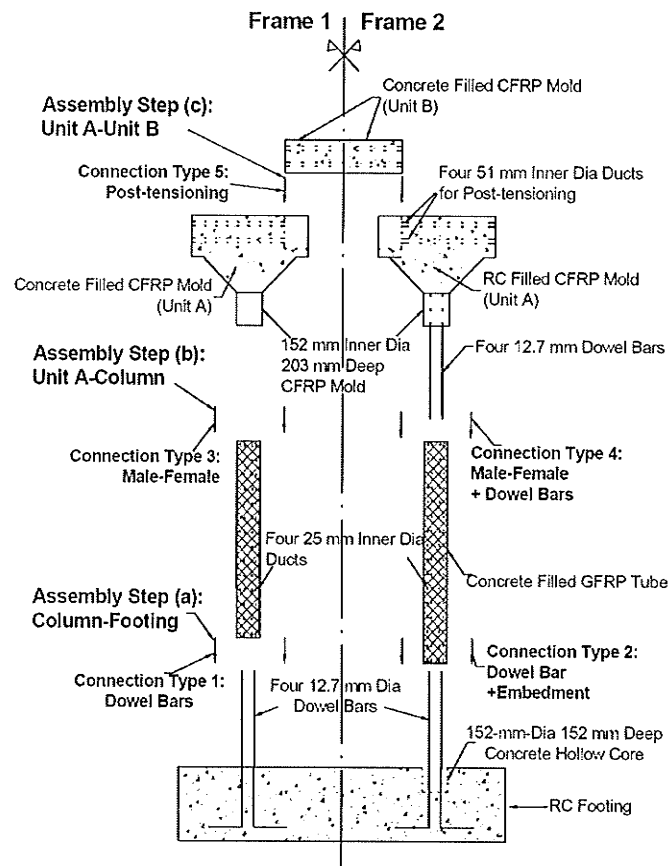


Figure 2-17 CFRT column-pier cap assembly (Zhu et al., 2004)

## Chapter 3

### The Effects of Driving Forces and Mechanical Splicing of CFFT

#### 3.1 Introduction

This chapter presents the details of an experimental program that was undertaken to study the effect of driving forces on CFFT piles and the effectiveness of the proposed splicing system. In this program, four 367 mm diameter and 13.7 m long CFFT piles, one of which was spliced, were driven into the ground and then extracted. The piles were then cut into 6.0 m and 0.3 m long portions, which were used for beam tests, tension and compression coupon tests, tension-tension fatigue tests, and push-off bond tests. Test results were compared to those of control specimens, which were not subjected to driving forces. Beam tests conducted on the 6.0 m long portions were also used to evaluate the structural performance of the splices (Helmi et al. 2005a).

#### 3.2 Materials

This section provides a description of the materials used in the fabrication of the test specimens, including the FRP tubes, concrete and the splice components.

##### 3.2.1 GFRP tubes

Figure 3.1(a) shows the GFRP filament wound tubes used in this study. The tubes had an external diameter of 367 mm and a total wall thickness of 5.7 mm. The tubes were manufactured using the continuous filament winding process adopted by Ameron International in Burkburnett, Texas, USA. E-glass fiber rovings and anhydride epoxy resin were used in manufacturing the tubes. The glass fiber volume fraction as provided

by the manufacturer is 50.8 percent. The stacking sequence of the different layers in the tubes, as given by the manufacturer, is  $[87.3^\circ/1.4^\circ/87.3^\circ/1.4^\circ/87.3^\circ/1.4^\circ/87.3^\circ/1.4^\circ/87.3^\circ]$ , where the  $[87.3^\circ]$  represents the angle between hoop layers and the longitudinal axis, and the  $[1.4^\circ]$  represent the angle between longitudinal layers and the longitudinal axis. A resin burnout test was conducted on a specimen cut from the tube to expose the fibers, as shown in Figure 3.1(b). The test confirmed the data given by the manufacturer except for the orientation of the fibers in the longitudinal direction which was found to be at  $10^\circ$ . The inner surface of the tubes has small circumferential ridges of about 0.3 mm projection and spaced at about 9 mm in the longitudinal direction, as shown in Figure 3.1(c).

The tubes were provided for this study in two lengths, namely 13.7 m and 6.0 m. Approximately, a 10.7 m long section of each of the 13.7 m long tubes has a rough outer surface to enhance skin friction with the soil, whereas the rest of the lengths of the tubes have a smooth surface.

### **3.2.2 Concrete**

The concrete mixture used for filling the GFRP tubes included super plasticizers to achieve high workability and insure a complete filling of the tubes. Additionally, an expansive agent was used to compensate for the shrinkage of concrete after hardening and prevent separation of the concrete core from the tubes. Table 3.1 provides the details of the concrete mix design. Standard cylinders were prepared and tested according to ASTM C39 (ASTM, 1996). The average strength of the concrete cylinders was 59 MPa at the time of beam tests.



### **3.2.3 Splices**

The splice used in this program consists of two 50 mm thick circular plates, as shown in Figure 3.2(a). Eight, 19 mm diameter and 2.7 m long, reinforcing steel bars with threaded ends are screwed into eight threaded holes in the plates, as shown in Figure 3.2(b). The 2.7 m embedment length was essentially over designed to avoid premature pull-out bond failure and also increase the midspan moment capacity beyond the potential moment resistance of the spliced section, to insure that the former does not occur before the latter. Each plate is installed at the end of one GFRP tube such that the bars are embedded inside the tubes, and bonded to the concrete core after filling the tubes. Each plate has four T-shaped grooves around its perimeter. To form a splice, the two parts of the pile are placed together such that the T-grooves are aligned to form an I-shaped groove. An I-shaped key is then inserted in each of the grooves to connect both ends of the splice. Part of the side of each edge of the T-grooves is originally machined to form a lip. After inserting the keys, these lips are hammered towards the keys to secure them in place and prevent their movement during the driving process.

### **3.3 Mechanical Properties of the Tubes**

The mechanical properties of the tubes used in the experimental program, as provided by the manufacturer, are presented in Table 3.2. The following section presents an experimental program that was conducted to determine the mechanical properties of the tubes experimentally.

### 3.3.1 Tension properties in the longitudinal direction

One of the challenges facing researchers and designers is determining reliable mechanical properties of circular filament-wound FRP tubes accurately, especially tensile properties in the longitudinal direction. The tube laminate structure is anisotropic in nature and the fibers are typically aligned at various angles with respect to the longitudinal direction of the tube, which is the principal direction of loading. The most accurate way to determine the tensile properties of the tubes is to test the whole tube in tension. However, performing such a test is quite difficult and costly due to size and gripping difficulties. Therefore, some researchers have used coupons cut from the tubes and shaped according to different ASTM standards (Shao and Mirmiran 2004, Fam et al. 2005), which makes testing easier and more economical and enables researchers to test a much larger number of specimens. However, using standard coupon tests may result in a fiber pull-out or splitting failure mode, which is different from the typical fiber fracture failure experienced when the whole tube is tested in bending and fails in tension. Failure strains of standard coupons have been found to be, in some cases, significantly lower than those measured in beam tests (Mandal 2004). This is attributed to the fact that the fibers are oriented at an angle with respect to the longitudinal axis of the tube, and as such, some fibers may not be continuous between the grips, within the coupon gage length. The following sections present the details and results of the program that was conducted to investigate and compare the use of different types of coupons cut from the tubes for tension tests. ASTM standard size coupons and other coupons of different lengths were examined, both in the fiber direction and in the longitudinal direction of the tube (Helmi et al., 2005b).

### 3.3.1.1 Coupon specimens

Tension coupons of five different configurations were cut from the tubes, as shown in Figure 3.3, and were designated TC1 to TC5. The TC1 coupons were cut in the longitudinal direction of the tubes and were machined according to ASTM D 638 (ASTM, 1991), as shown in Figure 3.3(b). TC2, TC3 and TC4 coupons were also cut in the longitudinal direction and were all 25 mm wide, but varied in length, as shown in Figure 3.3(c). The length of TC2 coupons complied with ASTM standard D 3039 (ASTM, 2000), which states that the length of the specimen between the machine grips should be equal to twice the width plus the gauge length, which is 50 mm, giving a total length between grips of 100 mm. The length of the specimen between the machine grips for coupons TC3 and TC4 were 50 mm and 25 mm, respectively, in order to examine the length effect. In order to obtain a fiber breakage failure mode, the TC5 coupons were cut at an angle with respect to the longitudinal axis, such that the coupons were parallel to the fiber direction, as shown in Figure 3.3(a) and (c). The TC5 coupons had the same dimension as the TC2 coupons. Since the angle between the longitudinal fibers and the tube axis is small ( $10^\circ$ ), it is reasonable to assume that the TC5 coupons could be used to estimate the properties of the tubes in the axial direction (which is the direction of the loading) without any significant error.

### 3.3.1.2 Coupon monotonic testing

At least 3 tests were performed on each coupon type. The monotonic tension tests were conducted using a 1000 kN MTS testing machine equipped with hydraulic grips. Coupons types TC1, TC2 and TC5 were instrumented with a 50 mm extensometer to measure the elongation in the specimens, as shown in Figure 3.4(a). Electric resistance

strain gauges were attached to the surface of coupon types TC3 and TC4, due to the lack of space to mount the extensometer, as shown in Figure 3.4(b). The machine load, stroke and extensometer or strain gauge data were recorded continuously during the test, using a data acquisition system.

### **3.3.1.3 Stress-strain response based on monotonic tension tests**

The average values measured for ultimate strength, Young's modulus and ultimate strains, using the various coupons are given in Table 3.3. Figure 3.5 also shows a sample stress-strain relationship for each coupon type. The strain gauges for coupon types TC3 and TC4 failed early during the test, due to the formation of surface cracks and only the initial part of the curves are shown. All specimens had a slightly nonlinear behavior at the beginning, due to the cracking of the matrix in the hoop layers. All coupon types had almost the same initial Young's modulus for all cases. The nonlinearity of the curves increases for coupon types TC1 and TC2 at a more rapid rate than in coupon TC5, after reaching a stress of 150 to 200 MPa.

### **3.3.1.4 Failure modes based on monotonic tension tests**

As shown in Figure 3.6, failure occurred in coupon types TC1 and TC2 at an angle, mainly by fiber pullout and splitting along the fiber directions, due to the lack of continuity of fibers between the grips. The average stress at failure for the TC1 coupons was 232 MPa, while the average stress at failure for the TC2 coupons was 266 MPa. Failure occurred in coupon types TC3 and TC4 specimens by a combination of rupture of fibers and fiber pullout, due to the shorter coupon length. The percentage of fibers failing in tension, by rupture, seems to increase with decreasing the distance between the grips,

since the band width of the fibers, which are continuous between grips increase. This agrees with the findings of a previous study (Mandal, 2004). The average stress at failure for the TC3 coupons was 279 MPa, while the average stress at failure for the TC4 coupons was 348 MPa. Failure occurred for specimen type TC5, almost entirely by fiber rupture, since all fibers extends from one grip to the other. The average stress at failure for the TC5 coupons was 489 MPa.

### **3.3.2 Compression properties in the longitudinal direction**

Five 25x150 mm specimens were cut in the longitudinal direction and tested according to ASTM D 695 (ASTM, 1996). The specimens were tested in a 1000 kN MTS machine equipped with hydraulic grips. The length of the specimens between the grips was 50 mm. The specimens were instrumented in the same way as the TC3 and TC4 tension specimens.

Figure 3.7 shows a typical stress-strain relation for one of the specimens. The specimens failed by crushing accompanied by splitting. The measured ultimate compressive strengths of the coupons were, 275 MPa, 274 MPa, 272 MPa, 322 MPa, and 276 MPa with an average of 284 MPa.

### **3.3.3 Tension properties in the circumferential direction**

Three 50 mm wide ring specimens were tested using the split disk method according to ASTM D 2290 (ASTM, 2004), as shown in Figure 3.8(a). The specimens failed by fiber breakage in the circumferential direction, as shown in Figure 3.8(b). The average measured ultimate tensile strengths were, 258 MPa, 247 MPa, and 219 MPa, giving an average hoop tensile stress of 241 MPa.

### **3.4 Description of CFFT Pile Specimens and the Fabrication Process**

Four of the 13.7 m long tubes were used to fabricate the piles that were driven into the ground, which are identified as piles P1 to P4. The tube used for pile P3 was cut into two sections of lengths 10.7 m and 3 m to form a spliced pile. The 6.0 m tubes were used to fabricate the control specimens, which were not driven, and are identified as piles C1 to C5. Piles C4 and C5 were each cut into two 3 m long sections, to provide spliced control specimens.

The specimens were fabricated at LaFarge Canada precast plant in Winnipeg, Manitoba, Canada. The tubes were plugged at both ends using circular wooden plugs, shown in Figure 3.9(a,b). A 100 mm diameter circular hole was provided within one plug in order to facilitate pumping of concrete into the tube. The steel splice plates of pile specimens P3, C4, and C5 were used as bottom plugs, as shown in Figure 3.9(c). The tubes were then placed on an inclined surface and concrete was pumped through the upper end plug, as shown in Figure 3.10. After the tubes were filled, the opening at the top plug was sealed.

### **3.5 Driving, Splicing and Extraction of CFFT Piles**

After curing for 21 days, piles P1 to P4 were shipped to the yard of Agra Foundations Company in Winnipeg, Manitoba, Canada, and were driven into the firm silty clay ground, using the same procedure and equipment conventionally used for driving pre-cast prestressed concrete piles. A Linkbelt LB520 hammer with a rated energy of 3665 kg.m was used for pile driving. The driving force was applied to the entire cross-section, including the tube and concrete core, using a 50 mm thick wooden cushion. Piles P1, P2 and P3 were driven to the end of their lengths. Afterwards, a short steel mandrel was

added and the driving continued to the refusal depth of the soil, which was about 14.3 m. Pile P4 was driven to a depth of 12 m only, in order to perform a skin friction test. The details and results of this skin friction test are beyond the scope of this thesis. Figure 3.11(a,b) show the pile driving process. For spliced pile P3, the longer section ( 10.7 m long) was first driven all the way into the ground, the shorter section was then connected through the splice and driving was continued, as shown in Figure 3.11(c and d).

In order to extract the driven piles from the ground, four holes were drilled around each pile, using a 600 mm diameter auger to relieve the soil pressure, as shown in Figure 3.12. The piles were then pulled out of the ground using a crane. A visual inspection of the piles showed no signs of damage on the surfaces of piles P1, P2 and P3, while Pile P4 suffered from damage by the auger during the drilling, and hence the damaged part of pile P4 was not included in any further testing.

### **3.6 Description of Test Specimens Extracted from the Piles**

#### **3.6.1 CFFT beam specimens**

The objectives of this group of tests are: (1) to examine the effect of driving stresses on the flexural behavior of CFFT piles, (2) to evaluate the structural performance and adequacy of the splice described earlier, and (3) to examine the effect of driving stresses on this type of splices. It is worth noting that CFFT piles are mostly used in corrosive marine environments, where they are generally subjected to high bending moments and minimum axial compression loads, as in the case of fender piles. As such, bending tests were used to examine this type of piles.

Six beam specimens were cut from the piles using a diamond tip concrete saw, as shown in Figures 3.13 and 3.14, including three spliced and three unspliced beam specimens.

Table 3.4 presents a summary of the beam specimens. The specimens are given identification codes such that 'B' and 'S' indicate unspliced and spliced specimens, while 'P' and 'C' indicate driven and control specimens (undriven), 'U' and 'L' indicate specimens cut from the upper and lower ends of the driven piles and 'x' and '+' represent the orientations of the four keys in the spliced specimens during testing. Table 3.4 also shows the piles, from which the specimens are cut.

### **3.6.2 CFFT push-off specimens**

The objective of these tests is to evaluate the bond strength between the concrete core and GFRP tube and examine any negative effects of driving forces on bond strength at three locations along the length of the driven piles, namely the top, middle and bottom. The 27 specimens used for these tests are 300 mm long and were cut from both the control and driven piles. Table 3.5 provides summary of the different specimens, where 'C' and 'P' indicate control and driven piles and 'T', 'M' and 'B' indicate top, middle, and bottom of the pile. For example, C1B indicates a specimen cut from control pile C1 from the bottom end and P4M1 and P4M2 indicate two similar specimens cut from the middle of driven pile P4.

### **3.6.3 GFRP tension, compression and tension-tension fatigue coupon specimens**

The objective of these tests is to determine the effect of driving forces on the GFRP tube by measuring any variation that occurs in the tensile and compressive strengths in addition to the fatigue life of tension-tension fatigue coupons cut from the GFRP tubes. Six specimens were cut in the longitudinal direction, and six specimens were cut in the direction of the fibers. The coupons were cut from the push-off specimens taken from the



piles, after the push-off tests were concluded. Three of the six longitudinal strips were machined to the same dimensions as the TC1 tension coupons shown in Figure 3.3(b), while the other three were made into 150 x 25 mm coupons for compression tests. The other six specimens were cut and prepared in the same way as the TC5 tension coupons shown in Figure 3.3(c). Three of the specimens were used in tension tests while the other three were used for tension-tension fatigue tests. The fatigue specimens, however, were 15 mm wide. It should be noted that the fatigue tests described here are mainly to assess the effect of the driving stresses and only the control specimens were used in a larger fatigue study in this project, which will be discussed in detail in chapter 4. In total 54 TC1 type tension specimens, 61 TC5 type tension specimens, 56 compression specimens, and 55 tension-tension fatigue specimens were tested. Although the TC1 type specimens underestimate the actual tensile strength of the tubes as discussed earlier, the tests were conducted in order to obtain a relative comparison between the driven and the undriven conditions. As indicated in Tables 3.6 to 3.9, the specimens used were given the same identification as their respective push-off specimens

### **3.7 Test Setups and Instrumentation**

#### **3.7.1 Beam tests**

The unspliced beam specimens were tested under four-point bending over a span of 5 m and the distance between the two applied loads was 1 m, as shown in Figure 3.15. The spliced beam specimens, on the other hand, were tested under three-point bending over a span of 4.5 m and the splice was positioned at a distance of 550 mm from mid span, as shown in Figure 3.16. This setup was chosen so that the splice would be subjected to a combined high bending moment and shear force, and at the same time be far from the

disturbed region at the loading point. All test specimens were simply supported on roller supports. A 5000 kN MTS testing machine was used to apply the load under stroke control at a rate of 1.5 mm/min for the unspliced specimens and 2.5 mm/min for the spliced specimens. Figure 3.17 shows a general view of the test setup for specimen BP2L. Electric resistance foil strain gauges were attached to the outer surface of the FRP tube in the longitudinal direction of the tubes, as shown in Figure 3.18. Strain gauges were also attached to the outer surface of the four I-shaped keys connecting both ends of the splice. Two Linear Variable Displacement Transducers (LVDTs), were mounted on opposite sides at mid span for all specimens to measure deflection. Two additional LVDTs were also mounted at a distance of 550 mm from mid-span in both directions in the case of the spliced specimens, as shown in Figure 3.19(a). LVDTs were also mounted on the ends to measure slip between the concrete core and the FRP tube, as shown in Figure 3.19(b). The load was measured using a load cell integrated within the testing machine. A Data Acquisition System was used to record the data continuously during the test.

### **3.7.2 Push-off tests**

For the push-off tests, the specimens were positioned on top of a 330 mm diameter flat steel plate such that it would be in contact with the concrete core only. On top of the specimen, a steel plate with a circular void slightly larger than the inner diameter of the GFRP tube was positioned such that it would rest on the tube only and would not bear on concrete during the test. The load was applied to the plate using a 1000 kN MTS machine. A minimum of three LVDTs were positioned on top of the plate to measure slip during the test. The Load was measured through a load cell integrated within the testing

machine. The data was continuously recorded during the test using a Data Acquisition System. Figure 3.20 shows the push-off test setup and instrumentation.

### **3.7.3 GFRP coupon tests**

A 134 kN Baldwin universal testing machine was used for TC1 type tension coupon specimens, whereas a 1000 kN MTS testing machine equipped with hydraulic grips was used for the TC5 type coupons and the compression coupon tests. The load was applied monotonically up to failure. The maximum load was recorded at failure.

A 25 kN MTS table top machine was used for the tension-tension fatigue tests. The specimens were tested using a sine wave tension-tension fatigue loading scheme with maximum loads of 50% of the average monotonic ultimate load of the coupons, and a minimum load equals to 10% of the maximum fatigue load. The specimens were tested to failure, and the number of cycles at failure was recorded.

## **3.8 Test Results and Discussion**

### **3.8.1 CFFT beam tests**

#### **3.8.1.1 Load-deflection behavior**

Figure 3.21 shows the load-deflection behavior for the three unspliced CFFT specimens, BC2 (undriven) and, BP2U and BP2L (driven, upper and lower ends). The cracking moment, as indicated by control specimen BC2, is very low (18 kN.m), compared to the ultimate load (200 kN.m). Also, the stiffness of the specimens exhibits a slight gradual reduction up to failure. This is attributed to the non-linear characteristics of the concrete core as well as the GFRP laminate structure of the tube. The GFRP layers in the circumferential direction fail earlier than the longitudinal layers, resulting in softening of

the GFRP tube, which was also reported by Fam et al (2002). The behavior shows several minor load drops, which could be attributed to gradual cracking of the concrete core or minor slip between concrete and GFRP tube. These load drops are small in magnitude, which suggests that adequate bond between the tube and the concrete was maintained. This was also confirmed by the insignificant slip measurement, as will be discussed. By comparing the behavior of the three specimens it is noticed that the two specimens from the upper and lower ends of the driven pile, specimens BP2U and BP2L, did not show distinct cracking points similar to the control specimen BC2, which indicate that both specimens were likely cracked during the driving process. Most importantly, is that the driving process appears to have insignificant effect on the stiffness of the specimens, and only a very small reduction (5.5%) on the ultimate moment capacity of the pile. This minor reduction is more pronounced in the upper end of the pile. The ultimate moments based on maximum loads for specimens BC2, BP2L and BP2U were 200, 195 and 189 kN.m, respectively.

Figure 3.22 shows the load-midspan deflection behavior of the spliced CFFT beam specimens SCx and SC+ (undriven), and SP3Ux (driven). At load levels of about 175 to 200 kN, the specimens exhibit considerable reduction in stiffness, as a result of initiation of yielding in the bottom steel keys and rebar of the splices. The behavior of control specimens SCx and SC+ indicates that the orientation of the splice keys with respect to the direction of loading has a very small effect on ultimate load, where the '+' pattern results in a slightly higher load than the 'x' pattern. The behavior of the spliced beam from the upper end of the driven pile, SP3Ux, indicates that driving forces have very small effect (4% reduction) on the strength of spliced piles. The measured moments at the

splices for specimens SCx, SC+ and SP3Ux at failure were 215, 221, and 207 kN.m, respectively. All these values are slightly higher than the ultimate moment capacity of the unspliced and unreinforced specimens BC2, BP2U and BP2L, by about 7%. As such, this type of splice was successful, and in fact is considered optimum, in terms of developing an equivalent but slightly higher flexural strength to the CFFT pile. It should be noted, however, that the length of rebar used to anchor the end plates is over designed, as indicated earlier. Further research could lead to optimizing the rebar embedment length, especially when realizing the beneficial confinement effect of the tube. As will be discussed later, failure of spliced specimens occurred at the splice location and not at the maximum moment at mid-span. This is attributed to the presence of the eight-19 mm rebar, which increased the moment resistance of the CFFT. For example, specimen SCx reached 291 kN.m at mid-span, which is significantly higher than the moment resistance of unspliced, and hence unreinforced specimen BC2 (200 kN.m).

#### **3.8.1.2 Load-slip behavior**

The load-slip diagrams for the unspliced specimens are represented in Figures 3.23 to 3.25. Several jumps appear in some of the curves, which could be associated with cracking in the concrete core. Some of these jumps correspond to load drops in the load deflection curves. The slip increased rapidly prior to failure for specimens BC2 and BP2U, suggesting some loss of bond. However, the total measured slip in any of the beams did not exceed 0.025 mm, which suggests that these specimens have a very good composite action.

The spliced beam specimens, however, did not experience any slip until the load reached 200 kN as shown in Figures 3.26 to 3.28. The total slip prior to failure was less than 0.11 mm.

### **3.8.1.3 Load-strain behavior**

The strains in the longitudinal direction recorded from the top and bottom strain gauges of specimens BC2, BP1U, and BP1L are plotted versus the load in Figure 3.29. The diagram shows a drop in the load at about 18 kN corresponding to the first cracking load of the concrete for specimen BC2. The figure, however, does not show similar behavior for specimens BP1U and BP1L, indicating that the concrete in both of these specimens was cracked before the test, due to pile driving as indicated earlier when discussing the deflection behavior. The load-strain relation is slightly nonlinear up to a load of about 160 kN, after which, the nonlinearity increases and is corresponding to the points of increased slip. The bottom strain at the time of beam failure was not recorded due to the failure of strain gauges just before the specimens reached their maximum load. Figure 3.30 shows the load versus top and bottom tube strain relations for all of the spliced specimens. It is observed that the relation is linear until the keys reach yield, and then becomes nonlinear. The orientation of the keys and the driving do not seem to have any significant impact on the strain behavior of the tube.

The load versus bottom key strains relation is shown in Figure 3.31 for specimens SCx and SP3Ux and in Figure 3.32 for specimen SC+. From those figures it is noticed that the curves have a toe at the beginning, which indicates that it takes some load until the keys develop full interlock. The relation then becomes linear until the yield point is reached,

where the relation becomes non-linear. The behavior also shows some strain hardening before failure.

#### **3.8.1.4 Failure modes**

The unspliced beam specimens failed in tension within the constant moment region. Several snapping sounds were heard as the fibers began to rupture, followed immediately by a sudden failure, as shown in Figure 3.33. The specimens failed by rupture of the longitudinal fibers in tension, accompanied by splitting of the circumferential fibers. The spliced specimens, on the other hand, failed also suddenly but due to fracture of the steel reinforcement bars of the splice at the threaded ends mounted into the steel plates of the splice. Failure was accompanied by some slippage between the concrete core and the GFRP tube at the interface with the steel plate and formation of a small crushed zone on the top part of the tube, as shown in Figure 3.34.

#### **3.8.2 CFFT push-off tests**

The maximum measured load and maximum bond stress for each specimen are presented in Table 3.5. The bond stress  $\sigma$  at each load level is calculated using the following formula:

$$\sigma = \frac{P}{\pi D_i (h - s)} \quad (3.1)$$

Where  $P$  is the load,  $D_i$  is the inner diameter of the tube,  $h$  is the height of the specimen, and  $s$  is the slip at load level  $p$ . In general, the ultimate bond strength ranged from 0.51 to 0.83 MPa. The standard deviation for each group is also given in Table 3.5. Although some scatter of test data is observed due to the sensitive nature of bond, by grouping the specimens into control specimens and specimens cut from top, middle and bottom

sections of the piles, and taking the average for each group, it could be observed that the driving had no effect on the bond strength.

The load-slip curves for all the push-off specimens are plotted in Figures 3.35 to 3.40. All specimens experience an initial linear relation, followed by a sudden load drop, in some of the specimens, possibly due to the loss of adhesion. The load reaches a peak value and then shows a series of peaks and valleys, which are quite distinct and easily recognized in some specimens, more than others. The distance from peak to peak or valley to valley for all specimens, generally is almost constant and has a value of about 9 mm. This value is equal to the spacing of the internal ribs in the inner surface of the tubes, shown in Figure 3.1(c). This behavior indicates that once friction and adhesion between the concrete core and tube are broken, usually at very small values of slip, the mechanical interlock mechanism becomes quite effective as slip progresses. The series of peaks and valleys correspond to the concrete core riding over the ridges in a progressive manner. It is important to note that the bond strength, reflected by the peak loads, is maintained, even at very large values of slip (25 mm). It is concluded that internal ribs enhance the bond substantially and prevents total loss of bond strength once the maximum friction and adhesion strengths have been reached.

### **3.8.3 GFRP tension, compression and tension-tension fatigue coupon tests**

The ultimate loads recorded for all tension and compression tests are presented in Tables 3.6 to 3.8, while the number of cycles to failure for the tension-tension fatigue specimens are presented in Table 3.9. By grouping the specimens cut from control specimens and coupons cut from top and bottom ends of the driven piles and taking the average, some observations could be made.



The average failure stress for the control TC1 type tension coupon specimens was 237 MPa, while the average failure stresses for the top and bottom specimens, respectively were 230 MPa and 234 MPa, yielding a loss of strength of 3% and 1% for the top and bottom specimens respectively. The average failure stress for the control TC5 type tension coupon specimens was 486 MPa, while the average failure stresses for the top, middle, and bottom specimens, respectively were 459 MPa, 448 MPa, and 438 MPa, yielding a loss of strength of 5.6%, 7.8%, and 9.9% for the top, middle and bottom specimens, respectively. The average failure stress for the control compression coupon specimens was 284 MPa, while the average failure stresses for the top, middle, and bottom specimens, respectively were 300 MPa, 285 MPa, and 281 MPa, yielding a loss of strength of 1% for the bottom specimens, and an increase for the top and middle specimens. The average number of cycles at failure for the tension-tension fatigue coupon specimens was 35,153 cycles, while the average number of cycles at failure for the for the top, middle, and bottom specimens, respectively were 45,101 cycles, 44,757 cycles, and 44,829 cycles indicating an increase in the number of cycles to failure as compared to the control specimens.

Given the scatter of test data, one can only conclude that, generally, the driving stresses have insignificant effect on mechanical properties of CFFT piles.

Table 3-1 Details of concrete mix used to fill the tubes

LaFarge type 10 Cement (kg)	400
Sand (kg)	835
20 mm- 5mm Stone (kg)	970
Water (kg)	145
Master Builders 322N (ml)	1600
Master Builders MBVR (ml)	120
CONEX (kg)	11.3
Total Air (%)	5 ± 1.5

Table 3-2 Mechanical properties of the GFRP tubes as provided by the manufacturer (Lancaster Composite, Inc.)

Young's modulus E (Longitudinal – Tension) GPa	23.1
Tensile strength $f_u$ (Longitudinal) MPa	402
Young's modulus E (Longitudinal – Compression) GPa	15.86
Compressive strength $f_u$ (Longitudinal) MPa	241
Young's modulus E (Hoop) GPa	31
Tensile strength $f_u$ (Hoop) MPa	241
Poisson's ratio (Circ.-Long.)	0.26
Poisson's ratio (Long.- Circ.)	0.16

Table 3-3 Summary of tension coupon test results

Coupon type	$\sigma_{ult}$ (MPa)	$\sigma_{ult}$ avg. (MPa)	E (GPa)	E avg. (GPa)	$\epsilon_{ult}$	$\epsilon_{ult}$ avg.
TC1	199	232	22.8	24.2	0.018	0.016
	264		26.3		0.015	
	244		-		0.014	
	237		23.4		0.017	
	215		-		-	
TC2	254	266	22.2	24.7	0.019	0.0196
	266		28.1		0.0176	
	278		23.8		0.022	
TC3	274	279	26.6	25.2	N/A	N/A
	318		23.6		N/A	
	300		25.5		N/A	
TC4	340	348	21.2	21.8	N/A	N/A
	375		23.0		N/A	
	348		22.0		N/A	
	330		21.0		N/A	
TC5	526	489	-	26.5	-	0.0214
	444		-		-	
	464		25.1		0.0199	
	507		27.0		0.023	
	477		26.3		N/A	
	503		25.8		0.0208	
	518		28.9		0.0217	
	485		24.8		0.023	
	475		27.6		0.0197	

Table 3-4 Description of beam specimens




Specimen ID	Pile	Condition	Splice orientation	Test setup
BC2	C2	Control	No splice	Figure 3.15
BP2U	P2	Driven		
BP2L	P2	Driven		
SCx	C4	Control		Figure 3.16
SC+	C5	Control		
SP3Ux	P3	Driven		

Table 3-5 Results of push-off tests

Group	Specimen	Max stress MPa	Max load kN	Average stress (MPa)	Standard deviation	Average load (kN)	Standard deviation
Control undriven	C1B	0.77	245	0.62	0.0904	196	28.34
	C1T	0.65	203				
	C2B	0.63	193				
	C3B	0.51	163				
	C3T1	0.54	175				
	C3T2	0.61	198				
Top (driven)	P1T1	0.67	215	0.65	0.0986	209	32.86
	P1T2	0.76	246				
	P2T1	0.56	186				
	P2T2	0.52	165				
	P4T1	0.52	167				
	P4T2	0.69	221				
	P4T3	0.74	245				
	P4T4	0.71	229				
Middle (driven)	P1M	0.53	174	0.63	0.1337	204	40.35
	P2M	0.56	186				
	P3M	0.52	168				
	P4M1	0.83	261				
	P4M2	0.71	231				
Bottom (driven)	P1B1	0.53	149	0.63	0.1139	203	40.63
	P2B2	0.83	264				
	P3B1	0.55	176				
	P3B2	0.53	172				
	P4B1	0.55	177				
	P4B2	0.62	208				
	P4B3	0.73	239				
	P4B4	0.73	238				

Table 3-6 Results of TC1 type monotonic tension coupon tests

Group	Specimen	Stress MPa	Average stress & standard deviation	Group	Specimen	Stress MPa	Average stress & standard deviation
Control (undriven)	C1B	235	237 (15.75)	Bottom (driven)	P1B2	210	234 (26.00)
		240				250	
		229				245	
	C2B	235			P1B1	208	
		241				192	
		254				273	
	C3B	249			P2B2	230	
		220				227	
		250				249	
	C1T	220			P2B1	224	
		239				201	
		252				272	
	C3T1	199			P4B2	220	
		262				246	
		233				197	
	C3T2	242			P4B1	228	
		236				234	
		214				221	
Top (driven)	P1T1	233	230 (15.07)				
		222					
		231					
	P1T2	240					
		206					
		214					
	P4T1	242					
		234					
		191					
	P4T2	217					
		248					
		235					
	P2T1	238					
		245					
		225					
P2T2	241						
	236						
	244						

Table 3-7 Results of TC5 type monotonic tension coupon tests

Group	Specimen	Stress MPa	Average stress & standard deviation	Group	Specimen	Stress MPa	Average stress & standard deviation
Control (undriven)	control	521	486 (24.44)	Bottom (driven)	P1B2	444	438 (42.46)
		444				481	
		461				426	
		502			P1B1	387	
		473				403	
		497			P2B2	453	
		498				522	
		515			P2B1	403	
		478				483	
		475			481		
Top (driven)	P1T1	492	459 (41.5)		P2B1	416	
		503				362	
		370				492	
	P2T1	486			P4B2	435	
		497				396	
		420				467	
	P2T2	405			P4B1	409	
		468				420	
		506				421	
	P4T1	414			P3B2	483	
		500				373	
		440				423	
	P4T2	460			P3B1	415	
		468				491	
		449					
Middle			448 (37.06)			515	
						P1M	426
							419
							463
						P2M	428
							475
							372
						P4M2	460
							486
							429
P3M	445						
	464						

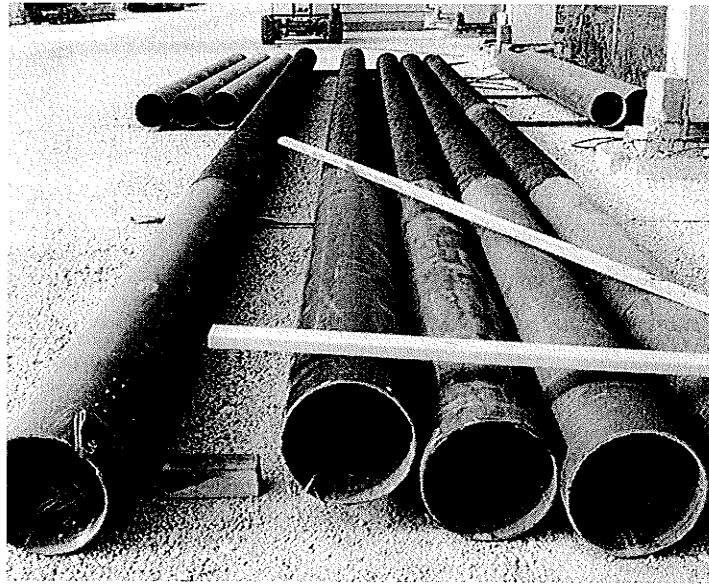
Table 3-8 Results of monotonic compression coupon tests

Group	Specimen	Stress MPa	Average stress & standard deviation	Group	Specimen	Stress MPa	Average stress & standard deviation			
Control (undriven)	control	275	284 (21.49)	Bottom (driven)	P1B2	330	281 (31.00)			
		274				330				
		272				306				
		Top (driven)			P1T1	322		300 (22.18)	P1B1	306
						317				333
286	263									
P2T1	344		P2B2		284					
	310				260					
	286		268							
P2T2	325		P2B1		261					
	282				226					
	289				252					
P4T1	298		P4B2		295					
	293				322					
	283				272					
P4T2	267		P4B1		292					
	299				293					
	317		285							
	P3B2	267	226							
		271	243							
284		254								
Middle (driven)	P1M	289	285 (22.33)	P3B1	259					
		285			282					
		318			299					
	P2M	299		P3M	243					
		326			278					
		288			273					
	P4M2	278		P3M	243					
		273			278					
		273			243					
		273			273					

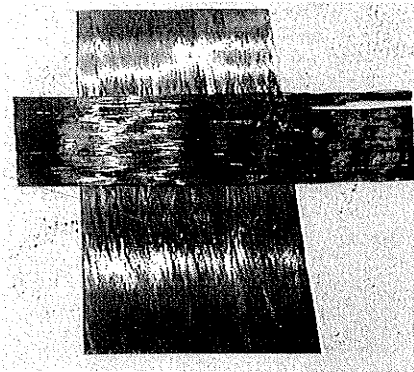
Table 3-9 Results of tension-tension fatigue tests

Group	Specimen	$N_f$	Avg. $N_f$ & standard deviation	Group	Specimen	$N_f$	Avg. $N_f$ & standard deviation
Control (undriven)	control	42,952	35,153 (10,776)	Bottom (driven)	P1B2	58,586	44,829 (21,179)
		32,462				65,301	
		48,300				44,094	
		20,729			P1B1	3,639	
		31,321				48,155	
Top (undriven)	P1T1	32,074	45,101 (15,274)		P2B2	51,299	
		23,482				53,175	
		-			36,369		
	P2T1	26,838			P2B1	78,408	
		43,471				59,372	
		32,988				87,985	
	P2T2	66,263			P4B2	36,072	
		61,926				51,684	
		74,355				72,558	
	P4T1	34,706			P4B1	35,776	
		43,526				13,243	
		37,374				33,237	
	P4T2	47,267			P3B2	28,318	
		51,590				15,236	
		55,547				19,864	
Middle (driven)	P1M	28,290	44,757 (36,662)	P3B1	36,502		
		35,294			35,309		
		69,680			42,602		
	P2M	18,022		P4M2	39,226		
		70,688			8,413		
		137,371			66,399		
	P3M	6,922		P3M	33,471		
		23,305			23,305		

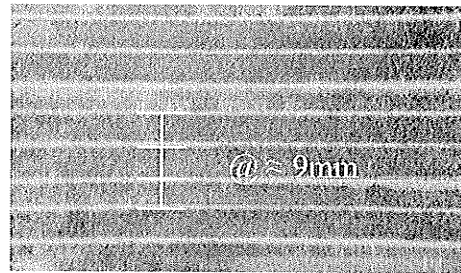




(a) General view as delivered

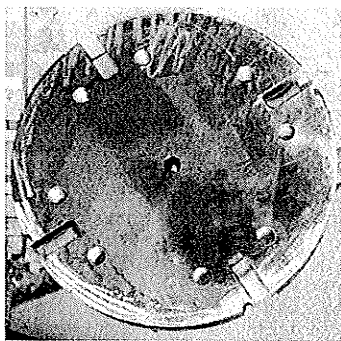


(b) Exposed fibers after resin burnout test

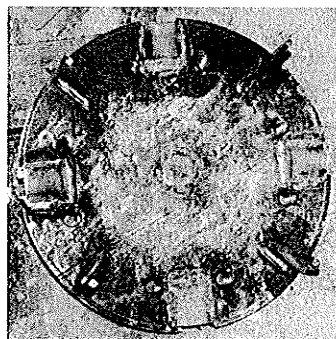


(c) Ribs at inner surface

Figure 3-1 GFRP tubes



(a) Splice plates



(b) Plate-bars assembly

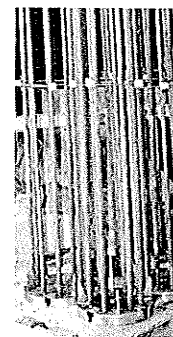


Figure 3-2 components of the mechanical splices

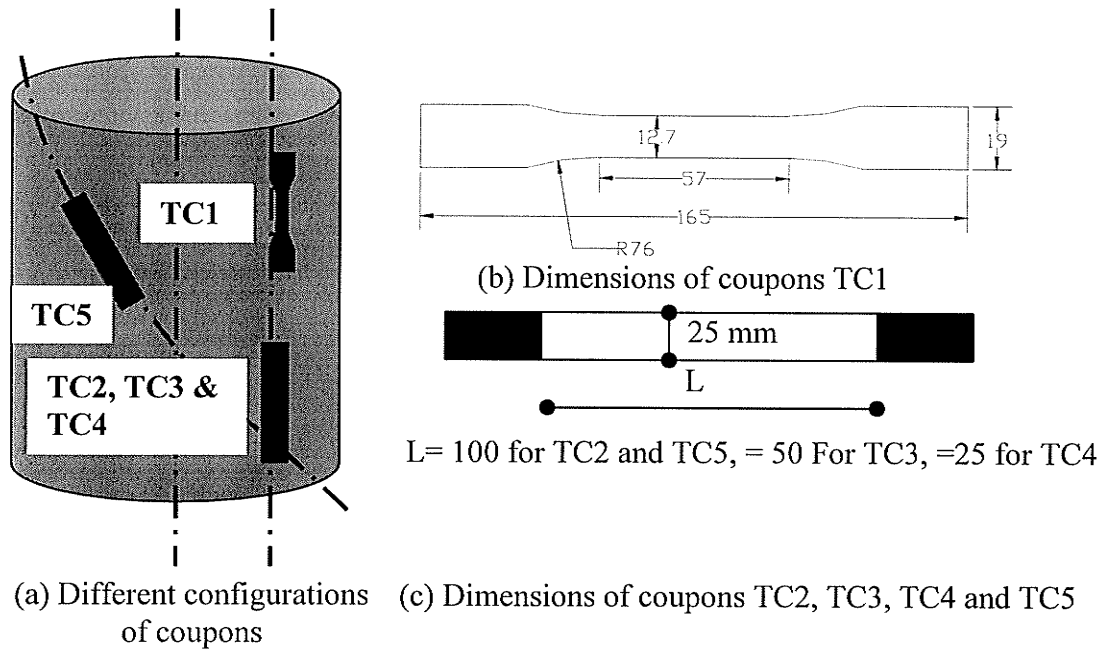
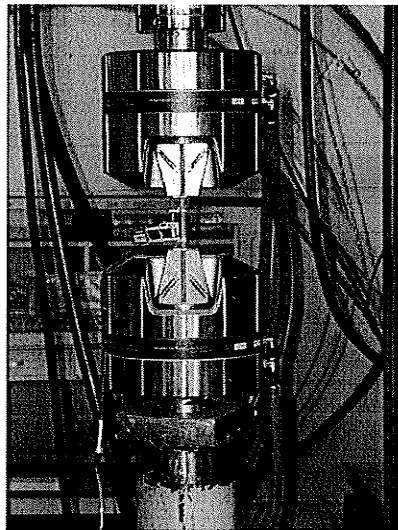
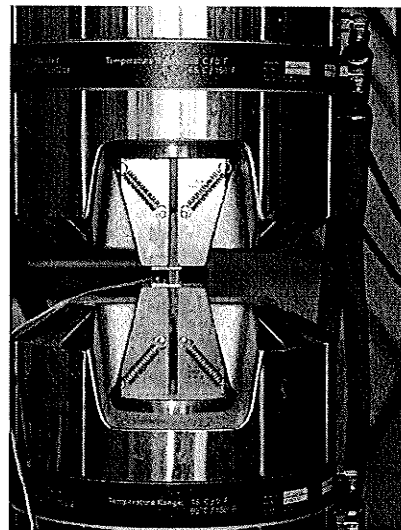


Figure 3-3 Tension coupons configurations



(a) Test setup (TC1, TC2 and TC5)



(b) Test setup TC3 and TC4

Figure 3-4 Tension coupons test setup

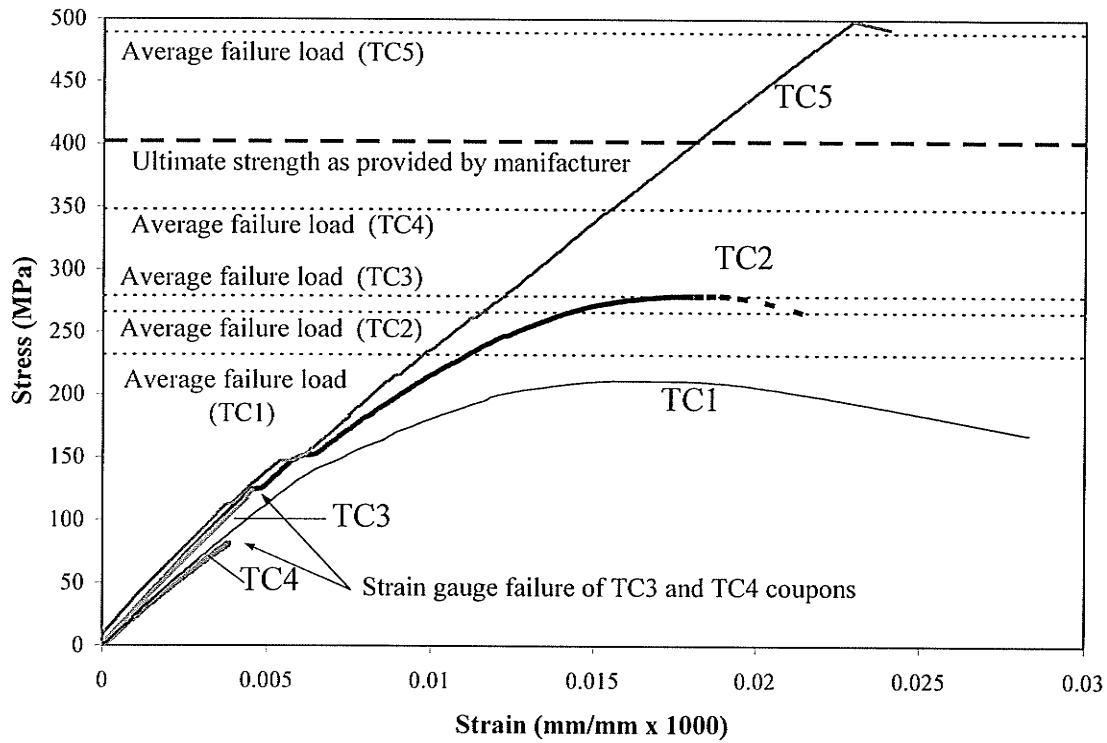


Figure 3-5 Typical Stress-strain relations for various monotonic tension coupons

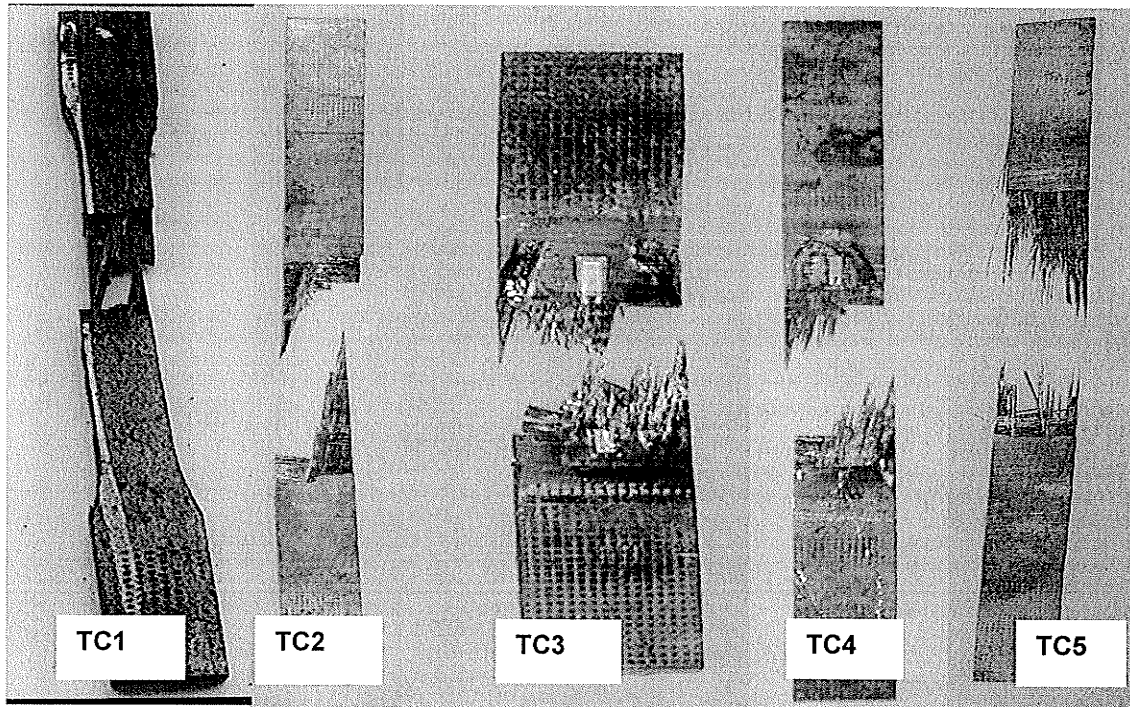


Figure 3-6 Failure modes of tension coupons

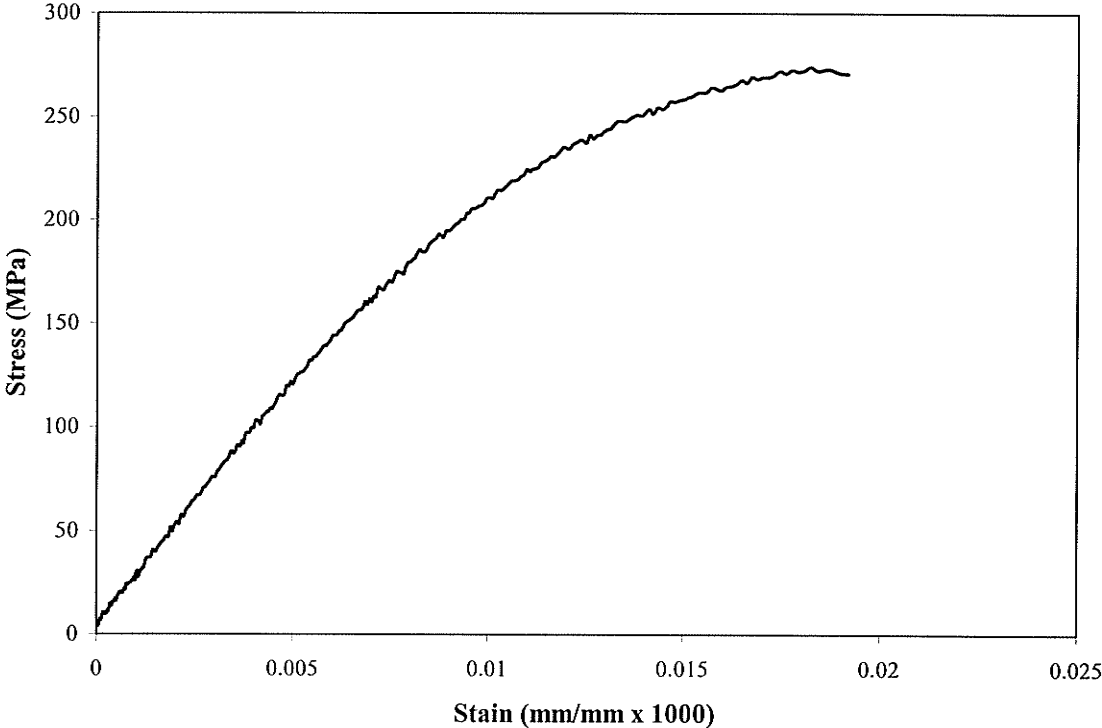
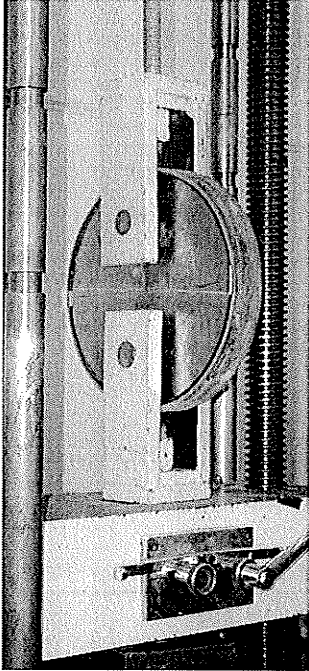
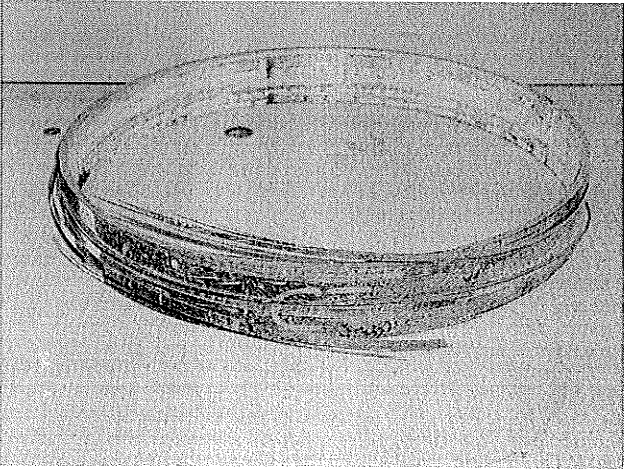


Figure 3-7 A typical monotonic compression coupon Stress-strain relation

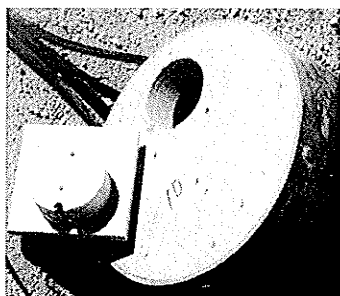


(a) Test setup

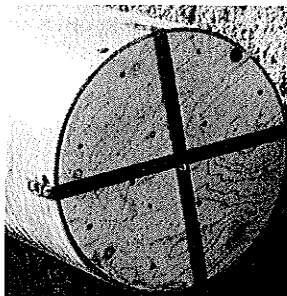


(b) Failure of test specimen in the hoop direction

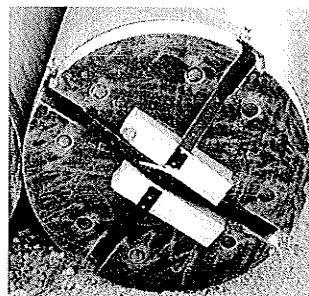
Figure 3-8 Split disk test



(a) Top plug



(b) Bottom plug



(c) Splice plate

Figure 3-9 Tube and plugs to prepare for casting

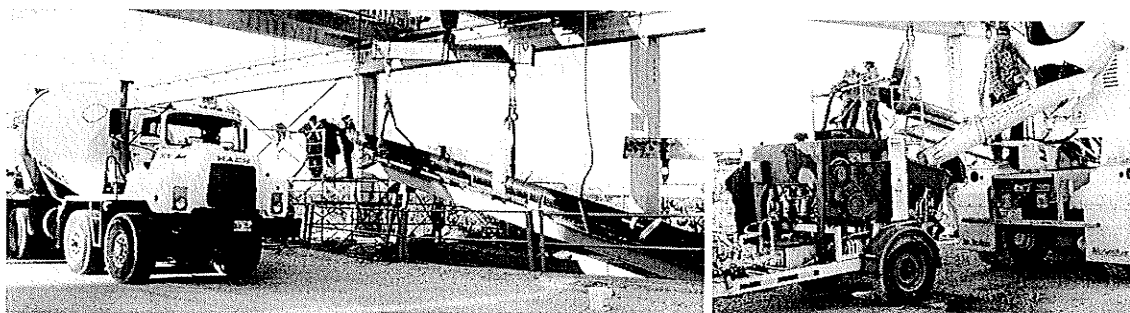
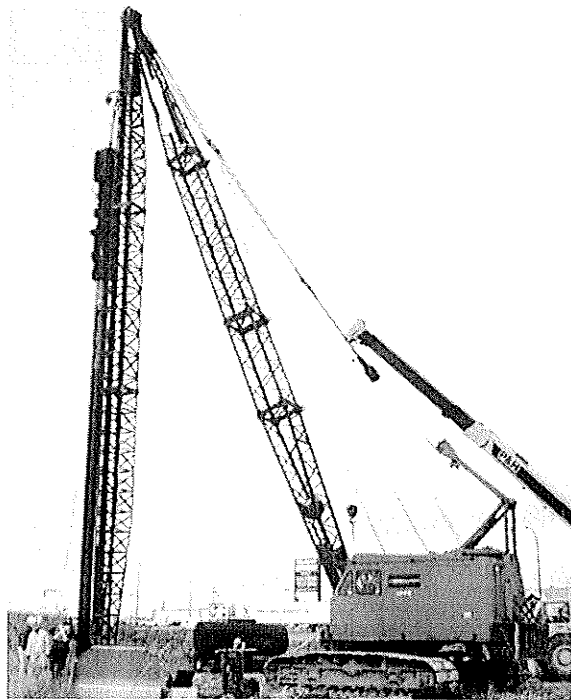


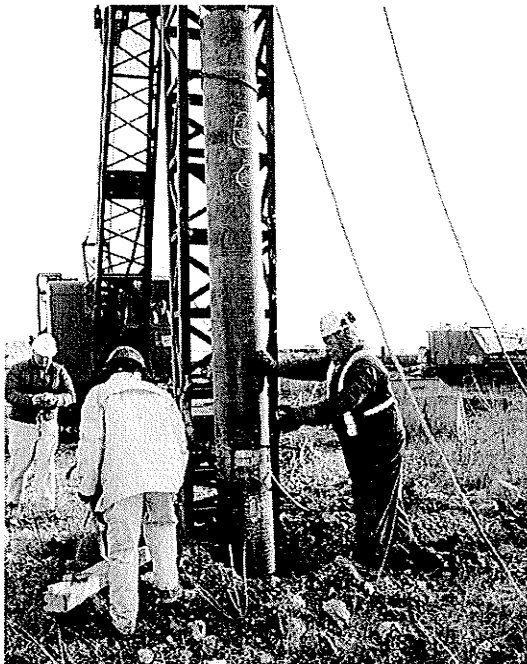
Figure 3-10 Pumping of concrete into tubes



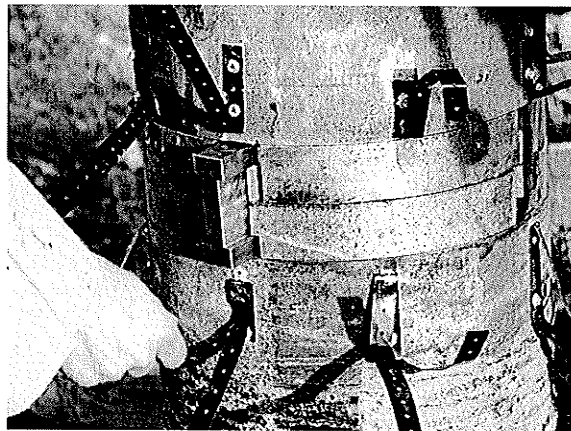
(a) Pile driving



(b) Continued driving using a steel mandrel



(c) Splicing of pile



(d) Inserting I- keys in the splice

Figure 3-11 Pile driving and splicing process



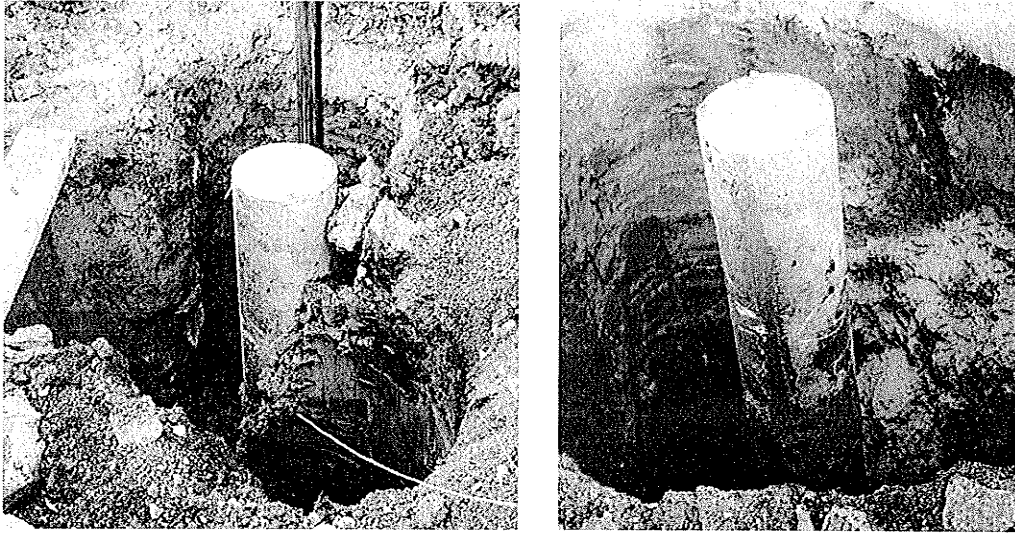


Figure 3-12 Drilling around piles for extraction

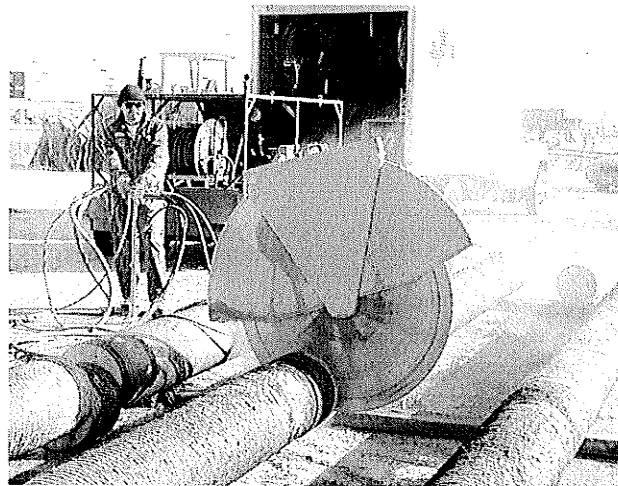


Figure 3-13 Cutting of various specimens from the CFFT piles

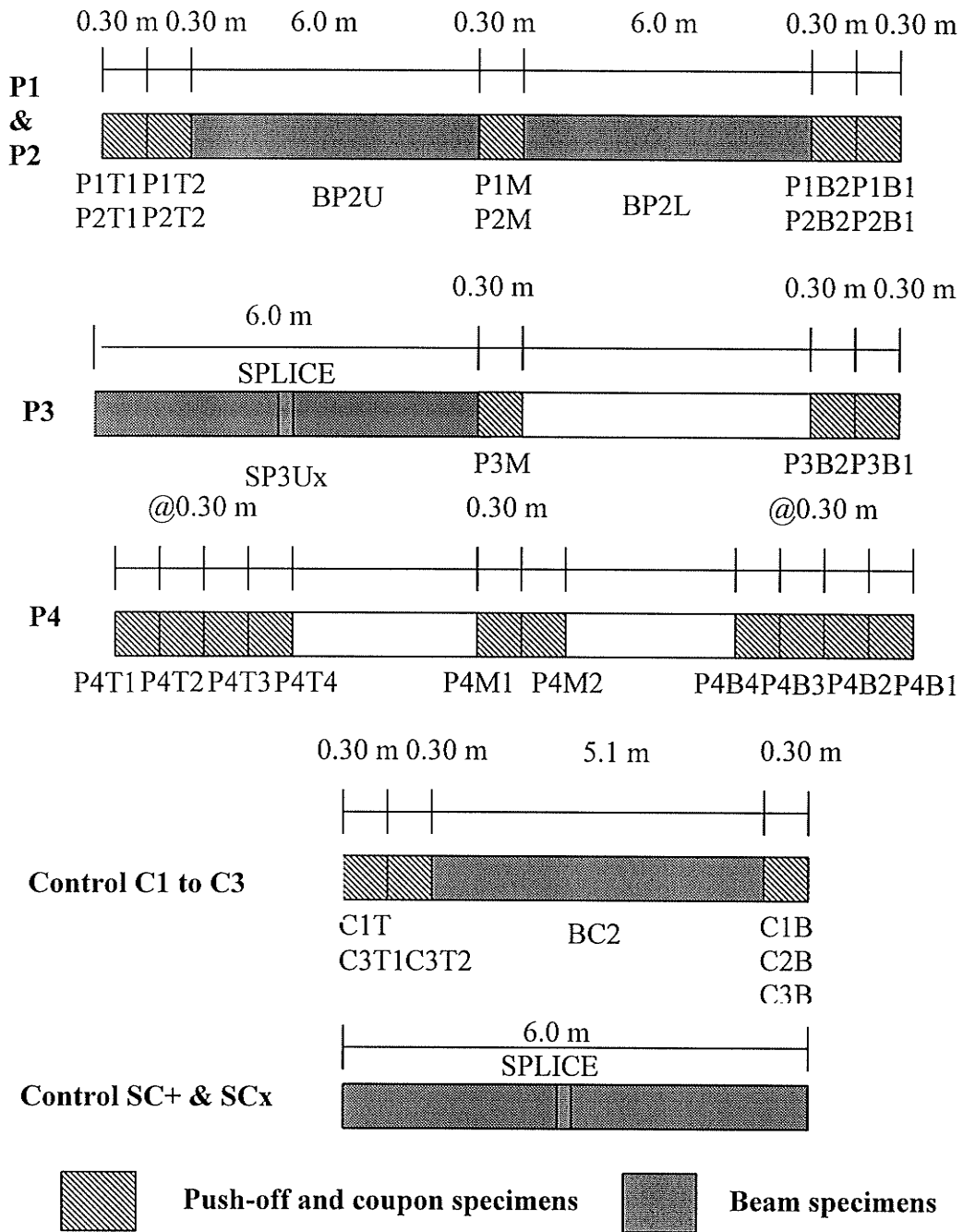


Figure 3-14 Test specimens extracted from CFFT piles



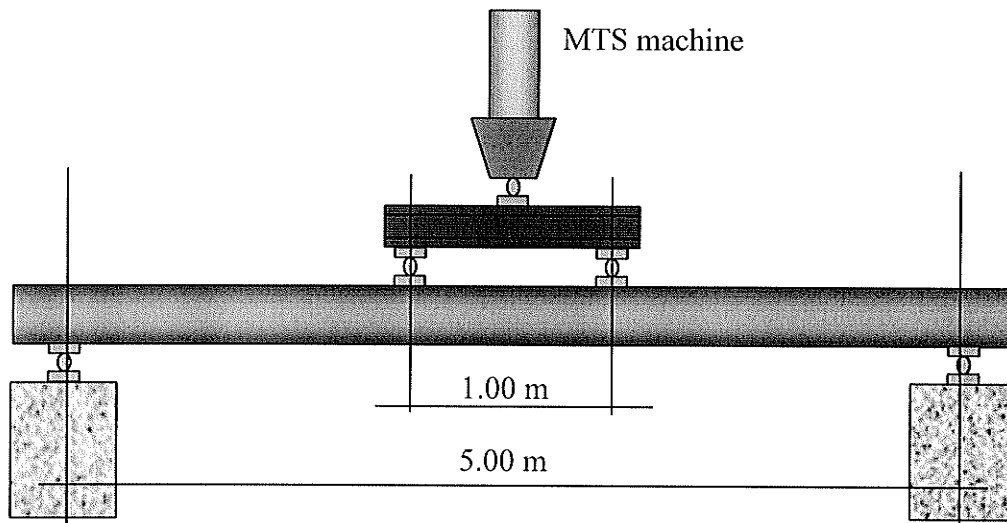


Figure 3-15 Unspliced monotonic beam test setup

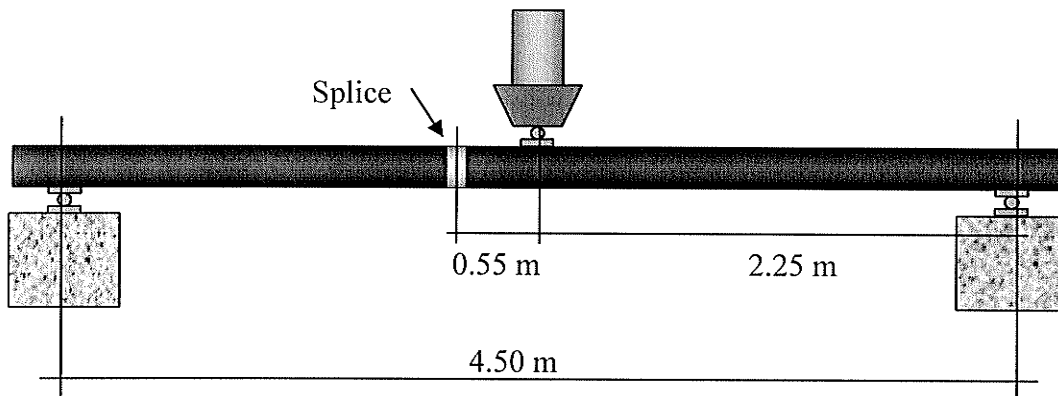


Figure 3-16 Spliced monotonic beam test setup

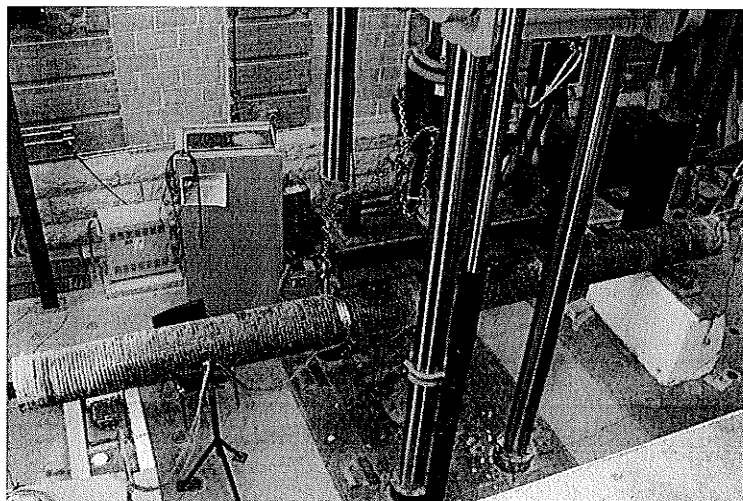


Figure 3-17 General view of test setup for BP2L

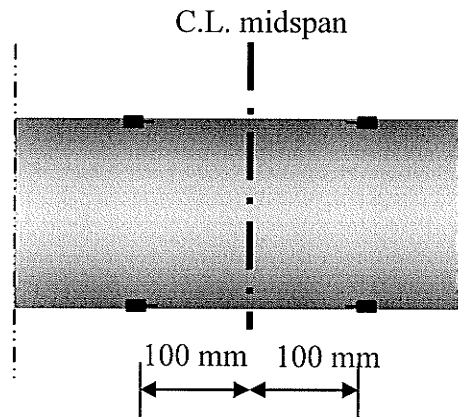
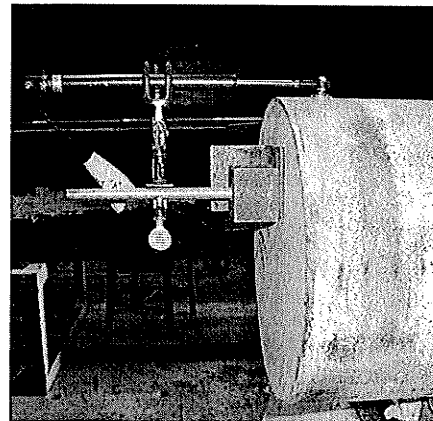
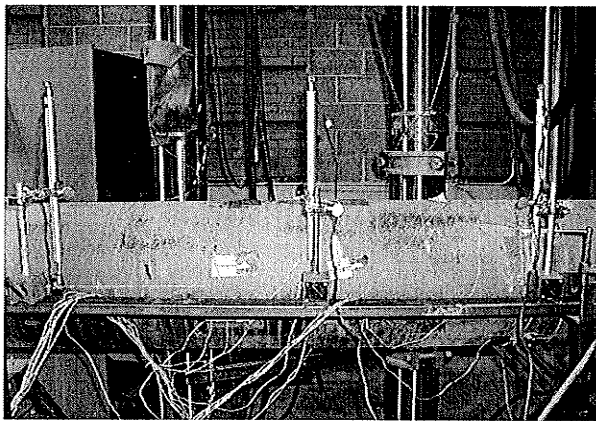


Figure 3-18 Strain gauge locations at midspan of monotonic beam specimens



(a) LVDT locations for spliced beam tests

(b) LVDT for end slip measurement

Figure 3-19 LVDT locations

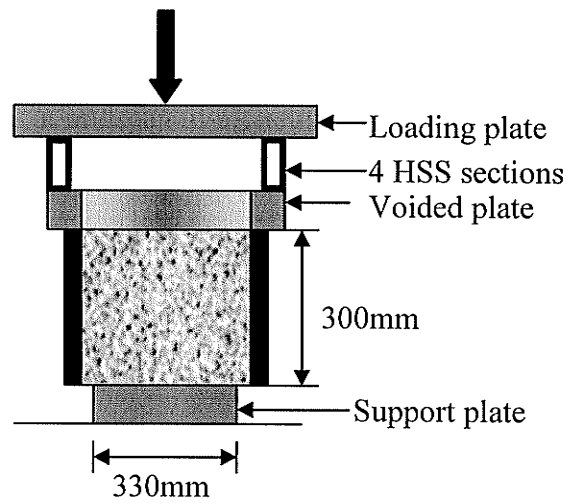
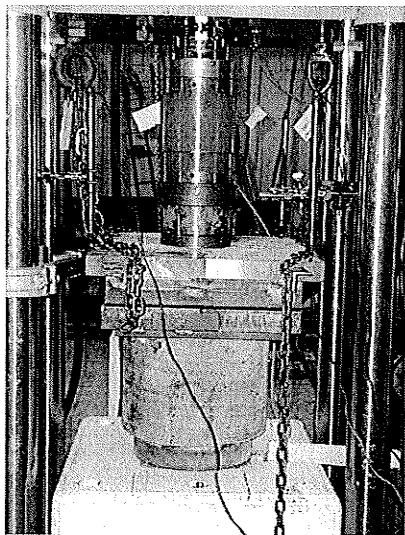


Figure 3-20 Push-off test setup

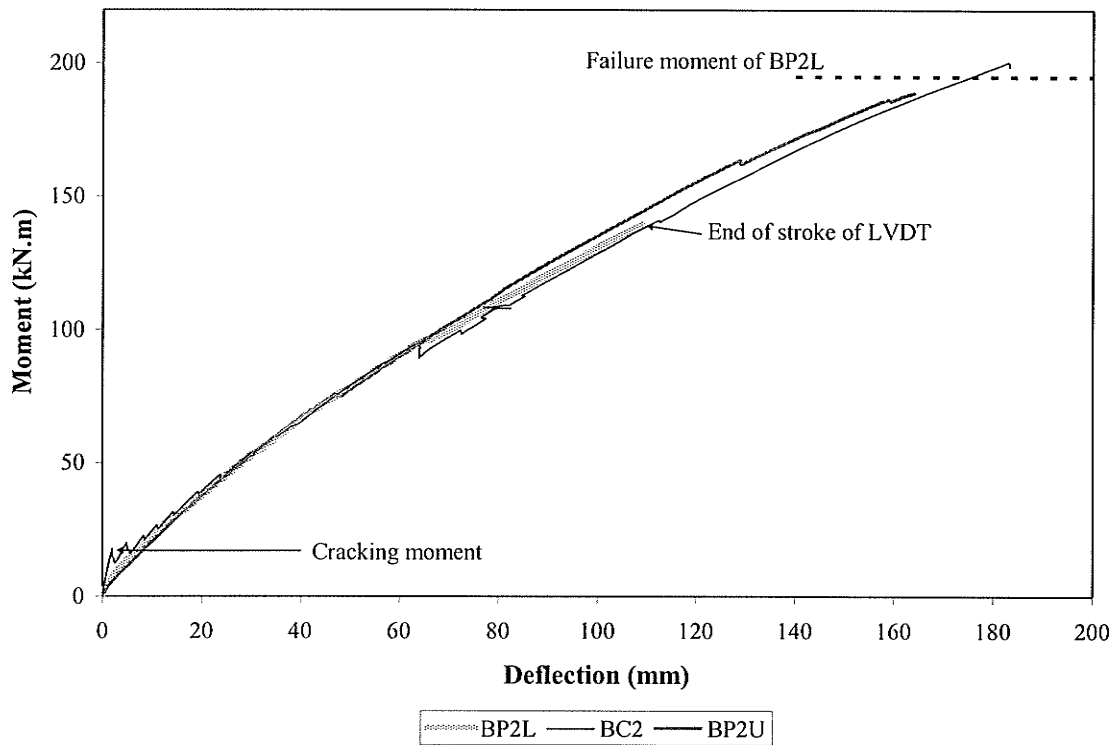


Figure 3-21 Load-deflection behavior (unspliced CFFT beams)

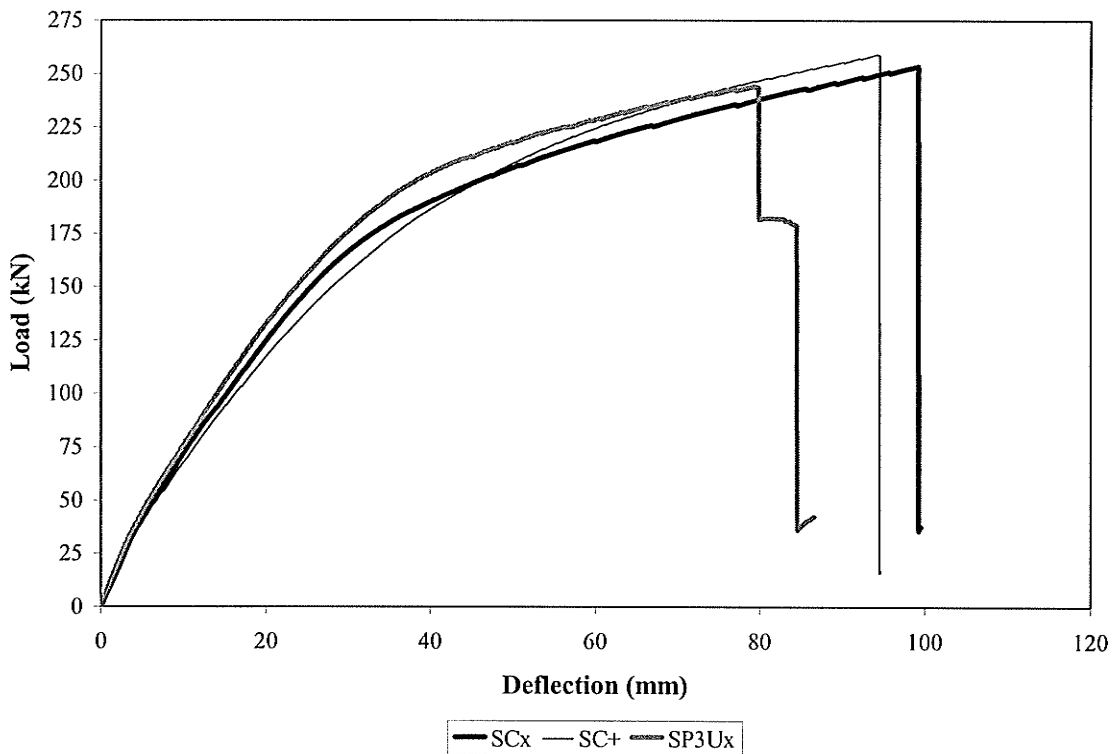


Figure 3-22 Load-deflection behavior (spliced CFFT beams)

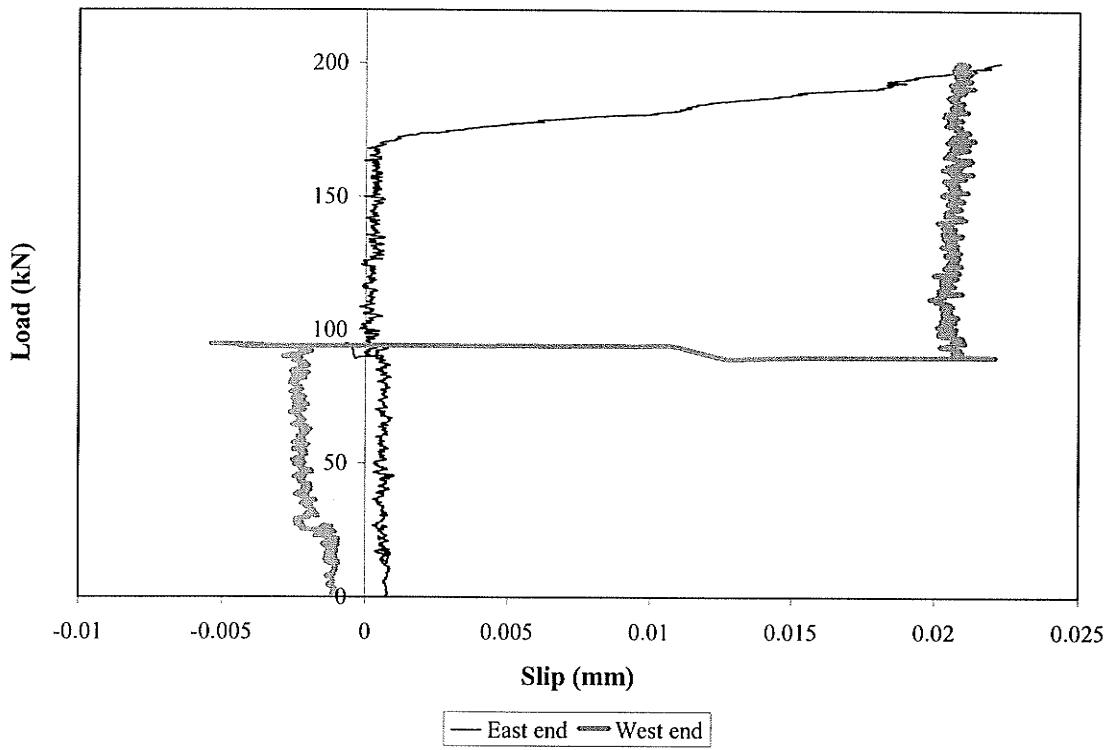


Figure 3-23 Load-slip behavior of BC2

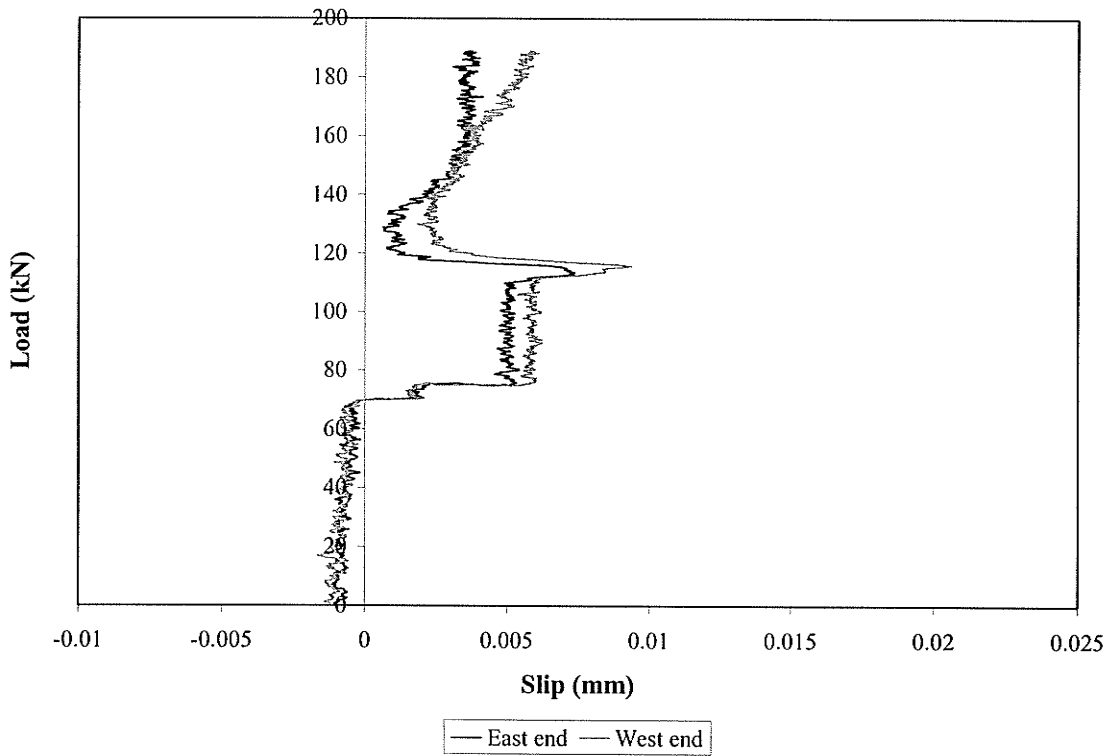


Figure 3-24 Load-slip behavior of BP2U

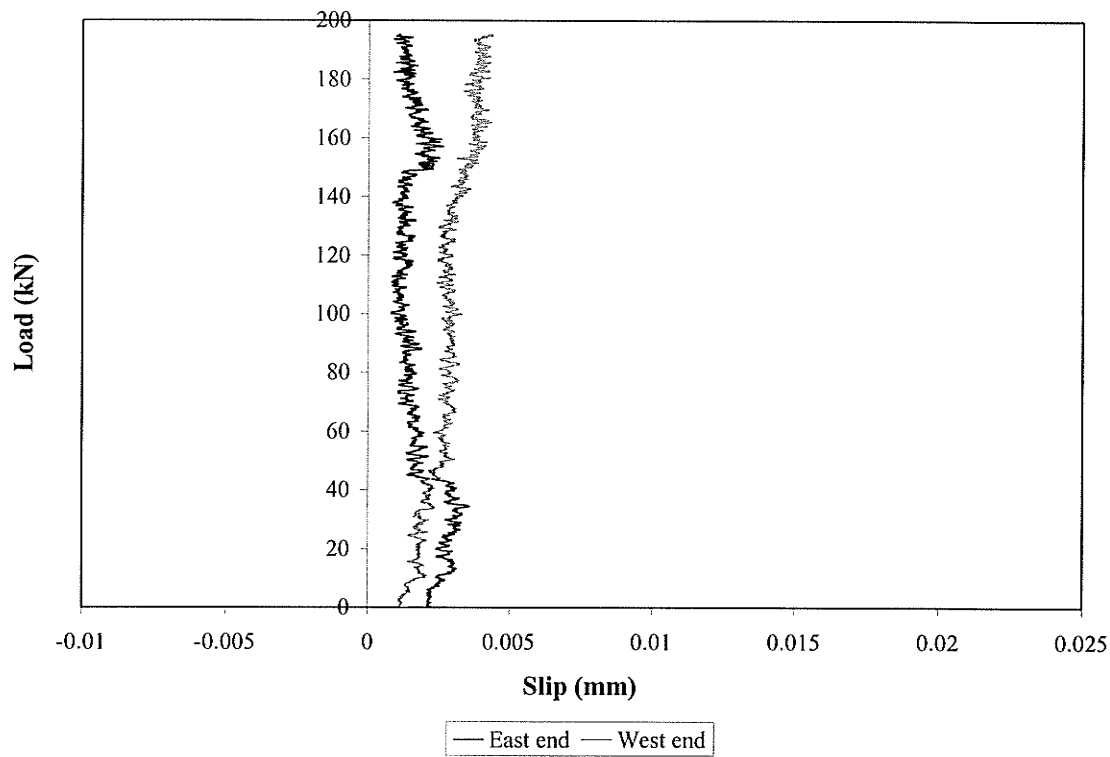


Figure 3-25 Load-slip behavior of BP2L

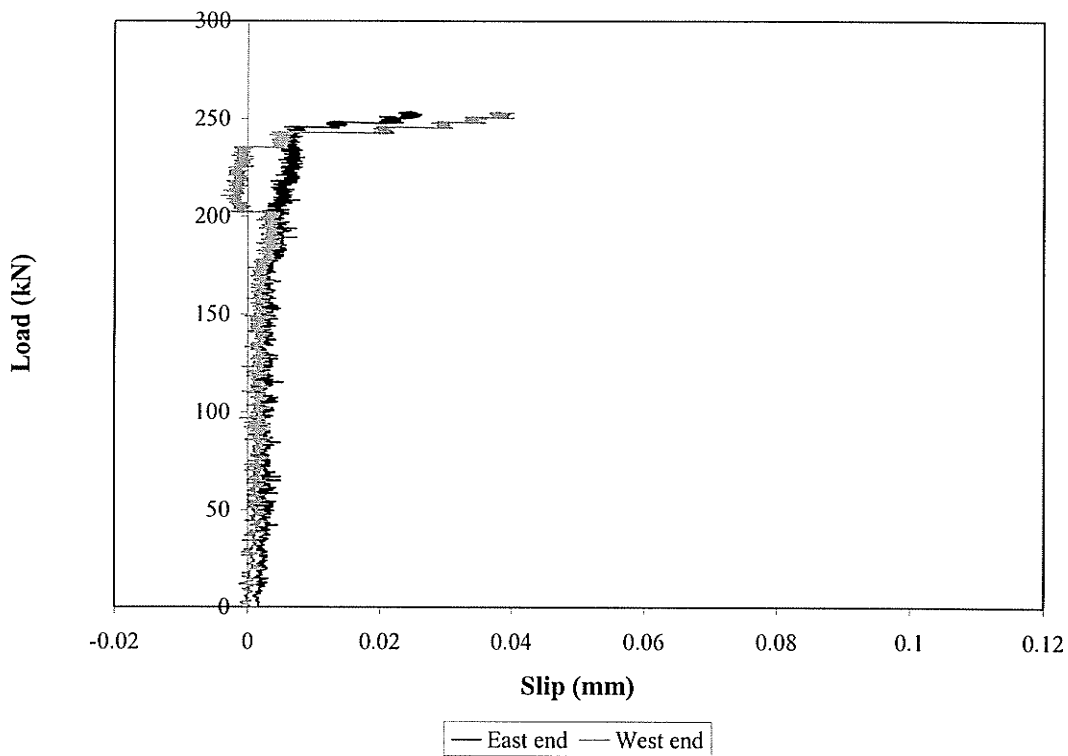


Figure 3-26 Load-slip behavior of SCx

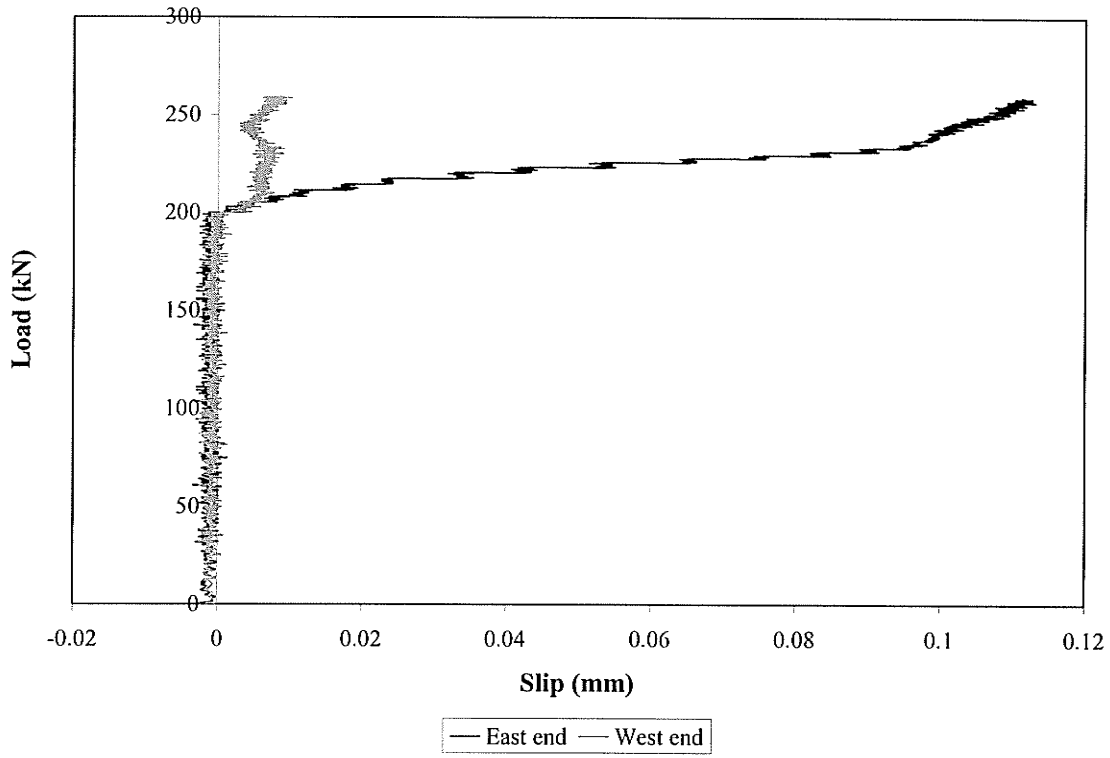


Figure 3-27 Load-slip behavior of SC+

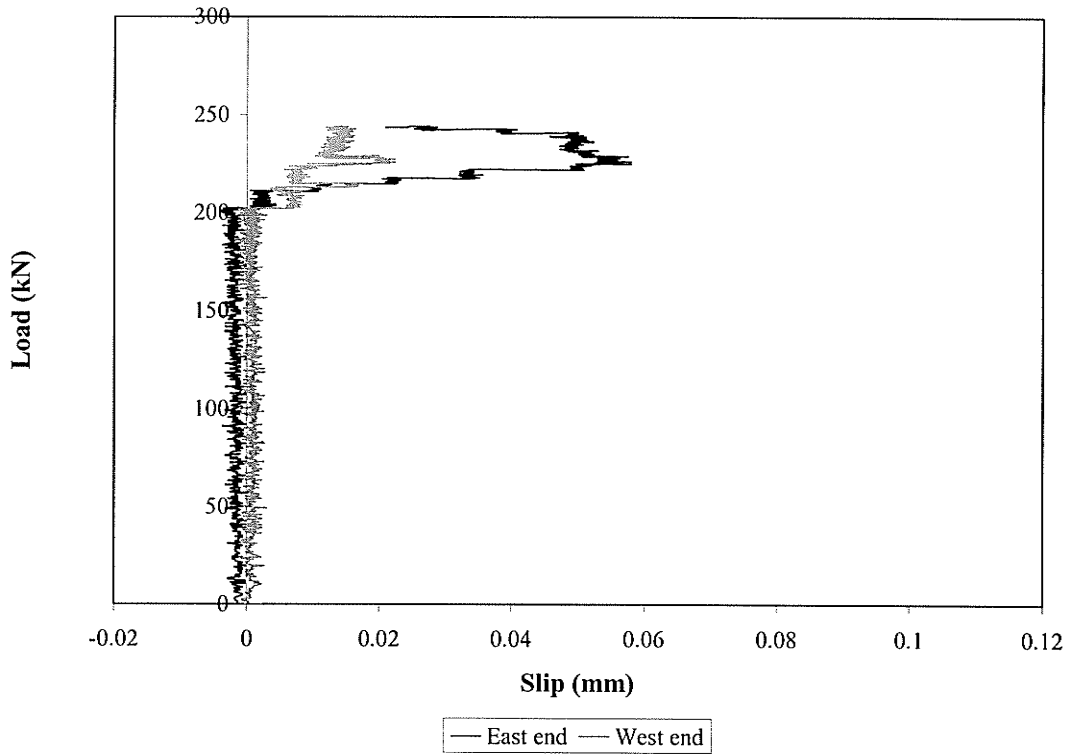


Figure 3-28 Load-slip behavior of SP3Ux

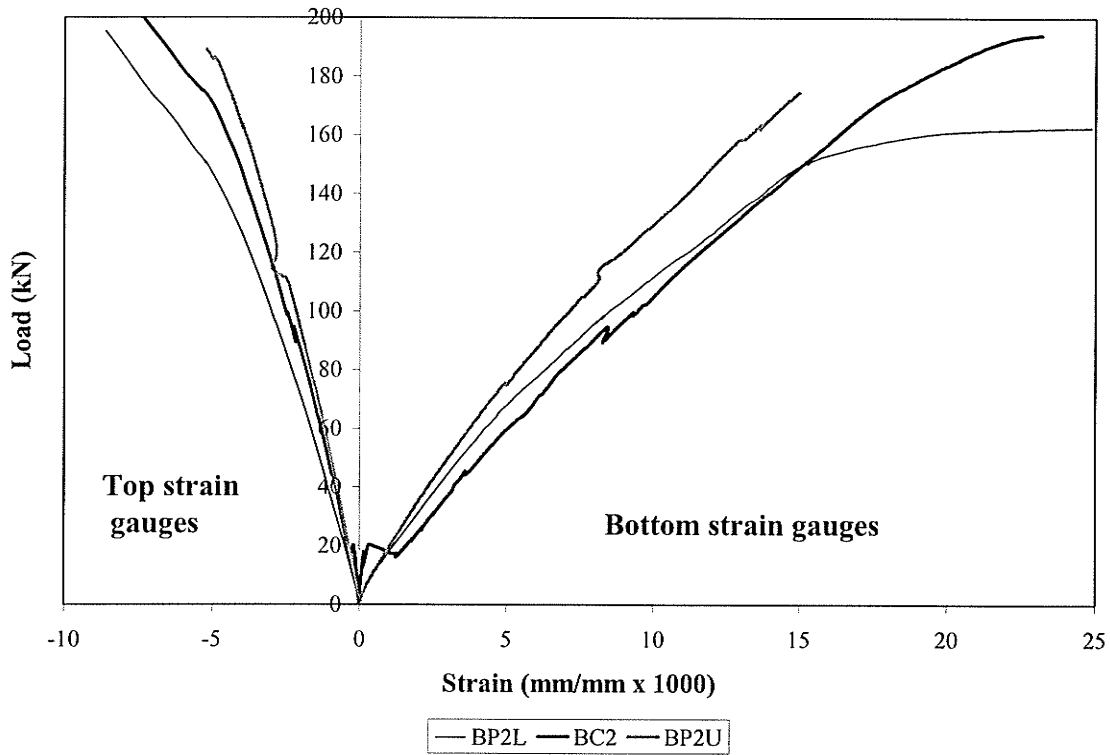


Figure 3-29 Load-tube strain (unspliced CFFT beams)

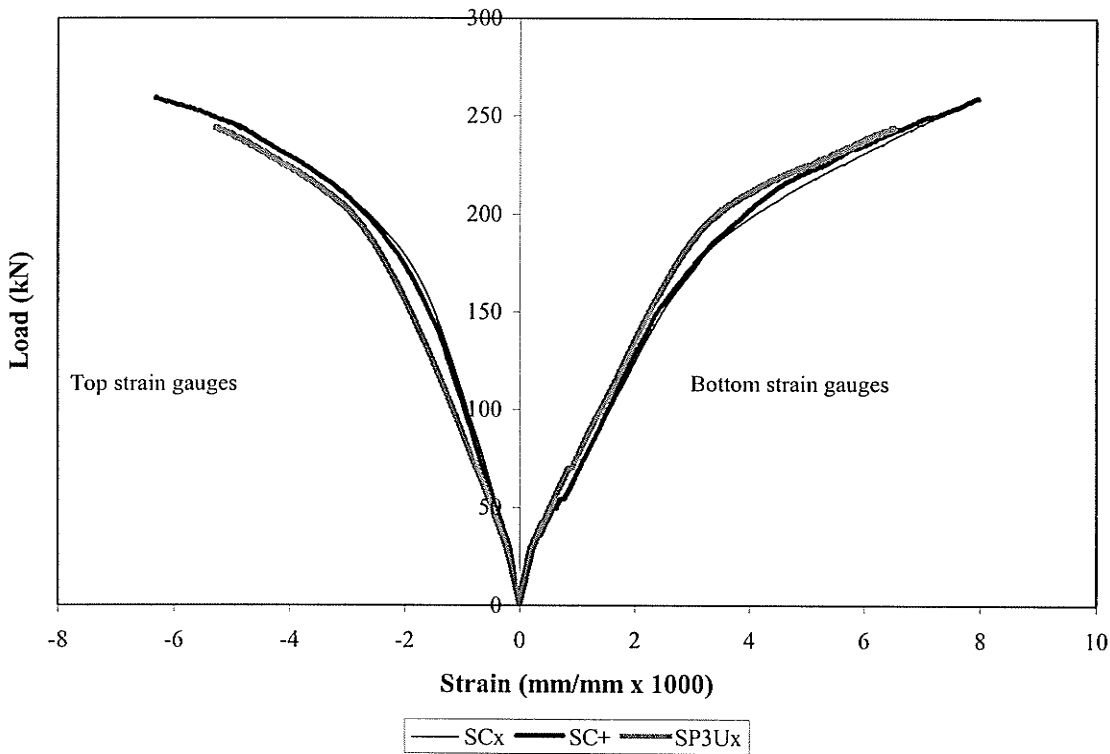


Figure 3-30 Load-tube strain (spliced CFFT beams)(Average of two strain gauges)

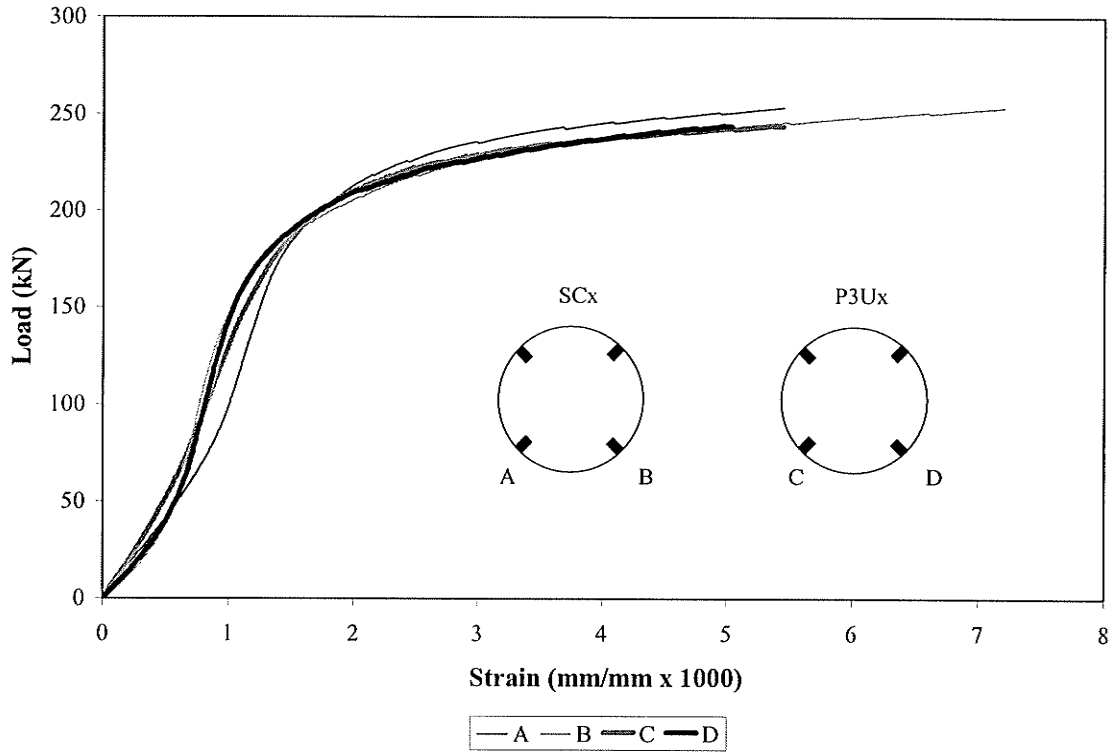


Figure 3-31 Load-bottom key strains in specimens SCx and SP3Ux

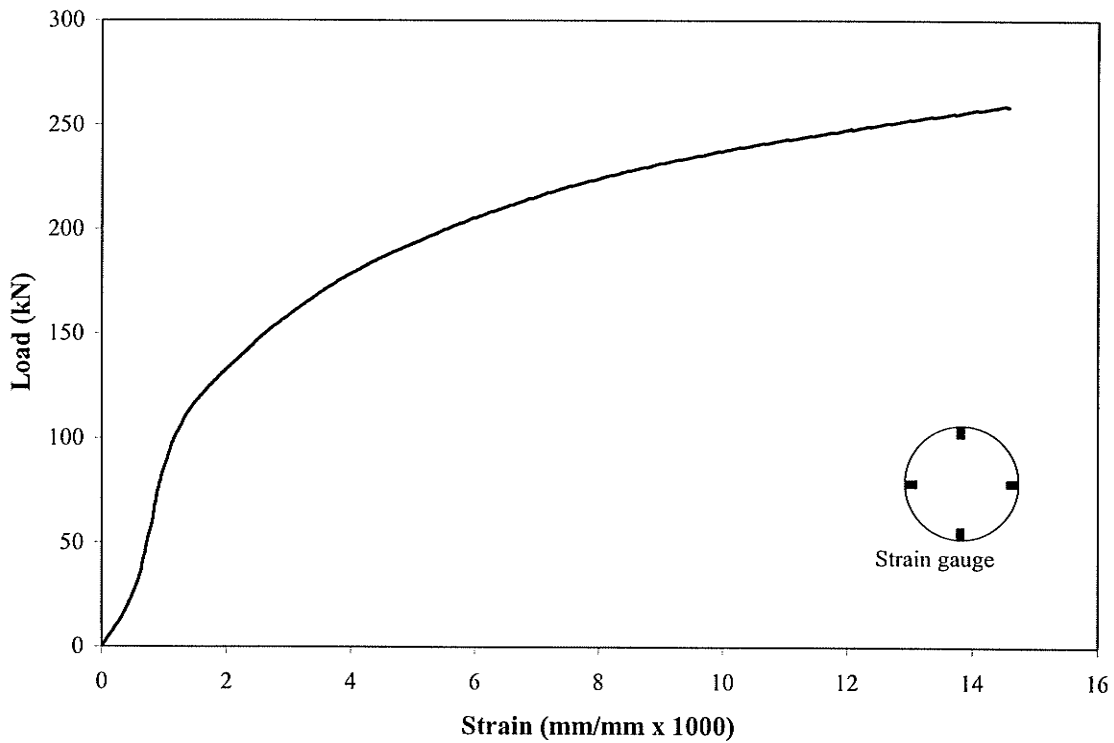


Figure 3-32 Load-bottom key strain in specimen SC+





Figure 3-33 Failure mode of unspliced beams

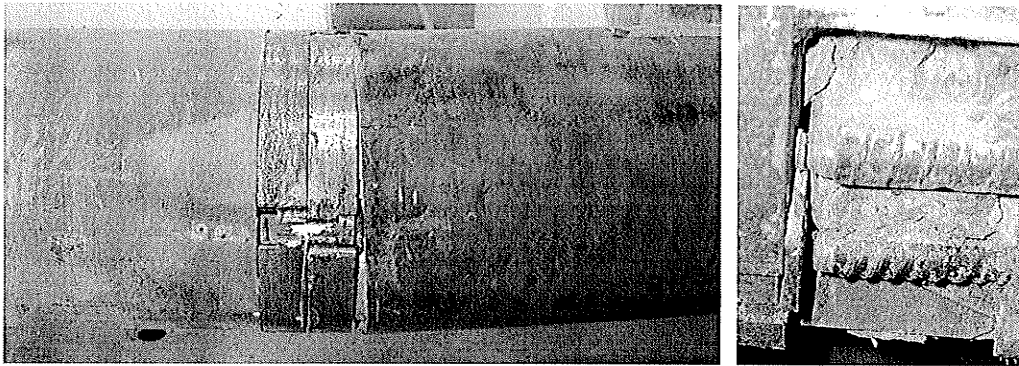


Figure 3-34 Failure mode of spliced beams

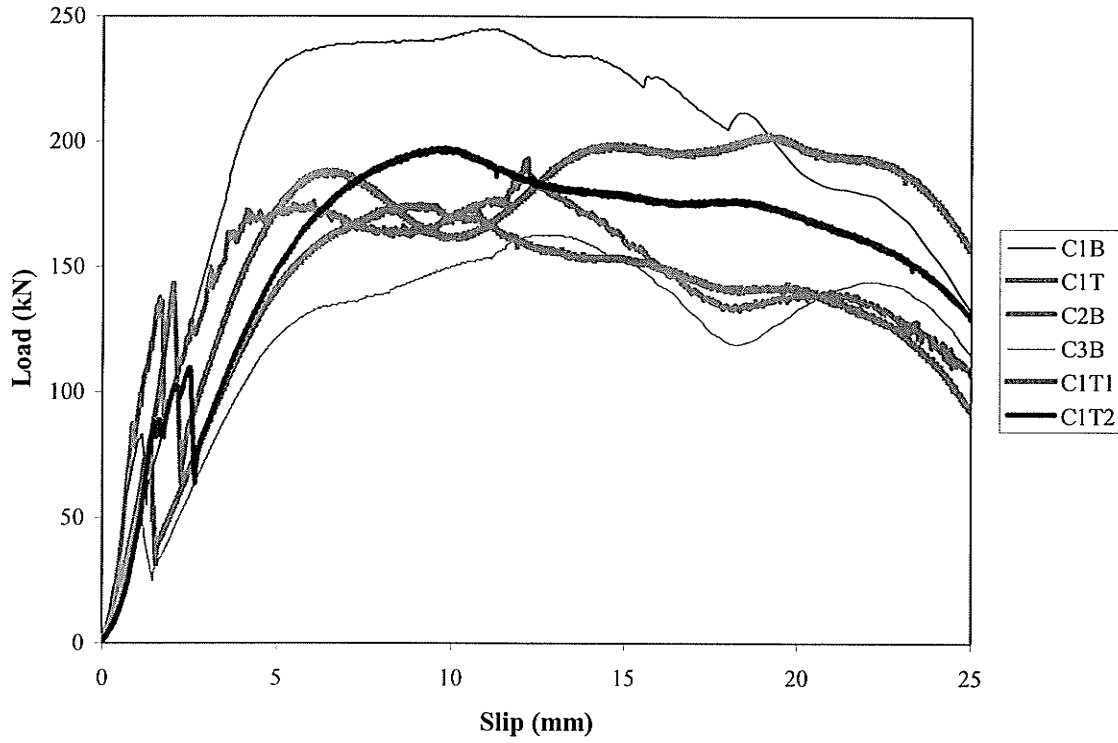


Figure 3-35 Load-slip behavior of control push-off specimens

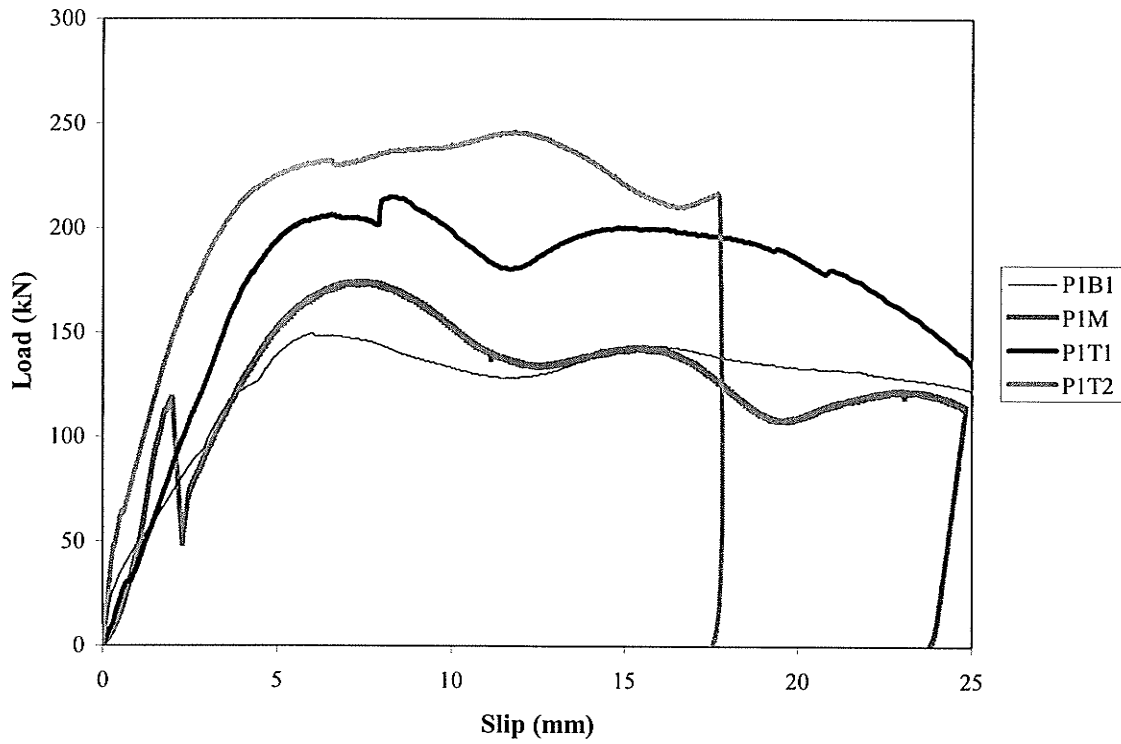


Figure 3-36 Load-slip behavior of push-off specimens from driven pile P1

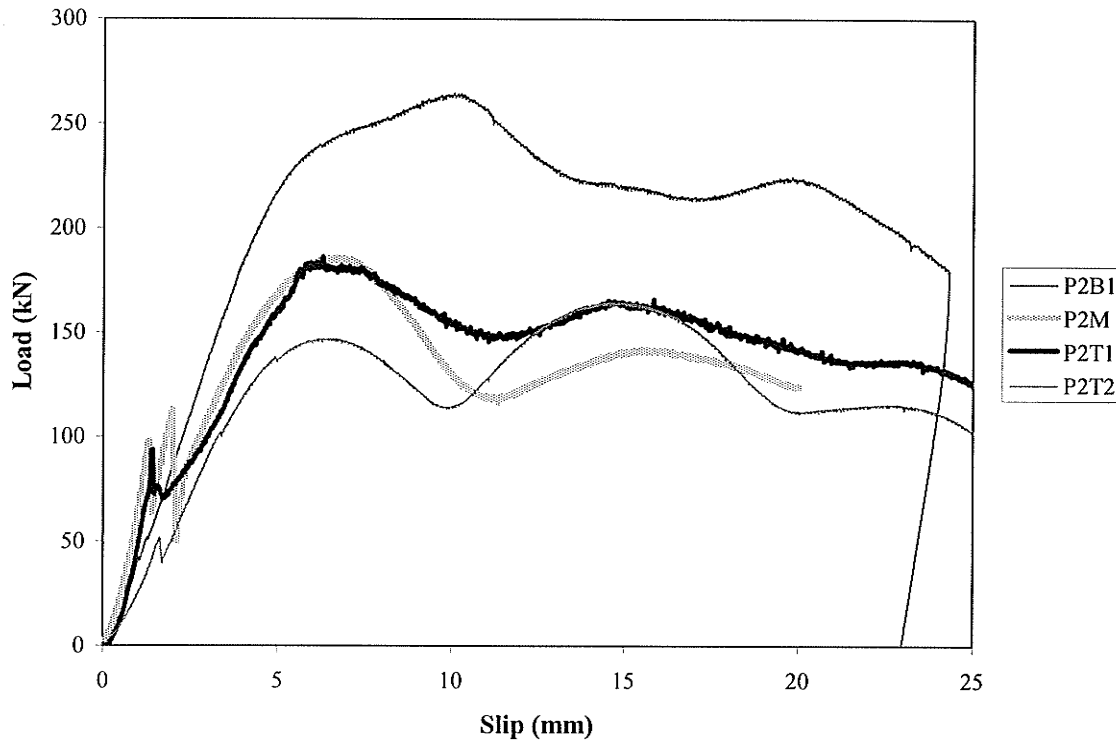


Figure 3-37 Load-slip behavior of push-off specimens from driven pile P2

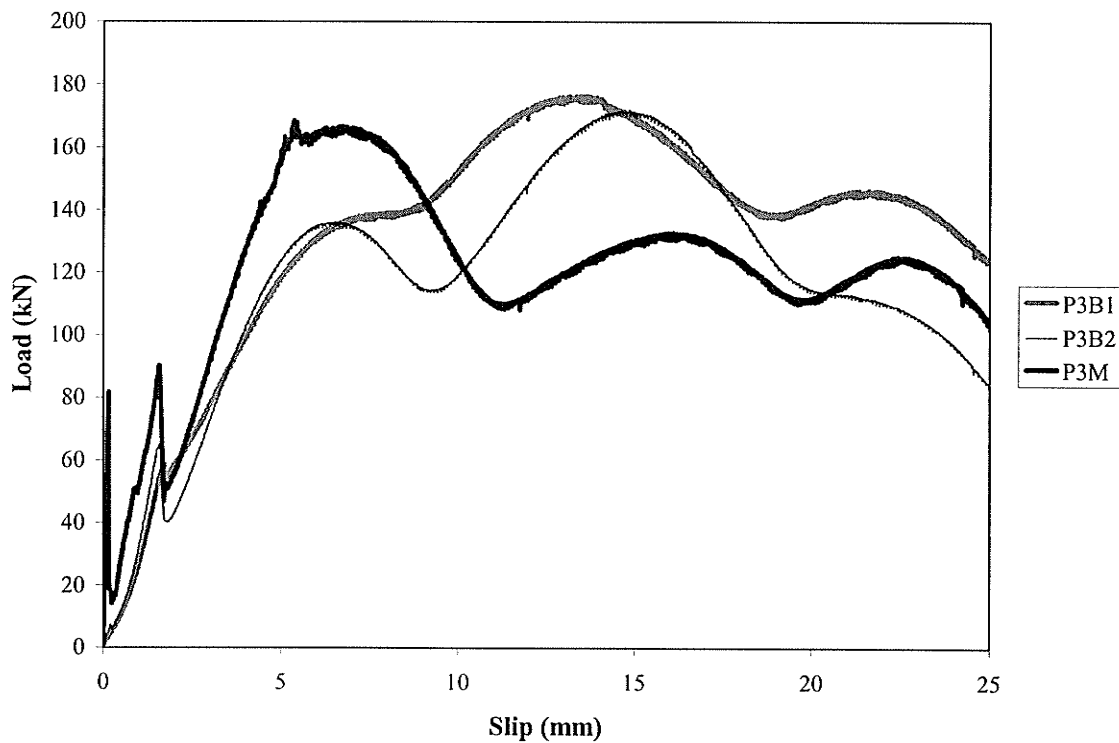


Figure 3-38 Load-slip behavior of push-off specimens from driven pile P3

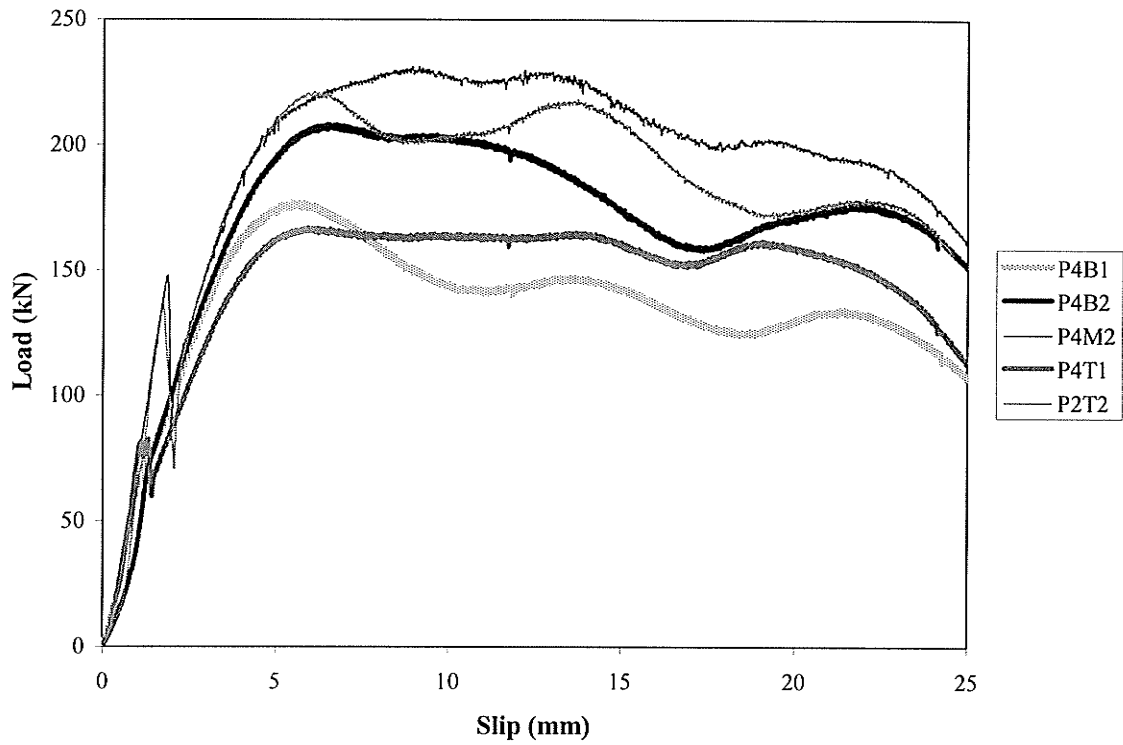


Figure 3-39 Load-slip behavior of push-off specimens from driven pile P4-I

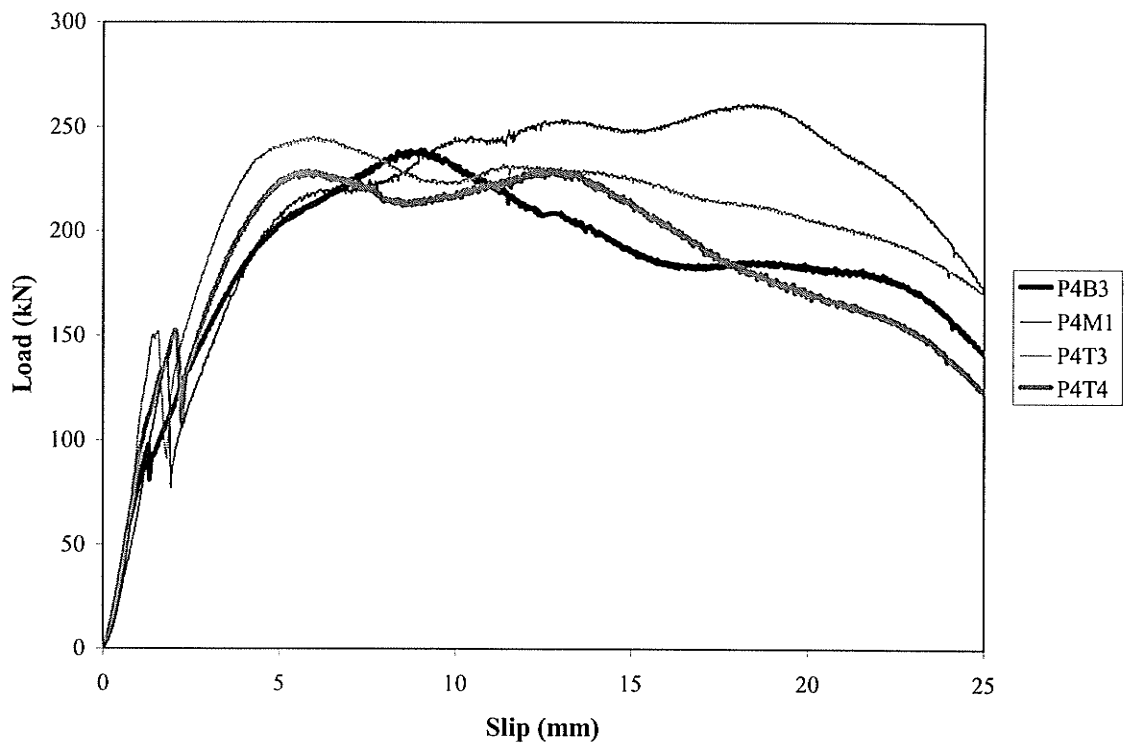


Figure 3-40 Load-slip behavior of push-off specimens from driven pile P4-II

## **Chapter 4**

### **Experimental Investigation of the Fatigue Behavior of CFFT Members under Reversed Bending**

#### **4.1 Introduction**

In this chapter, the experimental program conducted to study the fatigue behavior of CFFT flexural members is discussed. The experimental program included the testing of three full-scale CFFT beam specimens under fully reversed cyclic bending. The experimental program also included the testing of 81 GFRP coupons cut from the tubes under tension-tension and tension-compression fatigue, in order to establish the stiffness degradation and fatigue properties of the tube material. Various parameters were studied in these tests, including the type of GFRP coupons, the frequency of the applied load ( $f$ ), and the ratio of the minimum-to-maximum stresses during the fatigue test ( $R$ ). This chapter also presents analysis of the test results, which is used to establish the fatigue life prediction and stiffness degradation models for the tube material.

#### **4.2 Description of Test Specimens**

##### **4.2.1 Full-scale CFFT beam specimens**

The objective of this group of tests is to study the behavior of CFFT beams under reversed cyclic bending, including the deflection behavior, slip between the FRP tube and concrete core, and strain behavior, as well as to establish the number of cycles to failure. Three full-scale specimens were tested in this series. The specimens were cut from untested piles that were cast for the study of the effect of the driving forces discussed in

chapter 3. The test specimens were designated as BFC1, BFC3 and BFP1U and were cut from the undriven piles C1 and C3 and the upper portion of driven pile P1, respectively. Pile P1 was used in this study although it was driven into the ground and extracted, since the tension-tension fatigue tests that were conducted on coupons cut from all driven pile, as described in the chapter 3, showed that the driving process did not have any adverse effect on the fatigue life of the tube material.

#### **4.2.2 GFRP coupon specimens**

The objective of this group of tests is to establish fatigue life prediction and stiffness degradation models for the tube material. The study examined the effect of several parameters, including the frequency of the applied load, the ratio between the maximum and minimum applied loads and the coupon type on the fatigue life (Helmi et. al, 2006b). In total, 81 coupons were tested, all of which were cut from different locations of the undriven piles C1, C2 and C3. Seventy two of the coupons were cut in the direction of the longitudinal fibers as in the case of the TC5 type tension coupon specimens discussed in chapter 3 (i.e. at  $10^\circ$  from the longitudinal direction). This configuration was chosen for the coupons because it gives the same fiber breakage failure mode as in the full scale bending CFFT specimens, and since the angle between the longitudinal fibers and the axis of the tube is small ( $10^\circ$ ), it could be assumed that these coupons represent the properties of the tubes in the axial direction without any significant error. Fifteen of the 72 specimens were cut at a width of 15 mm, in order to be tested to failure within the capacity of the testing machine, and were tested first in a pilot program (Helmi et. al, 2006a&c). Later, a higher capacity machine became available, and as such, the other 57 specimens were cut to a width of 25 mm. 21 of the 57 coupons were tested in tension-

tension fatigue and 36 were tested in tension-compression fatigue. The nine remaining coupons were cut in the longitudinal direction of the tubes and machined into a dumbbell shape according to ASTM D638, similar to the TC1 type tension coupon specimens discussed in chapter 3. These nine coupons were tested in order to study the effect of the coupon type on the fatigue life of the tube material.

### **4.3 Test Setups and Instrumentations**

#### **4.3.1 Full-scale CFFT beam test setup and instrumentation**

The full-scale CFFT beam specimens were tested under four point bending over a span of 4 m and the distance between the two applied loads was 1 m, as shown in Figure 4.1. As the specimens were cycled in reversed bending, a system of supports shown in Figures 4.2 and 4.3, was designed to allow for the push-pull loading scheme and permit the associated rotations and horizontal movements at the ends and loading points. Electric resistance foil strain gauges were attached to the outer surface of the FRP tube in the longitudinal direction at different levels along the depth of the tube. However only the strain gauges at mid height of the section survived through the entire duration of the fatigue test, due to the low strains at this level. As a result, it was decided to use two displacement-type strain gauges (PI gauges) within the constant moment region at the top and bottom surfaces of the tubes in the second and third tests (i.e. specimens BFC1 and BFP1U). All specimens were tested in a load control mode. A 5000 kN MTS testing machine was used to apply the load for specimens BFC3 and BFP1U, whereas for specimen BFC1, testing started using the 5000 kN MTS machine and later continued using a 1000 kN MTS machine due to a maintenance program for the first machine. Two Linear Motion Transducers (LMTs) or two LVDTs were usually mounted on both sides

of the specimens at mid span to measure the midspan deflection. LVDTs were also mounted at both ends to measure slip between the concrete core and the FRP tube, similar to that shown in Figure 3.19(b) of chapter 3. The load was measured using a load cell integrated within the testing machines. A Data Acquisition System was used to record data continuously during the test.

#### **4.3.2 Coupon tests setup and instrumentation**

A 25 kN MTS table top machine was used for the tension-tension fatigue tests for the TC1 type specimens and the 15 mm wide TC5 type specimens. Mechanical grips were used to hold the specimens during testing. The total length of the specimens between the grips was 80 mm. Some of the specimens were instrumented with a 50 mm extensometer in order to measure the elongation in the specimen, as shown in Figure 4.4. For the 25 mm wide TC5 type specimens, since some of the specimens were subjected to tension-compression fatigue, hydraulic grips, as shown in Figure 3.4 of chapter 3, were necessary to hold the specimens. As such they were tested in a 1000 kN MTS testing machine. The total length of the specimens between the grips was 50 mm. Some of the specimens were instrumented with a 10 mm extensometer in order to measure elongation. The load was measured using load cells integrated within the testing machines. Machine load, stroke and extensometer readings were periodically taken to measure the stiffness degradation characteristics of the specimens.



## **4.4 Testing Procedures**

### **4.4.1 Full-scale CFFT beam specimens**

Table 4.1 presents a summary of the testing program for the full-scale CFFT beam specimens, including the source pile of the specimen, the ratio of maximum applied moment to the ultimate static moment established in chapter 3 ( $M_{\max}/M_{\text{ult}}$ ), frequency, type of testing machine, and the condition at termination of the test. All specimens were tested in this program under totally reversed cyclic bending moment. In each cycle, the specimen was loaded in a certain direction (upward or downwards) until it reached a predetermined load  $P_{\max}$  producing a bending moment  $M_{\max}$  within the constant moment zone. The direction of the load was then reversed until it reached the same value in the opposite direction. This loading was applied repeatedly in the form of a sinusoidal wave, as shown in Figure 4.5. Specimens BFC3 and BFP1U were tested to failure at a loading rate of 0.05 Hz. Specimen BFC3 was tested under a maximum load of 160 kN producing a maximum target moment equals to 60% of the ultimate monotonic bending moment in the constant moment zone, while specimen BFP1U was tested under a maximum load of 120 kN producing a maximum target moment equals to 45% of the ultimate monotonic bending moment in the constant moment zone. The target loads, however, could not be maintained due to loss of stiffness and the load levels had to be raised occasionally. As such, the actual average maximum moment for specimen BFC3 was 59% of the ultimate monotonic bending moment, while the actual average maximum moment for specimen BFP1U was 44% of the ultimate monotonic bending moment. Specimen BFC1 was tested under a maximum load of 66.7 kN producing a maximum target moment equals to 25% of the ultimate monotonic bending moment at a rate of 0.1 Hz for 676,532 cycles. The

loading rate was then reduced to 0.07 Hz due to the inability of testing machine to sustain this loading condition. The specimen was then cyclically loaded under the same load for another 417,782 cycles. The setup and the specimen were then moved to the 1000 kN MTS machine, where the specimen was cyclically loaded under the same load at a rate of 0.09 Hz for another 8,556 cycles. In total the specimen was cycled for 1,102,870 cycles under a target bending moment equals to 25% of the ultimate monotonic bending moment, without failure. The actual average maximum moment for specimen BFC1 in this first stage of loading was 25.35% of the ultimate monotonic bending moment. It was then decided to raise the load to 100 kN producing a maximum target moment equals to 37.5% of the ultimate monotonic bending moment. The specimen was cyclically loaded at this load level at a rate of 0.09 Hz until it failed. The average actual maximum moment for specimen BFC1 in the second stage of lading was 37% of the ultimate monotonic bending moment.

#### **4.4.2 Coupon tests**

All coupon specimens were cyclically tested to failure between a maximum stress ( $\sigma_{\max}$ ) and a minimum stress ( $\sigma_{\min}$ ). The load was applied in the form of a sine wave as shown in Figure 4.5. A summary of the test matrix is presented in Table 4.2. Two different  $\sigma_{\max}$  to  $\sigma_{\min}$  load ratios (R) were used in loading the specimens, in order to study the effect of the R ratio on the fatigue life of the tubes. An R value of 0.1 was used to represent the tension-tension fatigue case, whereas an R value of -0.25 was used to represent the tension-compression fatigue case. The specimens were subjected to different ( $\sigma_{\max}/\sigma_u$ ) stress ratios ranging from 0.2 to 0.7, where  $\sigma_u$  is the average ultimate monotonic tensile strengths of their respective tension coupon specimens as reported in chapter 3. The

loading frequency ( $f$ ) also varied between 0.1 Hz to 8 Hz to study its effect on the fatigue life of the tubes. Three identical specimens were tested for each combination of  $R$ ,  $(\sigma_{\max}/\sigma_u)$ , and  $f$ .

## **4.5 Test Results**

### **4.5.1 Full-scale CFFT beam test results**

In this section the results and observations of the full-scale CFFT beam tests in fatigue are presented.

#### **4.5.1.1 Deflection behavior**

Figures 4.6 and 4.8 show the envelope curves for the maximum and minimum mid-span deflections versus the number of cycles for specimens BFC3 and BFP1U respectively. Figures 4.7 and 4.9, on the other hand, show the load-deflection hysteretic curves for specimens BFC3 and BFP1U, respectively, as the cyclic loading progressed. The figures show a gradual increase in the deflection over time. This is likely due to stiffness degradation of the system as will be discussed later.

Figure 4.10 shows the envelope curves for the maximum and minimum mid-span deflections versus the number of cycles for specimen BFC1. Figures 4.11 and 4.12, on the other hand, show the load-deflection hysteretic curves for specimen BFC1 under maximum moments of 25% and 37% of the ultimate bending moment, respectively, as the cyclic loading progressed. The figures show a trend of a gradual increase in deflection over time, similar to specimens BFC3 and BFP1U. The sudden increase in deflection after 1.1 million cycles corresponds to changing the  $M_{\max}/M_{\text{ult}}$  ratio from 25% to 37.5% as explained in Table 4.1. Figure 4.12 shows that the relatively rapid increase of

deflection within the first few cycles did not occur under a maximum bending moment of 37.5% of the ultimate bending moment, as it did in the first few cycles under a maximum bending moment of 25% of the ultimate bending moment, because the specimen was previously loaded for 1.1 million cycles and already suffered some stiffness degradation. The figures also show rapid increase in the deflection just prior to failure.

#### **4.5.1.2 Slip behavior**

Figures 4.13 to 4.15 show the history of slip between the concrete core and the FRP tube for specimens BFC3, BFP1U and BFC1, respectively. Figure 4.13 shows a large sudden slip at the north end at the beginning of the test, probably due to the cracking of the specimen in the first cycle in a similar manner to the specimens tested under monotonic bending which were presented in chapter 3. This slip increases slightly, as the cycling continues, to about 1.2 mm then stabilizes. The south end, however, showed no sudden slip at the beginning but a gradual slip up to about 0.2 mm occurred as the cycling progressed. Figure 4.14 shows small continuous slip of about 0.01 mm at the north end of specimen BFP1U. The readings from the south LVDT are not presented due to errors that occurred in the setup during the test. Figure 4.15 shows a stable level of slip of about 0.06 mm in the north end during the first stage of loading, up to 1.1 million cycles. The initial slip in the south side was not recorded. The slip in the south end for the recorded part, however, was quite stable up to the end of the first stage of loading. In the second stage of loading the figure shows a sudden increase in slip initially, which stabilized later at the north end, whereas the south end showed very little slip initially but increased near the end. It should be noted that the south end slip is shown to start from zero in Figure 4.15, but in reality it starts from an unknown value as stated earlier. The measured slip in

general was small, and it therefore could be concluded that good bond generally existed between the tube and the concrete, and that slip normally occurs in one side more than the other.

#### **4.5.1.3 Strain behavior**

Figures 4.16 to 4.18 show the mid-height strain gauge readings, which were the only surviving groups as indicated earlier, versus number of cycles for specimens BFC3, BFP1U and BFC1, respectively. These figures show an increase in the strain initially, followed by stabilization or lower rate increases, due to the initial rapid loss of stiffness of the FRP tube, which will be discussed when presenting the coupon test results. Figures 4.19 and 4.20 show the extreme top and bottom fiber strains measured by the PI gauges for specimen BFP1U and the strains measured in the first phase of loading by the top PI gauge of specimen BFC1, respectively.

#### **4.5.1.4 Failure mode and total number of cycles**

Specimen BFC3 failed suddenly, after 2,365 cycles, by rupture of the longitudinal fibers at a single location, just outside the south end of the pure moment zone, as shown in Figure 4.21(a). The specimen suffered a sudden large loss in its stiffness at failure, as shown in Figure 4.7. After failure, the FRP tube was cut at the location of the failure, as shown in Figure 4.21(b). It is apparent from this figure that a full depth concrete crack occurred at the location of failure. Further investigation showed similar cracks along the length as well. Specimen BFP1U failed after 28,619 cycles in a similar manner, within the pure moment zone, as shown in Figure 4.22. The loss of stiffness was not as sudden as in the case of specimen BFC3, and took place over a few cycles. Specimen BFC1

sustained 1,102,870 cycles at a moment equals to 25% of the ultimate monotonic bending moment without failure; it then failed after 406,787 cycles at a moment equals to 37.5% of the ultimate monotonic bending moment. The loss of stiffness for specimen BFC1, was progressive taking place over a large number of cycles as shown in Figure 4.10. The main location of failure was just outside the south end of the pure moment zone, as shown in Figure 4.23. The FRP tube was removed after the test was concluded, revealing a number of full depth cracks as in the case of specimen BFC3, starting at about 0.8 to 0.9 m from the supports on both sides, as shown in Figure 4.24. Dust appeared in the crack at the location of failure and some of the other crack locations, indicating friction and evidence of relative movement between the concrete sections on both sides of the crack.

#### **4.5.2 Coupon test results**

The number of cycles to failure and the type of failure for all coupon tests are presented in Table 4.3. A discussion of the test results are presented in the following sections.

##### **4.5.2.1 Failure modes of coupon specimens**

All specimens, with the exception of two, failed as expected in tension in a similar manner to their counterparts tested under monotonic tension (i.e. by fiber pullout for the TC1 type coupon specimens and by fiber breakage for the TC5 type coupon specimens). Two of the specimens that were tested under tension-compression failed in compression by splitting along their mid-width and then buckled.

#### **4.5.2.2 Effect of coupon type**

The fatigue life data of the two types of coupon specimens used in this study (TC1 and TC5) and described in Table 4.2 is plotted in Figures 4.25 and 4.26 in terms of  $(\sigma_{\max}/\sigma_u)$  and  $\sigma_{\max}$  versus  $\log N$ , respectively. Each point represents the average of several repeated test results, all given in Table 4.3. For both types of specimens the testing frequency was 5 Hz and R was equal to 0.1. It is apparent from both figures that, for the same testing conditions, using different coupons will result in different fatigue life curves, due to the difference in the failure mode. In this case, the TC1 type coupons which failed by fiber pullout, showed longer fatigue life, particularly at low stress ratios. Also the TC5 coupons which failed by fiber breakage, showed a steeper fatigue curve.

#### **4.5.2.3 Effect of loading frequency**

Figures 4.27 and 4.28 present the fatigue life results for the groups of specimens tested with  $R=0.1$  (tension-tension) and  $R=-0.25$  (tension-compression), respectively. It is apparent from these figures that generally the fatigue life increases with the increase in the loading frequency, similar findings were also reported by other researchers (Scharpery, 1975, Mandell and Meier, 1983, Saff, 1983, and Sun and Chan, 1979).

#### **4.5.2.4 Effect of tension-tension and tension-compression fatigue**

Figures 4.29 and 4.30 present the results for the groups of tension-tension and tension-compression specimens tested under loading frequencies of 5 Hz and 1 Hz, respectively. It is apparent from these figures that the presence of a compression component in the loading program decreases the fatigue life of the specimens. This agrees with the findings

of other researchers (Gamstedt and Sjoegren, 1999). This effect, however, seems to diminish at high and low ( $\sigma_{max}/\sigma_u$ ) ratios and is most pronounced at 0.5 and 0.6 ratios.

#### 4.5.2.5 Stiffness degradation behavior

Figures 4.31 to 4.33 show the stiffness degradation behavior of four of the tested coupons, represented in terms of the ratio of Young's modulus  $E$  at any number of cycles  $N$ , to the initial Young's modulus  $E_0$ , plotted against the ratio of number of cycles  $N$ , to the total number of cycles at failure  $N_f$ . Figures 4.34 and 4.35 show the stress-strain hysteretic curves as the cycling progressed for two of the tested specimens, one tension-tension and the other tension-compression. It is apparent from these figures that some stiffness loss occurs at a rapid rate initially then continues at a much lower rate. This behavior is similar to that of  $[0^\circ/90^\circ]$  laminates where the initial rapid stiffness degradation is attributed to cracking of the transverse ply, in which the matrix provides most of the stiffness (Ogin et al., 1985). The degradation then continues at a much lower rate. It is also apparent from Figures 4.31 and 4.32 that the specimens suffer more stiffness degradation in compression when subjected to tension-compression fatigue.

#### 4.5.2.6 Fatigue life modeling of GFRP coupons

It could be observed from the Figures 4.25 to 4.30 that when the fatigue life is plotted on a logarithmic scale against the  $\sigma_{max}/\sigma_u$  ratio the data could be fitted with a linear relation when this ratio is in the range of 0.4 to 0.6. At values of 0.3 and lower the fatigue life increases nonlinearly at a higher rate with the decrease in the  $\sigma_{max}/\sigma_u$  ratio. Similarly, for coupons with  $\sigma_{max}/\sigma_u$  higher than 0.6, fatigue life may be reduced nonlinearly, as shown in Figure 4.27, depending on the frequency. As such the fatigue life data could not be



represented by a single linear relation. Additionally, in some cases, fitting the data with a straight line will produce a  $\sigma_{max}/\sigma_u$  ratio larger than one for a fatigue life of one cycle (monotonic loading case). Fitting the data with multiple lines or a polynomial requires a larger number of tests at a wide range of  $\sigma_{max}/\sigma_u$  ratios. A method is therefore needed that could represent the fatigue life within the whole range of  $\sigma_{max}/\sigma_u$  ratios, while requiring a relatively small number of tests as in this study. Epaarachchi and Clausen (2003) developed an empirical method for curve fitting of fatigue data of composite laminates. The method uses a single function to represent the entire range of  $\sigma_{max}/\sigma_u$  ratios. The method also could predict the fatigue life for different frequencies ( $f$ ) and minimum-to-maximum stress ratios ( $R$ ) beyond the range used to fit the curves. The following are the equations suggested by Epaarachchi and Clausen (2003);

$$\frac{D}{\alpha} = (N^\beta - 1) \quad (4.1)$$

$$\text{where; } D = \left( \frac{\sigma_u}{\sigma_{max}} - 1 \right) \left( \frac{\sigma_u}{\sigma_{max}} \right)^{0.6 - \psi |\sin \theta|} \left[ \frac{1}{(1 - \psi)^{1.6 - \psi |\sin \theta|}} \right] f^\beta \quad (4.2)$$

$$\begin{aligned} \psi &= R & -\infty < R < 1 \text{ (tension - tension and tension - compression)} \\ \psi &= 1/R & 1 < R < \infty \text{ (compression - compression)} \end{aligned} \quad (4.3)$$

and  $\alpha$  and  $\beta$  are curve fitting parameters;  $f$  is the frequency of the applied load;

$\theta$  is the smallest angle of fibers between the loading direction and the fiber direction, and

$N$  is the number of cycles.

The values of  $\alpha$  and  $\beta$  are obtained through a trial and error process. A value of  $\beta$  is assumed and the values of  $D$  and  $(N^\beta - 1)$  are calculated for all the data points. These values are then plotted with  $D$  as the Y-axis and  $(N^\beta - 1)$  as the X-axis, as shown in Figure 4.36, and the data is fitted with a straight line. This process is then repeated for different

values of  $\beta$  until the straight line passes through the origin. The value of  $\alpha$  is the slope of this line and this  $\beta$  is then used to establish the fatigue life curves.

#### 4.5.2.6.1 The effectiveness of the empirical method

The curve fitting parameters  $\alpha$  and  $\beta$  were calculated for every set of data that is based on the same coupon type and  $R$  and  $f$  values. Additionally, the curve fitting parameters were calculated using the entire data obtained from all the tested 25 mm wide TC5 type coupons. Fatigue life curves were then constructed using these parameters and the goodness of fit values ( $R^2$ ) were then calculated for these curves. The values of  $\alpha$ ,  $\beta$  and  $R^2$  are presented in Table 4.4. The empirical equation seems to represent the data very well, as shown in Figures 4.37 to 4.40, which present the fatigue life curves for the following four  $R$  and  $f$  combinations, respectively: ( $R = 0.1$  and  $f = 5$  Hz); ( $R = 0.1$  and  $f = 1$  Hz); ( $R = -0.25$  and  $f = 5$  Hz); and ( $R = -0.25$  and  $f = 1$  Hz). In each figure four, plots are presented; the solid thin line presents the fatigue life curve calculated using parameters obtained by fitting test data, where  $f$  and  $R$  values similar to the combination used to establish the experimental points under study were used. The dashed line presents the fatigue life curve calculated using parameters obtained by fitting test data, where a similar  $f$  and a different  $R$  value of the combination under study were used in the tests. The dash-dot line presents the fatigue life curve calculated using parameters obtained by fitting test data where a similar  $R$  and a different  $f$  value to the combination under study were used in the tests. The solid thick grey line presents the fatigue life curve calculated using parameters obtained by fitting the test data of all tested 25 mm wide TC5 type specimens. The  $R^2$  for all these curves are also presented in Table 4.4. It is apparent from the figures and the  $R^2$  values presented in the table that the equation can represent

reasonably well the fatigue life for specimens subjected to the same loading frequency but a different  $R$  ratio from the one used to obtain the curve fitting parameters. The equation, however, was not as effective in representing the fatigue life for specimens subjected to the same  $R$  ratio but a different loading frequency from the one used to obtain the curve fitting parameters. The fatigue life curves obtained by using the curve fitting parameters that were calculated using the entire sets of data obtained from all the tested 25 mm wide TC5 type specimens, gave good representations in some cases while in other cases it gave poor representation.

#### **4.5.2.6.2 Estimating fatigue life of full-scale CFFT specimens using empirical method**

Conducting large full scale experiments on fatigue behavior of CFFTs is quiet costly and time consuming. It also requires large testing machines that are not always readily available. In any case, only a few number of tests could be practically conducted. If CFFTs are to be widely used in applications where cyclic loading is a concern, a method is needed to predict the fatigue life of CFFT based on simple coupon tests, which are easier and less expensive to conduct. In addition, they could be conducted using small testing machines that are usually readily available. An attempt was made to estimate the fatigue life of the full scale CFFT specimens BFC1, BFC3 and BFP1U based on coupon tests, using the following procedure;

1. The strain at the extreme top and bottom fibers were obtained from the load-strain relation of the monotonic load test presented in Figure 3.29 for all value of  $M_{max}/M_{ult}$  that the specimens were subjected to (0.25, 0.375, 0.45 and 0.60).

2. The maximum and minimum stresses were then calculated for each  $M_{max}/M_{ult}$  from the stress-strain relation for the TC5 type tension coupons and the compression coupons presented in Figures 3.5 and 3.7.
3. The values of  $\sigma_{max}$ ,  $\sigma_u$  and  $R$  were then calculated for each  $M_{max}/M_{ult}$ .
4. The number of cycles to failure  $N_f$  were calculated for each set of  $M_{max}/M_{ult}$  and loading frequency  $f$  using equations 4.1 and 4.2. The values of  $\alpha$  and  $\beta$  that were obtained from test data where  $f = 0.1$  and  $R = -0.25$  were used in equations 4.1 and 4.2 since they represent the conditions closest to the one used in the full scale CFFT tests.

The calculations using this procedure are presented in Table 4.5. The values of the number of cycles to failure calculated using the procedure described above, were directly compared to those obtained from the full scale CFFT tests for specimens BFC3 and BFP1U, because the value of  $M_{max}/M_{ult}$  and loading frequency  $f$  for these specimens remained constant throughout the test. For specimen BFC1, however, there were four loading phases as described in Table 4.1. For each loading phase the values of the number of cycles to failure was calculated using the procedure described above and the values of  $N/N_f$  were calculated, where  $N$  is the actual number of cycles in each loading phase. A linear accumulative damage relation was assumed and the damage value was calculated as  $\Sigma(N/N_f)$ , and was compared to unity, the value of damage at failure.

The results are of this procedure are presented in Table 4.6, and Figure 4.41. It could be seen from this table and the figure that the predicted fatigue life compared well to the full scale test results.

#### 4.5.2.7 Modeling stiffness degradation

Ogin et al. (1985) developed an equation for calculating the stiffness degradation of [0°/90°] laminates assuming linear relationship between the elastic modulus and crack density, and the total crack length as the power function of the stored elastic energy, given by

$$-\frac{1}{E_0} \frac{dE}{dN} = A \left( \frac{\sigma_{\max}^2}{E_0^2 \left(1 - \frac{E}{E_0}\right)} \right)^{ng} \quad (4.4)$$

where  $\left[-\frac{1}{E_0} \frac{dE}{dN}\right]$  is the modulus reduction rate at a given value of  $E/E_0$ ,  $E_0$  is the uncracked elastic modulus,  $E$  is the secant modulus of FRP at a given number of cycles  $N$ ,  $\sigma_{\max}$ , is the maximum applied stress, and  $ng$  and  $A$  are the material constants, which are obtained by fitting test data. This is done by plotting both sides of the equation on a log-log scale, then fitting the data with a straight line, where  $ng$  represents the slope and  $\log A$  represents the intercept at the Y-axis. Using this procedure, the values of  $A$  and  $ng$  were calculated for both the tension and compression cases, as shown in Figure 4.41. However, since the tests that were conducted to obtain this data had a variety of  $R$  and  $f$  values which have a large impact on the fatigue life, the value of the normalized number of cycles  $N/N_f$  was used instead of the absolute value of  $N$  in equation 4.4, where  $N_f$  is the total number of cycles to failure. By integrating equation 4.4 (Deskovic, 1993), the following function is obtained for the stiffness degradation;

$$\frac{E}{E_0} = 1 - [(ng + 1)A]^{1/(ng+1)} \left[ \frac{\sigma_{\max}}{E_0} \right]^{2ng/(ng+1)} \left[ \frac{N}{N_f} \right]^{1/(ng+1)} \quad (4.5)$$

Substituting for  $A$  and  $ng$  obtained from Figure 4.42, results in the following stiffness degradation equations for tension and compression;

$$\frac{E}{E_0} = 1 - 393 \left[ \frac{\sigma_{\max}}{E_0} \right]^{1.608} \left[ \frac{N}{N_f} \right]^{0.196} \quad (\text{for tension}) \quad (4.6)$$

$$\frac{E}{E_0} = 1 - 1100 \left[ \frac{\sigma_{\max}}{E_0} \right]^{1.67} \left[ \frac{N}{N_f} \right]^{0.167} \quad (\text{for compression}) \quad (4.7)$$

Figures 4.31 to 4.33 present the stiffness degradation curves for the GFRP tube obtained from the above equations, compared to the test data. The curves show good representation of the test data.

Table 4-1 Summary of full-scale Fatigue CFFT beam test program

Specimen ID	Source pile	$M_{max}/M_{ult}$	Frequency Hz	Testing machine	Condition of termination
BFC3	C3	0.60	0.05	5000 kN MTS	To failure
BFP1U	P1	0.45	0.05	5000 kN MTS	To failure
BFC1	C1	0.25	0.10	5000 kN MTS	676532 cycles
		0.25	0.07	5000 kN MTS	417782 cycles
		0.25	0.09	1000 kN MTS	8556 cycles
		0.375	0.09	1000 kN MTS	To failure

Table 4-2 Fatigue coupon test matrix

Coupon type	R	Specimen width	Freq. (Hz)	$\sigma_{max}/\sigma_u$
TC1 <sup>1</sup>	0.1	12.7-19.3 mm	5	0.4/ 0.5/ 0.6
TC5 <sup>2</sup>	0.1	15 mm	8	0.2/0.3/0.4/ 0.5/ 0.6
TC5 <sup>2</sup>	0.1	25 mm	5	0.4/ 0.5/ 0.6/ 0.7
TC5 <sup>2</sup>	0.1	25 mm	1	0.5/ 0.6/ 0.7
TC5 <sup>2</sup>	-0.25	25 mm	5	0.3 /0.4 /0.5 /0.6 / 0.7
TC5 <sup>2</sup>	-0.25	25 mm	1	0.4/ 0.5/ 0.6/ 0.7
TC5 <sup>2</sup>	-0.25	25 mm	0.1	0.5/ 0.6/ 0.7

<sup>1</sup> Dumbbell shape (ASTM D 638 - see Figure 3.3 of Chapter 3)

<sup>2</sup> Cut in the direction of the longitudinal fibers (ASTM D 3039 - see Figure 3.3 of Chapter 3)

Table 4-3 Coupon test results

Coupon type	f	R	$\sigma_{\max}/\sigma_{\text{ult}}$	$N_f$	failure type
TC1	5	0.1	0.6	12,590	T-FP
			0.6	15,325	T-FP
			0.6	18,014	T-FP
			0.5	137,563	T-FP
			0.5	134,541	T-FP
			0.5	69,314	T-FP
			0.4	286,582	T-FP
			0.4	673,447	T-FP
			0.4	1,342,447	T-FP
TC5	8	0.1	0.6	8,470	T-FB
			0.6	11,611	T-FB
			0.6	11,781	T-FB
			0.5	48,300	T-FB
			0.5	42,952	T-FB
			0.5	32,462	T-FB
			0.5	20,729	T-FB
			0.5	31,321	T-FB
			0.4	70,281	T-FB
			0.4	68,241	T-FB
			0.4	111,198	T-FB
			0.3	729,697	T-FB
			0.3	390,342	T-FB
			0.3	475,970	T-FB
			TC5	5	0.1
0.7	348	T-FB			
0.7	255	T-FB			
0.6	4,568	T-FB			
0.6	7,764	T-FB			
0.6	9,790	T-FB			
0.5	15,851	T-FB			
0.5	19,720	T-FB			
0.5	28,648	T-FB			
0.4	55,523	T-FB			
0.4	54,530	T-FB			
0.4	32,023	T-FB			
TC5	1	0.1	0.7	380	T-FB
			0.7	329	T-FB
			0.7	721	T-FB
			0.6	1,516	T-FB
			0.6	5,828	T-FB



Coupon type	f	R	$\sigma_{\max}/\sigma_{\text{ult}}$	$N_f$	failure type
			0.6	2,074	T-FB
			0.5	15,153	T-FB
			0.5	9,623	T-FB
			0.5	20,258	T-FB
TC5	5	-0.25	0.7	230	T-FB
			0.7	703	T-FB
			0.7	333	T-FB
			0.6	1,675	T-FB
			0.6	826	T-FB
			0.6	1,330	T-FB
			0.5	7,000	C-S-B
			0.5	9,027	T-FB
			0.5	5,954	T-FB
			0.4	43,000	T-FB
			0.4	53,339	T-FB
			0.4	84,050	T-FB
			0.3	322,699	T-FB
			0.3	166,594	T-FB
0.3	204,327	T-FB			
TC5	1	-0.25	0.7	634	T-FB
			0.7	150	C-S-B
			0.7	304	T-FB
			0.6	860	T-FB
			0.6	916	T-FB
			0.6	726	T-FB
			0.5	4,381	T-FB
			0.5	4,751	T-FB
			0.5	2,593	T-FB
			0.4	21,141	T-FB
			0.4	47,319	T-FB
0.4	16,093	T-FB			
TC5	0.1	-0.25	0.7	78	T-FB
			0.7	372	T-FB
			0.7	192	T-FB
			0.6	1,239	T-FB
			0.6	479	T-FB
			0.6	496	T-FB
			0.5	2,195	T-FB
			0.5	4,734	T-FB
			0.5	4,519	T-FB

T-FP Tension failure by fibers pull-out.

T-FB Tension failure by fiber breakage.

C-S-B Compression failure by splitting and buckling.

Table 4-4  $R^2$  values under different conditions

R	f	$\alpha$	$\beta$	$R^2$ test data empirical method	$R^2$ test data same f different R	$R^2$ test data same R different f	$R^2$ test data from all TC5 specimens
0.1	8	0.0763	0.3872	0.947	N/A	N/A	N/A
0.1	5	0.1056	0.3567	0.867	0.685	0.217	0.681
0.1	1	0.2145	0.2287	0.909	0.802	0.301	0.803
-0.25	5	0.1135	0.3163	0.973	0.886	0.781	0.969
-0.25	1	0.1191	0.275	0.915	0.743	0.636	0.668
-0.25	0.1	0.092	0.2446	0.843	N/A	N/A	N/A

Table 4-5 Calculation of  $N_f$  for CFFT beams

$M/M_{ult}$	$\epsilon_{bottom} \times 10^3$	$\epsilon_{top} \times 10^3$	$\sigma_{bottom}$ (MPa)	$\sigma_{top}$ (MPa)	$\sigma_{max}/\sigma_{ult}$	R	f	$N_f$
0.25	3.59	-1.14	88.73	-29.54	0.18	-0.33	0.1	10,844,703
							0.07	7,645,245
							0.09	9,641,533
0.37	5.62	-1.75	136.73	-44.57	0.28	-0.33	0.09	349,426
0.44	7.04	-2.17	169.51	-54.62	0.35	-0.32	0.05	36,060
0.59	10.28	-3.18	241.33	-77.97	0.50	-0.32	0.05	1,697

Table 4-6 Fatigue life predictions for full-scale CFFT specimens using coupon test results

Specimen	Number of Cycles (Experimental) (N)	Predicted number of Cycles to failure ( $N_f$ )	$N/N_f$	$N/N_f$ (log scale)
BFC3	2,365	1,697	139.36%	104.46%
BFP1U	28,619	36,060	79.36%	97.80%
BFC1 (stage 1)	676,532	10,844,703	6.24%	N/A
BFC1 (stage 2)	417,782	7,645,245	5.46%	
BFC1 (stage 3)	8,556	9,641,533	0.09%	
BFC1 (stage 4)	406,787	349,426	116.42%	
$\Sigma$ BFC1			128.21%	

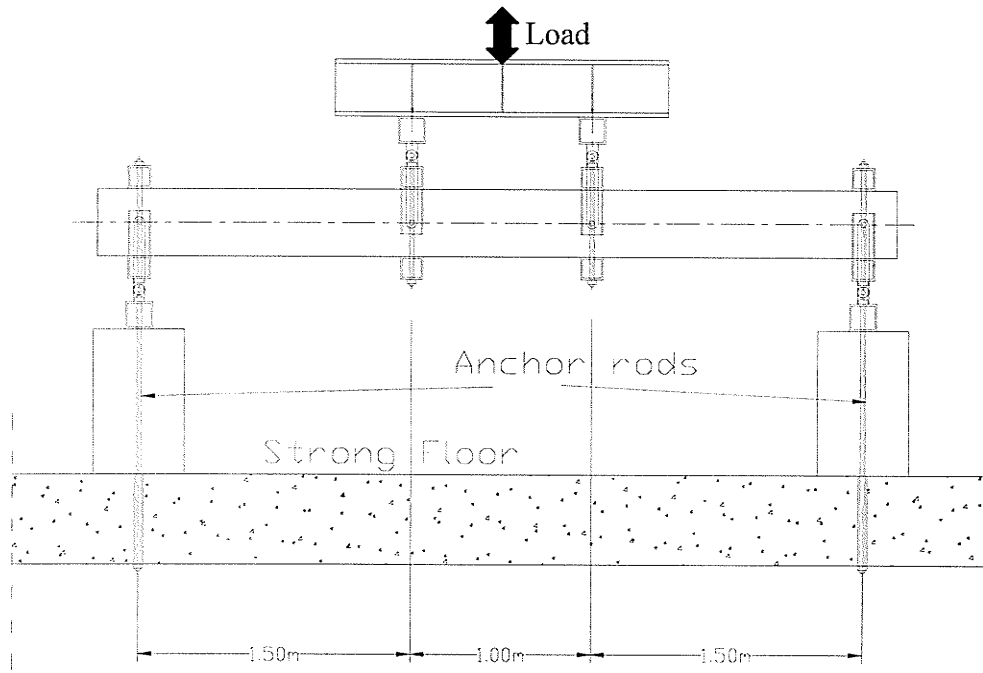


Figure 4-1 Schematic of full-scale CFFT beam test setup

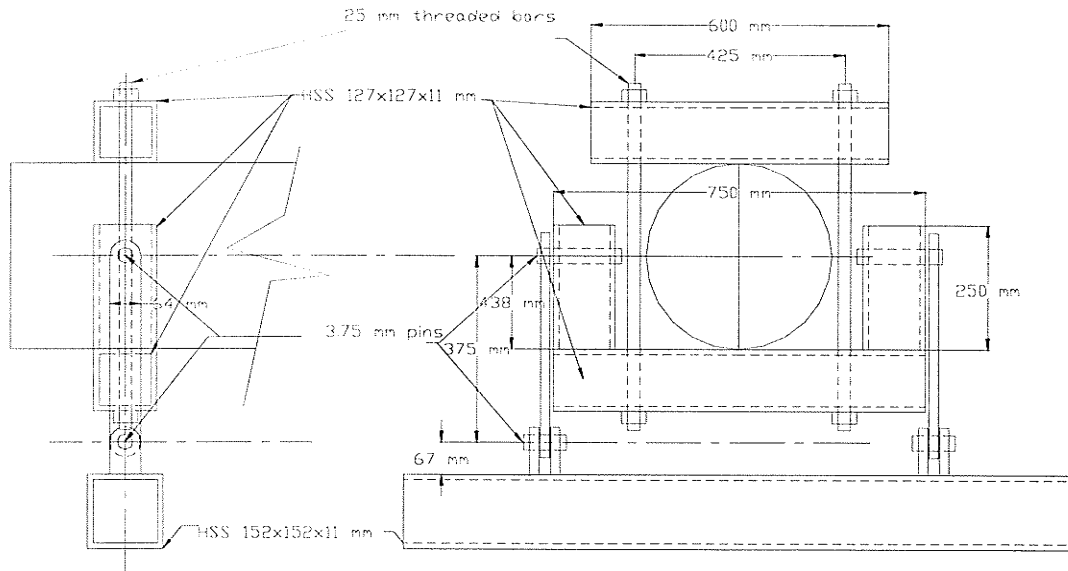


Figure 4-2 Schematic of support system to take reaction of push and pull loading

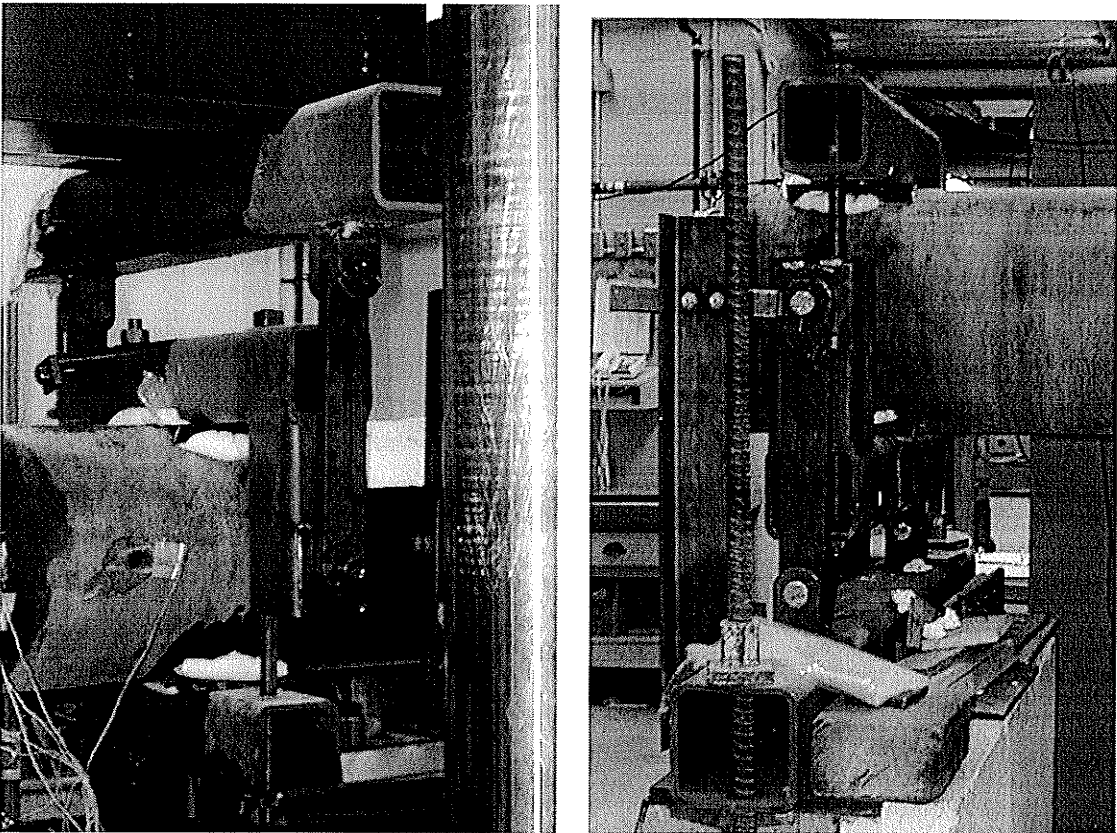


Figure 4-3 View of support system and loading point

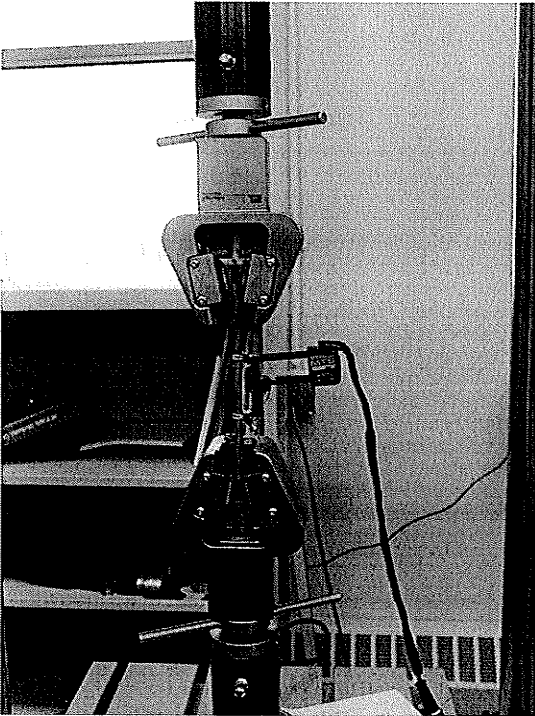


Figure 4-4 Coupon test setup in the 25 kN machine

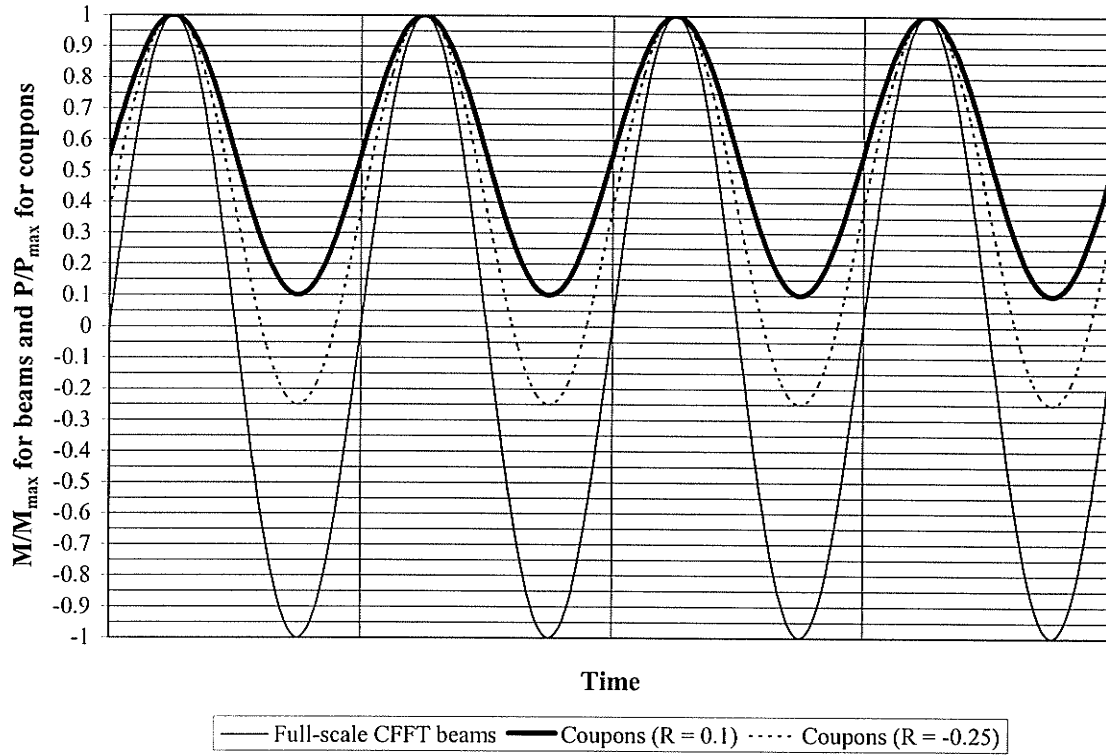


Figure 4-5 Loading history of test specimens

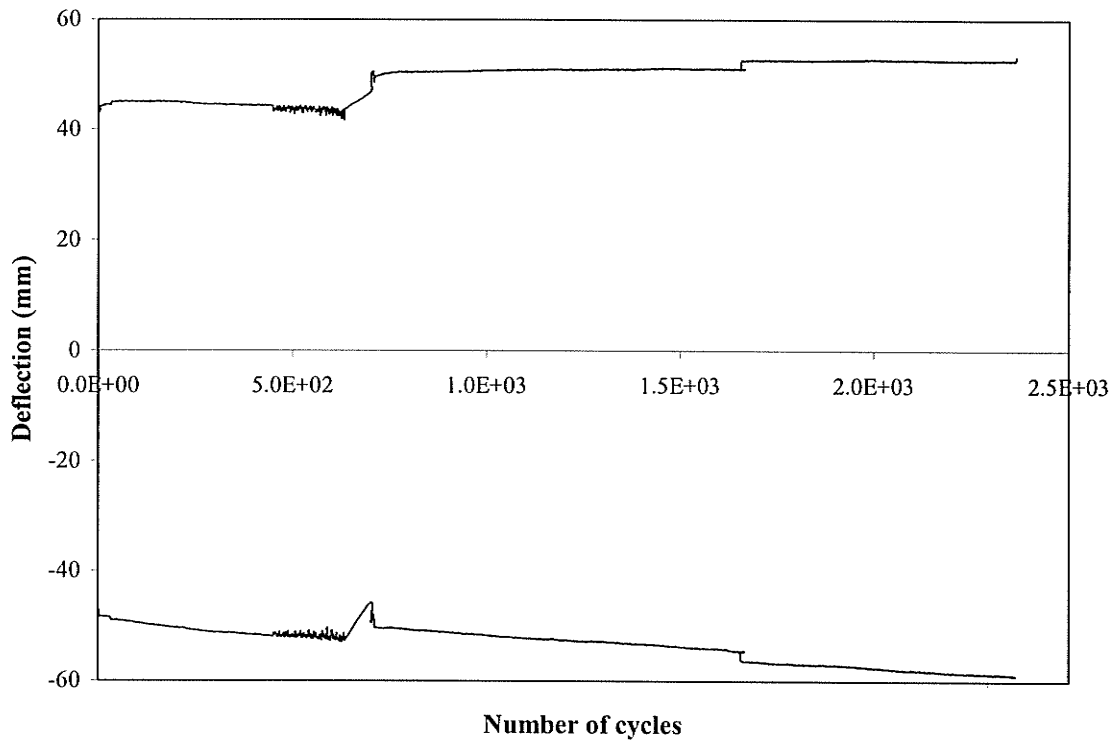


Figure 4-6 Mid-span deflection vs. number of cycles for specimen BFC3

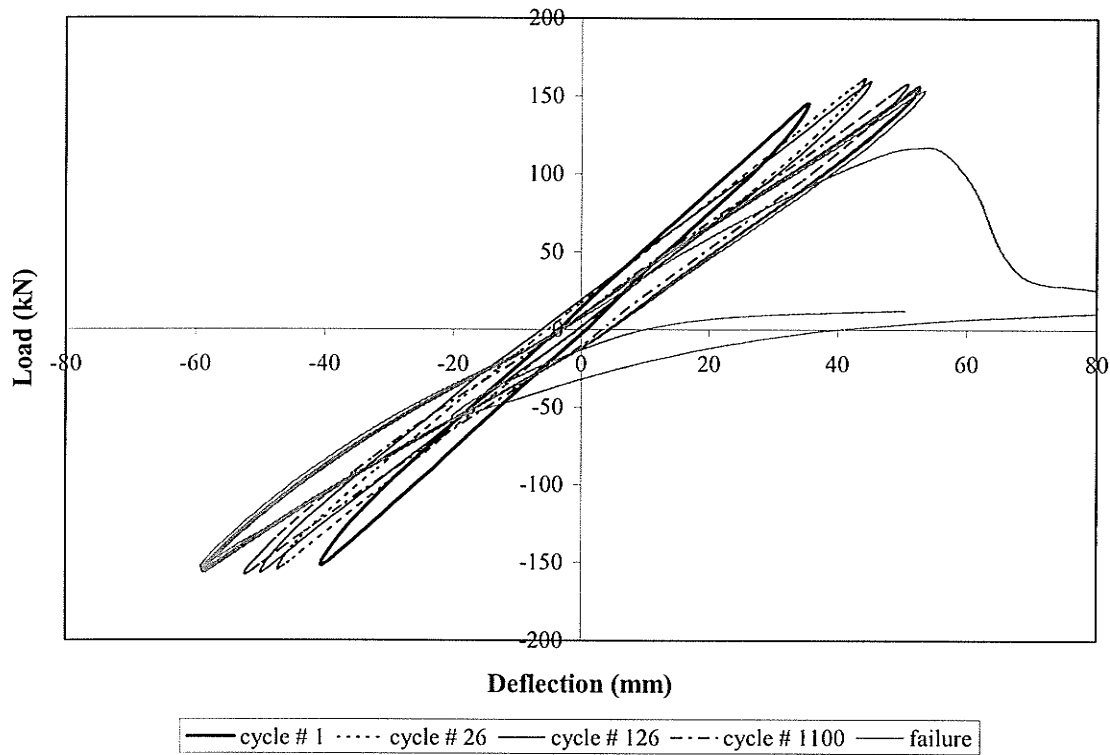


Figure 4-7 Load-deflection behavior for specimen BFC3 at different number of cycles

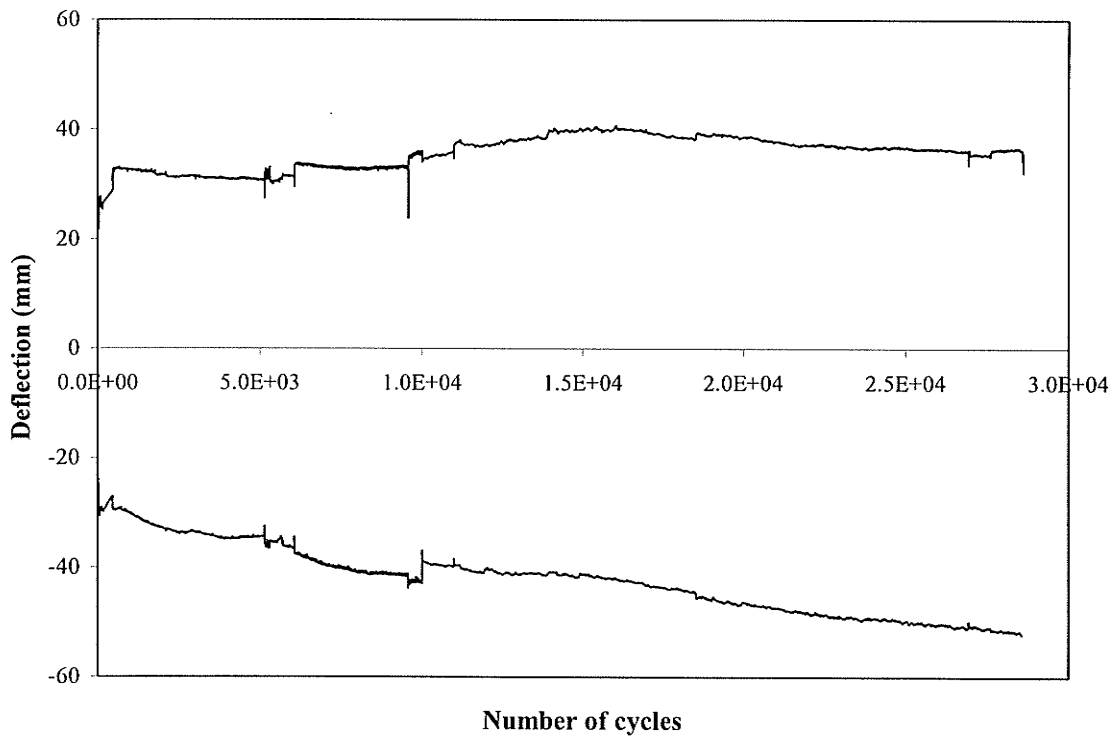


Figure 4-8 Mid-span deflection vs. number of cycles for specimen BFP1U

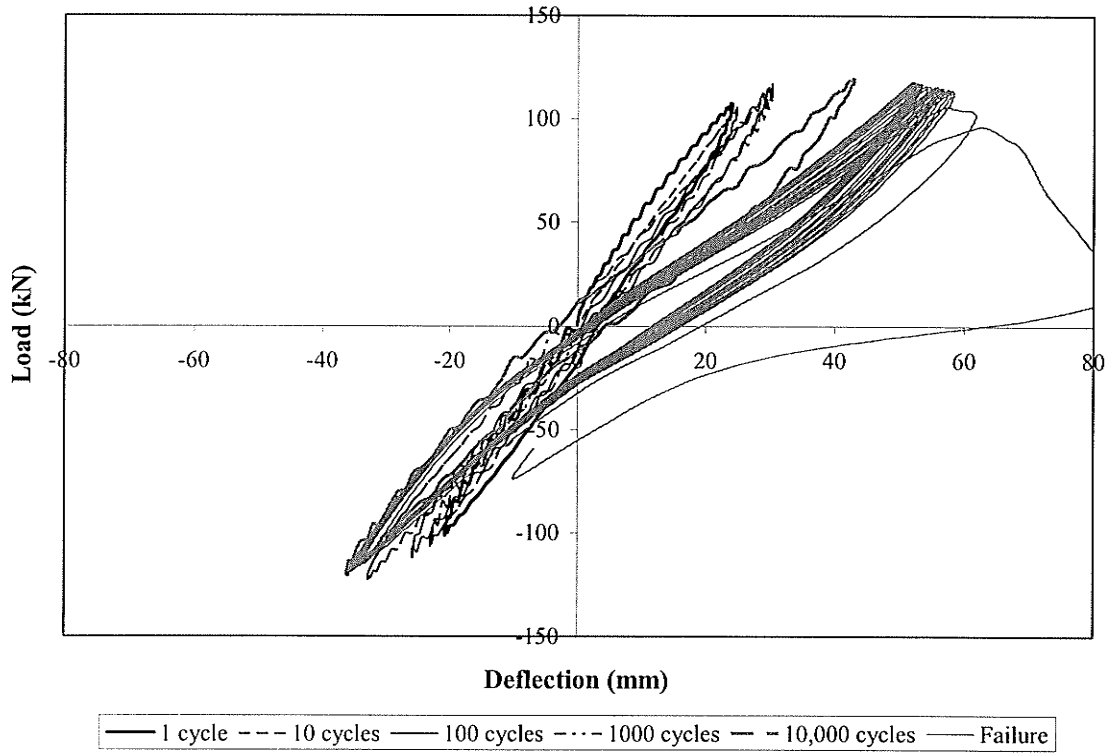


Figure 4-9 Load-deflection behavior for specimen BFP1U at different number of cycles

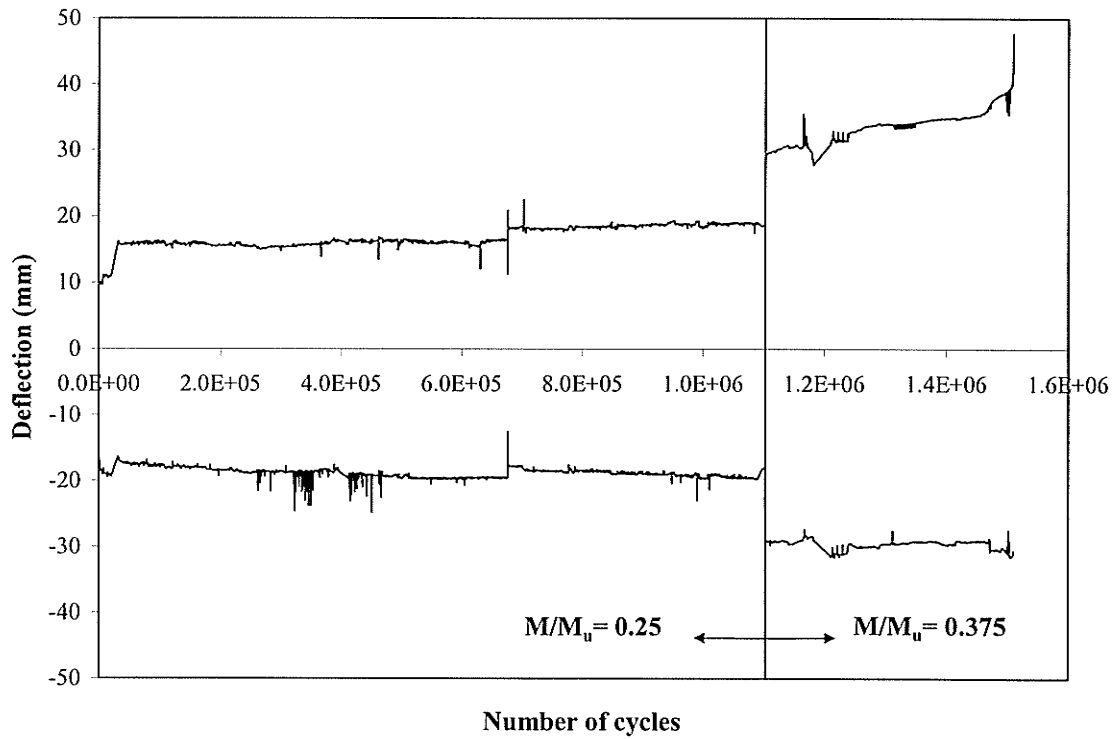


Figure 4-10 Mid-span deflection vs. number of cycles for specimen BFC1

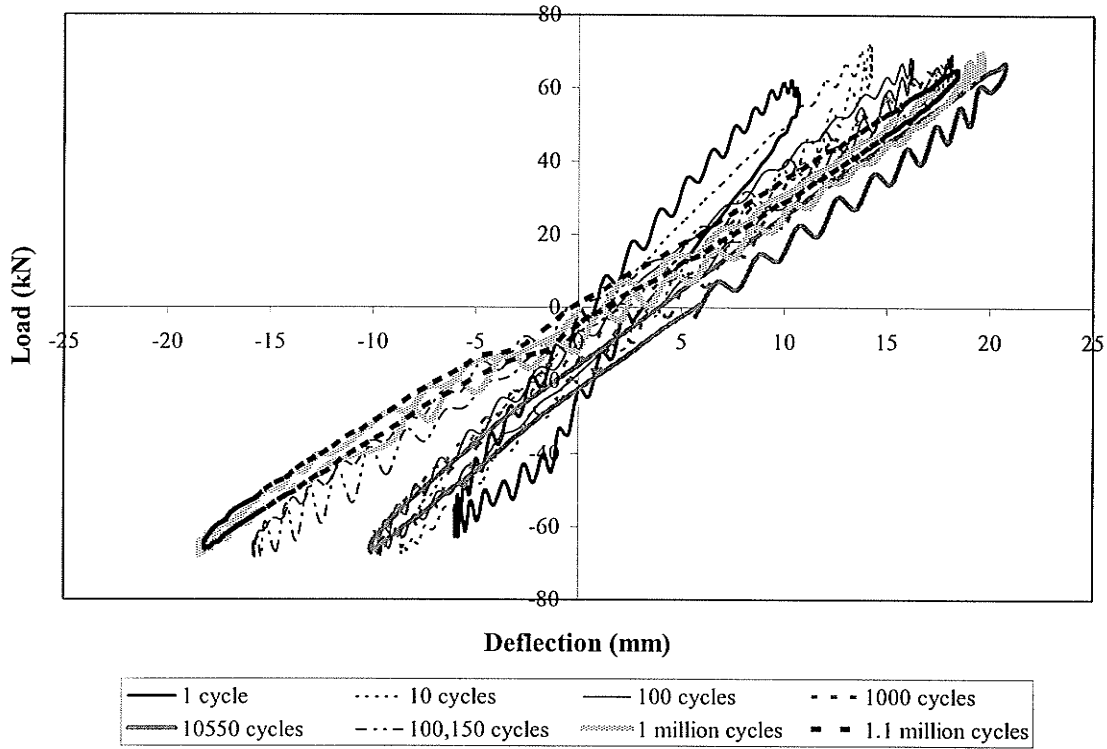


Figure 4-11 Load-deflection behavior for specimen BFC1 ( $M_{max}/M_{ult}=0.25$ )

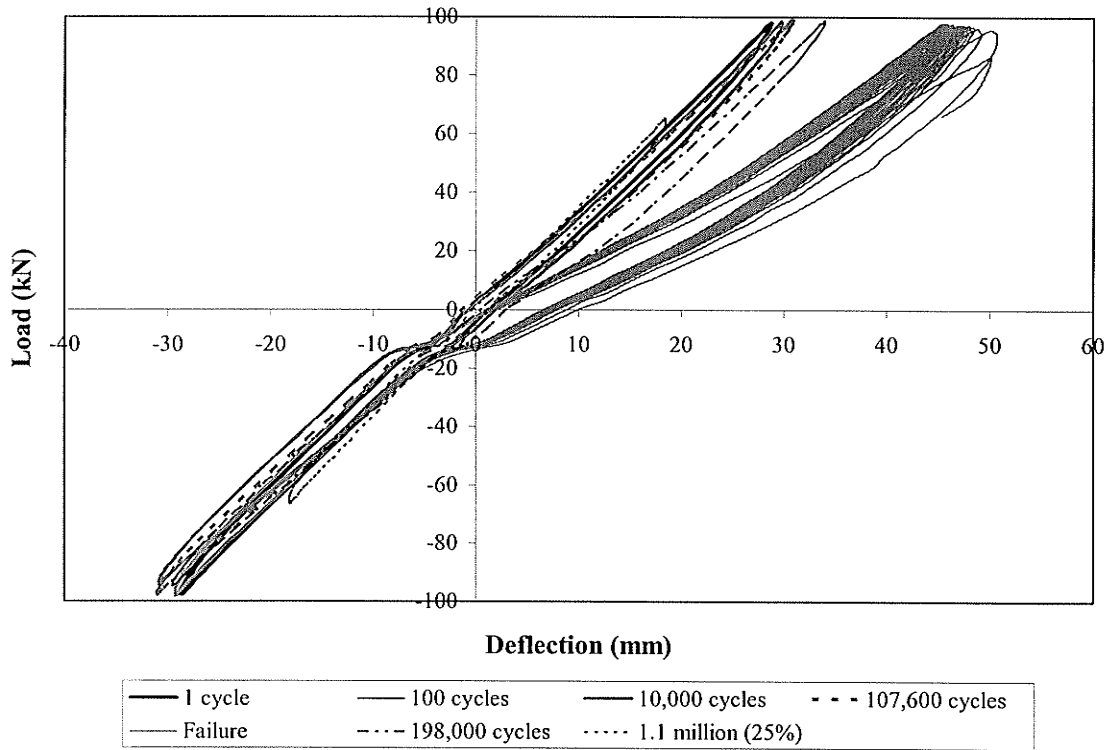


Figure 4-12 Load-deflection behavior for specimen BFC1 ( $M_{max}/M_{ult}=0.375$ )



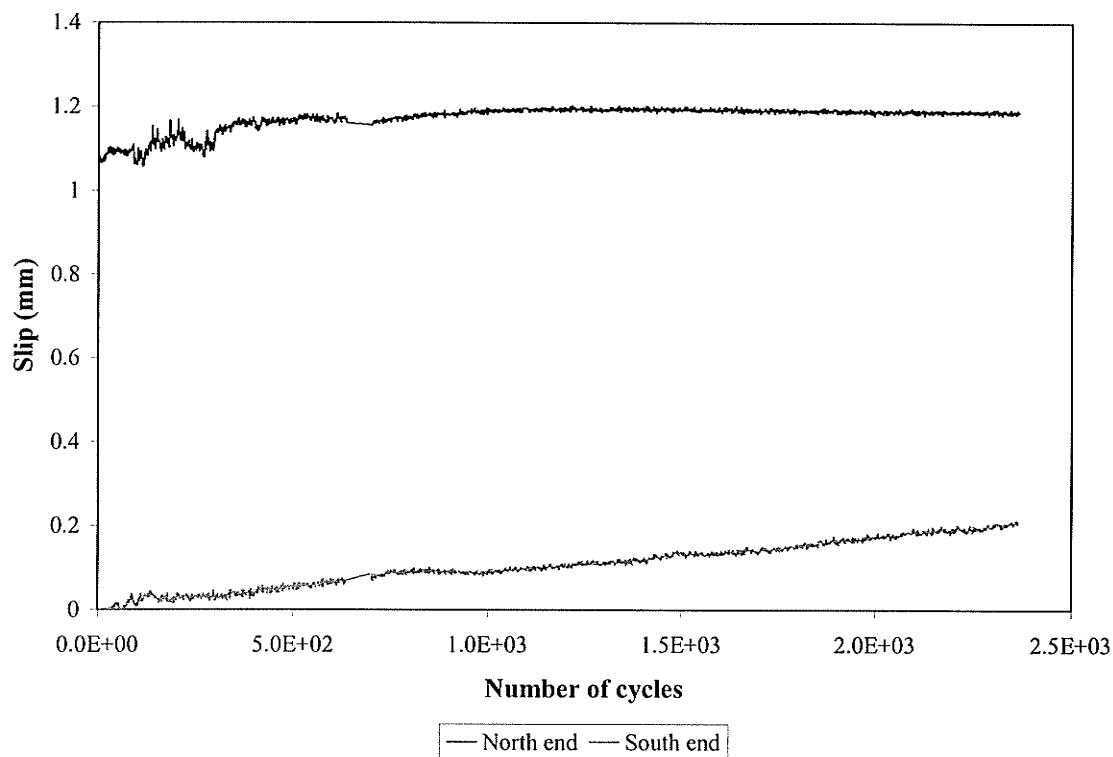


Figure 4-13 End slip history of specimen BFC3

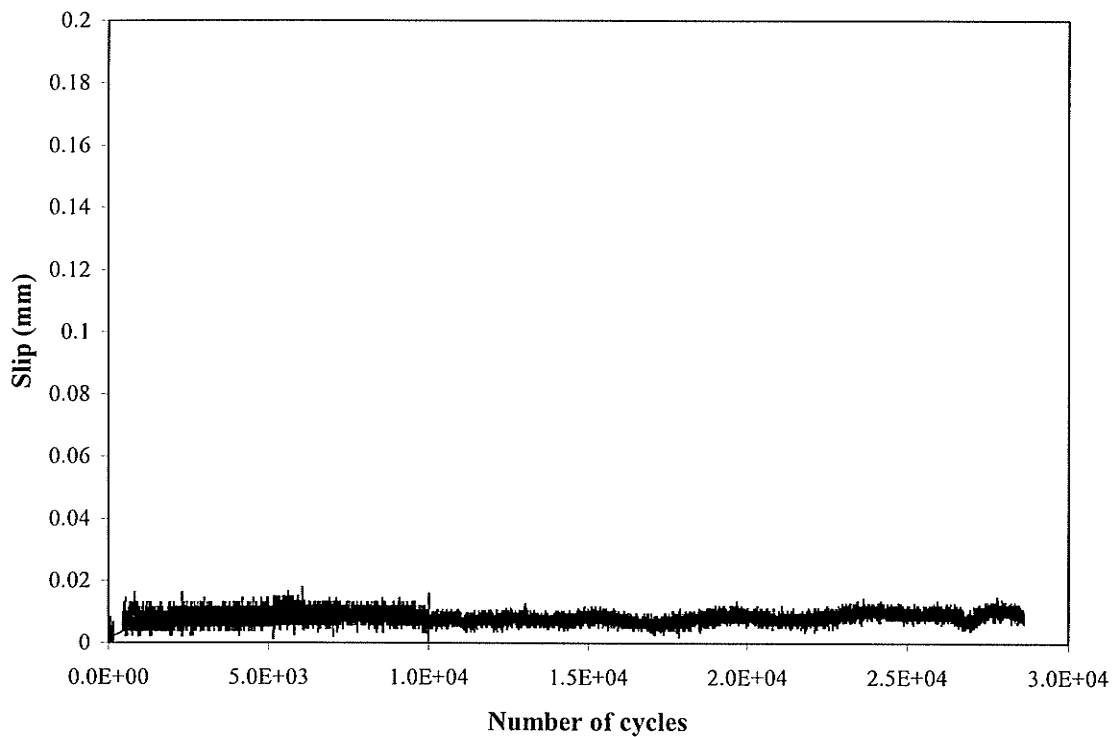


Figure 4-14 End slip history of specimen BFP1U

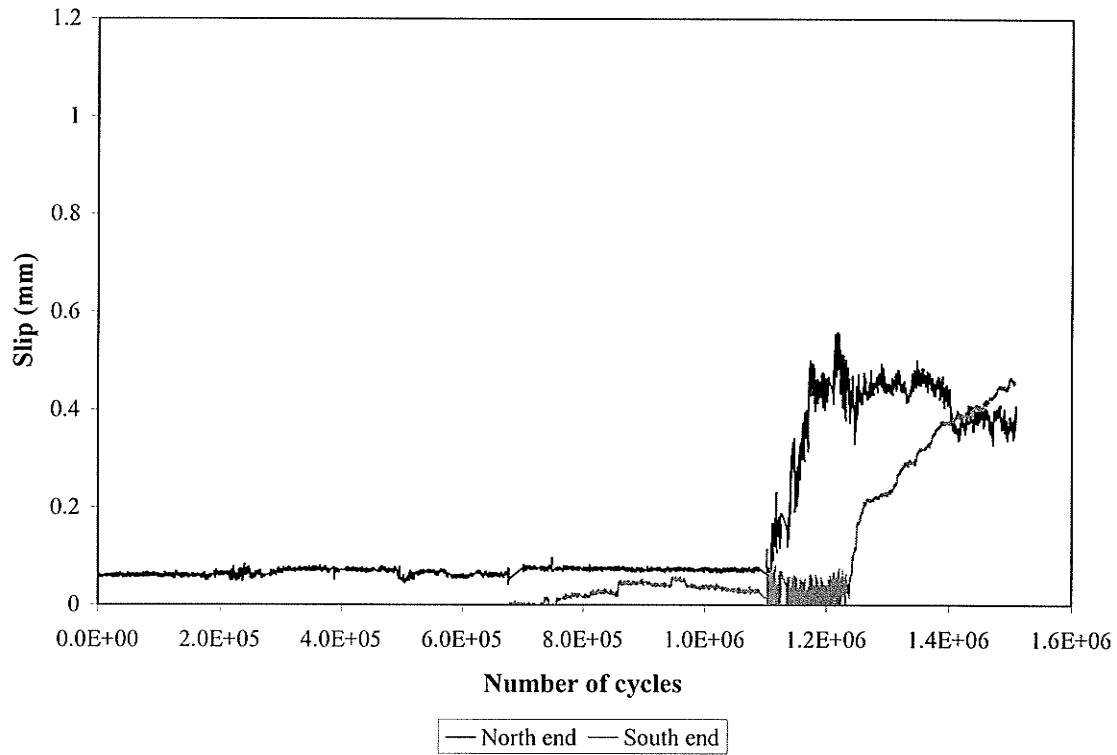


Figure 4-15 End slip history of specimen BFC1

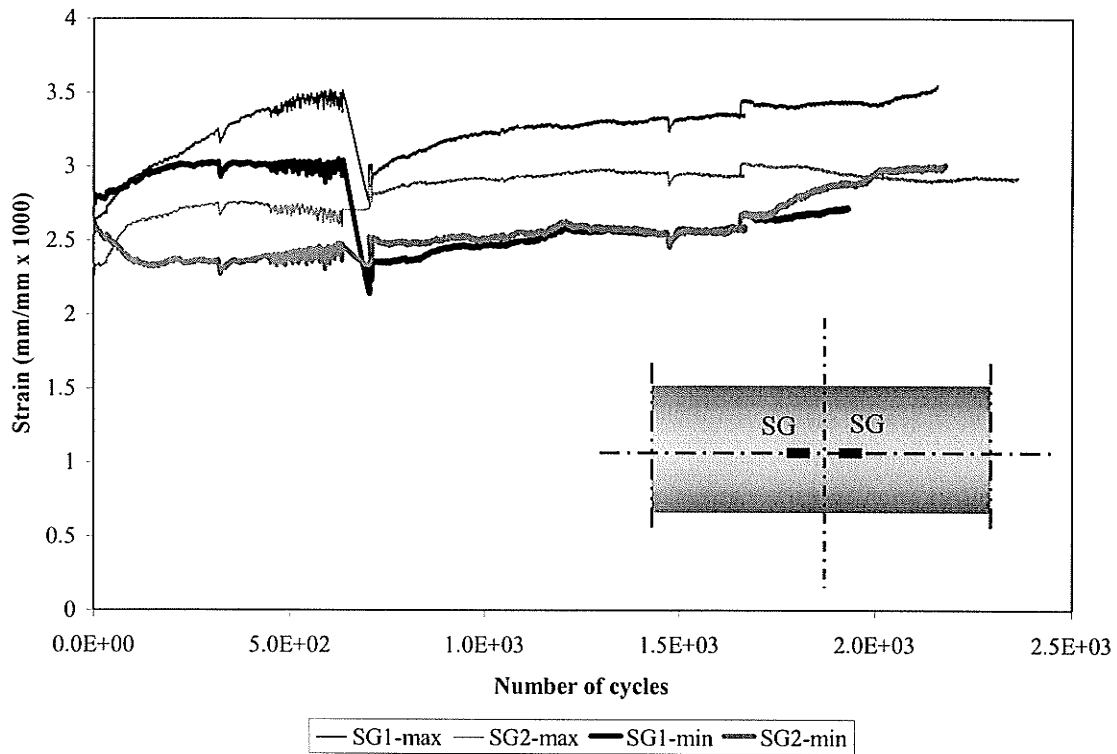


Figure 4-16 Mid-height strain history of specimen BFC3

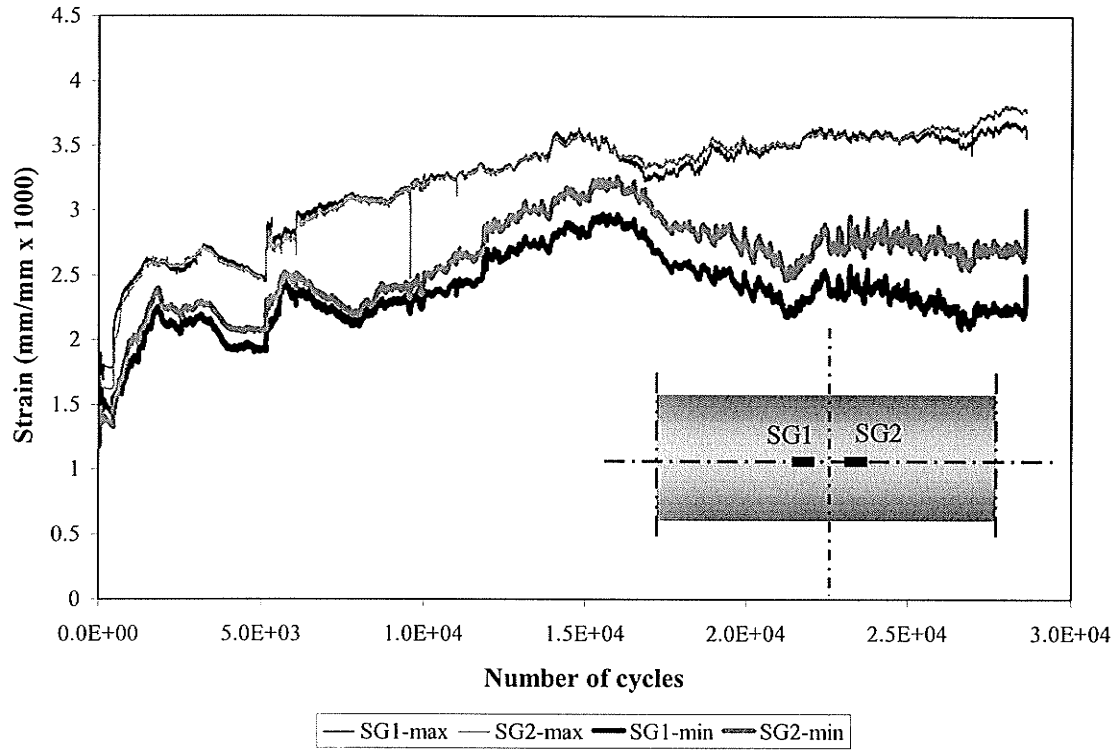


Figure 4-17 Mid-height strain history of specimen BFP1U

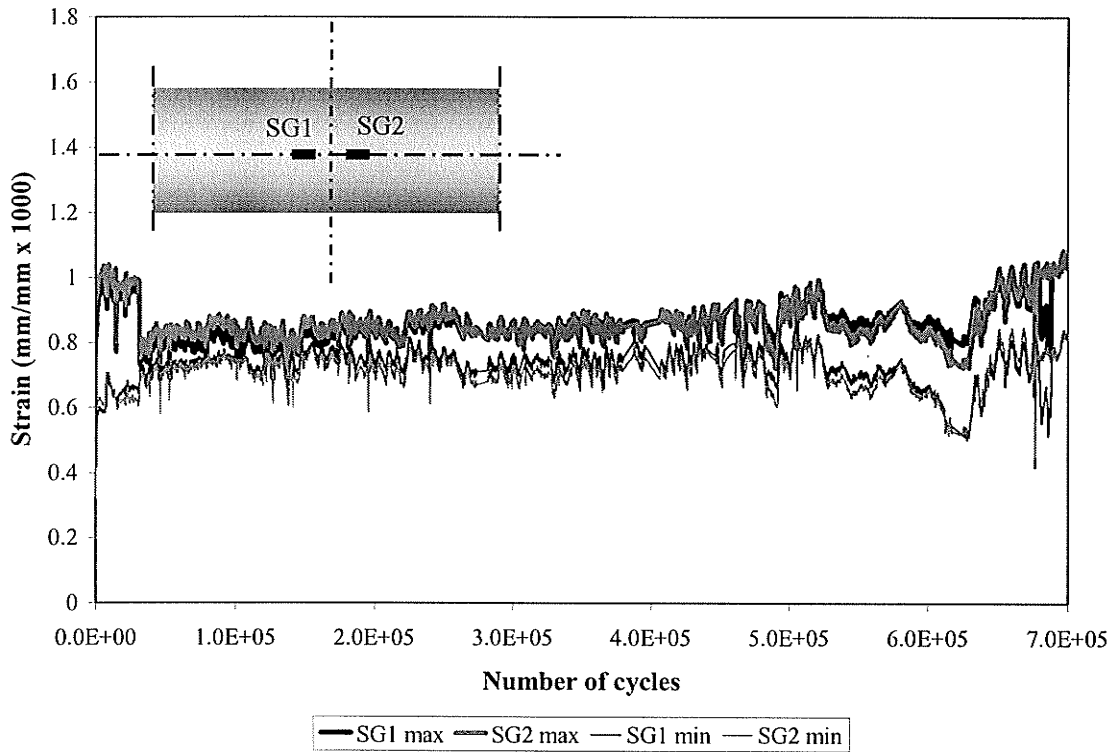


Figure 4-18 Mid-height strain history of specimen BFC1

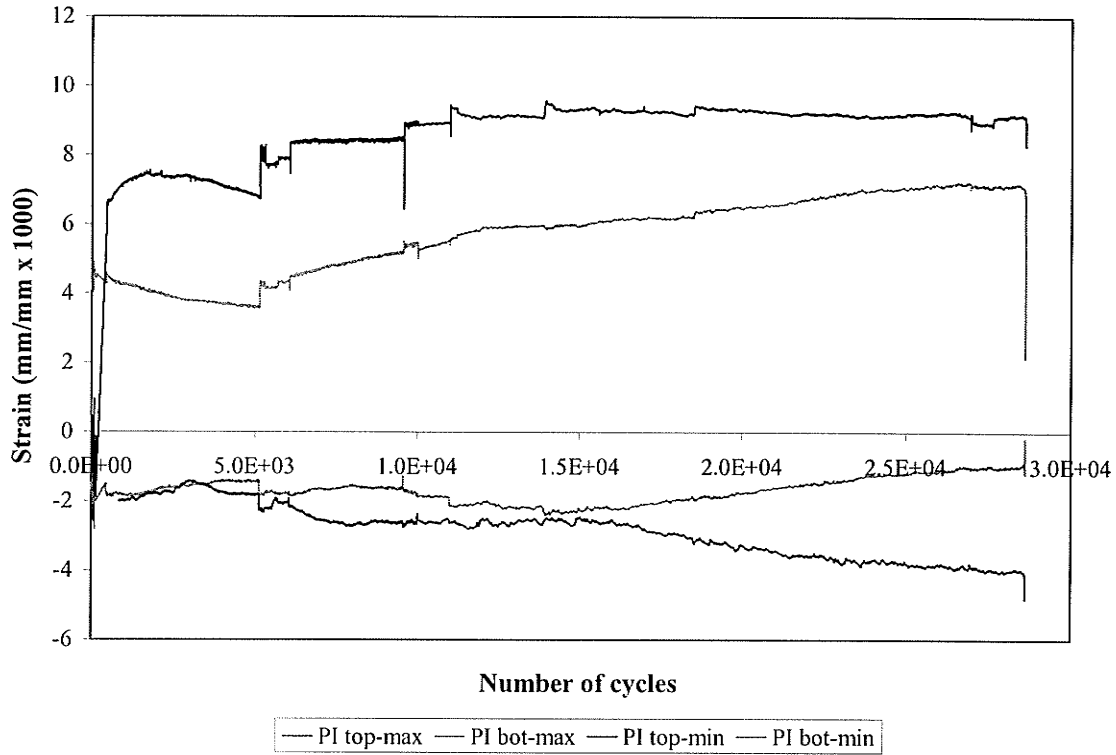


Figure 4-19 PI gauge readings of specimen BFP1U

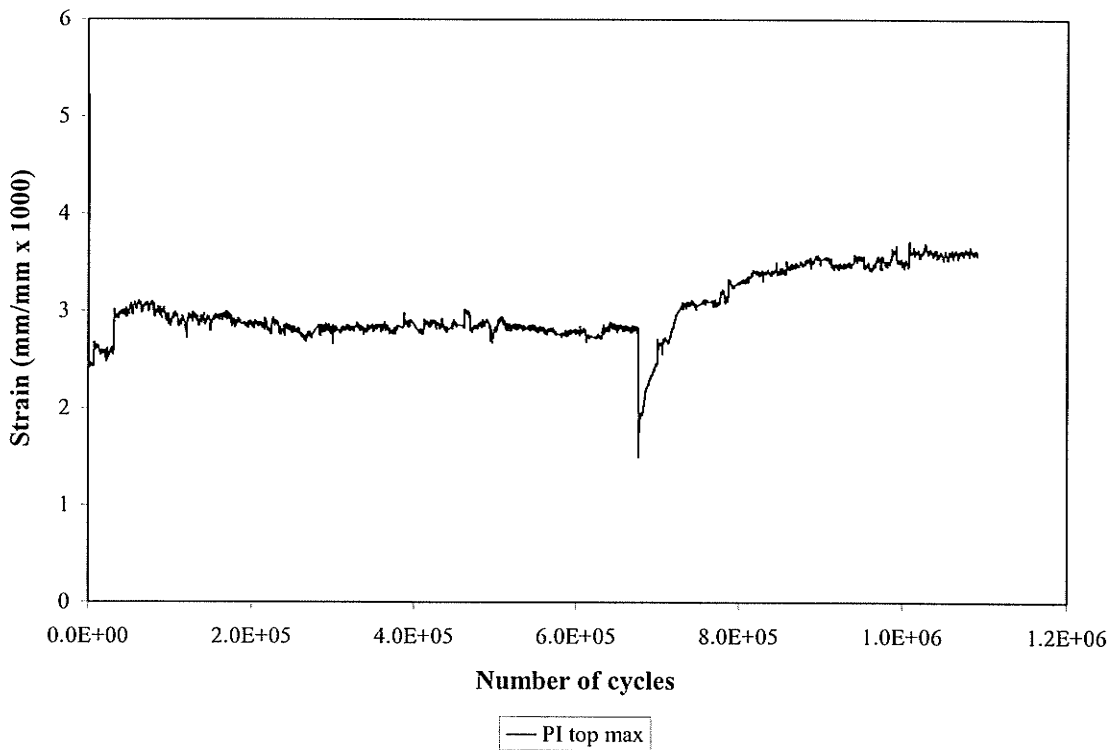
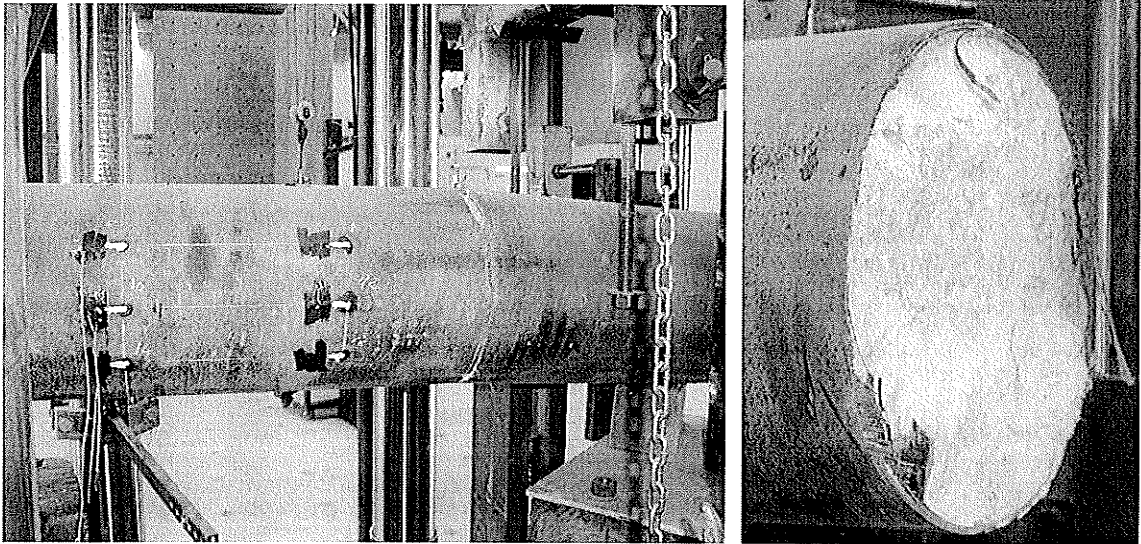


Figure 4-20 PI gauge readings of specimen BFC1



(a) Failure location

(b) Full depth crack

Figure 4-21 Failure of specimen BFC3

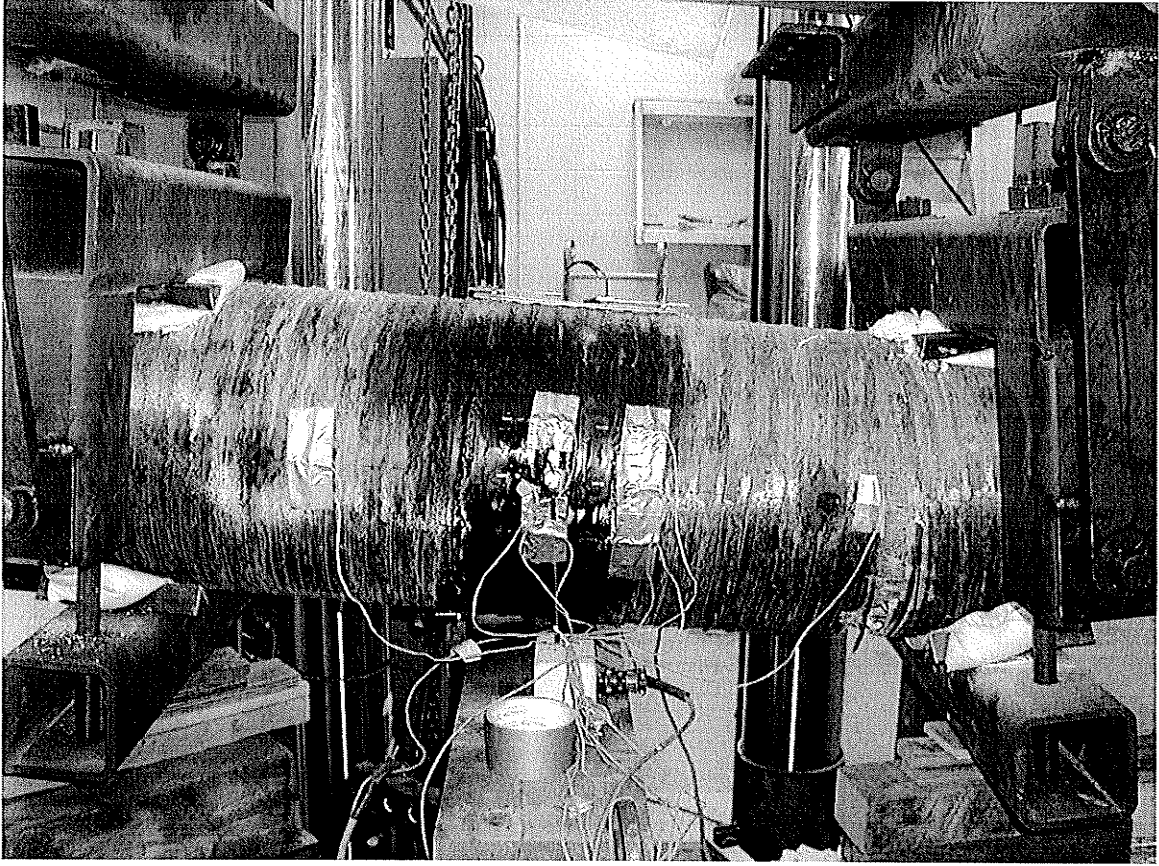


Figure 4-22 Failure of specimen BFP1U



Figure 4-23 Failure of specimen BFC1

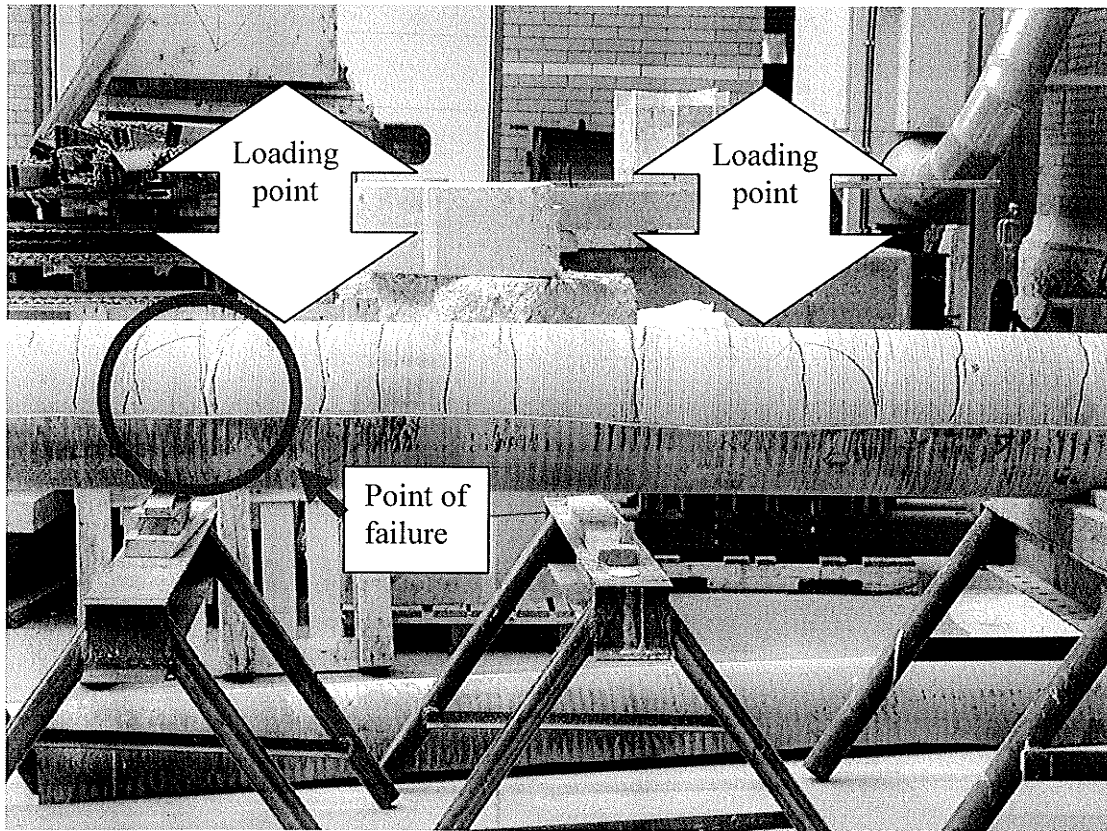


Figure 4-24 Cracks in specimen BFC1 after removing the GFRP tube

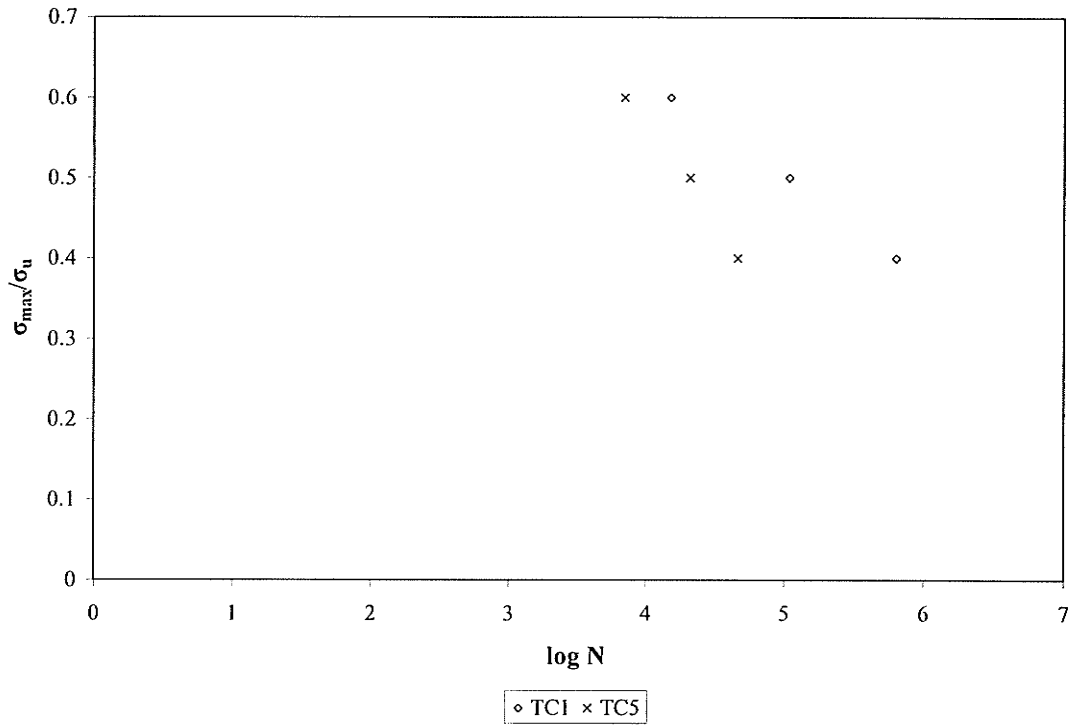


Figure 4-25 Effect of coupon type on fatigue life in terms of ( $\sigma_{max}/\sigma_{ult}$ ) ratio

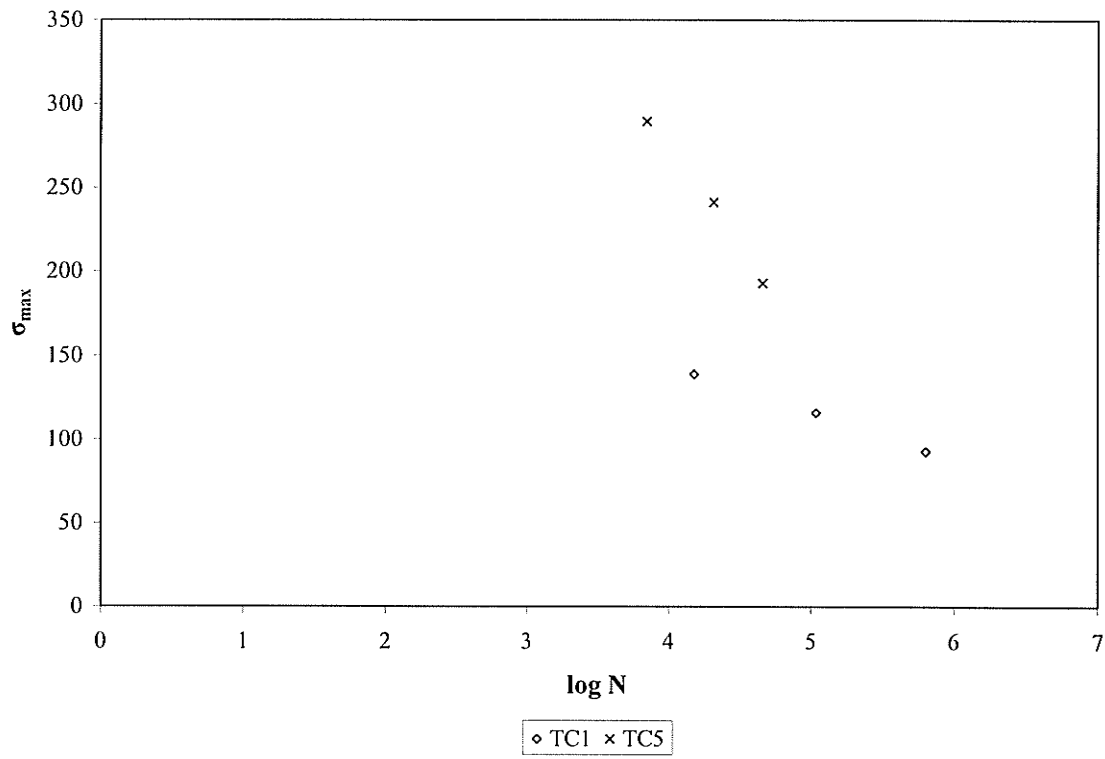


Figure 4-26 Effect of coupon type on fatigue life in terms of  $\sigma_{max}$

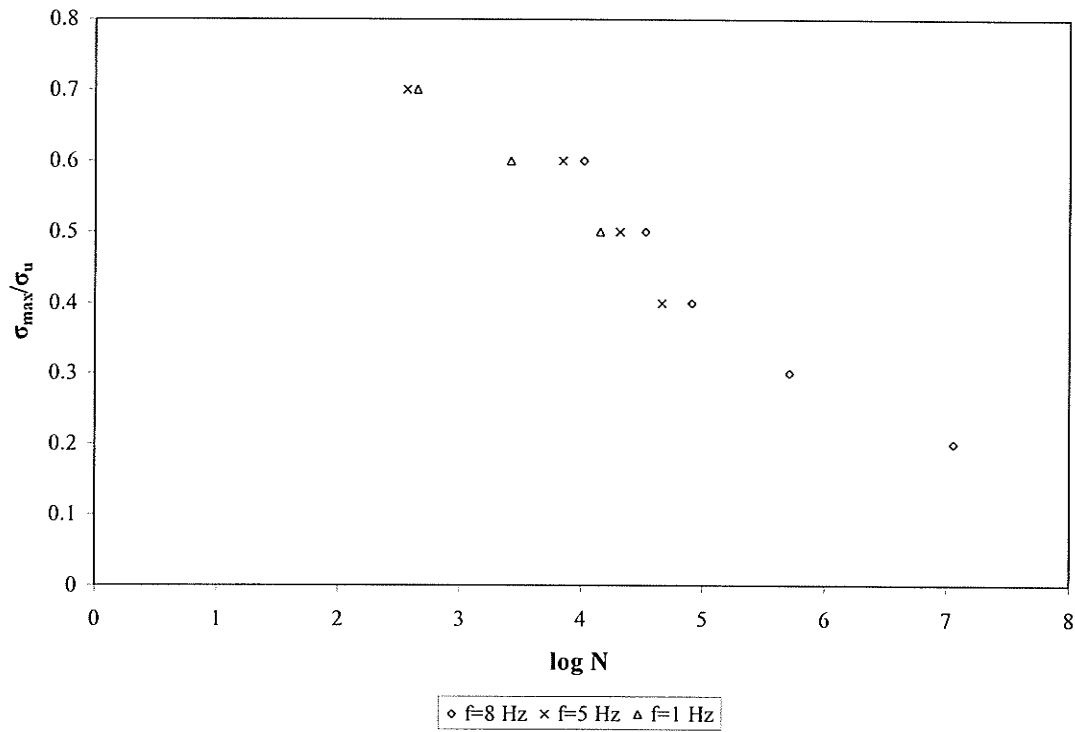


Figure 4-27 Effect of loading frequency on fatigue life of tension-tension coupons (R = 0.1)

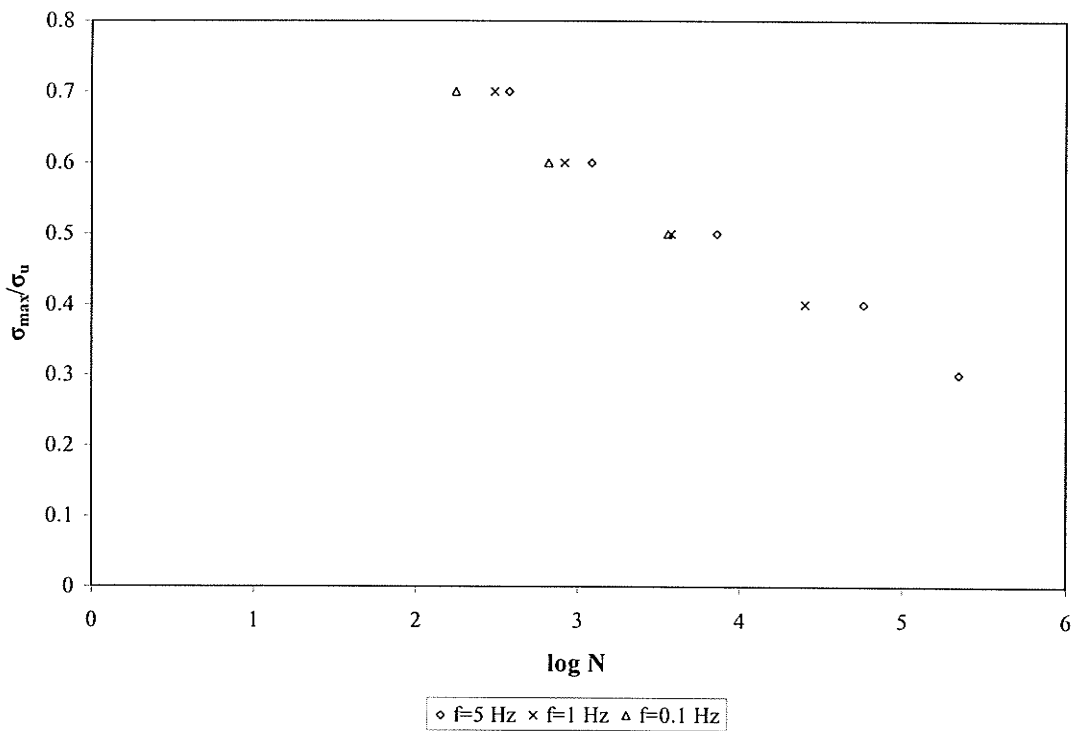


Figure 4-28 Effect of loading frequency on fatigue life of tension-compression coupons (R = -0.25)



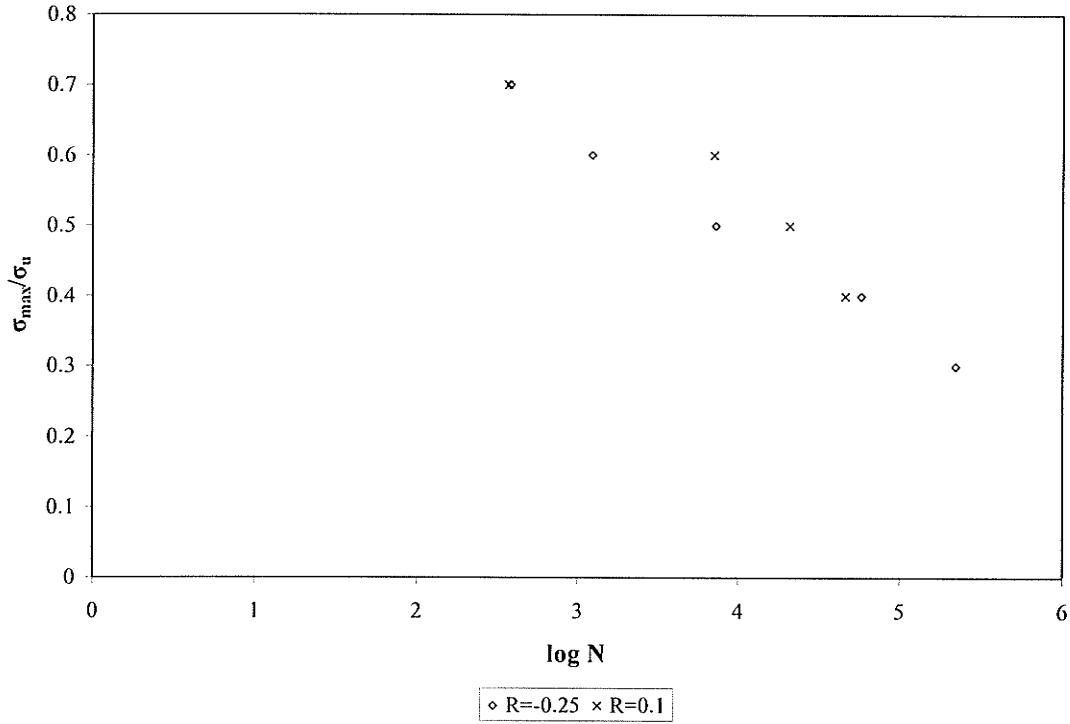


Figure 4-29 Effect of tension-tension and tension-compression loading on fatigue life of specimens with  $f = 5$  Hz

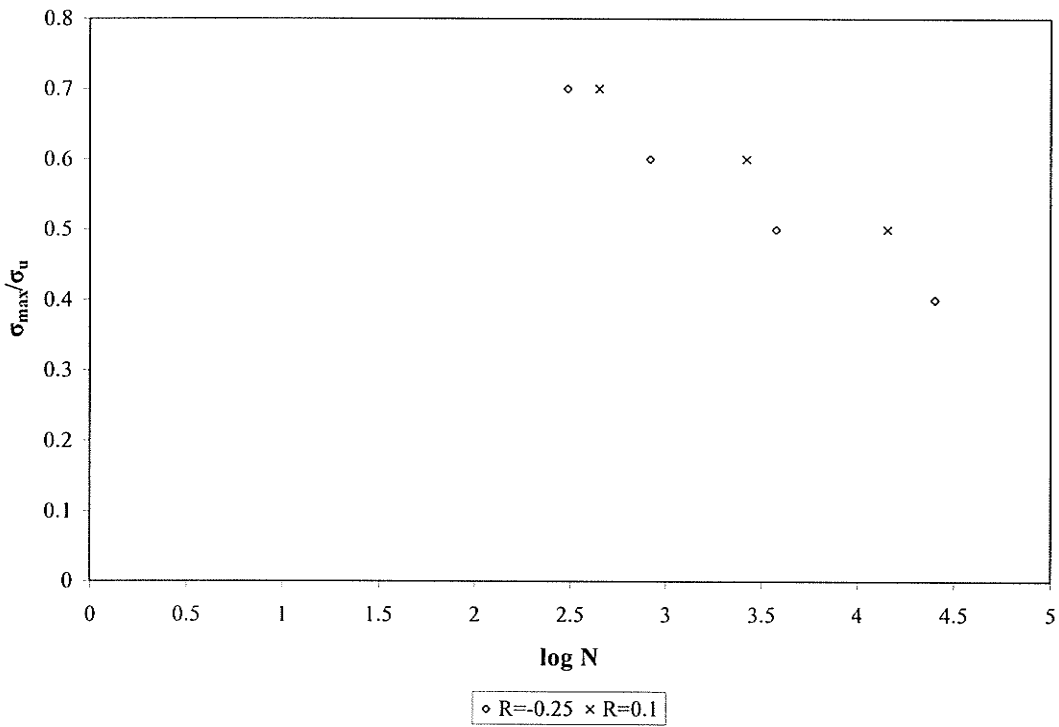


Figure 4-30 Effect of tension-tension and tension-compression loading on fatigue life of specimens with  $f = 1$  Hz

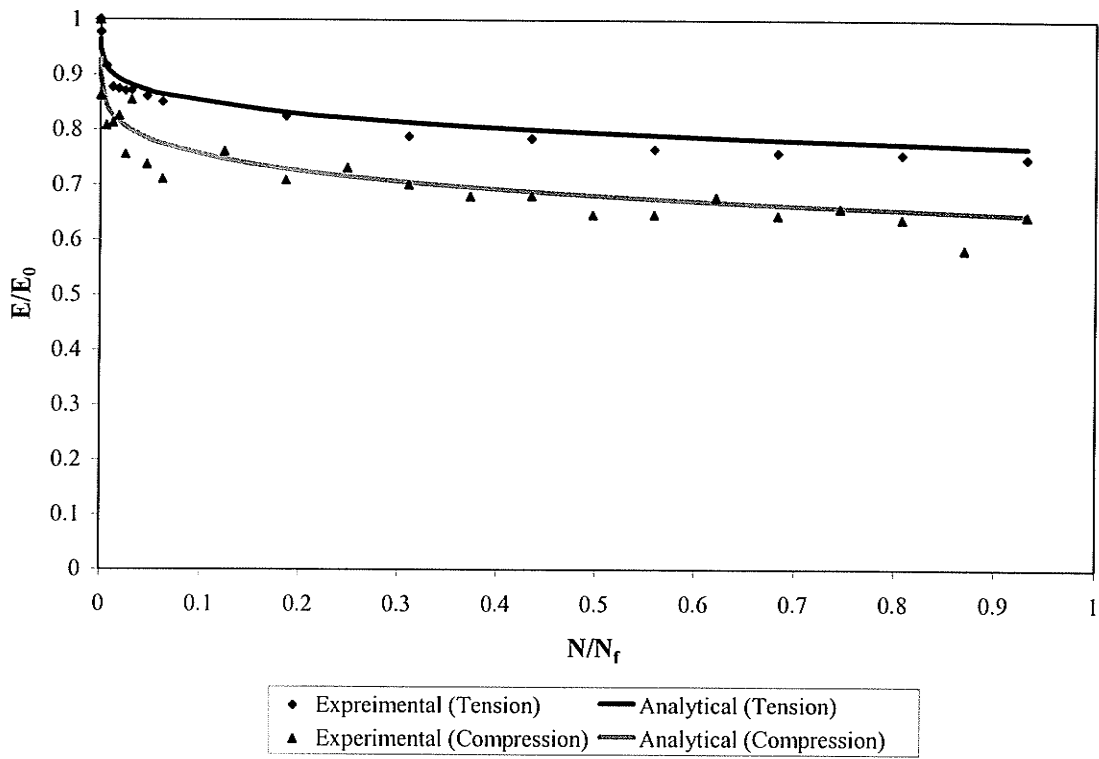


Figure 4-31 Stiffness degradation history ( $R = -0.25$ ,  $f = 1$  Hz and  $\sigma/\sigma_{max} = 0.4$ )

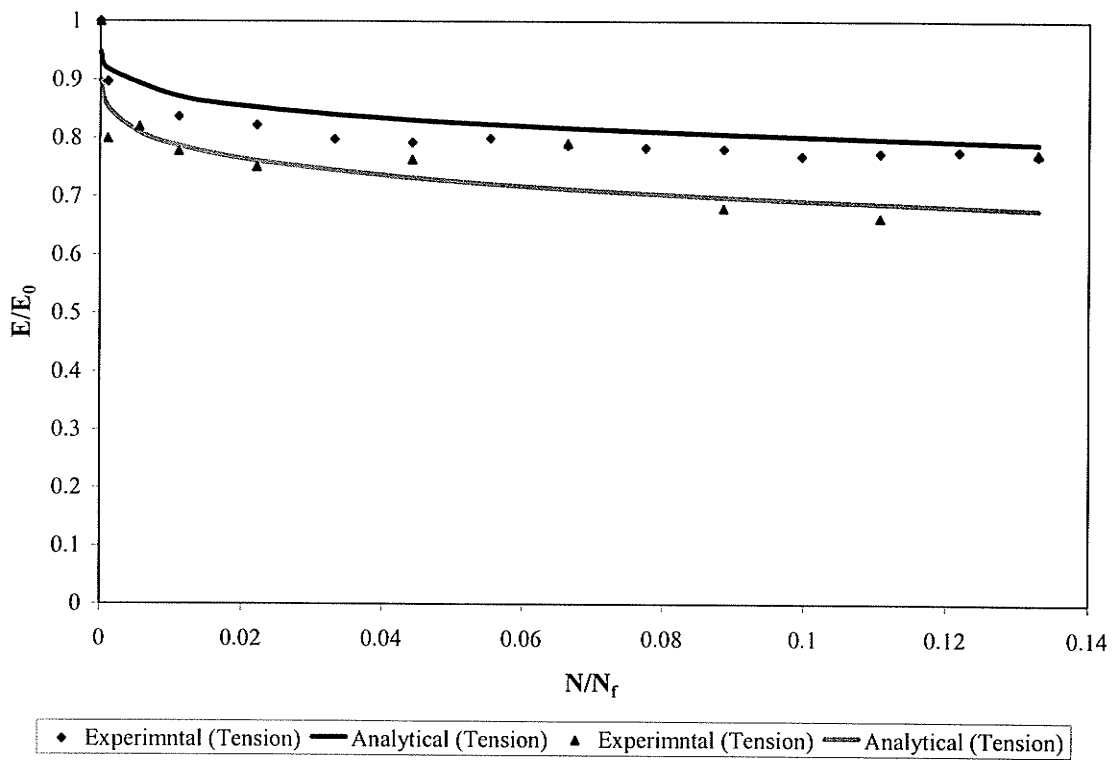


Figure 4-32 Stiffness degradation history ( $R = -0.25$ ,  $f = 5$  Hz and  $\sigma/\sigma_{max} = 0.5$ )

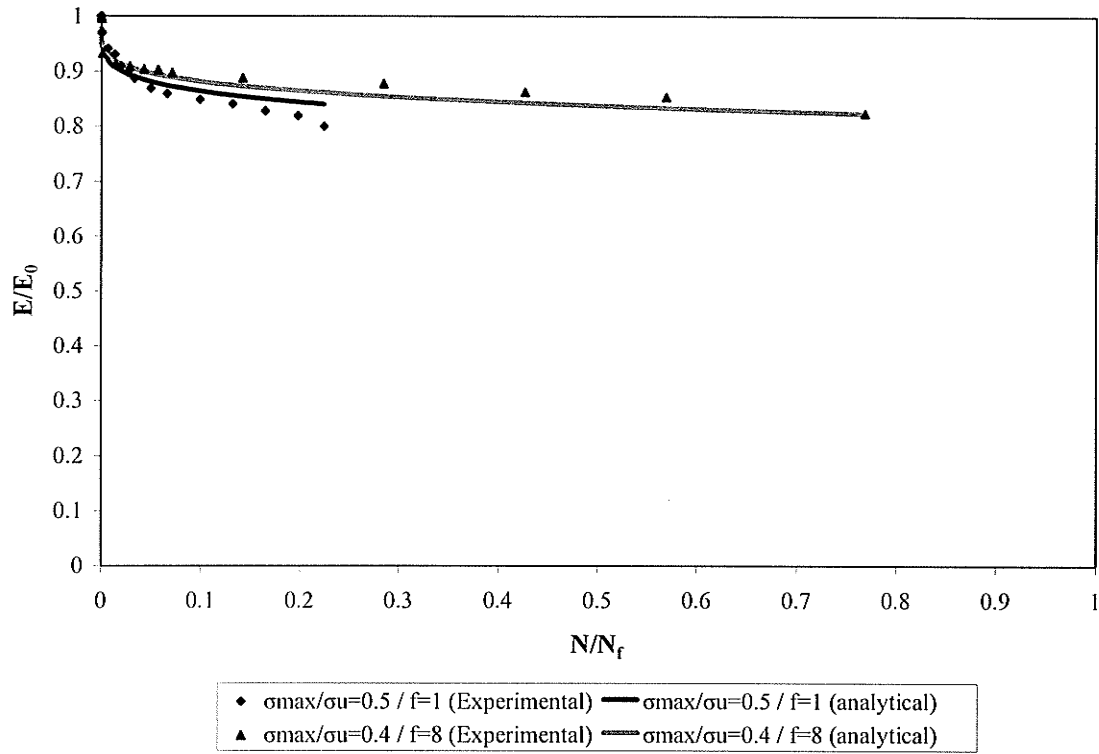


Figure 4-33 Stiffness degradation history (R = 0.1)

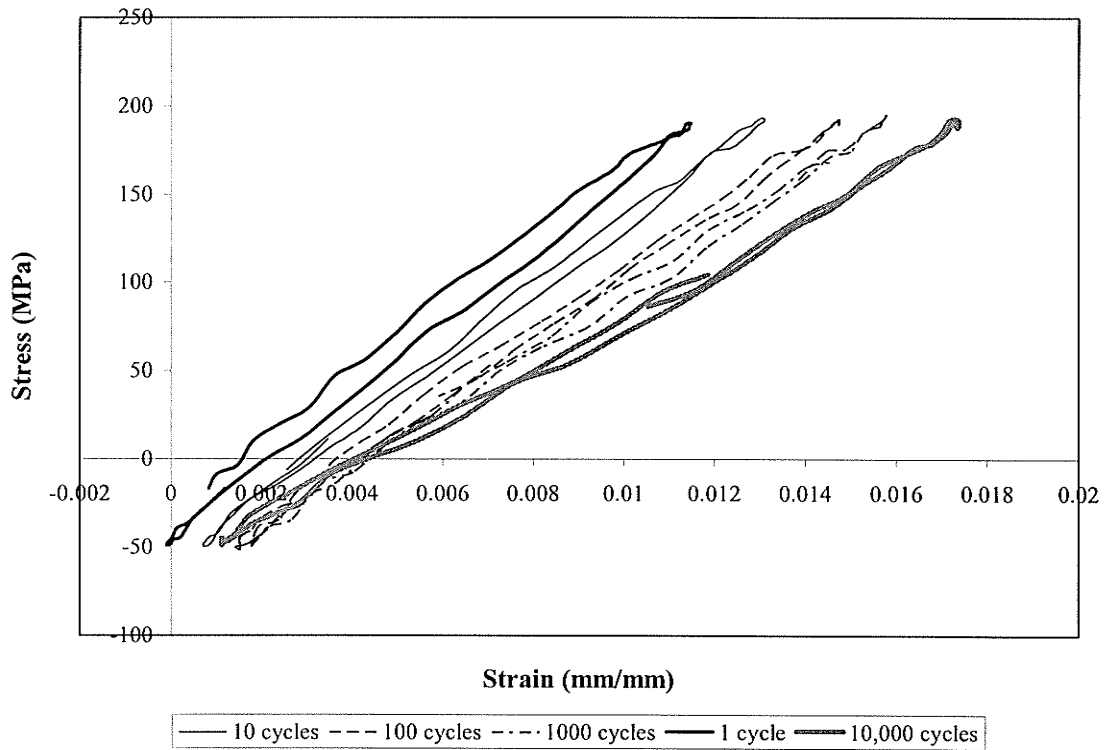


Figure 4-34 Stress-strain hysteresis (R = -0.25, f = 1 Hz and  $\sigma_{max}/\sigma_{It} = 0.4$ )

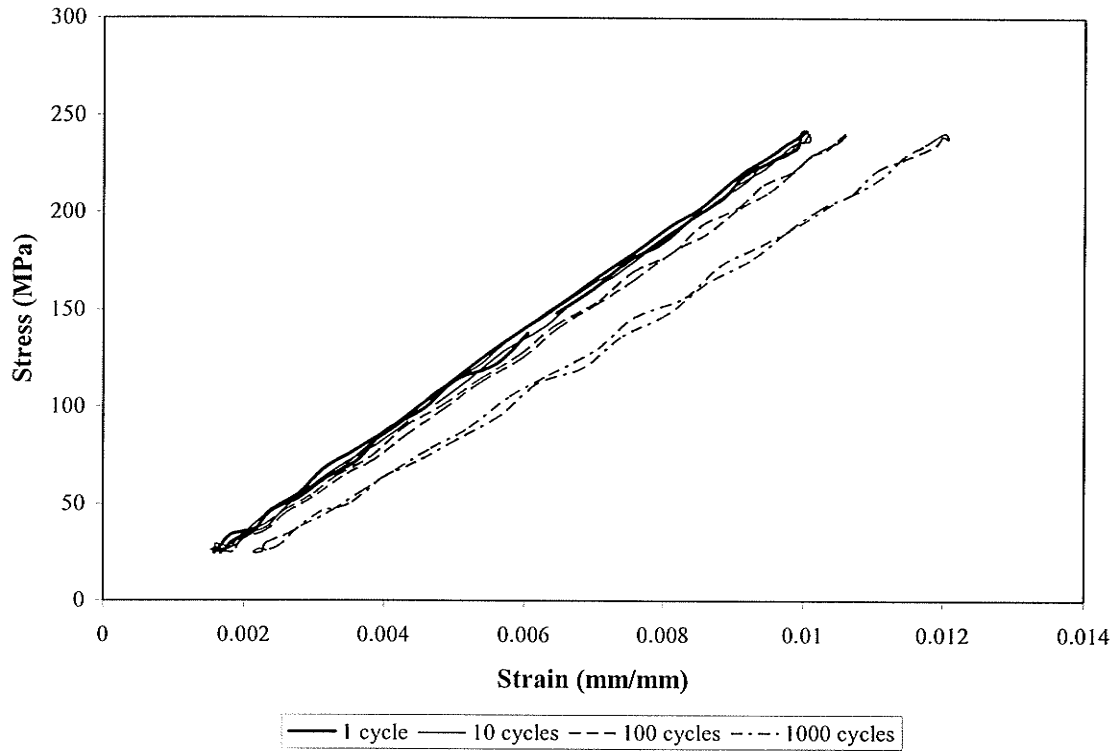


Figure 4-35 Stress-strain hysteresis ( $R=0.1$ ,  $f = 1$  Hz, and  $\sigma_{max}/\sigma_{ult} = 0.5$ )

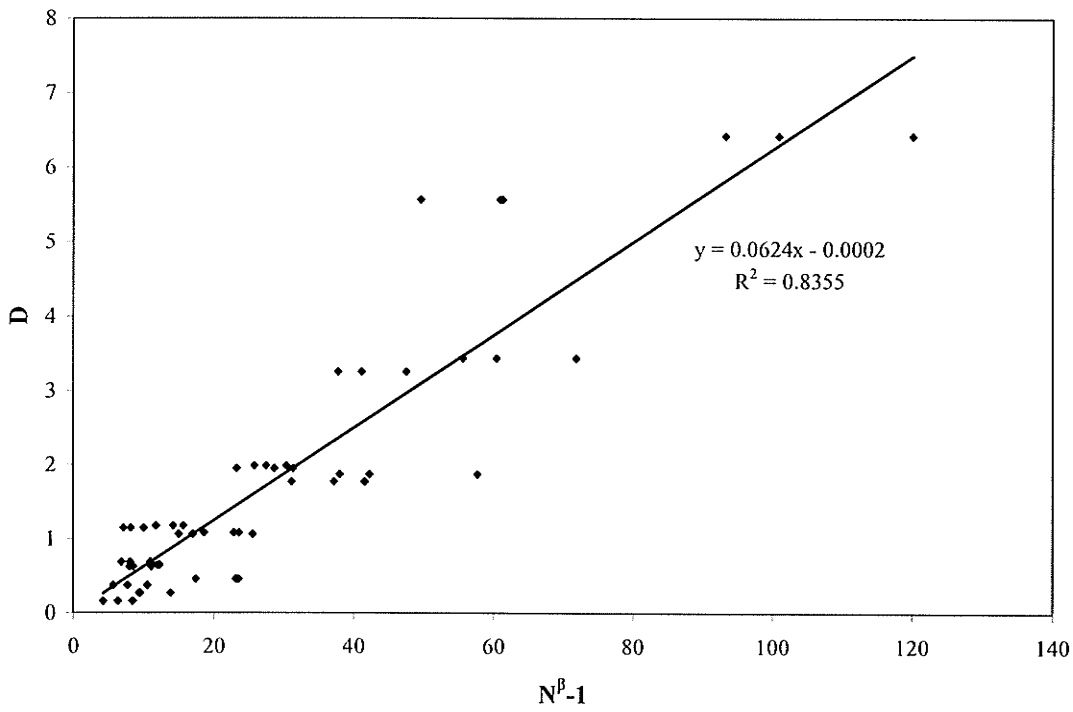


Figure 4-36 Estimating the  $\alpha$  and  $\beta$  parameters using results from all 25 mm TC5 specimens

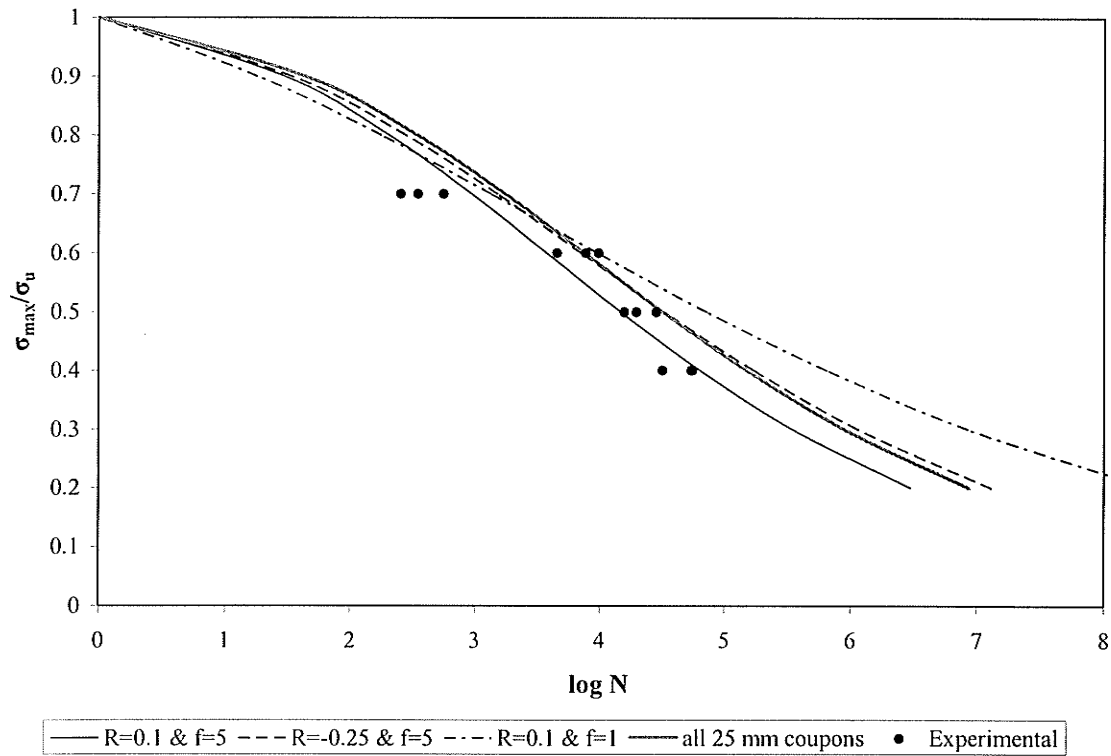


Figure 4-37 Formula predictions for coupons tested at  $R = 0.1$  and  $f = 5$  Hz

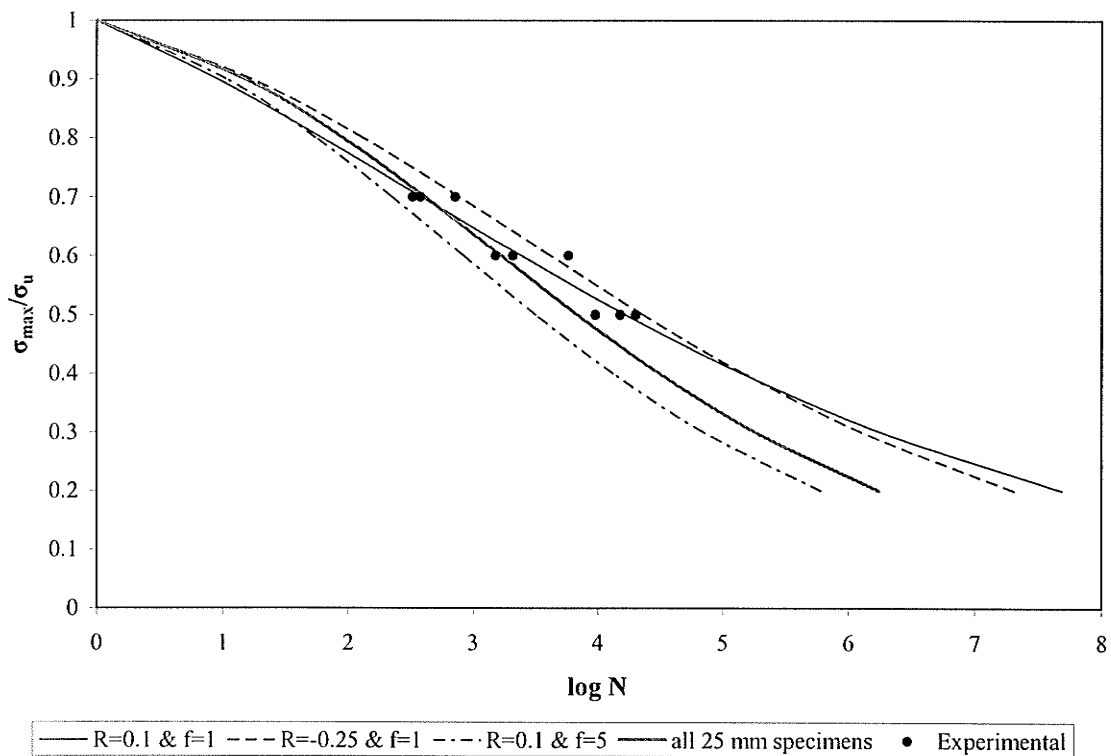


Figure 4-38 Formula predictions for coupons tested at  $R = 0.1$  and  $f = 1$  Hz

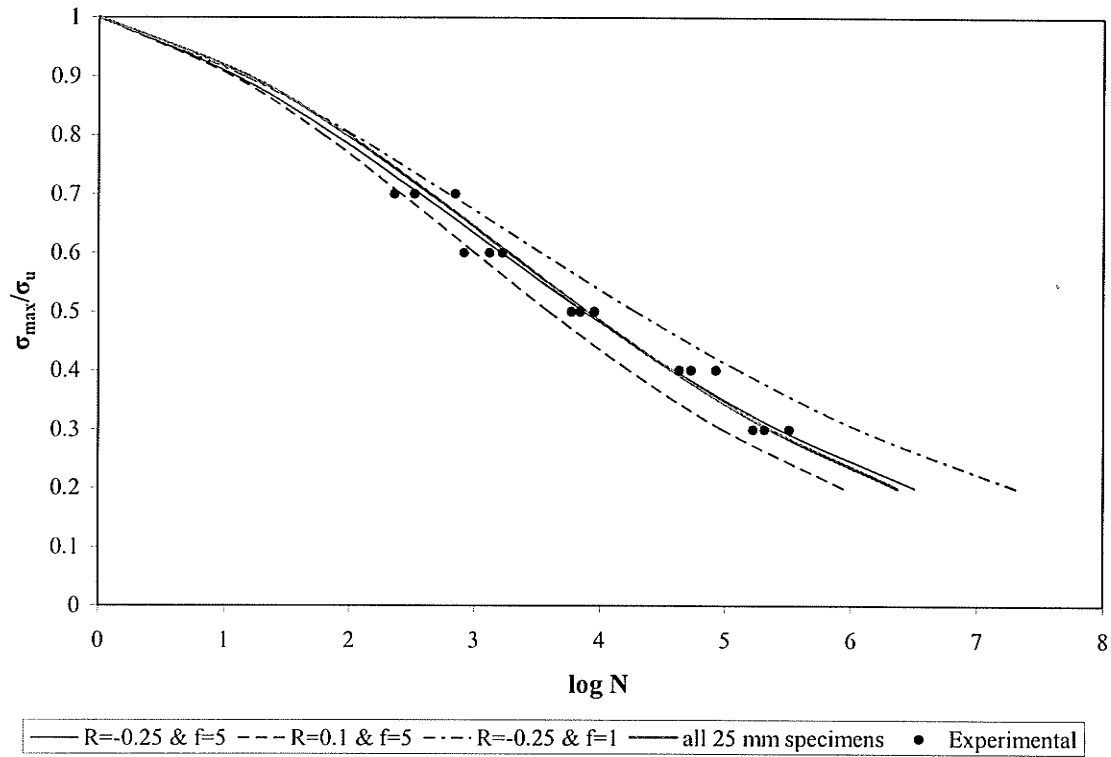


Figure 4-39 Formula predictions for coupons tested at  $R = -0.25$  and  $f = 5$  Hz

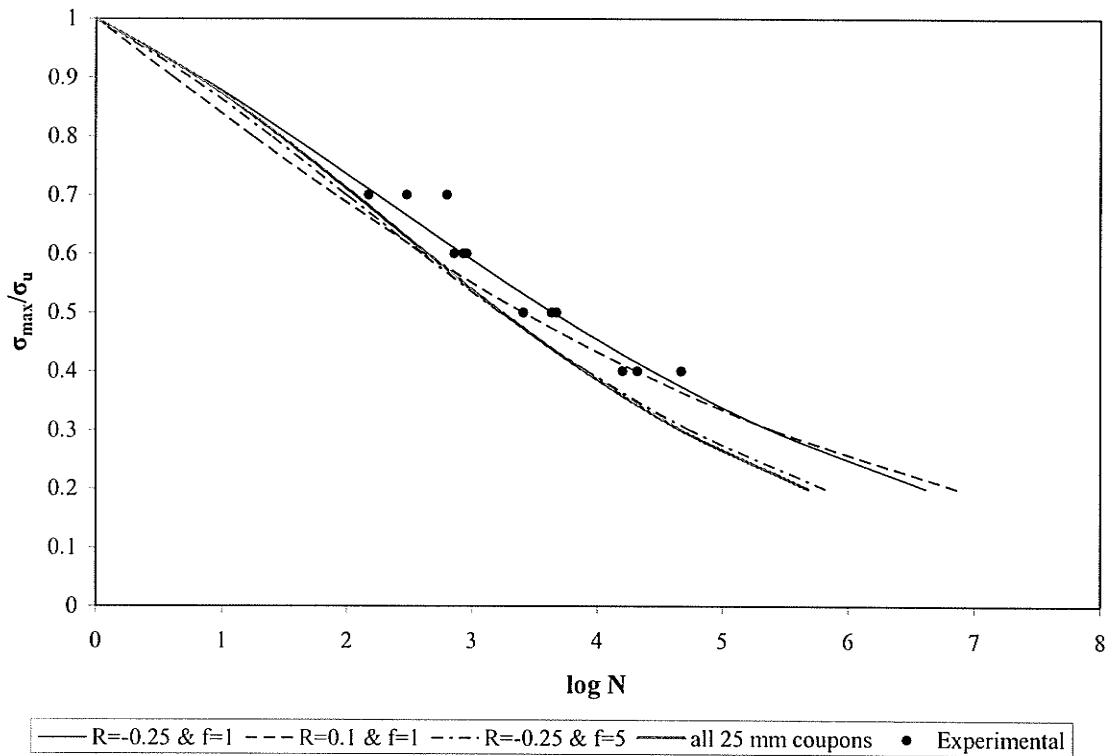


Figure 4-40 Formula predictions for coupons tested at  $R = -0.25$  and  $f = 1$  Hz

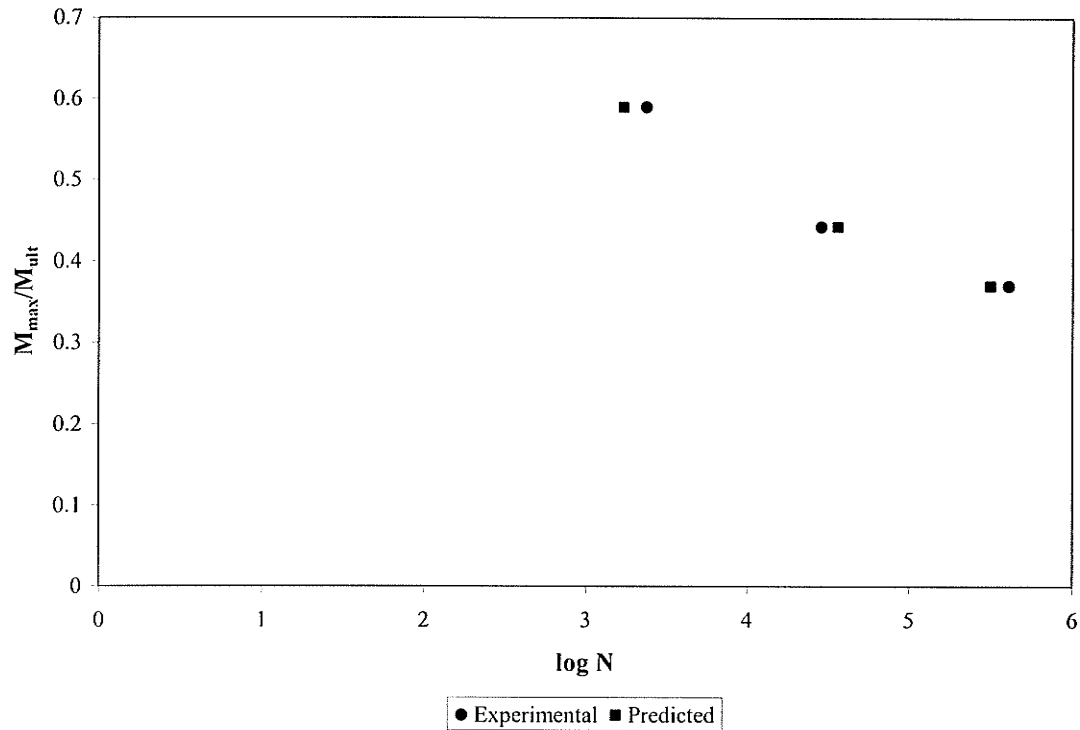


Figure 4-41 Comparison of predicted and experimental fatigue lives of full scale CFFT beam specimens

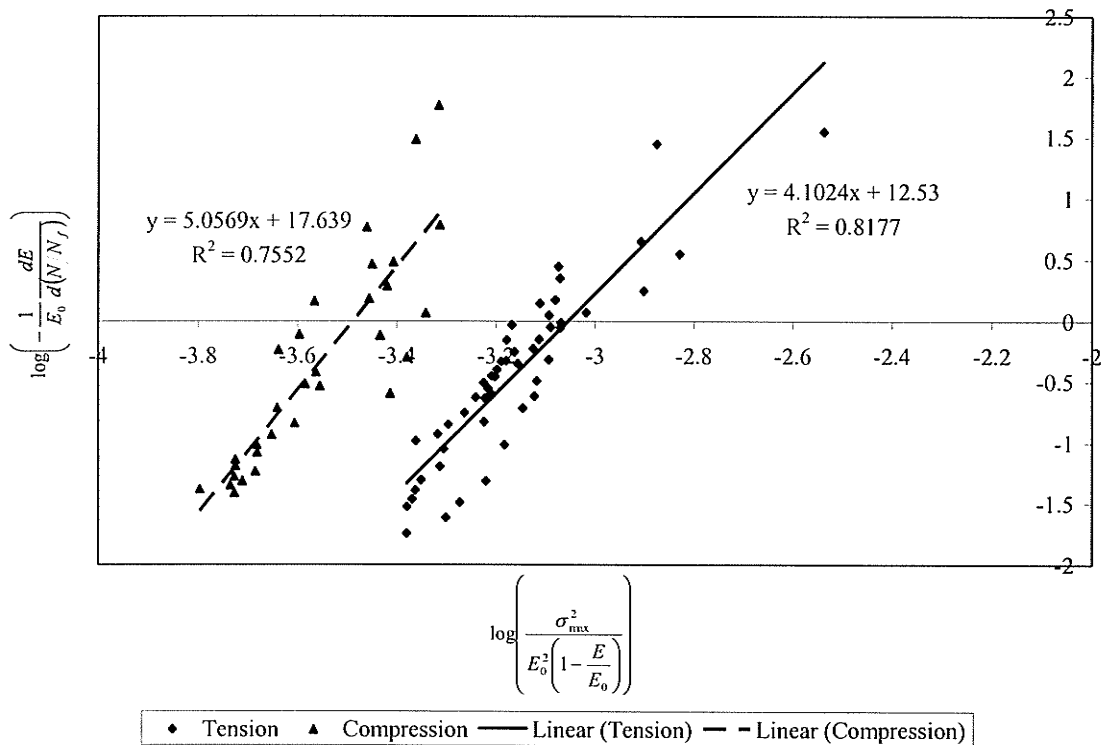


Figure 4-42 Estimating A and ng constants for stiffness degradation models

## Chapter 5

### **Analytical Modeling of CFFTs under Reversed Bending Fatigue**

#### **5.1 Introduction**

This chapter presents the details and results of an analytical study conducted to model the behavior of CFFT beams under reversed cyclic bending. The analytical model used is adapted from the sectional analysis method developed by Deskovic (1993) to model the creep and cyclic behavior of hybrid FRP/concrete members. This method uses the stiffness degradation model by Ogin (1985) and the creep model by Findely (1961) for FRP, while using the concrete creep and stiffness degradation model developed by Holmen (1982). A FORTRAN program was developed based on this method to model the behavior of CFFT beams under reversed cyclic bending loads. The results of this analytical model were compared to the experimental results of CFFTs tested under reversed cyclic bending and presented in chapter 4. A parametric study was also conducted to study the effect of different material deterioration properties, and maximum applied moment on the behavior of CFFT beams under reversed cyclic bending.

#### **5.2 Static Analysis**

In order to model the behavior of any member under cyclic loading, static analysis is first needed to model the static force equilibrium of this member. The time dependent properties of the material could then be incorporated into this model and the updated material properties would then be used to model the behavior in the time domain as well. A fiber section model that satisfies strain compatibility and equilibrium was used to model the static behavior of CFFT beams in this study. In this model, the CFFT beam is



divided into longitudinal segments. In each segment, the cross section is divided into a number of layers or fibers as shown in Figure 5.1. For a given strain profile, the respective uniaxial constitutive models of the materials are used to find the internal forces at each layer. The internal forces are then numerically integrated to satisfy equilibrium. The curvature at each section is calculated and the displacement is found by numerically integrating the curvatures.

The following assumptions were made in this model;

1. Plane sections remain plane after bending. (i.e. strains will vary linearly along the depth of the section)
2. Perfect bond exists between the concrete and the FRP tube. (i.e. FRP and concrete layers at the same distance from the neutral axis will have equal strains)

### **5.2.1 Constitutive models**

#### **5.2.1.1 Concrete in compression**

The model by Fam and Rizkalla (2001b) for FRP-confined concrete was used to model the concrete in compression. This model is based on equilibrium, radial displacement compatibility, and a variable confinement pressure, using a step by step strain increment technique. The model utilizes the equations proposed by Mander (1988) for concrete under a constant confining pressure.

Figure 5.2 shows the predicted stress-strain relation using the model by Fam and Rizkalla for the CFFT specimens used in this experimental study (i.e.  $D_t=367$  mm). The other two curves in the same graph are for CFFTs used in the parametric study. Since the output from this model is in the form of discrete stress and strain data points, rather than a closed form equation or a set of equations, incorporating this model in the static analysis model

of CFFT beams would be cumbersome. Therefore, a number of curves were fitted using these data points for use in the model, to facilitate computer programming.

### 5.2.1.2 Concrete in tension

Although CFFT members in bending usually exhibit tensile strains that are much larger than the cracking strains of concrete, the tension stiffening effect which is the contribution of concrete between cracks was considered in some cases, using the model suggested by Vecchio and Collins (Collins and Mitchell, 1997). The tensile stress in concrete  $\sigma_c$  is given as follows:

$$\sigma_c = E_{co}\varepsilon \quad \text{for } \varepsilon < \varepsilon_{crc} \quad (5.1)$$

$$\sigma_c = \frac{\alpha_1 \alpha_2 \sigma_{cr}}{1 + \sqrt{500\varepsilon}} \quad \text{for } \varepsilon > \varepsilon_{crc} \quad (5.2)$$

where;

$\varepsilon$  is the strain of concrete, and  $E_{co}$  is the tangent modulus of concrete, calculated by,

$$E_{co} = 5000\sqrt{f'_c} \quad (5.3)$$

where  $f'_c$  is the unconfined compressive strength of concrete.

$\sigma_{cr}$  is the cracking strength of concrete, calculated by,

$$\sigma_{cr} = 0.6\sqrt{f'_c} \quad (5.4)$$

$\varepsilon_{crc}$  is the cracking strain of concrete, calculated by,

$$\varepsilon_{crc} = \frac{\sigma_{cr}}{E_{co}} \quad (5.5)$$

$\alpha_1$  is a factor accounting for the bond characteristics of the reinforcement, a value of 0.3 was suggested for GFRP tubes (Fam, 2000).

$\alpha_2$  is a factor accounting for the nature of loading, a value of 1.0 is used for short term monotonic loading.

### 5.2.1.3 FRP tube

The FRP material is assumed to be linear elastic. Some nonlinearity exists in the stress-strain relation of FRP in tension and compression, as shown in chapter 3, due to the nonlinear behavior and cracking of the matrix (Fam, 2000). This nonlinearity, however, was ignored in the current study.

## 5.2.2 Modeling procedure

Figure 5.1 shows a cross section of a CFFT beam with strain and stress profiles across the section. The FORTRAN program developed for the static analysis of CFFT beams involves the following steps similar to the procedure adopted by Fam (2000):

1. Input geometric and material properties of the section, number of layers  $n$ , and number of sections along the shear span  $ns$ .
2. Calculate the area of each layer.
3. Input the moment at the midspan section at which the values of deflection and strain profile are required,  $M_t$ . Note that  $M_t$  is constant between the two applied loads.
4. At each cross section  $j$  within the shear span calculate the bending moment as

$$M_j = M_t \frac{j}{ns}$$

5. Assume a bottom strain  $\epsilon_b$ .
6. Assume a depth of the neutral axis  $C$ .
7. Calculate the strains at each layer from the linear strain profile.

8. Calculate the stress at each layer from the constitutive models.
9. Calculate the forces at each layer by multiplying the stress and the area.
10. Calculate the moment at each layer by multiplying the force by the distance from the neutral axis.
11. Check for force equilibrium. In case of pure moment, as in this study, the total force must be equal to zero. If force equilibrium is not satisfied change the neutral axis depth and repeat steps 7 to 11 until convergence is achieved.
12. Calculate the total moment of the section and compare to  $M_j$ , if the difference is more than the specified tolerance change the value of the bottom strain  $\varepsilon_b$  and repeat steps 6 to 12 until convergence is achieved.
13. Calculate the curvature of the section  $\psi = \varepsilon_b / (D_t - C)$ , where  $D_t$  is the outer diameter of the tube
14. Repeat steps 4 to 13 for each section.
15. Perform a numerical integration of the curvature profile along the span to calculate the deflection using the moment-area method.
16. Repeat steps 3 to 14 for different midspan moments to obtain the full moment-deflection curve.

### **5.2.3 Verification of the model**

The model described in the previous section was verified against the CFFT beams BC2, BP2U, and BP2L tested under monotonic bending. The details of these tests were presented in chapter 3. Two cases were considered in the analytical model, in the first case the tension stiffening effect of the concrete was considered while in the second case the contribution of the concrete in tension was ignored completely. Figures 5.3 and 5.4

compare the results of the analytical model to the experimental results for the load-deflection and load-strain curves, respectively. A good agreement exists between the analytical and the experimental results, particularly when accounting for tension stiffening in concrete until the load reaches about 70% of the failure load where the specimen undergoes some softening that the model does not predict. This may be attributed to the nonlinearity in the FRP material which becomes more pronounced prior to failure, and possibly due to the minor slippage between the concrete and the tube that occurs prior to failure. It should be noted, however, that the bending moment limits that were considered in the cyclic loading analysis to follow are generally within the region of good agreement.

### **5.3 Cyclic Loading Analysis**

The static model described in the previous section was extended to model CFFT beams under reversed cyclic bending, by introducing time dependent changes in the stress-strain relationships of the materials. The main goal of the analysis is to trace the moment-curvature response of a section at any given time or at the equivalent number of cycles, if the frequency of the applied load is kept constant throughout the loading history. In order to analyze a CFFT beam section under cyclic bending, constitutive models for creep and fatigue of the different materials need to be incorporated.

#### **5.3.1 Constitutive models**

##### **5.3.1.1 Fatigue and creep model for concrete under compression**

Holmen (1982) suggested that the total strain for concrete subjected to cyclic loading as the sum of two components, as follows:

$$\varepsilon_{tot} = \varepsilon_e + \varepsilon_{cr} \quad (5.6)$$

Where, the first component  $\varepsilon_e$  is related to the endurance of the concrete specimen, and the second part  $\varepsilon_{cr}$ , is a function of the loading time, and essentially is a creep strain.

It was observed from tests (Holmen, 1982) that three distinct strain development phases could be observed. A rapid increase phase until about 10% of the fatigue life, followed by a uniform increase phase until about 80% of the fatigue life, and finally another rapid increase phase until failure. Holmen (1982) suggested the following equation to predict the total strain in the first two phases.

$$\varepsilon_e = \varepsilon_o \left| 1 + \frac{3.18}{S_{max}} (1.183 - S_{max}) \left( \frac{N}{N_f} \right)^{0.5} \right| \quad \text{for } 0 < \frac{N}{N_f} \leq 0.1 \quad (5.7)$$

$$\varepsilon_e = \frac{1.11\varepsilon_o}{S_{max}} \left| 1 + 0.677 \frac{N}{N_f} \right| \quad \text{for } 0.1 < \frac{N}{N_f} \leq 0.8 \quad (5.8)$$

$$\varepsilon_{cr} = 0.413 \times 10^{-3} S_c^{1.184} \ln(t+1) \quad \text{for both phases} \quad (5.9)$$

where

$\varepsilon_o$  is the maximum total strain in the first load cycle,  $N$  is the number of load cycles,  $N_f$  is the total number of cycles to failure calculated by,

$$\log_{10} N_f = 1.978 (S_{max}^{-3.033}) (-\log_{10} L_p)^{0.596} \quad (5.10)$$

where  $L_p$  is  $1-p$  or the complimentary probability, and  $p$  is the probability of failure usually taken as 0.95.

$S_{max}$  is the ratio of the applied maximum stress level  $\sigma_{max}$  to the unconfined concrete strength  $f'_c$ .

$S_c$  is the characteristic stress level or sum of the mean stress level,  $S_m = (S_{max} + S_{min})/2$ , where  $S_{min}$  is the stress ratio for the minimum applied stress level,  $\sigma_{min}$  to the unconfined concrete strength  $f'_c$ , and the root mean square value (RMS) defined as;

$$RMS = \sqrt{\frac{1}{T_o} \int_0^{T_o} f^2(t) dt} \quad (5.11)$$

Where  $f^2(t)$  is the stress at any given time  $t$ , and  $T_o$  is the entire duration of the cyclic loading.

The RMS value of a sinusoidal loading with an amplitude of  $(S_{max} - S_{min})/2$  is given by

$$RMS = \frac{(S_{max} - S_{min})}{2\sqrt{2}} \quad (5.12)$$

$$\text{Hence: } S_c = \left( \frac{S_{max} + S_{min}}{2} \right) + \left( \frac{S_{max} - S_{min}}{2\sqrt{2}} \right) \quad (5.13)$$

This model has been widely accepted and incorporated in the model by Deskovic (1993) for hybrid concrete/FRP beams and by El-Tawil et al. (2001) to model reinforced concrete beams strengthened with FRP sheets. Although this model has been developed based on experimental results of unconfined concrete it was adapted by Ahmad (2004) to model CFFT beams subjected to unidirectional cyclic loading by replacing the unconfined concrete strength  $f'_c$  with the confined concrete strength  $f'_{cc}$  and produced good results. While no justification was presented by the author this might be attributed to the fact that for the majority of the sections and layers the maximum strain in the concrete is less than or close to  $\epsilon'_c$  (the strain at  $f'_c$ ), which is usually around 0.002. In this region, as explained in chapter 2 the effect of confinement is very small and the concrete

behavior is similar to that of unconfined concrete. It should be noted that the model discussed above is for concrete subjected to repeated loading in compression.

### **5.3.1.2 Application of concrete fatigue and creep models in reversed bending conditions**

When a CFFT member is subjected to a reversed bending moment, during the first half of each cycle the moment will be in a certain direction, causing tension on one side and compression on the other. In the second half of each cycle, the direction of the moment is reversed and so are the tension and compression sides, as shown in Figure 5.5. The variation of the depth of the neutral axis with the moment is predicted for specimen BC2 under unidirectional static bending, as shown in Figure 5.6. It is clear that the neutral axis depth is quite stable over the loading history, up to about 70% of the failure moment. Similar observation was also concluded by Fam (2000). Therefore, it could be assumed that the location of the neutral axis remains unchanged during each half cycle of loading. As such, layers located between the extreme top and bottom fibers of the section and a distance equal to the neutral axis depth from the top and bottom will be subjected to compression in one half of the cycle and tension in the other half of the cycle, as shown in Figure 5.5. On the other hand layers near the middle of the section will always be subjected to tension, but at smaller strains. The contribution of the concrete in tension is normally very small in CFFT beams. Additionally, the reversed cyclic bending results in full-depth cracks, as mentioned in chapter 4. It is therefore a reasonable assumption to neglect the contribution of the concrete in tension. The stress in the concrete layers during the cycling is assumed to follow the same function as the loading and could therefore be represented by a series of half sine waves with the minimum stress equals to



zero, as shown in Figure 5.7, where duration of the loading in compression will be half the time of each cycle. The following equations are used to represent the time dependant behavior of the concrete;

$$S_{\max} = \frac{\sigma_{\max}}{f'_{cc}} \quad (5.14)$$

$$S_{\min} = 0 \quad (5.15)$$

$$\text{and therefore } S_{cc} = \frac{S_{\max}}{2} + \frac{S_{\max}}{2\sqrt{2}} = 0.854S_{\max} \quad (5.16)$$

where  $S_{cc}$  is the characteristic stress level for concrete,

$$\text{and, the duration of the load } T_o = \frac{N}{2f} \quad (5.17)$$

where  $N$  is the total number of cycles, and  $f$  is the frequency of the applied load.

### 5.3.1.3 GFRP creep model

The magnitude of the creep of a material depends on the bond energy. Since the atomic bonds define the elastic modulus it is apparent that materials with higher elastic modulus will show smaller creep strains. The elastic modulus of glass fibers is approximately 20 times higher than that of the matrix. It is therefore justified for engineering applications to neglect the creep of the fibers. The response of matrix polymers is that of a viscoelastic material, representing a combination of viscous and elastic components. The viscous component in polymers is caused by chains moving past one another in the crystalline zones and depends on time (Deskovic, 1993).

Findley (1960) proposed the following empirical power law to describe total strain at time  $t$  for polymers and FRP laminates subjected to sustained loads;

$$\varepsilon_{cr} = \varepsilon_o (1 + mt^{nc}) \quad (5.18)$$

Where  $\varepsilon_o$  represents instantaneous strain at time  $t = 0$ ,  $m$  and  $nc$  are material dependant parameters obtained from experimental data, and  $t$  is the duration of sustained load, usually in hours. The net creep strain  $\varepsilon_{cm}$  could be calculated as;

$$\varepsilon_{cm} = \varepsilon_o m t^{nc} \quad (5.19)$$

A creep test was conducted by the author on 25 mm wide strip cut from the tubes used in this study to calibrate the parameters of Findley' model. The setup was similar to that of the tension tests shown in Figure 4.4 with the load kept constant at 15 kN for 50 hours. This corresponds to a stress ratio of about 0.26 of the ultimate. Figure 5.8 shows the results of the test. Using the least square method to fit the experimental results, yielded a value of 0.0434 for  $m$  and a value of 0.143 for  $nc$ , as shown in Figure 5.8.

#### 5.3.1.4 GFRP stiffness degradation model

The model by Ogin et al. (1985), which was discussed in chapter 4, was used to model the stiffness degradation of the GFRP tube. The model was adapted by substituting the absolute number of cycles with the ratio of the number of cycles  $N$  to the total number of cycles to failure  $N_f$ , which is calculated using the empirical formula suggested by Epaarachchi and Clausen (2003), as discussed in chapter 4. This was done because in this problem some layers of the materials will be subjected to tension-tension fatigue while others will be subjected to tension-compression fatigue. It has been shown that specimens subjected to tension-compression fatigue suffer more damage per cycle than specimens subjected to tension-tension fatigue (Gamstedt and Sjoegren, 1999). Using the data from the fatigue tests conducted on specimens cut from the tube, the following equations, which were also presented in chapter 4, were used to model the stiffness reduction in tension and compression respectively;

$$\phi(\sigma_{\max}, N) = \frac{E_{fN}}{E_{f0}} = 1 - 393 \left[ \frac{\sigma_{\max}}{E_{f0}} \right]^{1.608} \left[ \frac{N}{N_f} \right]^{0.196} \quad (\text{Tension}) \quad (5.20)$$

$$\phi(\sigma_{\max}, N) = \frac{E_{fcN}}{E_{fc0}} = 1 - 1100 \left[ \frac{\sigma_{\max}}{E_{fc0}} \right]^{1.67} \left[ \frac{N}{N_f} \right]^{0.167} \quad (\text{Compression}) \quad (5.21)$$

where;

$E_{f0}$  is the initial modulus of elasticity for FRP in tension,  $E_{fc0}$  is the initial modulus of elasticity for FRP in compression,  $E_{fN}$  is the modulus of elasticity for FRP in tension after  $N$  cycles,  $E_{fcN}$  is the modulus of elasticity for FRP in compression after  $N$  cycles,  $\sigma_{\max}$  is the maximum stress, and  $N_f$  is the number of cycles to failure.

#### 5.3.1.5 Application of the GFRP stiffness degradation and creep models in a reversed bending condition

For an FRP specimen subjected to a sustained loading the strain will increase with time due to creep as shown in Figure 5.9 (Mallick, 1988). After removing the load, the elastic deformation is recovered immediately, while leaving a permanent deformation that will be slowly recovered if the specimen is not reloaded. An FRP specimen subjected to a constant repeated loading will therefore undergo an increase in strain. This increase can be divided into two components, the first component is due to the reduction in the elastic modulus and the second component is due to creep as shown in Figure 5.10. The total strain could then be calculated as follows;

$$\varepsilon_{tot} = \frac{1}{\phi(\sigma_{\max}, N)} \varepsilon_o + \varepsilon_{cm} \quad (\text{Adapted from Deskovic, 1993}) \quad (5.22)$$

Where  $\varepsilon_o$  is the initial undamaged strain.

Equation 5.19 is used to calculate the net creep for specimens subjected to a constant applied stress. In this case the applied stress is variable, and therefore it was decided to use the characteristic stress for the FRP  $S_{cf}$ , in a similar manner to the equations suggested by Holmen (1982), to calculate the creep in the FRP tube. Equation 5.22 therefore becomes;

$$\varepsilon_{tot} = \varepsilon_o \left( \frac{1}{\phi(\sigma_{max}, N)} + S_{cf} mt^{nc} \right) \quad (5.23)$$

Fibers of the FRP tube located at equal distances from mid height of the sections in a CFFT beam subjected to reversed cyclic bending will alternate their maximum and minimum values of strains in each cycle as shown in Figure 5.5. These elements will effectively have the same maximum and minimum strains, and since a linear relation is assumed for FRP, they will have the same maximum and minimum stresses. Consequently, they will suffer the same degradation in the elastic modulus and will have the same permanent creep deformation resulting from the cyclic loads. All elements at equal distance from the midheight of the sections must be considered simultaneously when solving for the time dependent deformations of FRP elements in a CFFT beam subjected to reversed cyclic bending as follows;

$$\varepsilon_o^{\max} = \frac{\varepsilon_{tot}^{\max}}{\left( \frac{1}{\phi(\sigma_{max}, N)} \right) + S_{cf} mt^{nc}} \quad (5.24)$$

$$\varepsilon_{crn} = S_{cf} \varepsilon_o^{\max} (mt^{nc}) \quad (5.25)$$

$$\varepsilon_o^{\min} = \frac{\varepsilon_{tot}^{\min} - \varepsilon_{crn}}{\left( \frac{1}{\phi(\sigma_{max}, N)} \right)} \quad (5.26)$$

where

$$S_{cf} = \frac{1+R}{2} + \frac{1-R}{2\sqrt{2}} \quad (5.27)$$

$$R = \frac{\sigma_{\max}}{\sigma_{\min}} \quad (5.28)$$

### 5.3.1.6 Estimation of fatigue life

The experimental results of the full-scale CFFT tests presented in chapter 4 showed that the specimens fail in tension at the extreme fibers. Therefore, the fatigue life could be estimated by calculating the damage at the extreme top and bottom fibers. As explained earlier, at the beginning of cycling, the top and bottom fibers will alternate the maximum and minimum stresses and strains, producing certain  $\sigma_{\max}/\sigma_{ult}$ , and  $R$  values that will produce a certain fatigue life  $N_f$ . As the cyclic loading progresses, there will be a redistribution of the stresses along the section and the values of the stresses and strains at the extreme fibers will change and so will the  $\sigma_{\max}/\sigma_{ult}$ , and  $R$  values, and as a result value of the fatigue life  $N_f$  will change. If a linear accumulative damage model is assumed, and since the analysis is conducted at discrete time steps, the damage  $DMG$  at a certain calculation step  $k$  could be calculated as the ratio of the number of cycles at this step and the average number of cycles to failure  $N_f$  at the beginning and the end of this step as follows;

$$DMG_k = \frac{N_k - N_{k-1}}{\left( \frac{N_{f(k)} + N_{f(k-1)}}{2} \right)} \quad (5.29)$$

and for the first calculation step the damage is calculated by,

$$DMG_1 = \frac{1}{N_{f(1)}} \quad (5.30)$$

where  $DMG_k$  is the damage at time step  $k$ ,

$N_k$  is the number of cycles at time step  $k$ ,

$N_{f(k)}$  is the number of cycles to failure calculated at step  $k$ .

The total damage  $DMG_{tot}$  at a time step  $k$  could be calculated as;

$$DMG_{tot} = \sum_{k=1}^k DMG_k \quad (5.31)$$

Failure will occur when  $DMG_{tot}$  is equal to unity.

### 5.3.2 Modeling procedure

A FORTRAN program was developed for the reversed cyclic bending analysis of CFFT beams with the following steps:

1. Input of geometric and material properties of the section, number of layers  $n$ , number of sections along the span  $ns$ , stiffness degradation and creep properties (i.e.  $m$ ,  $nc$ ,  $A$ ,  $ng$ ,  $\alpha$ ,  $\beta$ ), and frequency of applied load  $f$ .
2. Calculate the area of each layer.
3. Input the moment at the midspan section  $M_t$ , at which the values of deflection and strain profile are required.
4. Start with number of cycles  $N=1$ .
5. Calculate time  $t$ 
  - $t=N/f$  for FRP layers
  - $t=N/2f$  for concrete layers.
6. At each section  $j$  calculate the bending moment as  $M_j = M_t \frac{j}{ns}$

7. Assume a bottom strain  $\varepsilon_b$ .
8. Assume a depth of the neutral axis  $C$ .
9. Calculate the total strains  $\varepsilon_{tot}$  in each layer from the linear strain profile.
10. Calculate an initial value for the stress  $\sigma_i$  at each layer from the undamaged static constitutive models.
11. Calculate the initial strain  $\varepsilon_o$  for each layer as follows;

For concrete:

- i. Calculate  $S_{\max} = \frac{\sigma_i}{f'_{cc}}$ .
- ii. Calculate  $N_f$  from equation 5.10.
- iii. Calculate  $S_{cc}$  from equation 5.15.
- iv. Calculate  $\varepsilon_{cr}^i$  from equation 5.9.
- v. Calculate  $CC^i$  as follows;

$$CC^i = \left| 1 + \frac{3.18}{S_{\max}^i} (1.183 - S_{\max}^i) \left( \frac{N}{N_f} \right)^{0.5} \right| \text{ for } 0 < \frac{N}{N_f} \leq 0.1$$

$$CC^i = \frac{1.11}{S_{\max}^i} \left| 1 + 0.677 \frac{N}{N_f} \right| \text{ for } 0.1 < \frac{N}{N_f} \leq 0.8$$

- vi. Calculate  $\varepsilon_o^i = \frac{(\varepsilon_{tot}^i - \varepsilon_{cr}^i)}{CC^i}$

For FRP

- i.  $\sigma_{\max} = \sigma_i$  and  $\sigma_{\min} = \sigma_{(n-i+1)}$
- ii. Calculate  $R = \frac{\sigma_{\max}}{\sigma_{\min}}$
- iii. Calculate  $N_f$  using equations 4.1 to 4.3.

- iv. Calculate  $S_{cf}$  using equation 5.27.
  - v. Calculate  $\phi(\sigma_{\max}, N)$  using equations 5.20 and 5.21.
  - vi. Calculate  $\varepsilon_o^{\max}$  using equation 5.24.
  - vii. Calculate  $\varepsilon_{cr}^i$  using equation 5.25.
  - viii. Calculate  $\varepsilon_o^{\min}$  using equation 5.26.
12. Calculate the stresses  $\sigma'_i$  at each layer from the undamaged static constitutive models based on the calculated initial strain  $\varepsilon_o$ .  $\sigma'_i$  is compared to  $\sigma_i$ , and if the difference is less than a specified tolerance,  $\sigma_i$  is changed to  $(\sigma_i + \sigma'_i)/2$  and steps 11 and 12 are repeated until convergence is achieved. If  $i = 1$  and  $j = ns$ , then  $N_{f(k)}$  is  $N_f$  which was calculated in step 11 – iii.
  13. Calculate the forces at each layer by multiplying the stress and the area.
  14. Calculate the moment at each layer by multiplying the force by the distance from the neutral axis.
  15. Check for force equilibrium. In this case the total force must be equal to zero under pure bending. If force equilibrium is not satisfied change the neutral axis depth and repeat steps 8 to 15 until convergence is achieved.
  16. Calculate the total moment at the section and compare to  $M_j$ , if the difference is less than the specified tolerance change the value of the bottom strain  $\varepsilon_b$  and repeat steps 7 to 16 until convergence is achieved.
  17. Calculate the curvature of the section  $\psi = \varepsilon_b / (D_t - C)$
  18. Repeat steps 6 to 17 for each section.



19. Integrate the moment curvature profile numerically along the span to calculate the deflection using the moment area method.
20. Calculate the total damage using equations 5.29 to 5.31
21. If  $DMG_{tot}$  is less than one increase the number of cycles in step 4 and repeat steps 5 to 20, otherwise terminate the program.

The fixed point iteration method was used for stress convergence. However, iteration step was taken as  $(\sigma_i + \sigma'_i)/2$ . For force and moment equilibrium the secant method of iteration was used. The first two estimates were selected using the ranges obtained from static analysis as guidance.

### 5.3.3 Verification of the model

The model was compared to the test results specimens BFC1, BFC3 and BFP1U that were tested under reversed cyclic bending as presented in chapter 4. Figures 5.11 to 5.16 show a comparison between the experimental and the analytical results with regard to deflection and strains versus the number of cycles. The analysis for specimen BFC1 was carried out for the first 670,000 cycles of loading only due to the change of the loading frequency that occurred afterwards. The analytical results show good agreement with the experimental results. The experimental results from specimen BFC1 show stiffer response than the analytical solution. This may be attributed to the fact that the maximum moment at the midspan section for this specimen was 50 kN.m and the cracking moment is about 18 kN.m. As such, a significant length of the member was uncracked and had higher stiffness than calculated by the model which ignores the contribution of concrete in tension. Additionally, since the maximum moment is low, the effect of the tension stiffening relative to the over all behavior will be higher than for the other specimens,

which had much higher midsection moment. Table 5.1 and figure 5.17 show the results of the fatigue life estimation of the full-scale CFFT specimens, compared to the experimental results. The error bars represented in the experimental results were established assuming that the full-scale CFFT specimens will have the same scatter as the fatigue coupon specimens. It is apparent from the figure that the model overestimates the fatigue life at high  $M_{\max}/M_{\text{ult}}$  values; however the predictions become more accurate as the value of  $M_{\max}/M_{\text{ult}}$  approaches 0.40.

#### **5.4 Parametric Study**

A parametric study was conducted using the computer program developed, based on the procedures described earlier. Three different tube diameters were considered, namely, 256 mm, 367 mm, and 456 mm. The same thickness and properties for all the tubes were assumed to be the same as the tubes used in the experimental study and discussed in chapter 4, to achieve different FRP reinforcement ratios. Since the tube diameter would affect the confinement effectiveness of the concrete, a stress-strain relation was constructed for each tube diameter using the model developed by Fam and Rizkalla (2001b) as shown in Figure 5.2. A group of curves were then fitted to this data for programming purposes. A static analysis was conducted for all tubes. For each tube diameter, two different maximum loading levels were considered in reversed bending, namely 25% and 50% of the ultimate bending moment calculated from the static analysis. These load levels were chosen as they represent the loading levels for factors of safety of 2 and 4. For each load level two loading frequencies were considered, namely 1 Hz and 5 Hz. For each combination of tube diameter, maximum loading level and frequency, three loading cases were considered. The first case considers the effect of the time dependant

properties of both the tube and concrete. The second case only considers the time dependant properties of the tube, and ignores those of concrete. The third case only considers the time dependant properties of the concrete, and ignores those of FRP. A summary of the parametric study is presented in Table 5.2. The objective of this analysis is to study the effects of the various parameters stated earlier on the deflection, top and bottom strains and, neutral axis depth throughout the loading history.

#### **5.4.1 Results of the parametric studies**

In total 36 analyses were conducted to study the effect of the different parameters on the behavior of CFRT members subjected to reversed cyclic bending. The fatigue life prediction results are presented in Table 5.3. To avoid repetition, only representative curves of these results are presented in this chapter. The entire results of all these analyses are presented in Appendix A.

##### **5.4.1.1 Effect of time dependant properties of materials**

Figures 5.18, 5.19 and 5.20 present sample curves of the deflection, strain, and depth of the neutral axis versus  $N/N_f$ , respectively, for the three different cases of time dependant properties for a maximum moment of 50% of the ultimate. Figures 5.21, 5.22 and 5.23 on the other hand present sample curves of the deflection, strain, and depth of the neutral axis verses  $N/N_f$ , respectively, for the three different cases of time dependant properties for a maximum moment of 25% of the ultimate. It is apparent from these figures that both the concrete and FRP time dependant properties have some effect on the deflection behavior of CFRT members subjected to reversed cyclic bending. The FRP time dependant properties have more effect which increases as the maximum moment

increases. It is also apparent that the time dependant properties of the FRP tube have a more significant effect on the increase in the bottom strain which increases as the maximum moment increases. On the other hand, the time dependant properties of the concrete have a more significant effect on the increase in the top strain, which increases also as the maximum moment decreases. The depth of the neutral axis tends to increase when only considering the time dependant properties of the concrete, and tends to decrease when only considering the time dependant properties of the tube. When considering the time dependant properties of both materials, a smaller increase in the neutral axis depth than in the case where only the concrete's time dependant properties is considered occurs for specimens subjected to maximum moment of 25% of the ultimate. For specimens subjected to maximum moment of 50% of the ultimate, a decrease in the neutral axis depth initially occurs followed by an increase, smaller than in the case where only the concrete's time dependant properties is considered. Table 3 shows that the fatigue life of CFFT beams increases when ignoring the time dependant properties of the concrete. This increase becomes more pronounced as the maximum moment and the frequency decreases.

#### **5.4.1.2 Effect of loading frequency and load level**

Figures 5.24, 5.25 and 5.26 present sample curves of the relative bottom strain ( $\epsilon_b/\epsilon_{bstatic}$ ), the relative top strain ( $\epsilon_t/\epsilon_{tstatic}$ ), and the relative deflection ( $\delta/\delta_{static}$ ) versus  $N/N_f$ , respectively, for the two maximum loading levels and the two loading frequencies. It is apparent from these curves that increasing the loading frequency decreases the deterioration in the response of CFFT members, in terms of the excessive deflection, whereas the opposite is true for the maximum loading level, at a given number of cycles.

**5.4.1.3 Effect of tube diameter (i.e. FRP reinforcement ratio)**

Figures 5.27, 5.28 and 5.29 present sample curves of the relative bottom strain ( $\epsilon_b/\epsilon_{bstatic}$ ), the relative top strain ( $\epsilon_t/\epsilon_{tstatic}$ ) and the relative deflection ( $\delta/\delta_{static}$ ) versus  $N/N_f$ , respectively, for three tube diameters. It is apparent from these figures that the larger diameter members (i.e. with smaller FRP reinforcement ratio) will suffer slightly larger deterioration in their cyclic response than CFFT of smaller diameter (i.e. with larger FRP reinforcement ratio). It could be observed, however from Table 3 and figure 5.30 that the tube diameter (FRP reinforcement ratio) did not have any significant effect on the fatigue life of the CFFT beams.

Table 5-1 Fatigue life predictions compared to experimental results

Specimen	Number of Cycles (Experimental) (N)	Predicted number of Cycles to failure ( $N_f$ )	$N/N_f$	$N/N_f$ (log scale)
BFC3	2,365	16,023	14.8%	80.2%
BFP1U	28,619	116,391	24.6%	88.0%
BFC1 (stage 1)	676,532	12,838,462	5.3%	N/A
BFC1 (stage 2)	417,782	8,815,836	4.7%	
BFC1 (stage 3)	8,556	11,311,041	0.1%	
BFC1 (stage 4)	406,787	690,442	58.9%	
$\Sigma$ BFC1			69%	96.8%*

\* Calculated assuming that the required number of cycles is  $0.9 N_f$  after 10% total damage from previous loading cycles.

Table 5-2 Summary of the parametric study

outer diameter of the tube (mm)	$M_{\max} / M_{\text{ult}}$	f (Hz)	Case *
256	50%	1	1
			2
			3
		5	1
			2
			3
	25%	1	1
			2
			3
		5	1
			2
			3
367	50%	1	1
			2
			3
		5	1
			2
			3
	25%	1	1
			2
			3
		5	1
			2
			3
456	50%	1	1
			2
			3
		5	1
			2
			3
	25%	1	1
			2
			3
		5	1
			2
			3

\* Case 1: FRP time dependant properties only are considered.

Case 2: Concrete time dependant properties only are considered.

Case 3: Time dependant properties of both concrete and FRP are considered.

Table 5-3 Fatigue life predictions of parametric study

$D_t$	$M_{max}/M_{ult}$	f (Hz)	Case *	$N_f$
256	50%	1	1	102,913
			2	70,523
			3	92,449
		5	1	127,667
			2	94,596
			3	121,675
	25%	1	1	9,270,985
			2	7,585,735
			3	6,829,016
		5	1	6,911,034
			2	5,955,114
			3	5,623,656
367	50%	1	1	119,848
			2	81,511
			3	104,937
		5	1	146,478
			2	108,764
			3	137,702
	25%	1	1	10,200,799
			2	8,400,955
			3	7,348,036
		5	1	7,565,672
			2	6,540,373
			3	6,052,023
459	50%	1	1	116,561
			2	78,852
			3	101,404
		5	1	143,073
			2	105,986
			3	134,032
	25%	1	1	9,713,878
			2	8,091,118
			3	6,976,300
		5	1	7,289,130
			2	6,335,542
			3	5,792,308

\* Case 1: FRP time dependant properties only are considered.

Case 2: Concrete time dependant properties only are considered.

Case 3: Time dependant properties of both concrete and FRP are considered.



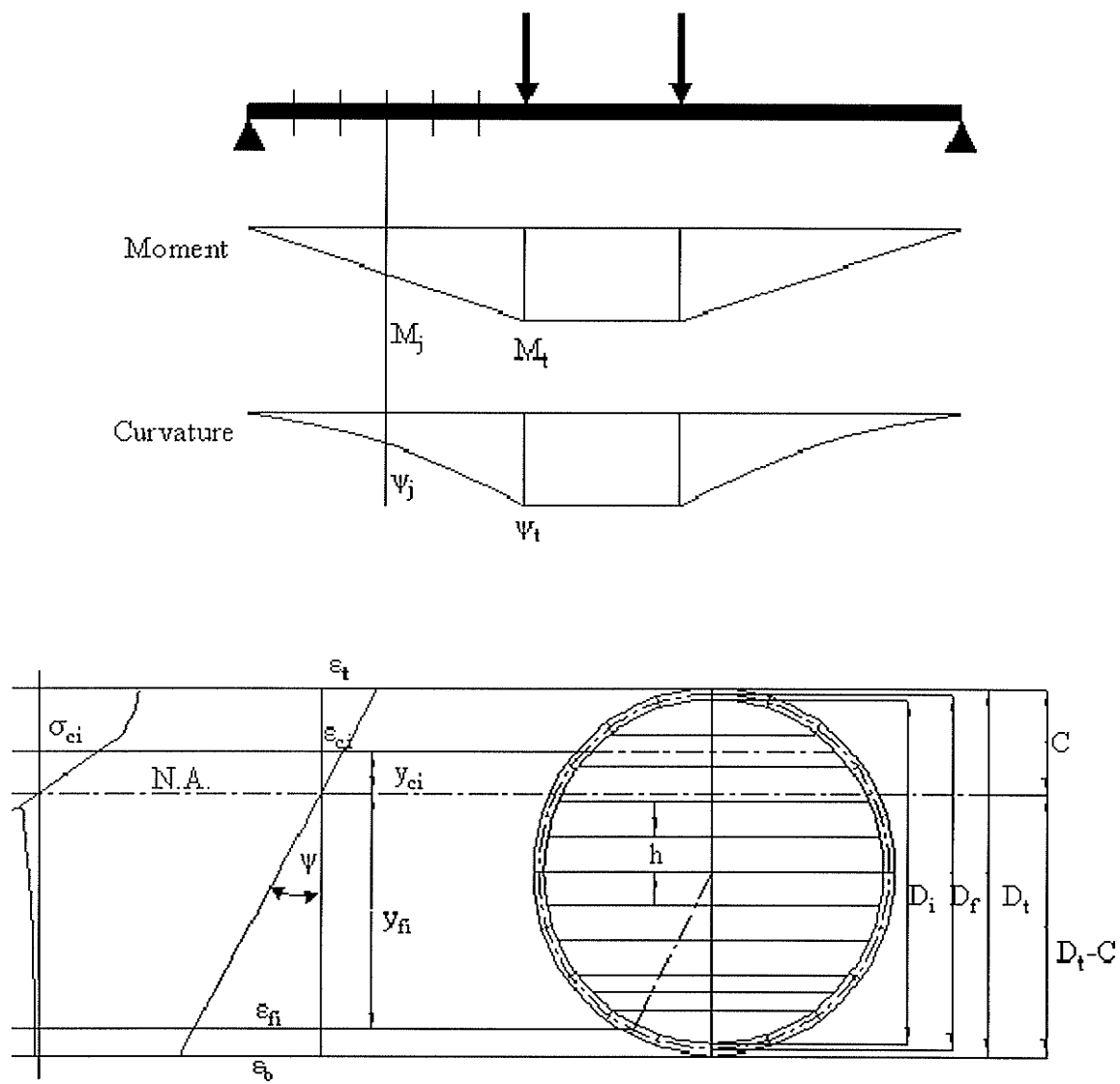


Figure 5-1 Schematic of CFFT model parameters in flexure

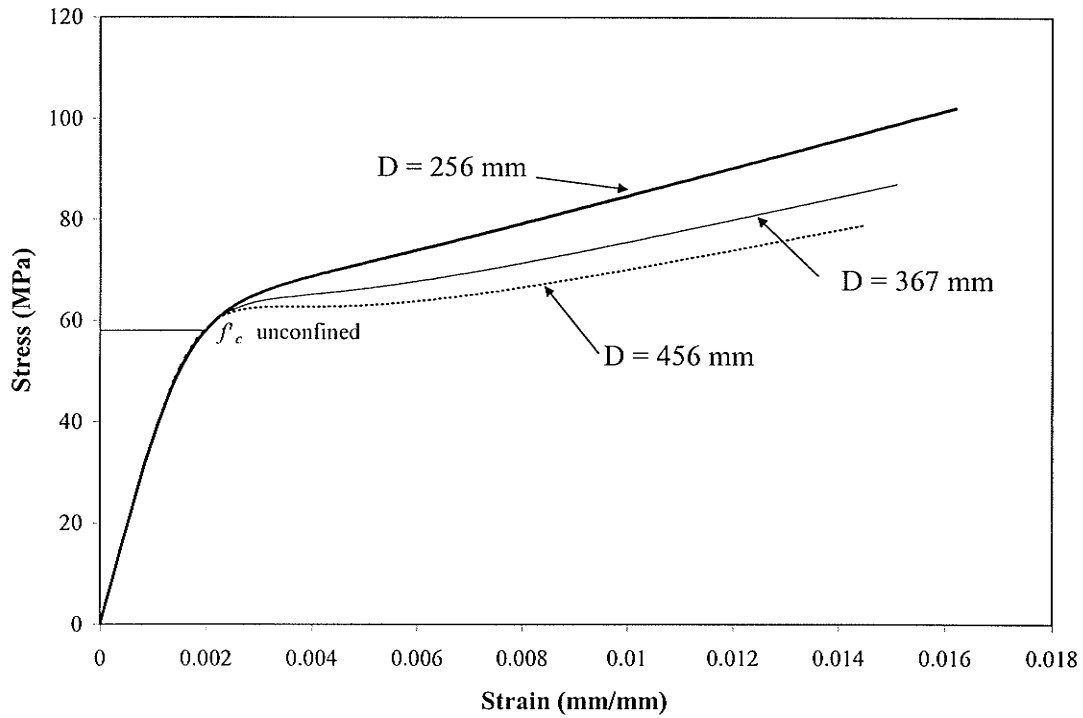


Figure 5-2 Predicted concrete stress-strain relation for CFFT members in compression using model by Fam and Rizkalla (2001b)

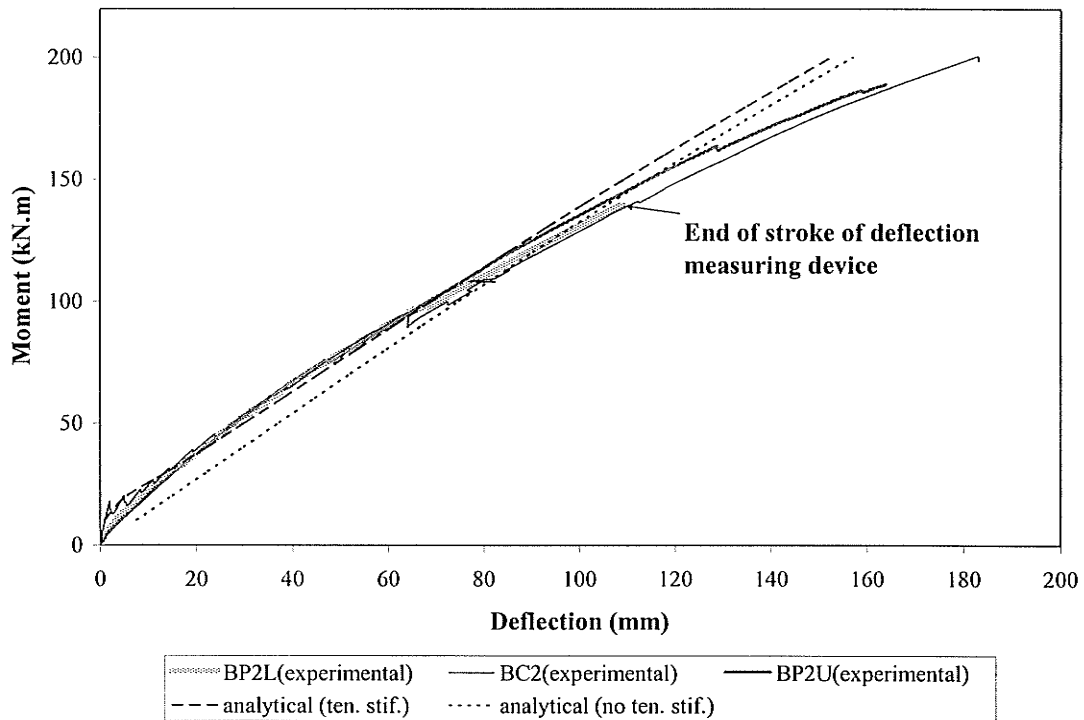


Figure 5-3 Predicted versus experimental load-deflection behavior of CFFT under monotonic static bending

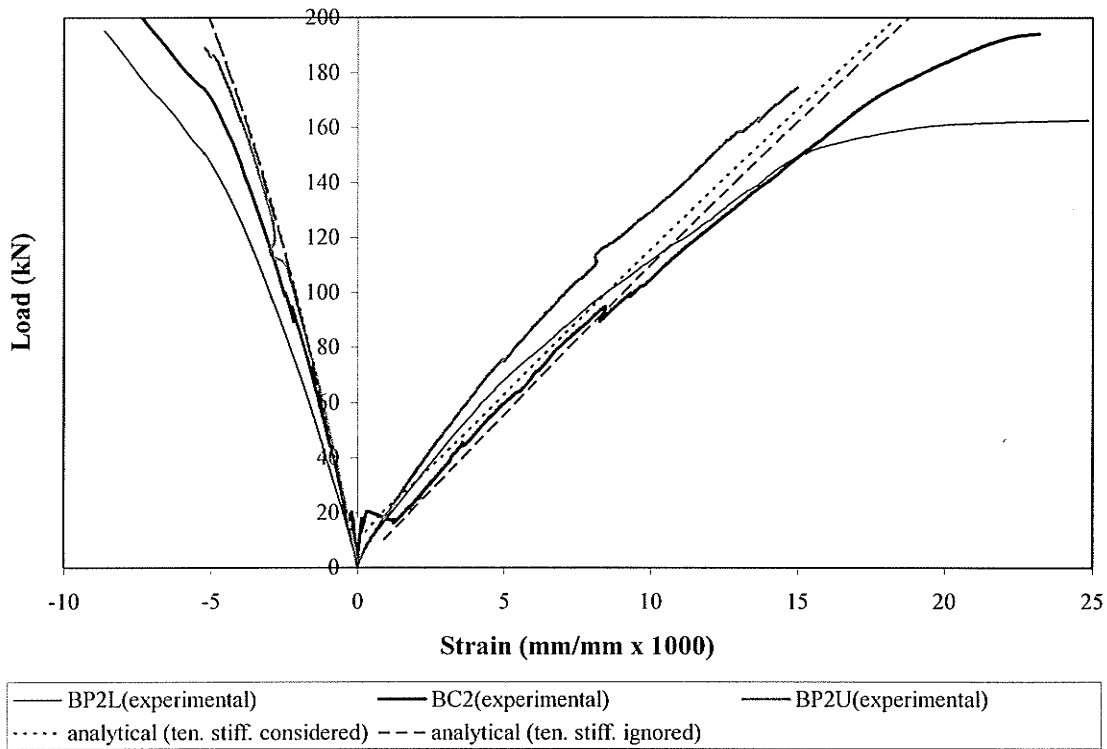


Figure 5-4 Predicted versus experimental load-strain behavior of CFFT under monotonic static bending

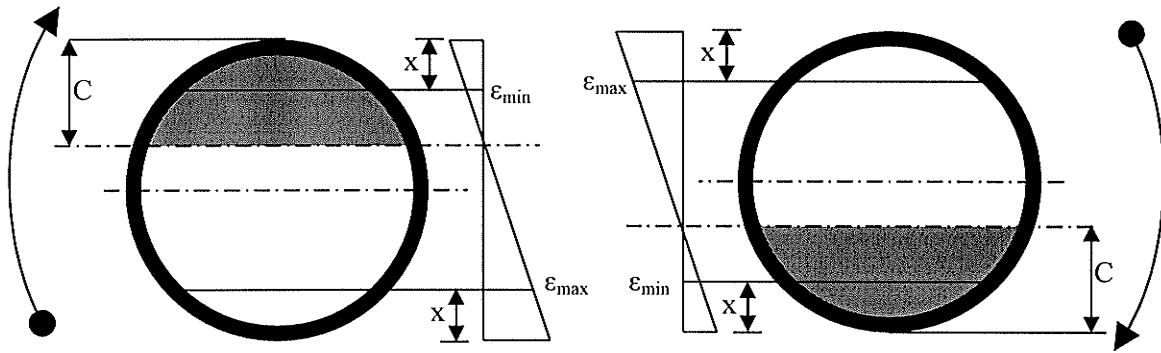


Figure 5-5 CFFT sections subjected to reversed bending

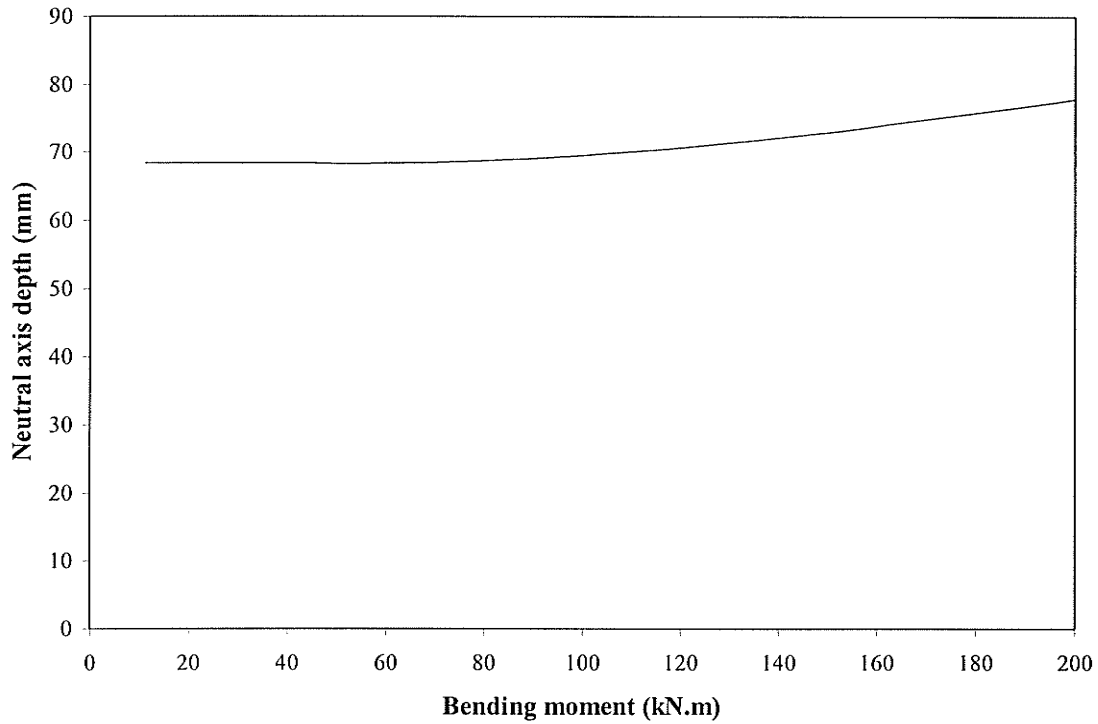


Figure 5-6 Predicted neutral axis depth versus static bending moment for CFFT specimen BC2

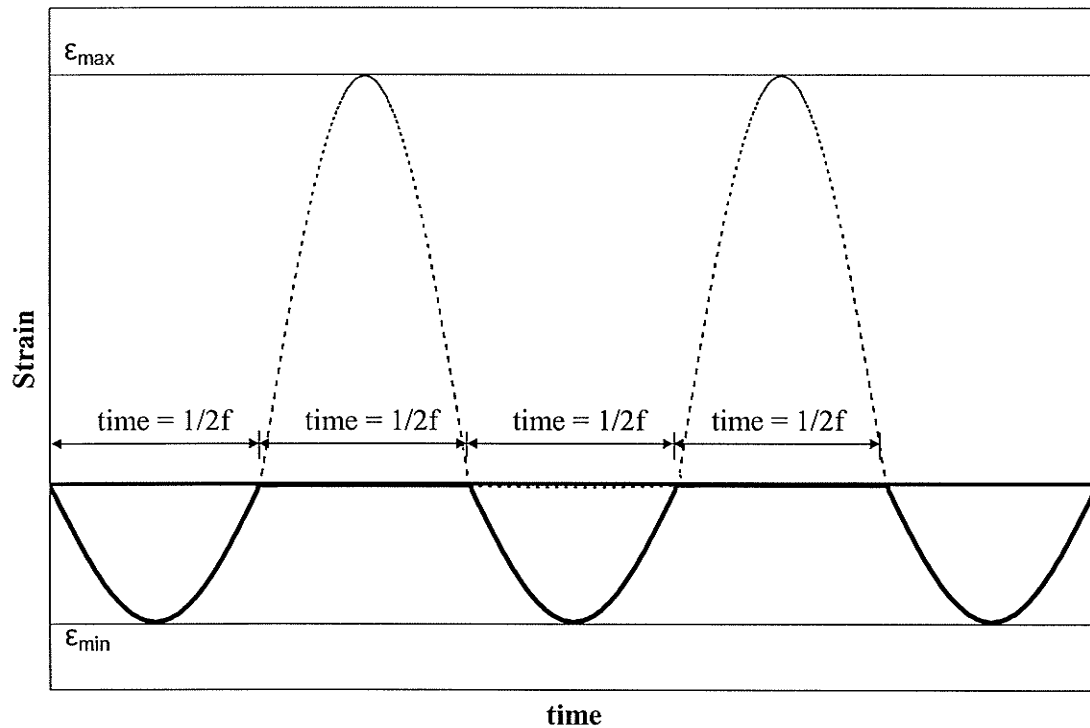


Figure 5-7 Strain versus time for concrete layers in a CFFT member

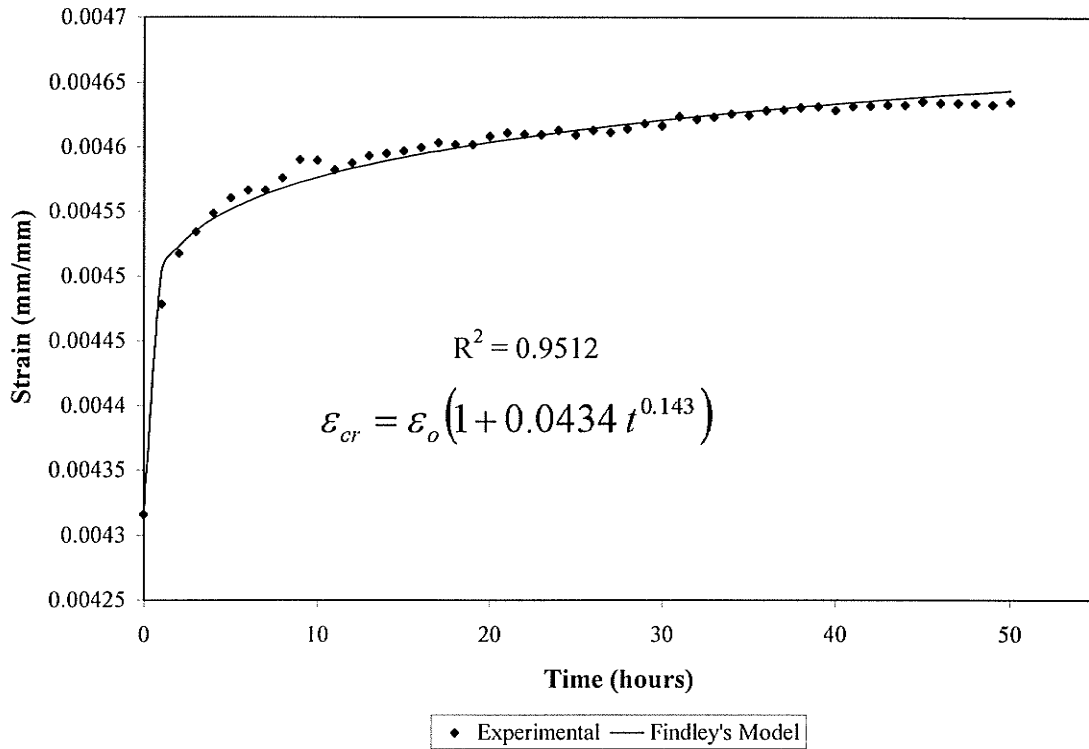


Figure 5-8 Calibration of Findley's (1960) creep model using FRP tube test data

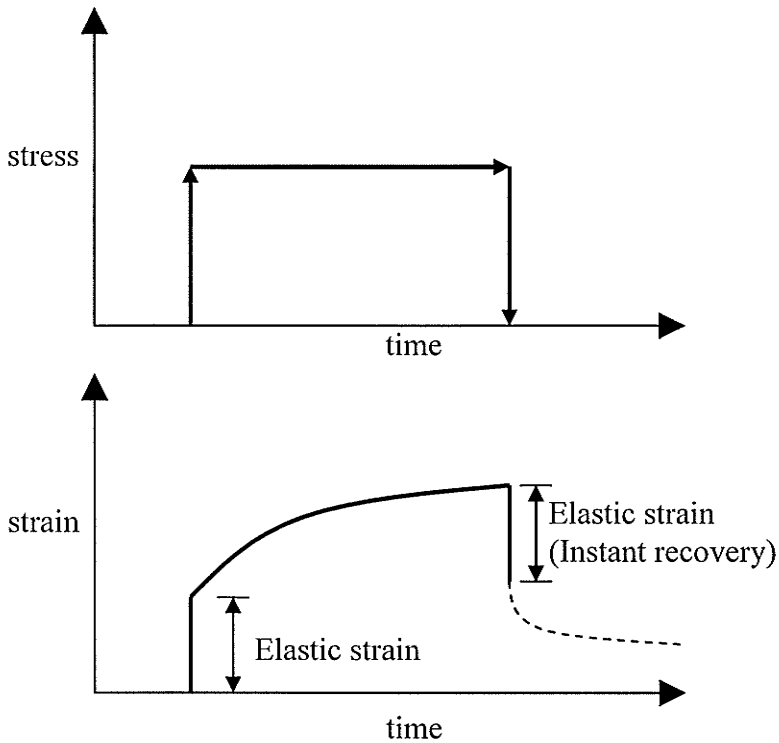


Figure 5-9 Schematic of FRP creep behavior (Mallick, 1998)

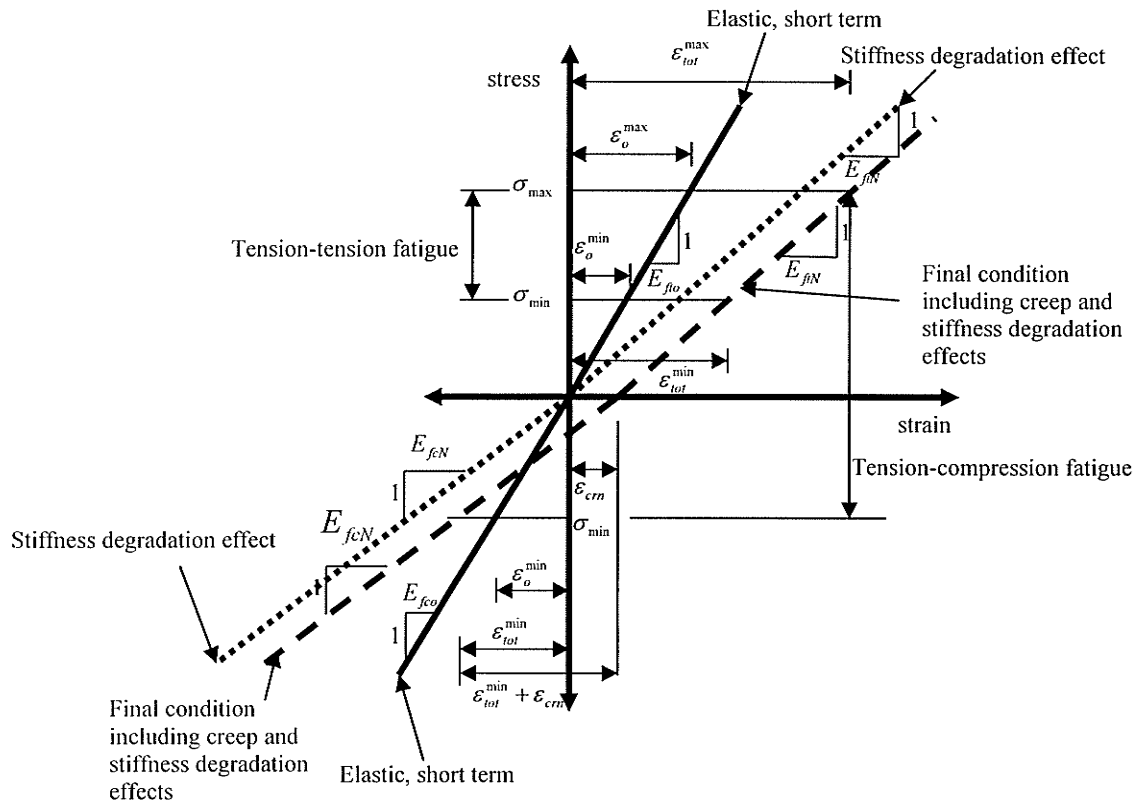


Figure 5-10 Creep and stiffness degradation models for FRP in tension and compression (Based on Deskovic, 1993)

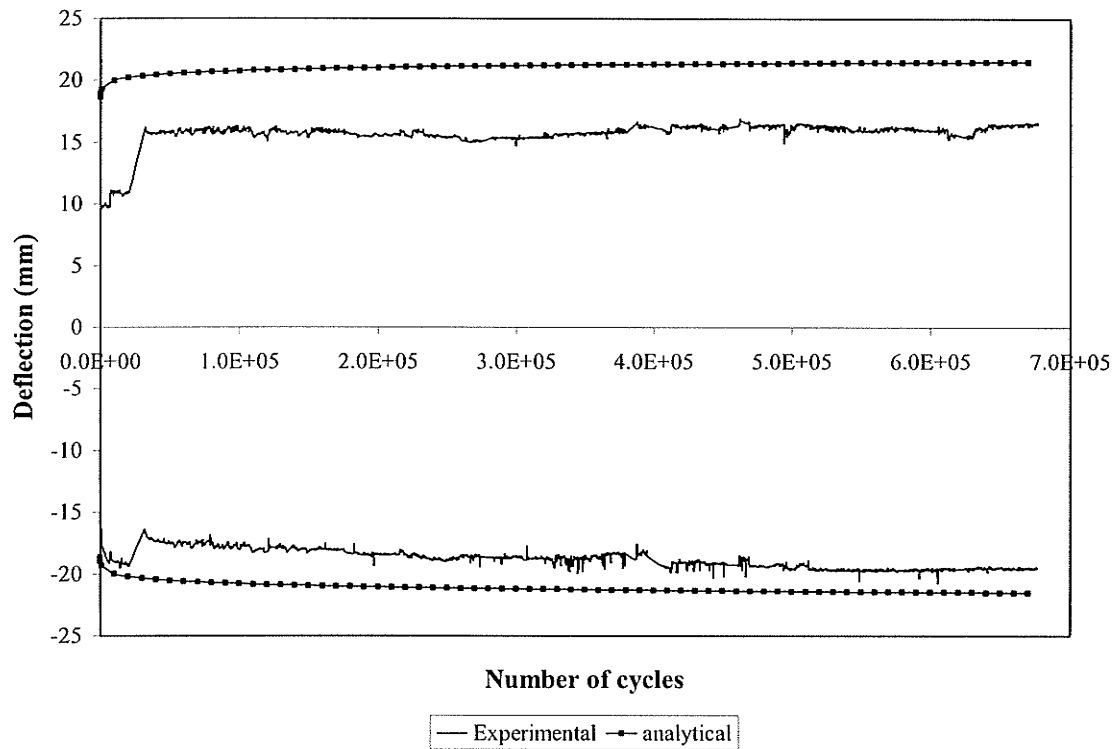


Figure 5-11 Comparison of deflection behavior for specimen BFC1

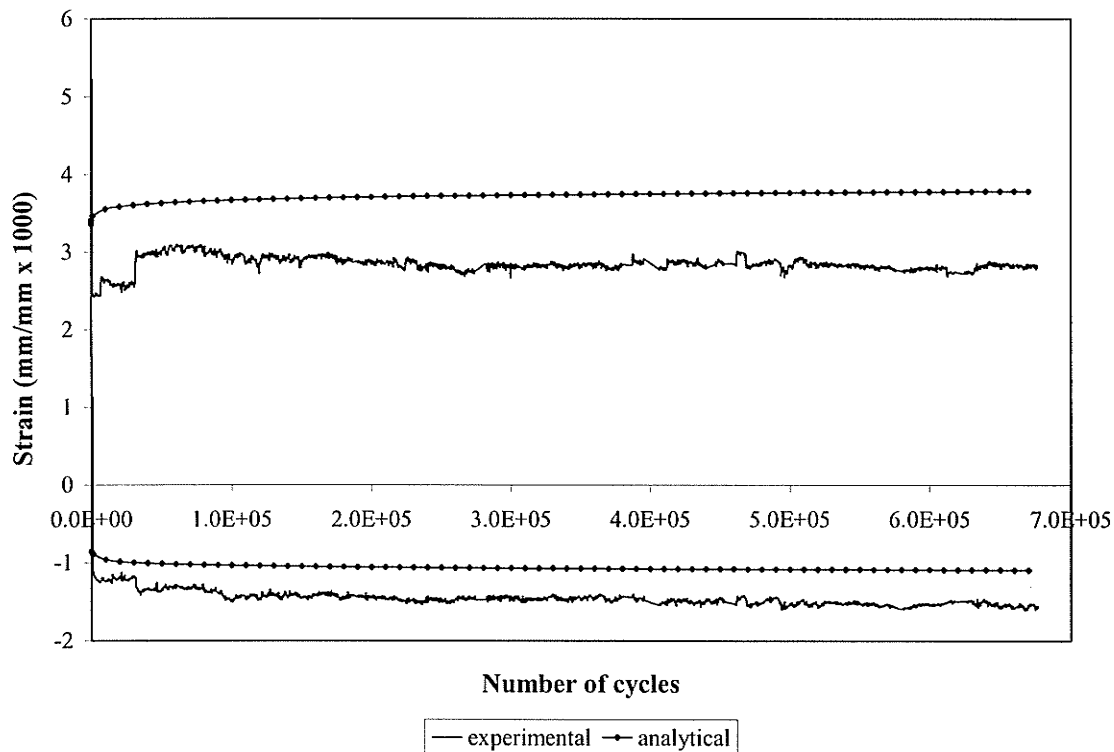


Figure 5-12 Comparison of strain behavior for specimen BFC1

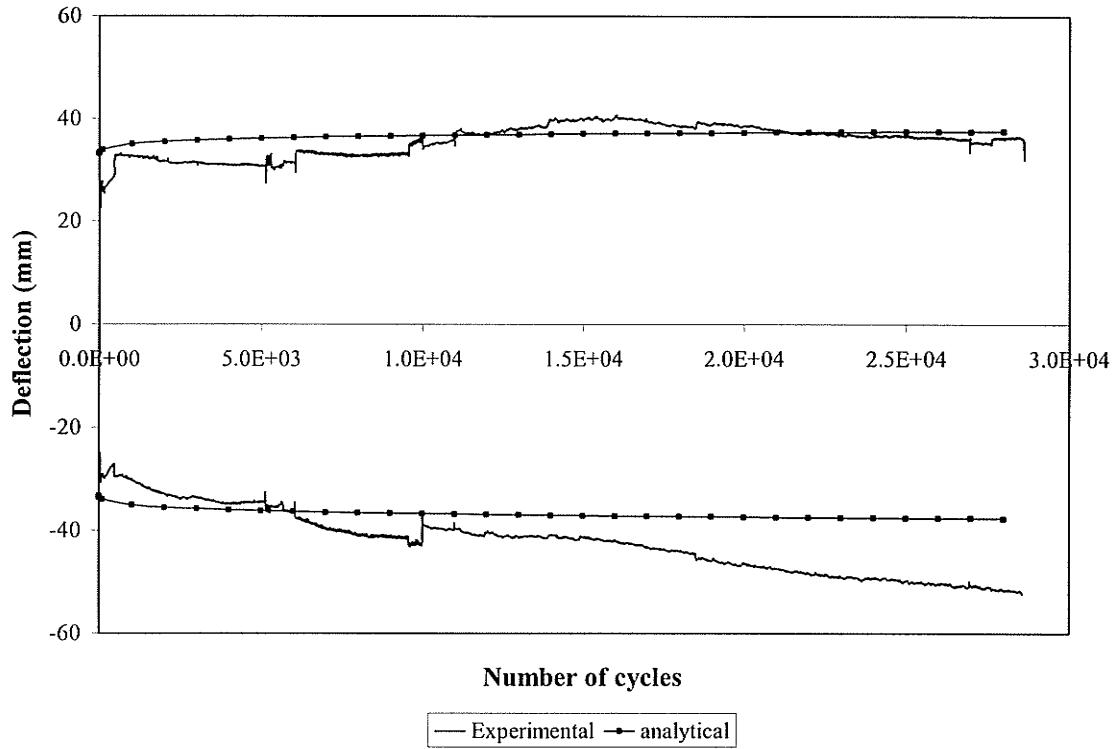


Figure 5-13 Comparison of deflection behavior for specimen BFP1U

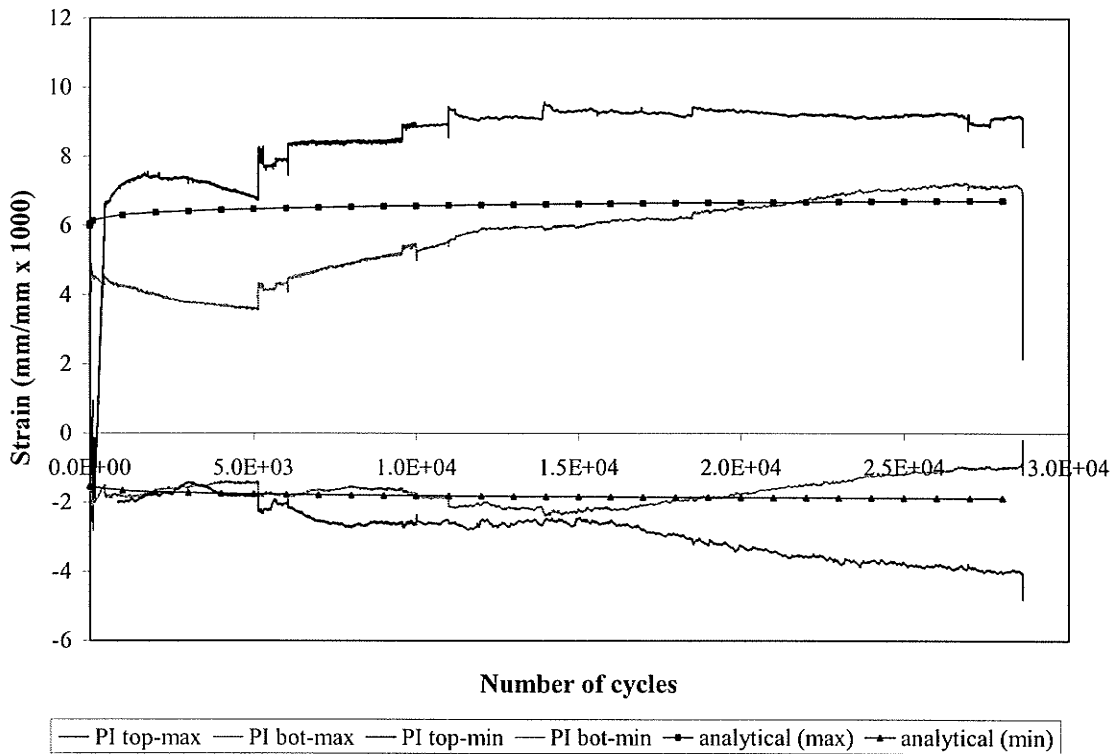


Figure 5-14 Comparison of strain behavior for specimen BFP1U



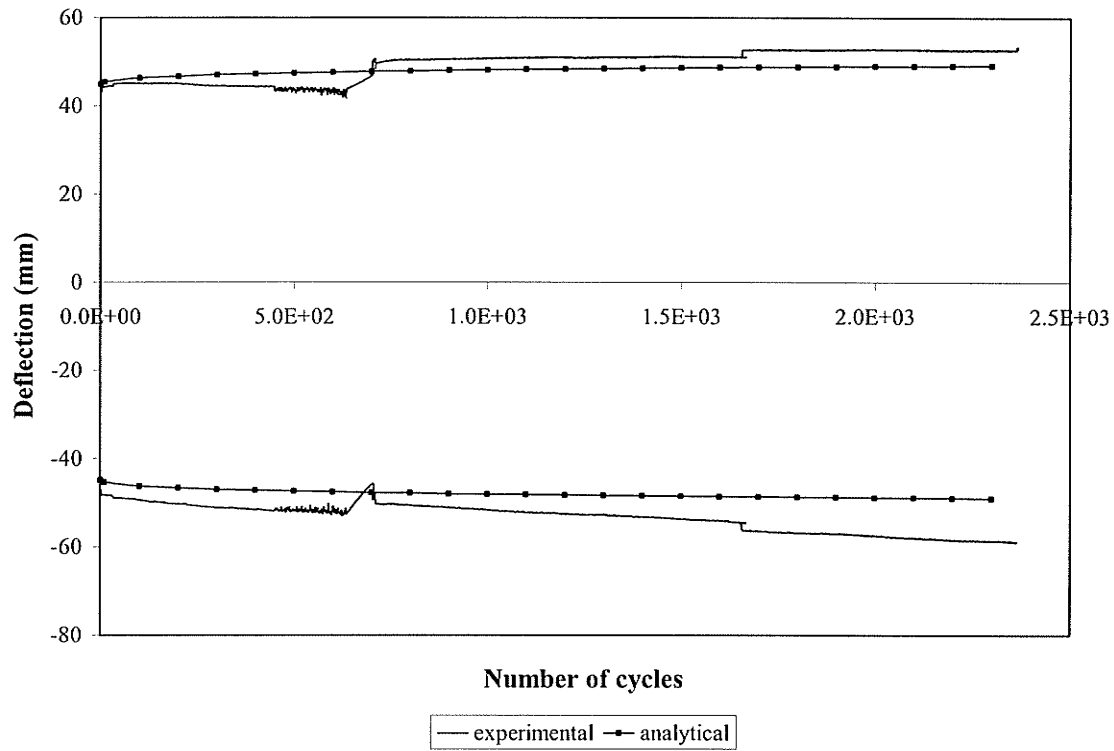


Figure 5-15 Comparison of deflection behavior for specimen BFC3

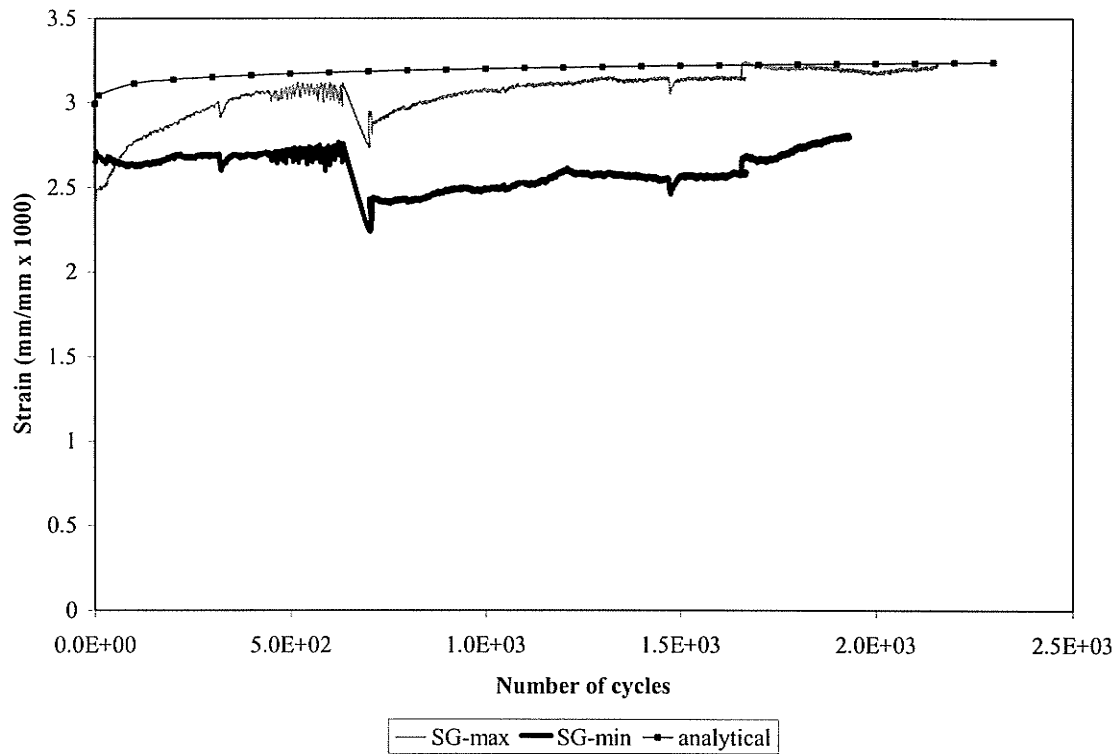


Figure 5-16 Comparison of strain behavior for specimen BFC3

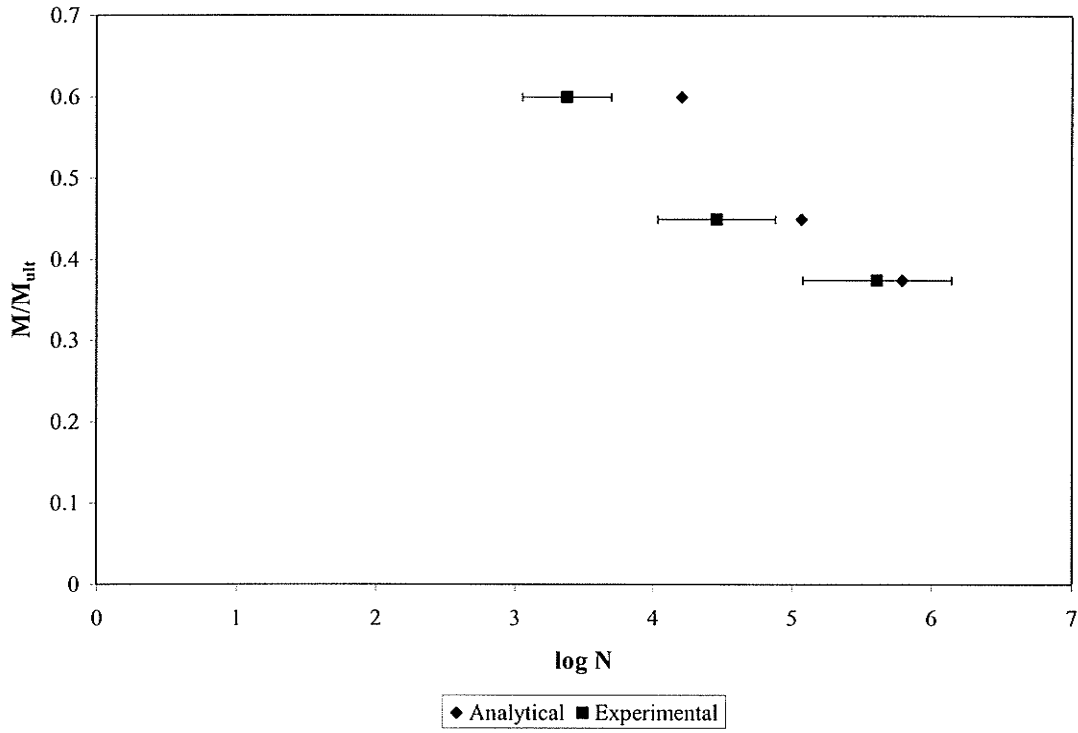


Figure 5-17 Comparison of predicted and experimental fatigue lives

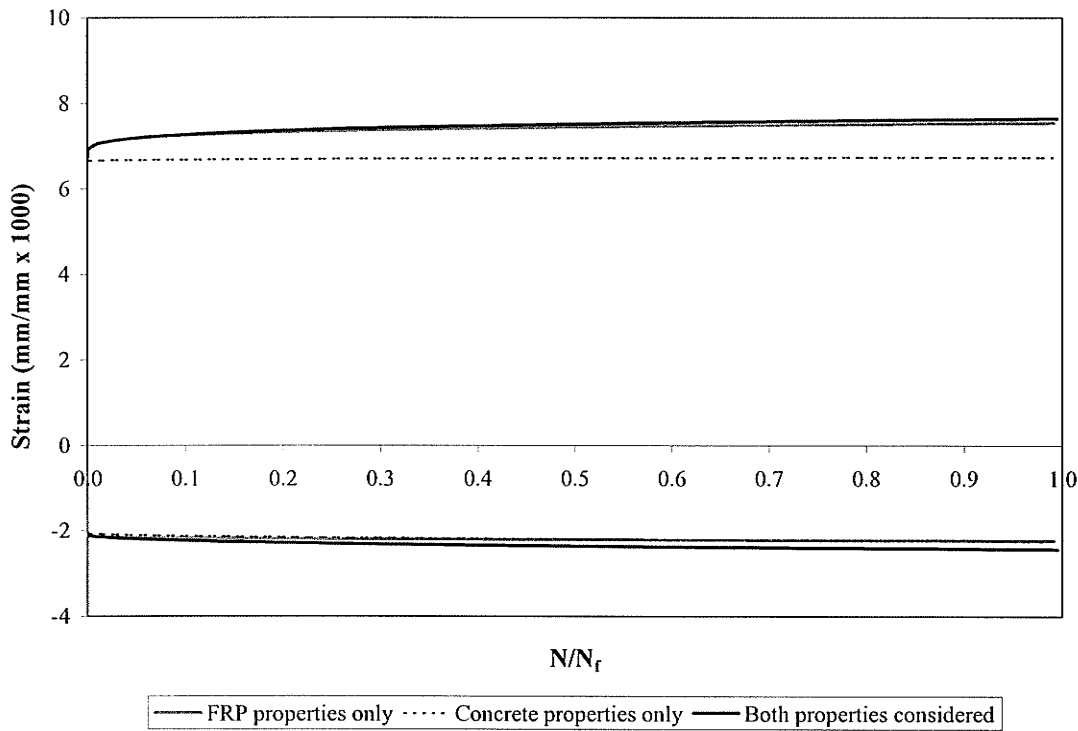


Figure 5-18 Effect of the time dependent properties of the materials on the strain behavior ( $D_t=256 - M_{max}/M_{ult} = 50\% - f = 1\text{Hz}$ )

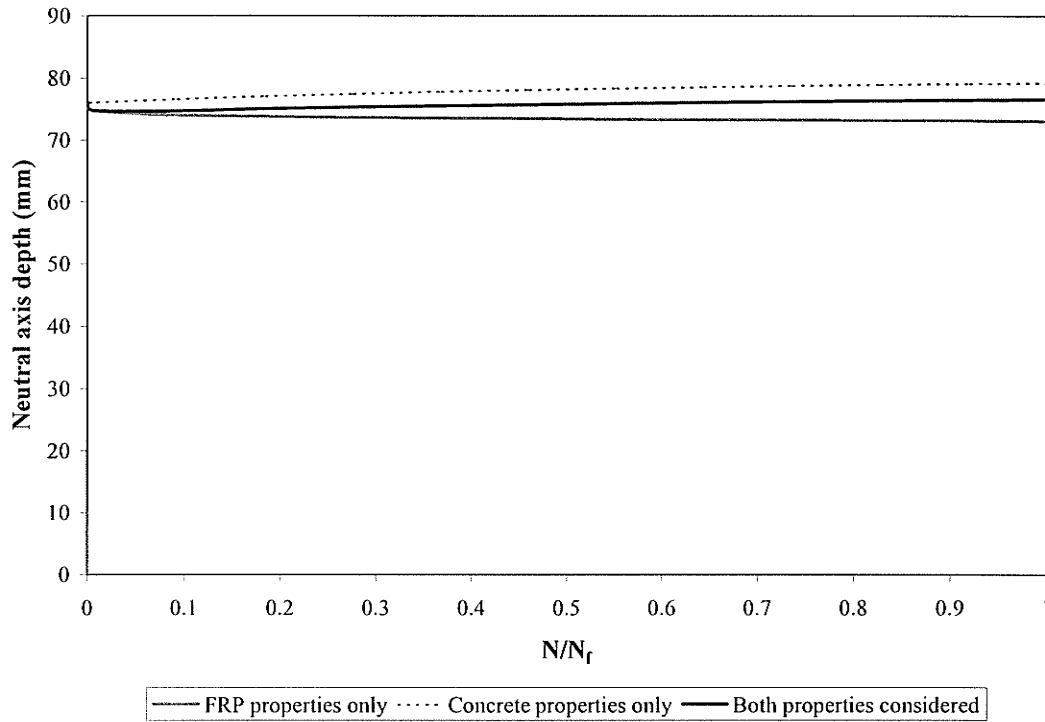


Figure 5-19 Effect of the time dependant properties of the materials on the depth of the neutral axis ( $D_t=367 - M_{max}/M_{ult} = 50\% - f = 5\text{Hz}$ )

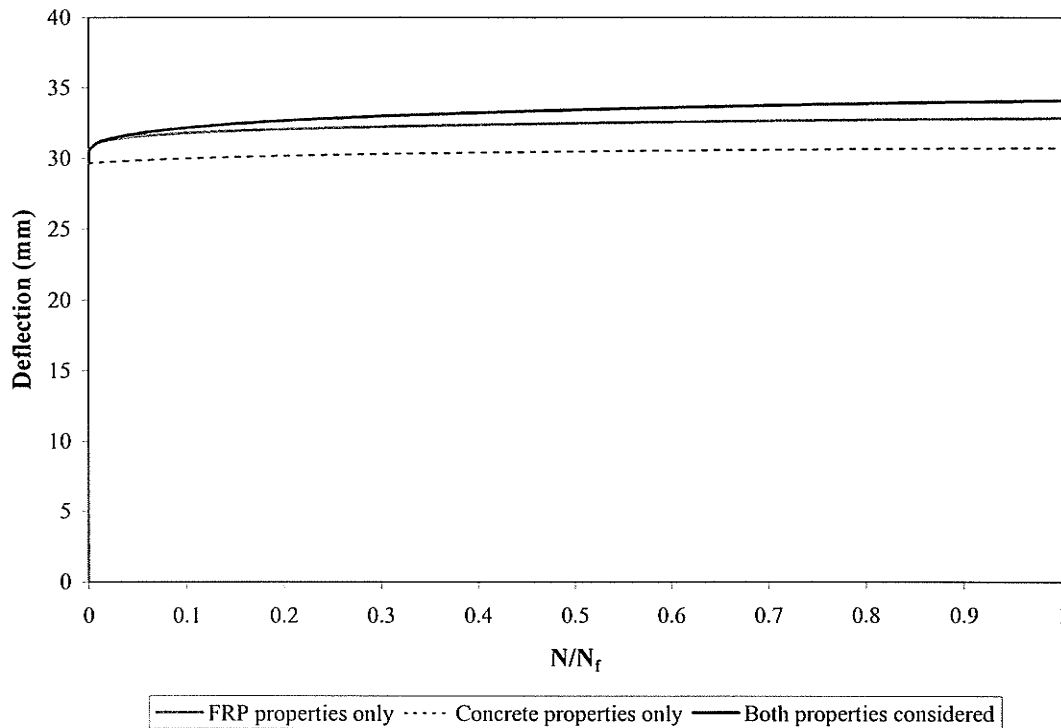


Figure 5-20 Effect of the time dependant properties of the materials on the midspan deflection ( $D_t=456 - M_{max}/M_{ult} = 50\% - f = 1\text{Hz}$ )

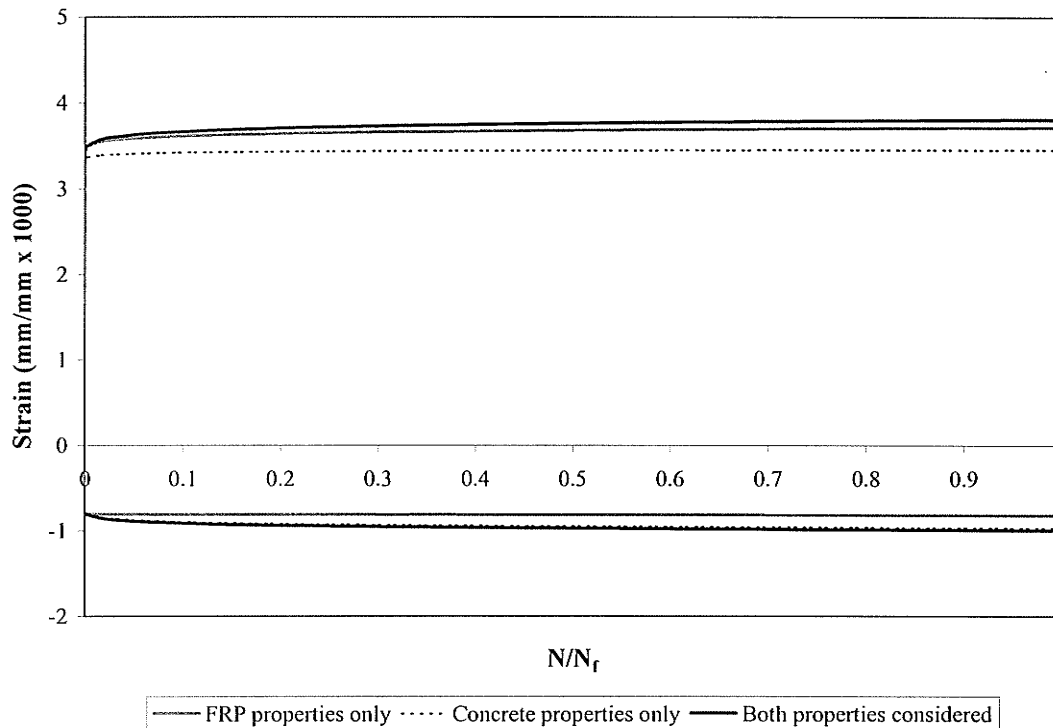


Figure 5-21 Effect of the time dependant properties of the materials on the strain behavior ( $D_t = 456 - M_{max}/M_{ult} = 25\% - f = 5\text{Hz}$ )

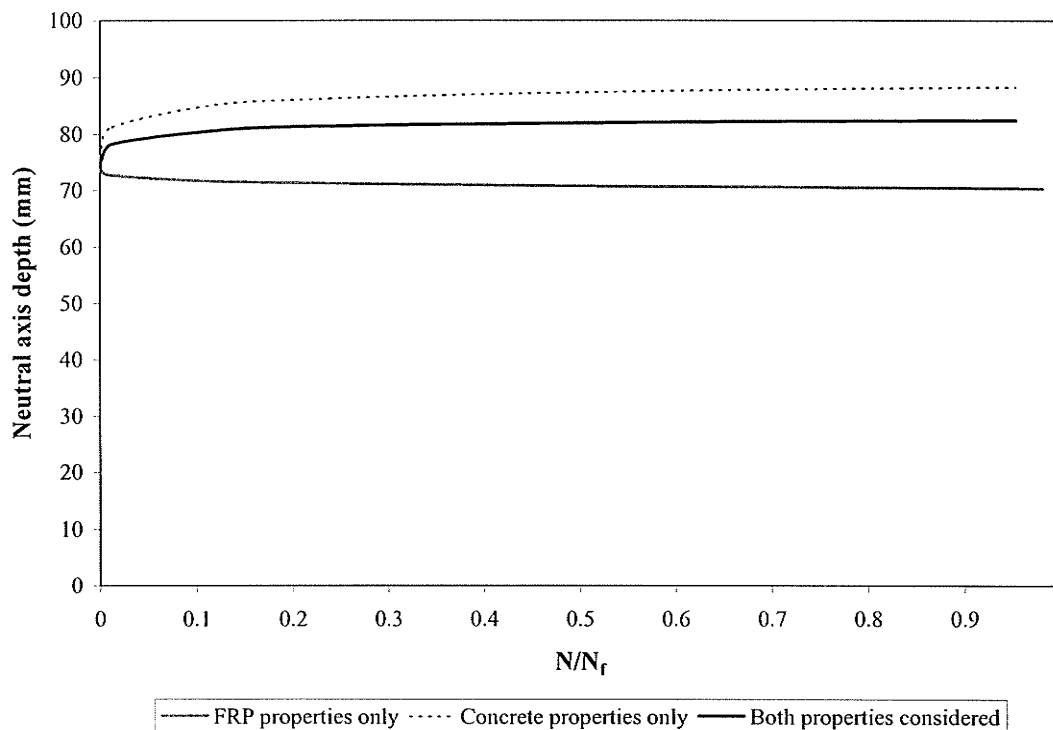


Figure 5-22 Effect of the time dependant properties of the materials on the depth of the neutral axis ( $D_t = 367 - M_{max}/M_{ult} = 25\% - f = 1\text{Hz}$ )

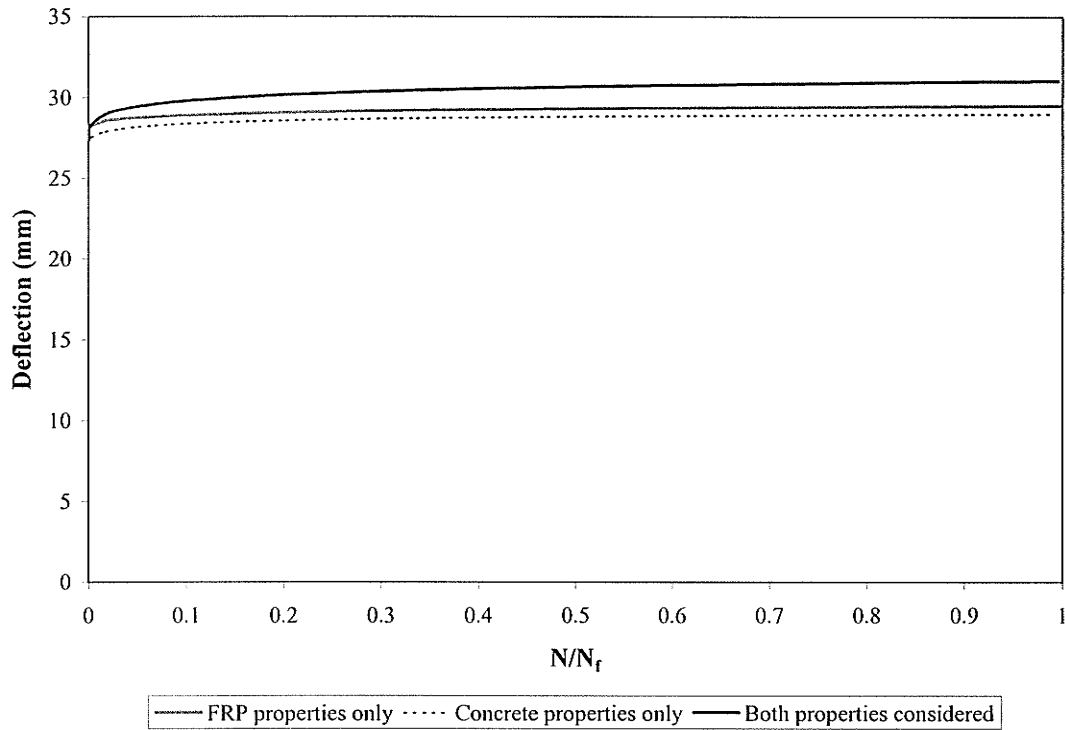


Figure 5-23 Effect of the time dependant properties of the materials on the midspan deflection ( $D_t=256 - M_{max}/M_{ult} = 25\% - f = 5\text{Hz}$ )

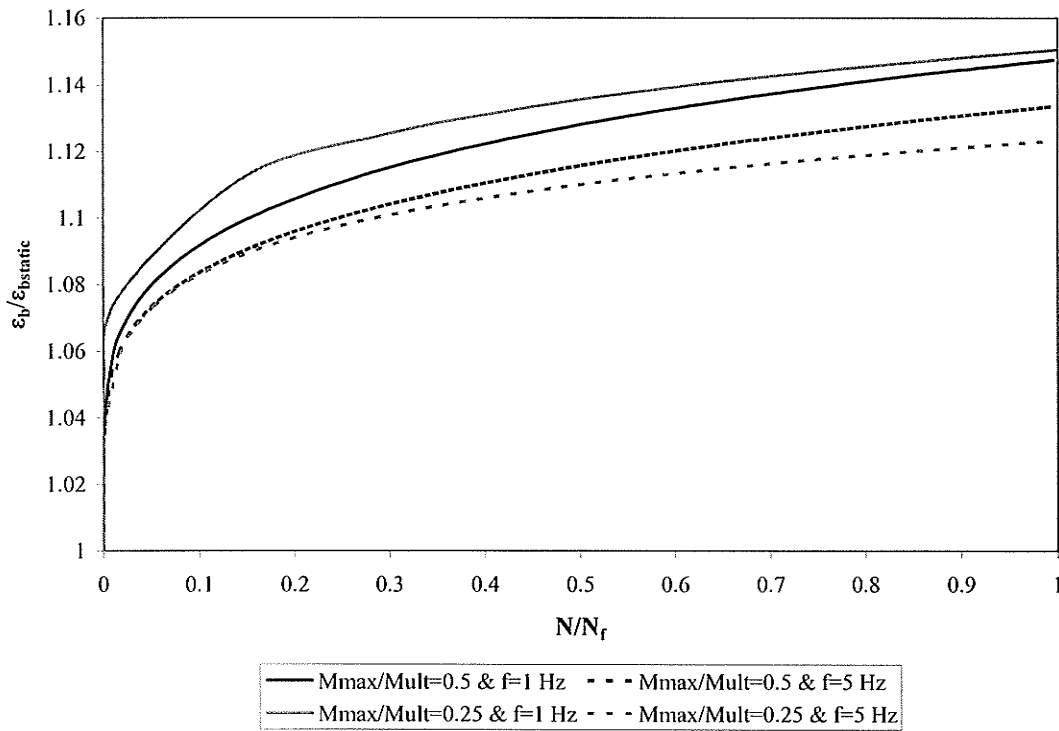


Figure 5-24 Effect of loading frequency and load level on bottom strain behavior ( $D_t = 256 \text{ mm}$ )

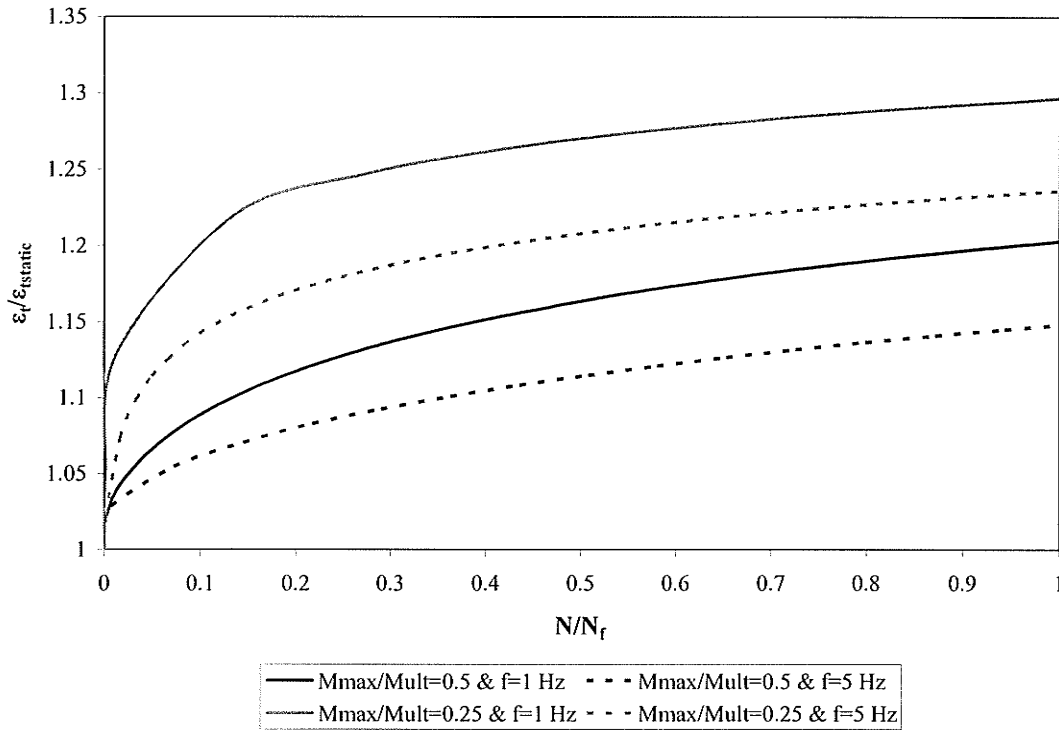


Figure 5-25 Effect of loading frequency and load level on top strain behavior ( $D_t = 367$  mm)

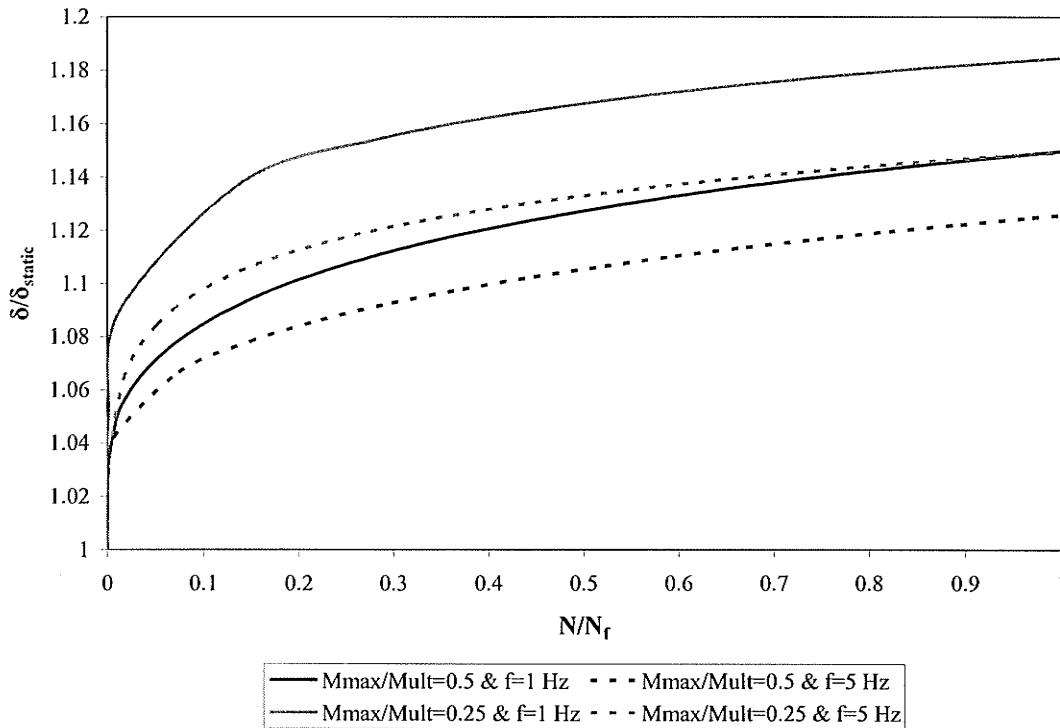


Figure 5-26 Effect of loading frequency and load level on deflection behavior ( $D_t = 456$  mm)

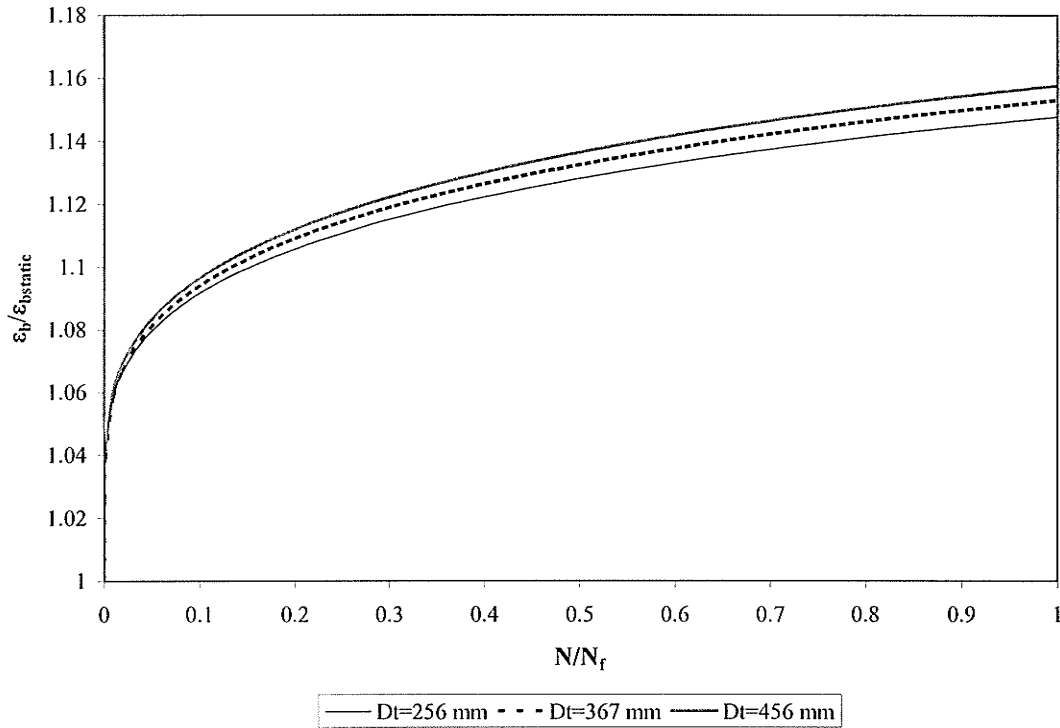


Figure 5-27 Effect of the tube diameter on bottom strain behavior ( $M_{max}/M_{ult} = 50\%$  -  $f = 1\text{Hz}$ )

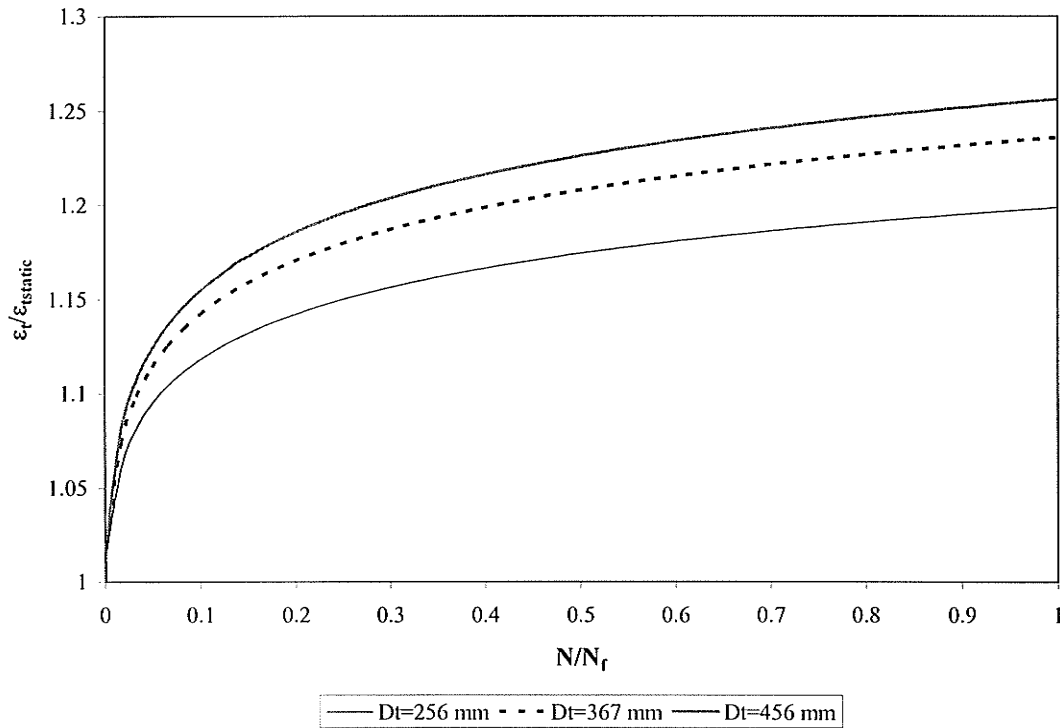


Figure 5-28 Effect of the tube diameter on top strain behavior ( $M_{max}/M_{ult} = 25\%$  -  $f = 5\text{Hz}$ )

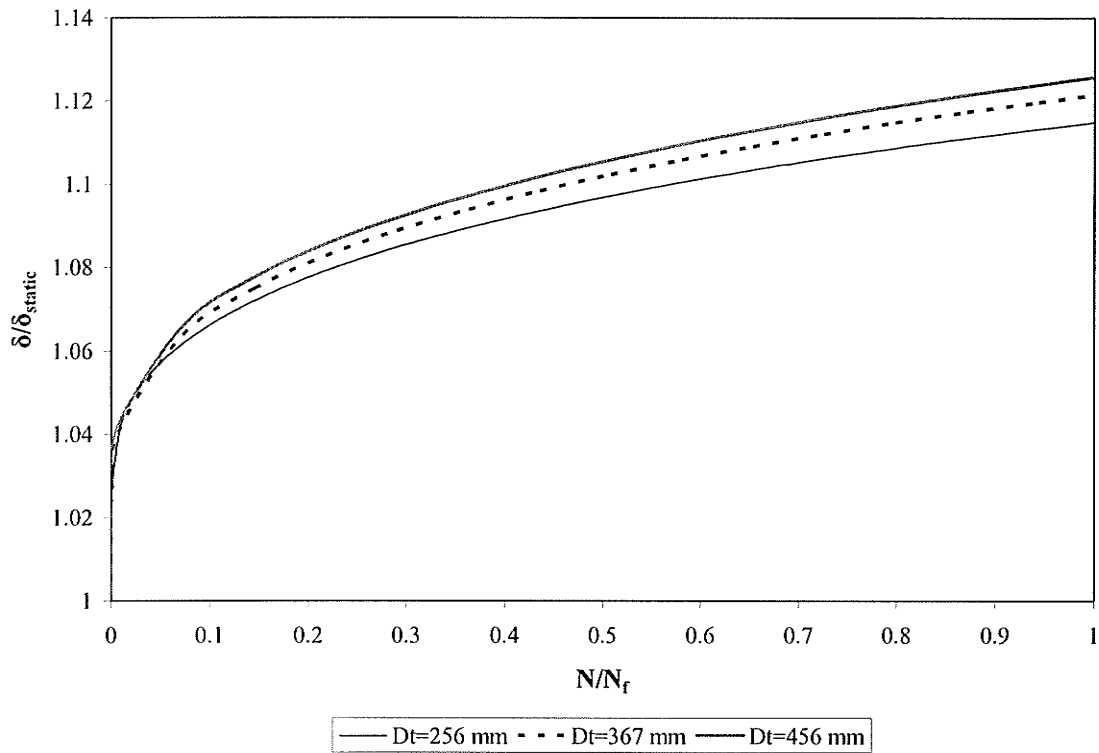


Figure 5-29 Effect of the tube diameter on deflection behavior ( $M_{max}/M_{ult} = 50\%$  -  $f = 5\text{Hz}$ )

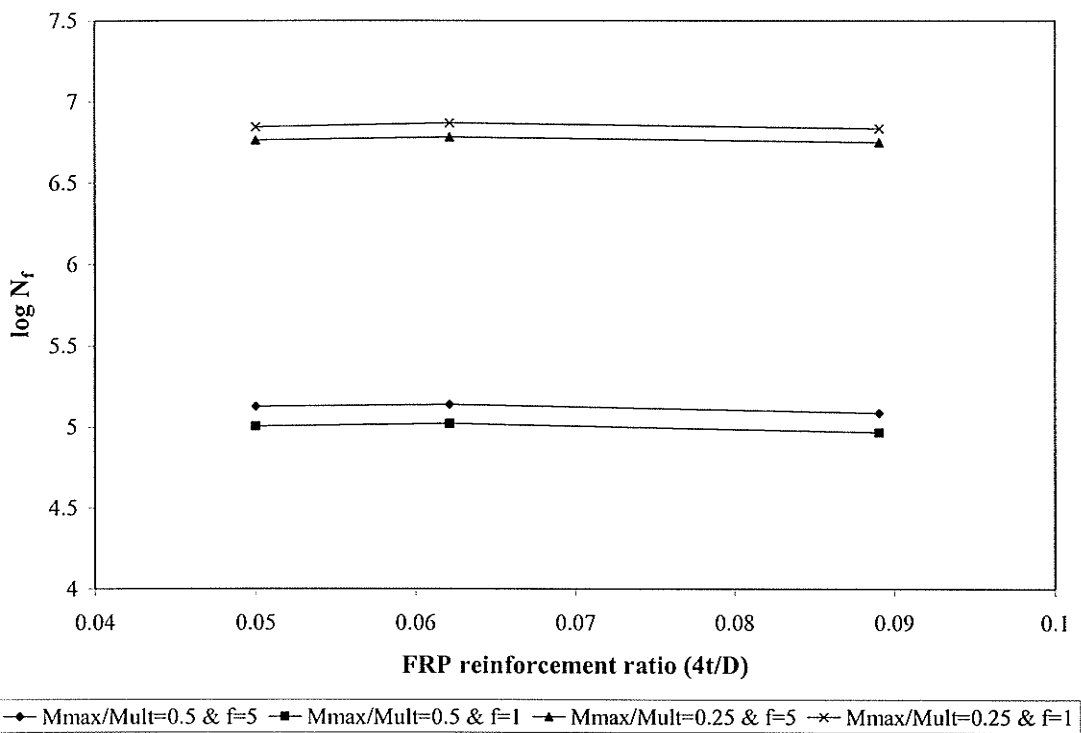


Figure 5-30 Effect of FRP reinforcement ration on fatigue life



## **Chapter 6**

### **Summary, Conclusions, Recommendations for Future Study, and Design Recommendations and Limitations**

#### **6.1 Summary**

In this thesis a research program was conducted to study the effect of driving forces on CFFT members used as piles along with a splicing system and the bending fatigue behavior of CFFT flexural members. The study of the effect of driving forces on CFFT members and splicing was conducted experimentally, whereas both experimental and analytical investigations were conducted on the fatigue behavior of CFFT flexural members.

To study the effect of driving forces on CFFT members, four full-scale CFFT piles, including a spliced pile, were driven using conventional pile driving equipment and procedures and were then extracted from the ground. Three beam specimens, of which one included a splice, were cut from the driven piles and tested in flexure in the laboratory. Test results were compared with those obtained from additional three CFFT beam tests conducted on control (undriven) specimens. A total of 27 push-off tests, 115 tension coupon tests, 56 compression coupon tests, and 55 tension-tension coupon fatigue tests were also conducted on specimens cut from the control and driven piles, from various locations along the pile length, to assess the effect of driving forces.

The experimental program for studying fatigue behavior of CFFT beams included testing of three full-scale specimens under reversed cyclic bending, using a four point bending configuration. The program also included testing of 81 coupons cut from the tubes, in

tension-tension fatigue and tension-compression fatigue, under different loading frequencies. Based on the results of the coupon fatigue tests, fatigue life prediction and stiffness degradation models for the FRP tube materials were developed.

An analytical study was conducted to model the behavior of CFFT beams under reversed cyclic bending. The analytical model used is adapted from the sectional analysis method developed by Deskovic (1993) to model the creep and cyclic behavior of hybrid FRP/concrete members. A FORTRAN program was developed using this method to model the behavior of CFFT beams under reversed cyclic bending loads and predict the fatigue life. The results of this analytical modeling were compared to that of the experimental results of the CFFT beams tested under reversed cyclic bending. A parametric study was also conducted to study the effect of the different material time dependant properties, maximum applied moment, and frequency on the behavior of CFFT beams and the fatigue life under reversed cyclic bending.

## **6.2 Conclusions**

Based on the research program the following conclusions could be made.

### **6.2.1 Effect of driving forces and splicing of CFFT**

1. Driving of CFFT piles, using conventional equipment and methods, is quite feasible and practical.
2. Driving stresses have marginal effect, about 5% reduction, on the flexural strengths of both the CFFT pile and splice and appear to have no effect on the flexural stiffness of CFFT piles.

3. Driving stresses have no effect on the bond strength between the concrete core and FRP tube. Corrugations in the tube's inner surface maintain adequate mechanical bond strength, after friction and adhesion strengths are overcome, even at large values of slip.
4. Driving stresses have little effect (5-10% reduction) on the tensile strength of GFRP tubes, but seems to have no effect on the compressive strength or tension-tension fatigue life of GFRP tubes.
5. The mechanical splice used in this study was successful and provided 7% higher moment capacity than that of the CFFT pile itself. Further research may be needed, however, to optimize the length of anchor rebar of the splice, given the advantage of confinement provided by the FRP tube, which enhances the bond strength of the rebars.
6. The orientation of the keys used in the splice with respect to the direction of applied load has insignificant effect on moment capacity. The '+' pattern showed only 2% higher moment than the 'x' pattern.
7. In filament-wound tubes with fibers oriented at an angle with respect to the longitudinal axis, standard FRP test coupons cut from the tubes longitudinally tend to fail prematurely, where the fibers split at an angle and fiber pullout occurs instead of fiber fracture. The full tensile strength of the FRP tube may not be fully developed in the coupons. This is attributed to the lack of continuity of some fibers between the grips.
8. All types of tension coupons used gave almost the same initial modulus of elasticity, but varied substantially in the tensile strength. Shorter longitudinal

coupons provided more accurate results when compared to full-scale CFFT test results, since the band width of the continuous fibers between grips increases as the coupon length decreases, and more fibers develop their full tensile strength rather than failing by pull-out.

9. Coupons cut at a small angle equal to the fiber orientation seem to give reliable results with respect to the failure mode, failure stress and failure strain, when compared to full-scale test results. However, these coupons were slightly warped, and in a case where the fibers are oriented at a larger angle the use of such coupons may not be practical; neither would it represent the effective mechanical properties of the tubes in the longitudinal direction.

### **6.2.2 Reversed cyclic bending behavior of CFFT members**

1. Concrete filled FRP tube flexural members seem to have a relatively short fatigue life under bending moments of 40% and higher of their ultimate static bending moment capacities. However, the fatigue life of CFFT increases dramatically at bending moments lower than 40% of their ultimate static bending moment capacities.
2. Slip in CFFT beams during reversed cyclic bending tends to stabilize at one end while continuing to increase at the other end.
3. CFFT beams subjected to reversed cyclic bending developed full depth cracks at various locations along the length of the member.
4. Deflections and strains of CFFT beams tend to increase at a relatively rapid rate initially then continue at a slower rate, reflecting some early stiffness degradation due to the cracking of the matrix in the hoop layers. This was also confirmed by

coupon test results, where some stiffness degradation occurs initially in tension-tension and tension-compression fatigue specimens due to the cracking of the matrix in the hoop layers then reduces.

5. The fatigue life of coupons cut from FRP tubes tends to have a linear relation on the log scale with the  $\sigma_{\max}/\sigma_u$  ratio, for ratios in the range of 0.4 to 0.6, but increases nonlinearly at stress ratios lower than 0.3.
6. Coupons cut parallel to the longitudinal fibers and those cut parallel to the longitudinal axis of the tube and tested in fatigue exhibit failure modes similar to their respective static tension coupons. They also produce different fatigue life curves.
7. The presence of a compression load component in fatigue reduces the fatigue life of coupons cut from FRP tubes; however, this effect tends to decrease at lower  $\sigma_{\max}/\sigma_u$  ratios.
8. Increasing the frequency of the applied load increases the fatigue life of coupons cut from FRP tubes.
9. The empirical equation developed by Epaarachchi and Clausen (2003) fits the test data of coupons cut from FRP tubes very well and successfully predicted the fatigue life of full-scale CFFT beams.
10. The empirical method (Epaarachchi and Clausen, 2003) can predict fairly well the fatigue life of other specimens subjected to the same loading frequency but to a stress ratio  $R$  different from the one used to obtain the curve fitting parameters. The equation, however, was not as effective in predicting the fatigue life for other

specimens subjected to the same stress ratio  $R$  but to a loading frequency different than the one used to obtain the curve fitting parameters.

11. The analytical method developed in this thesis predicts fairly well behavior of CFFT specimens subjected to reversed cyclic bending.
12. Both the concrete and FRP time dependant properties have a significant contribution to the cyclic behavior of CFFT members subjected to reversed cyclic bending.
13. Increasing the loading frequency causes less deterioration in the response of CFFT members, whereas the opposite is true for the load level at which cyclic loading is conducted for the same number of cycles.
14. The diameter-to-thickness ratio of the FRP tubes used in CFFT members has insignificant effect on the fatigue life of the system. However, members with larger diameter-to-thickness ratio tubes suffer slightly larger deterioration in their cyclic response.

### **6.3 Recommendations for Future Study**

This thesis addressed significant questions regarding the effect of driving forces on CFFT piles, splicing of CFFTs in practical piling applications, and the fatigue behavior of CFFT members. However, further research is still needed on the following topics;

1. Cyclic testing of CFFT members under combined axial and bending loads.
2. Developing creep and stiffness degradation models for CFFT members subjected to repeated axial loads.
3. Studying the cyclic behavior of CFFT members under different environmental conditions such as salt water and cold temperatures.

4. Enhancing the splicing system tested in this thesis, for example by optimizing the embedment length of the steel rebar anchors.

#### **6.4 Design Recommendations and Limitations**

In this thesis, analytical models and procedures were presented for predicting the fatigue life of filament-wound GFRP tubes and CFFT members, based on tests conducted on small coupons cut from the tubes in the direction of the longitudinal fibers. The results of these relatively simple and inexpensive coupon tests could then be used to predict the cyclic behavior and the fatigue life of full-scale CFFT flexural members, which are usually difficult and expensive to test. These models and procedures were shown to give relatively good predictions for the static and cyclic behavior and fatigue life of CFFT specimens, and therefore could be used in design. The models and procedures, however, should be limited to tubes where the longitudinal fibers are at a small angle with the longitudinal axis of the tube, which is the case for most current commercial CFFT pile applications and the case of this research program. In cases of large angles between the axis of the tube and the fibers, coupons cut in this direction will be largely warped, making them difficult and problematic to test. Additionally, the angle between the fibers (coupons) and the longitudinal direction of the tube, which is essentially the direction of the loading, will be too large to assume that the coupons represent the behavior of the tube in the longitudinal direction. The models and procedures developed in this thesis could still be used in cases of large angles; however, the tension and fatigue properties of the tubes need to be obtained using methods other than tests conducted on coupons cut from the direction of the fibers.

It is recommended to use the empirical method developed by Epaarachchi and Clausen (2003), presented in Chapter 4, to construct the fatigue life curves of filament-wound GFRP tubes because it requires a relatively small number of coupon tests to enable a full representation of the full fatigue life range, however, the tests must be conducted at a loading frequency that is very close to the one expected in the actual applications of the CFFT members under study.

The model presented in Chapter 5 could be used to predict the long-term deflections and strains as well as the fatigue life of CFFT flexural members. However, for cases where the maximum applied moment is at 40% and higher of the ultimate static moment capacity, it is recommended to use the procedure presented in section 4.5.2.6.2 of Chapter 4, to predict the fatigue life of a CFFT, rather than the analytical model explained in Chapter 5, as it overestimates the fatigue life at moments of 40% and higher of the ultimate static moment capacity.

Using these models, designers are now able to predict the number of cycles to failure at a given cyclic service load, and hence the life span of the CFFT member. Alternatively, for a given life span, a limiting service load moment could be specified.

It should also be noted that this study examined the case of a reversed bending about one axis only, whereas in some applications such as monopoles, reversed cyclic bending could occur about several axes, depending on the wind direction.



## **References**

Ahmad I., Zhu, Z., Mirmiran A., and Fam, A. "Shear Strength Prediction of Deep CFFT Beams," American Concrete Institute Special Publication, ACI-SP 230, 7<sup>th</sup> International Symposium on Fiber Reinforced Polymer (FRP) Reinforcement for Concrete Structures, November 6-9, 2005, Kansas City, MO, USA.

Ahmad, I. "Shear Response and Bending Fatigue Behaviour of Concrete-Filled Fibre Reinforced Polymer Tube," Ph.D. Thesis, North Carolina State University, Raleigh, NC, 2004.

American Concrete Institute ACI, ACI Committee 209 "Prediction of Creep, Shrinkage and Temperature Effects in Concrete Structures." ACI 209 R-92, ACI Publication SP-70, 1992, Detroit.

American Society for Testing and Materials, ASTM "Standard Test Method for Compressive Strength of Cylindrical Concrete Specimens (ASTM C39-96)," ASTM, Philadelphia, PA, 1996.

American Society for Testing and Materials, ASTM "Standard Test Method for Tensile Properties of Plastics (ASTM D638-91)," ASTM, Philadelphia, PA, 1991.

American Society for Testing and Materials, ASTM "Standard Test Method for Tensile Properties of Polymer Matrix Composite Materials (ASTM D3039/D3039M)," ASTM, Philadelphia, PA, 2000.

American Society for Testing and Materials, ASTM "Standard Test Method for Compressive Properties of Rigid Plastics (ASTM D695-96)," ASTM, Philadelphia, PA, 1996.

American Society for Testing and Materials, ASTM "Standard Test Method for Apparent Hoop Tensile Strength of Plastic or Reinforced Plastic Pipe by Split Disk Method," ASTM D2290-04)," ASTM, Philadelphia, PA, 1996.

Arduini, M., Di Tommaso, A., Manfroni, O., Ferrari, S., and Romagnolo, M. 1999, "II: Confinement o Passive di Element compressi in Calcestruzzo con Fogli di Materiale Composito." *Ind. Ital. Cemento*, 11, 836-841.

Ashford, S., and Jakrapiyanum, W. "Drivability of FRP Composite Piling," *Journal of Composites for Construction*, Vol. 5, No.2, 2001, pp.58-60

Aval, S., Saadeghvaziri, M., and Golafshani, A. "Comprehensive Composite Inelastic Fiber Element for Cyclic Analysis of Concrete Filled Steel Tube Columns," *Journal of Engineering Mechanics*, Vol. 128, No. 4, 2002, pp: 428-437.

Becque, J., Patnaik, A. K., and Rizkalla, S. H. "Analytical Models for Concrete Confined with FRP Tubes", *Journal of Composites for Construction*, Vol. 7, No. 1, 2003, pp. 31-38.

Burgueño, R. "System Characterization and Design of Modular Fiber Reinforced Polymer (FRP) Short- and Medium-Span Bridges," Ph.D. Dissertation, University of California, San Diego, La Jolla, California, 1999.

Burgueno, R., and Bhide, K. "Shear Stresses in Concrete-Filled FRP Cylindrical Shells in Bending," Proceedings of the 4th Advanced Composite Materials in Bridges and Structures, Calgary, Canada, 2004, pp. 1-8.

Chaallal, O., Hassan, M., and Shahawy, M. "Confinement Model for Axially Loaded Short Rectangular Columns Strengthened with Fiber-Reinforced Polymer Wrapping", ACI Structural Journal, Vol. 100, No. 2, 2003, pp. 215-221.

Cheng, H. L., Sotelino, E. D., and Chen, W. "Strength Estimation for FRP Wrapped Reinforced Concrete Columns." Steel and Composite Structures, Vol. 2, No. 1, 2002, pp. 1-20.

Chun, S. S. and Park. H. C. "Load Carrying Capacity and Ductility of RC Columns Confined by Carbon Fiber Reinforced Polymer." Proceedings of the 3rd International Conference on Composites in Infrastructure (CD-Rom), University of Arizona, San Francisco, 2002.

Cole, Britton "Flexural and Shear Performances of Reinforced Concrete-Filled Fibre Reinforced Polymer Tubes," MSc Thesis, Queen's University, Kingston, ON, Canada, 2005.

Cole, Britton and Fam, Amir "Flexural Load Testing of Concrete-Filled FRP Tubes with Longitudinal Steel and FRP Rebar," Journal of Composites for Construction, Vol. 10, No. 2, 2006, pp. 161-171.

Collins, M.P. and Mitchell, D., "Prestressed Concrete Structures," Ed. By response Publications, Canada, 1997.

Davol, A. "Structural Characterization of Concrete Filled Fiber Reinforced Shells," Ph.D. Dissertation, University of California, San Diego, La Jolla, California, 1998.

Deskovic, Nikola "Innovative Design of FRP Composite Members Combined with Concrete," Ph.D. thesis, Massachusetts Institute of Technology, Cambridge, Massachusetts, USA, 1993.

Dutta, Piyush K. and Lampo, Richard G. "Behavior of Composite Fender Piles in Cold," Proceedings of the Twelfth International Offshore and Polar Engineering Conference, Kitakyushu, Japan, May 26-31, 2002, pp. 143-149.

El-Tawil, S., Ogunc, C., Okiel, A., and Shahawy, M. "Static and Fatigue Analyses of RC Beams Strengthened with CFRP Laminates," Journal of Composites for Construction, ASCE, V. 5, No. 4, 2002, pp. 258-267.

Elwi, A. A., and Murray, D. W. "A 3D Hypoelastic Concrete Constitutive Relationship." Journal of the Engineering Mechanics Division, Vol. 105, No. 4, 1979, pp. 623-641.

Epaarachchi J.A., and Clausen P., "An Empirical Model for Fatigue Behaviour Prediction of Glass Fibre-Reinforced Plastic Composites for Various Stress Ratios and Test Frequencies", Composites: Part A, Vol. 34, 2003, pp. 313-326.

Fam, A., Flisak, B., and Rizkalla, S. "Experimental and Analytical Modeling of Concrete-Filled Fiber-Reinforced Polymer Tubes Subjected to Combined Bending and Axial Loads", ACI Structural Journal, Vol. 100, No. 4, 2003, pp. 499-509.

Fam, A., Greene, R., and Rizkalla, S., "SP-215—9: Field Applications of Concrete-Filled FRP Tubes for Marine Piles," American Concrete Institute, ACI, SP-215: Field

Applications of FRP Reinforcement: Case Studies, Edited by, Rizkalla, S., and Nanni, A., 2003(a)

Fam, A., Pando, M., Filz, G. , and Rizkalla, S. "Precast Piles for Route 40 Bridge in Virginia Using Concrete Filled FRP Tubes", PCI Journal, Vol. 48, No. 3, 2003(b), pp. 32-45.

Fam, A., Schnerch, D., and Rizkalla, S. "Rectangular Filament-Wound GFRP Tubes Filled with Concrete under Flexural and Axial Loading: Experimental Investigation.", ASCE Journal of Composites for Construction, Vol. 9, No. 1, 2005, pp. 25-33

Fam, A.Z., and Rizkalla, S.H. "Behavior of Axially Loaded Concrete-Filled Circular Fiber-Reinforced Polymer Tubes", ACI Structural Journal, Vol. 98, No. 3, 2001(a),pp. 280-289.

Fam, A.Z., and Rizkalla, S.H. "Confinement Model for Axially Loaded Concrete Confined by Circular Fiber-Reinforced Polymer Tubes", ACI Structural Journal, Vol. 98, No. 4, 2001(b), pp. 451-461.

Fam, A.Z., and Rizkalla, S.H. "Flexural Behavior of Concrete-Filled Fiber-Reinforced Polymer Circular Tubes", Journal of Composites for Construction, Vol. 6, No. 2, 2002, pp. 123-132.

Fam, Amir "Concrete filled Fiber Reinforced Polymer Tubes for Axial and Flexural Structural Members," PhD dissertation, University of Manitoba, Winnipeg , Manitoba, Canada , 2000.

Fardis, M.N. and Khalili, H. "Concrete Encased in Fiberglass-Reinforced Plastics," ACI Structural Journal, Title No. 78-38, Nov.-Dec., 1981, pp. 440-446.

Findley, W. "Mechanism and Mechanics of Creep of Plastics," SPE Journal, 1960, pp. 57-65.

Flisak, Bartlomiej "Concrete filled Fibre Reinforced Polymer Tubes for Structural Members" M.Sc. thesis, University of Manitoba, Winnipeg , Manitoba, Canada, 2004.

Gamstedt, E., and Sjogren, B., (1999) "Micromechanisms in Tension-Compression Fatigue of Composite Laminates Containing Transverse Plies," Composites Science and Technology, Vol. 59, 1999, pp. 167-178.

Gardener, N. J, "Triaxial Behavior of Concrete," ACI Journal, Vol. 66, No. 2, 1969, pp. 136-146.

Gerstle, K. H. "Simple Formulation of Biaxial Concrete Behavior." ACI Journal, Vol. 78, No. 1, 1981(b), pp. 62-68.

Gerstle, K. H. "Simple Formulation of Triaxial Concrete Behavior." ACI Journal, Vol. 78, No. 5, 1981(b), pp. 382-387.

Goble, G.G. and Rausche, F. "Wave Equation Analysis of Pile Foundations," Vols. 1-4, FHWA Report No. IP-86-19, Federal Highway Administration, Washington, D.C. , 1987.

Harmon, T. G., Ramakrishnan, S., and Wang, E. H. "Confined Concrete Subjected to Uniaxial Monotonic Loading." Journal of Engineering Mechanics, Vol. 124, No. 12, 1998, pp. 1303-1308.

Harries, K. A. and Kharel, G. "Behavior and Modeling of Concrete Subject to Variable Confining Pressure." ACI Materials Journal, Vol. 99, No.2, 2002, pp.180-189.

Helmi, K., Fam, A., and Mufti, A., "Behavior of Concrete Filled FRP Tubes under Fully Reversed Cyclic Bending", Accepted for publication in the Arabian Journal of Science and Engineering, 2006(a).

Helmi, K., Fam, A., and Mufti, A., "Bending Fatigue of Concrete Filled Fiber Reinforced Polymer Tubes," International Association for Bridge and Structural Engineering (IABSE) Symposium Budapest, Hungary, September 13-15, 2006(b).

Helmi, K., Fam, A., and Mufti, A., "Field Installation, Splicing and Flexural Testing of Hybrid FRP/Concrete Pile" American Concrete Institute Special Publication ACI-SP 230, 7th International Symposium on Fiber Reinforced Polymer (FRP) Reinforcement for Concrete Structures, November 6-9, 2005(a), Kansas City, MO, USA.

Helmi, K., Fam, A., Mufti, A., Hall, J. "Effect of Driving Forces and Bending Fatigue on the Structural Performance of a Novel CFFT Pile", Canadian Journal of Civil Engineering, Vol. 33, No. 6, June, 2006(c).

Helmi, K., Mufti, A., and Fam, A. "Fatigue and Tensile Properties of Filament-Wound Tubes Used in Structural Applications" The Third International Conference on Construction Materials (ConMat'05), August 22nd-24th, 2005(b), Vancouver, Canada.

Hognestad, E. "A Study of Combined Bending and Axial Load in Reinforced Concrete Members." Bulletin Series No. 399, Engineering Experiment Station, University of Illinois, Urbana, III, 1951.

Holmen, J. "Fatigue of Concrete by Constant and Variable Amplitude Loading," Fatigue of Concrete Structures, ACI SP-75, Detroit, MI, 1982, pp. 71-110.

Howie, I. and Karbhari, V.M. "Effect of Two sheet composite Wrap Architecture on Strengthening of Concrete due to Confinement: I- Experimental Studies," *Journal of Reinforced Plastics and Composites*, Vol. 14, September, 1995, pp. 1804-1826.

Iskander, M. G., Hanna, S., and Stachula, A. "Drivability of FRP Composite Piling," *Journal of Geotechnical and Geoenvironmental Engineering*, Vol. 127, No. 2, 2001, pp: 169-176.

Jin, X. N., Pan J. L., Liu, G. Y., and Lai, W. H. "Research of Stress-Strain Curve of Concrete Confined by Fiber Reinforced Plastics Under Axial Compression." *Journal of Buildings and Structures*, Vol. 24, No. 4, 2003, pp. 47-53.

Kanatharana, J., and Lu, L.W. "Strength and Ductility of Concrete Columns Reinforced by FRP Tubes," *Proceeding of the First International Conference on Composites in Infrastructure ICCI'96, Tucson Arizona, USA*, Edited by H. Saadatmanesh and M.R. Ehsani, Jan., 1998, pp.370-384.

Karbhari, V. M., and Gao, Y. "Composite Jacketed Concrete Under Uniaxial Compression Verification of Simple Design Equations." *Journal of Materials in Civil Engineering*, Vol. 9, No. 4, 1997, pp. 185-193.

Karbhari, V.M., Seible, F., Burgueno, R., Davol, A., Wernli, M., and Zhao, L. "Structural Characterization of Fiber-Reinforced Composite Short and Medium-Span Bridge Systems," *Applied Composite Materials*, Vol. 7, 2000, pp. 151-182,

Koch, G., et al. "Corrosion Cost and Preventive Strategies in the United States," *Office of Infrastructure Research and Development, FHWA, Report No. FHWA-RD-01-156*, 2001, pp. 773.



Kong, Andrew "Freeze-Thaw Behaviour of Circular Concrete Members Confined by Fibre Reinforced Polymer Jackets when Simultaneously Subjected to Sustained Axial Loads", MSc Thesis, Queen's University, Kingston, ON, Canada, 2005.

Kurt, C.E. "Concrete Filled Structural Plastic Columns," Journal of the Structural Division, Vol. 104, No. ST1, Jan., 1978, pp. 55-63.

Lampo, R. "Federal Interest Gives Recycled Plastic Lumber a Leg up" ASTM Standardization News, pp. 26-31, 1996

Lancaster Composite, Inc. "Precast Composite Containment Pile, Part (1)," Technical Report, 1000 Huston Street, Colombia, PA.

Li, G., Torres, S., Alaywan, W., and Abadie, C. "Experimental Study of FRP Tube-encased Concrete Columns," Journal of Composite Materials, Vol. 39, No. 13, 2005, pp. 1131-1145.

Lillistone, D., and Jolly, C. K. "An Innovative Form of Reinforcement for Concrete Columns Using Advanced Composites." Structural Engineer, Vol. 78, No. 23/24, 2000, pp. 20-28.

Lowery, L.L. "Pile Driving Analysis by the Wave Equation. In: Microwave Program Manual," Texas A&M University, College Station, Texas, USA, 1993.

Mallick, P.K. "Fiber-reinforced Composites: Materials, Manufacturing, and Design" Marcel Dekker Inc. New York, 1988.

Mandal, S., and Fam, A. "Modeling of Prestressed Concrete-Filled Circular Composite Tubes Subjected to Bending and Axial Loads", Journal of Structural Engineering, Vol. 132, No. 3, 2006, pp. 449-459.

Mandal, S., Hoskin, A., and Fam, A. "Influence of Concrete Strength on Confinement Effectiveness of Fiber-Reinforced Polymer Circular Jackets", *ACI Structural Journal*, Vol. 102, No. 3, 2005, pp. 383-392.

Mandal, Siddhwartha "Prestressed Concrete-Filled FRP Tubes", MSc Thesis, Queen's University, Kingston, ON, Canada, 2004.

Mandell, J. F., Meier, U., "Effect of Stress Ratio, Frequency and Loading Time on the Tensile Fatigue of Glass-Reinforced Epoxy," *ASTM Special Technical Publication "Long-Term Behavior of Composites,"* ASTM STP 813, Ed. O'Brian, pp. 55-77, 1983.

Mander, J. B., Priestley, M. J. N., and Park, R. "Theoretical Stress-Strain Model for Confined Concrete," *Journal of Structural Engineering*, Vol. 114, No. 8, 1988, pp.1804-1826.

Mirmiran, A. and Shahawy, M. "A New Concrete-Filled Hollow PRP Composite Column," *Composites Part B*, Vol. 27, No. 3-4, 1996, pp. 263-268.

Mirmiran, A., Shahawy, M., and Beitleman, T. "Slenderness Limit for Hybrid FRP Concrete Columns," *Journal of Composites for Construction*, Vol. 5, No. 1, 2001, pp: 26-34.

Mirmiran, A., Shahawy, M., El Khoury, C., and Naguib, W. "Large Beam-Column Tests on Concrete-Filled Composite Tubes," *ACI Structural Journal*, Vol. 97, No. 2, 2000, pp: 268-276.

Mirmiran, A., Shahawy, M., Samaan, M., El Echary, H., Mastrapa, J. C., and Pico, O. "Effect of Column Parameters on FRP Confined Concrete," *Journal of Composites for Construction*, Vol. 2, No. 4, 1998, pp: 175-185.

Mirmiran, A., Shao, Y., and Shahawy, M. "Analysis and Field tests on the Performance of Composite Tubes under Pile Driving Impact," *Composite Structures*, Vol. 55, 2002, pp: 127-135.

Mirmiran, Amir, and Shahawy, Mohsen "Behavior of Concrete Columns Confined by Fiber Composites," *Journal Structural Engineering*, May, 1997, pp: 583-590.

Miyauchi, K., Nishibayashi, S., and Inoue, S. "Estimation of Strengthening Effects with Carbon Fiber Sheet for Concrete Column." *Proceedings of the 3rd International Symposium on Non-Metallic (FRP) Reinforcement for Concrete Structures (FRPRCS-3)*, Sapporo, Japan, Vol. 1, 1997, pp. 217-224.

Moran, D. A. and Pantelides, C. P. "Stress-Strain Model for Fiber-Reinforced Polymer-Confined Concrete." *Journal of Composites for Construction*, Vol. 6, No. 4, 2002, pp. 233-240.

Naguib, Wassim, and Mirmiran, Amir "Time-Dependant Behavior of Fiber- Reinforced Polymer-Confined Concrete Columns under Axial Loads," *ACI Structural Journal*, Vol. 99, No. 2, 2002, pp: 142-148.

Nanni, A., and Bradford, N. M. "FRP Jacketed Concrete under Uniaxial Compression." *Construction and Building Materials*, Vol. 9, No. 2, 1995, pp. 115-124.

Ogin, S., Smith, P., and Beaumont, P. "Matrix Cracking and Stiffness Reduction During the Fatigue of (0/90)s GFRP Laminate," *Composites Science and Technology*, Vol. 22, 1985, pp. 23-31.

Pando, M., Lesko, J., and Case, S. "Preliminary Development of a Durability Model for Concrete Filled FRP Piles," 46<sup>th</sup> International SAMPE Symposium, May 6-10, 2001, pp. 1597-1611.

Pantazoupolou, S. J. and Mills, R. H. "Microstructural Aspects of the Mechanical Responses of Plain Concrete." *ACI Structural Journal*, Vol. 92, No. 6, 1995, pp. 605-616.

Parvathaneni, H. K., Iyer, S. L., and Greenwood, M. "Design and Construction of Test Mooring Pile using Superprestressing," *Proceedings of Advanced Composite Materials in Bridges and Structures*, Montreal, 1996, pp. 313-324

Pile Dynamics, Inc. (PDI) "GRLWEAP Wave Equation Analysis of Pile Driving, User Manual," Cleveland, Ohio, 1998.

Richard, R. M. and Abbott, B. J. "Versatile Elastic-Plastic Stress-Strain Formula." *Journal of Engineering Mechanics Division ASCE*, Vol. 101, No. 4, 1975, pp. 511-515.

Saafi, M., Toutanji, H. A., and Li, Z "Behavior of Concrete Columns Confined with Fiber Reinforced Polymer Tubes." *ACI Materials Journal*, Vol. 96, No. 4, 1999, pp. 500-509.

Saff C. R., "Effect of load frequency and lay-up on fatigue life of Composites ASTM Special Technical Publication "Long-Term Behavior of Composites," ASTM STP 813, Ed. O'Brian, pp. 78-91, 1983.

Samaan, M., Mirmiran, A., and Shahawy, M. "Model of Concrete Confined by Fiber Composites", *Journal of Structural Engineering*, Vol. 124, No. 9, 1998, pp. 1025-1031.

Sargin, M. "Stress-Strain Relationship for Concrete and the Analysis of Structural Concrete Section." PhD thesis, University of Waterloo, Waterloo, Ontario, Canada, 1971.

- Scharpery, R. A., "Deformation and Failure Analysis of Viscoelastic Composite Materials," AMD-vol. 13. New York: ASME, 1975.
- Seible, F., Karbhari, V. M., and Burgueño, R., "Kings Stormwater Channel and I-5/Gilman Bridges," Structural Engineering International, Journal of the International Association for Bridge and Structural Engineering, Vol. 9, No. 4, November, 1999.
- Shao, Yutian, and Mirmiran, Amir "Nonlinear Cyclic Response of Laminated Glass FRP Tubes Filled with Concrete," Composite structures, Vol. 65, No. 1, 2004, pp: 91-101.
- Spoelstra, M. R., and Monti, G. "FRP-confined concrete model," Journal of Composites for Construction, Vol. 3, No. 3, 1999, pp. 143-150.
- Sun, C. T. and Chan, W. S., "Frequency Effect on the Fatigue Life of a Laminated Composites," ASTM Special Technical Publication, ASTM STP 674, pp. 418-30, 1979.
- Taylor, R.L. "FEAP- A Finite Element Analysis Program. Manual," Department of Civil Engineering, University of California, Berkeley, CA, 1998.
- Teng, J.G., and Lam, L. "Behavior and Modeling of Fiber Reinforced Polymer-Confined Concrete", Journal of Structural Engineering, Vol. 130, No. 11, 2004, pp. 1713-1723
- Toutanji, H. A. "Stress-strain Characteristics of Concrete Columns Externally Confined with Advanced Fiber Composite Sheets." ACI Materials Journal, Vol. 96, No. 3, 1999, pp. 397-404.
- Toutanji, Houssam and Saafi, Mohamed "Durability Studies on Concrete Columns Encased in PVC-FRP Composite Tubes," Composite Structures, Vol. 54, 2001, pp. 27-35.

Wernli, M. and Seible, F. "Ductile Connections of Modular Bridge Girders Made of Concrete Filled FRP-Tubes," Second International Conference on Composites in Infrastructure, Tucson, Arizona, January 1998, pp. 356–369.

Xiao, Y, and Wu, H. "Compressive Behavior of Concrete Confined by Carbon Fiber Composite Jackets." *Journal of Materials in Civil Engineering*, Vol. 12, No. 2, 2000, pp. 139-146.

Xiao, Y, and Wu, H. "Compressive Behavior of Concrete Confined by Various Types of FRP Composites Jackets." *Journal of Reinforced Plastic Composites*, Vol. 22, No. 13, 2003, pp. 1187-1202.

Yu, Q. "A Study on the Stress-Strain Relationship of FRP-Confined Concrete in Axial Compression." *Industrial Construction*, Vol. 31, No. 4, 2001, pp. 5-8.

Yu, T., Wong, Y. L., Teng, J. G., Dong, S. L., and Lam, E. S. S., "Flexural Behavior of Hybrid FRP-Concrete-Steel Double-Skin Tubular Members," *Journal of Composites for Construction*, Vol. 10, No.5, 2006, pp.443-452.

Zhao, L., Sikorsky, C.S., Seible, F., and Karbhari, V.M. "Field Monitoring of the Kings Stormwater Channel Advanced Composite Bridge," 6<sup>th</sup> Caltrans Seismic Research Workshop, California Department of Transportation, Sacramento, California, June, 2001.

Zhenyu Zhu. "Joint Construction and Seismic Performance of Concrete-Filled Fiber Reinforced Polymer Tubes," Ph.D. Thesis, North Carolina State University, Raleigh, NC, 2004, pp. 215.

## Appendix A

## Results of Parametric Study

The effect of the time dependant properties of the materials

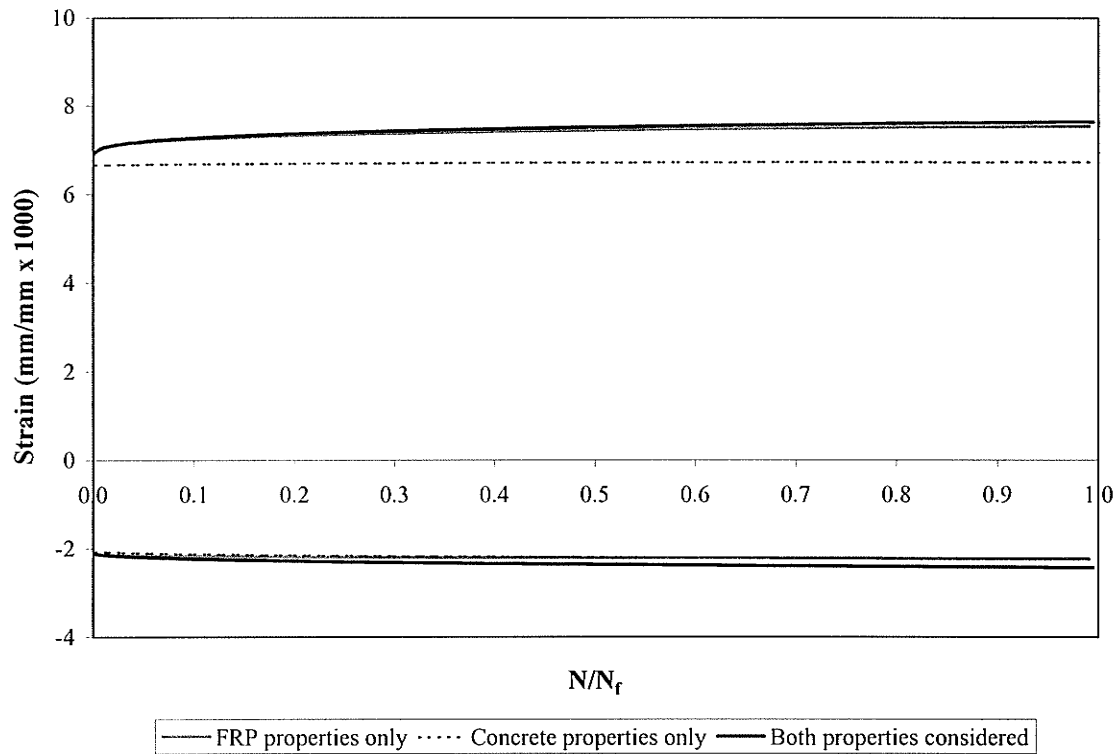


Figure A-1 Effect of the time dependant properties of the materials on the strain behavior ( $D_t = 256 - M_{max}/M_{ult} = 50\% - f = 1\text{Hz}$ )

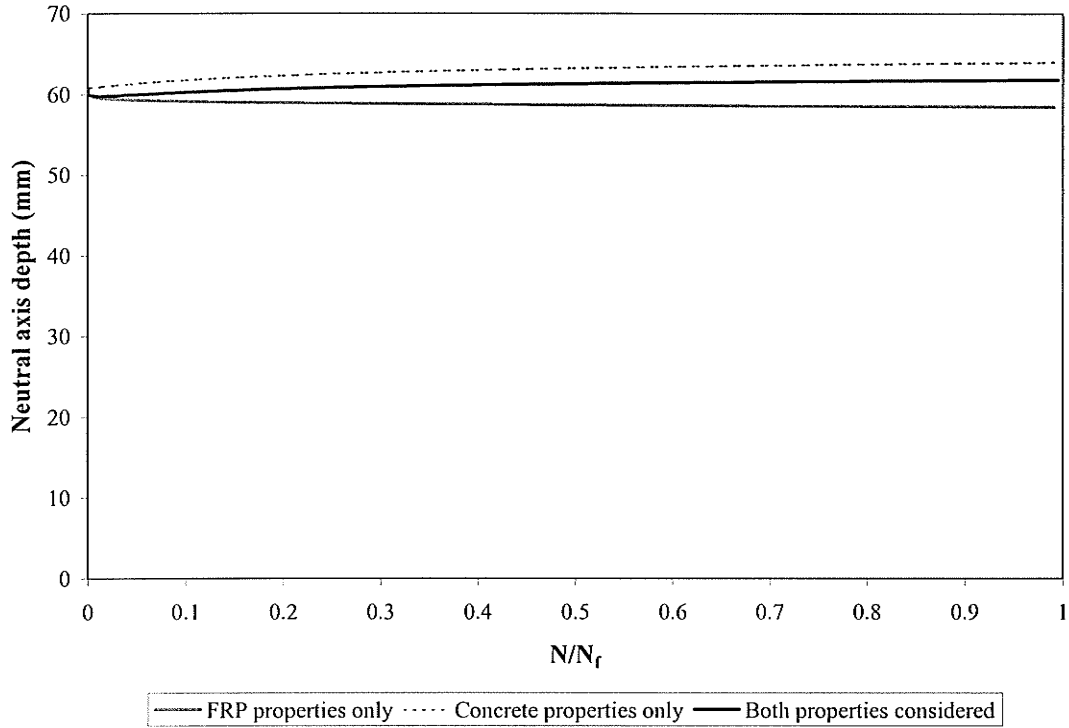


Figure A-2 Effect of the time dependant properties of the materials on the depth of the neutral axis ( $D_t=256 - M_{max}/M_{ult} = 50\% - f = 1\text{Hz}$ )

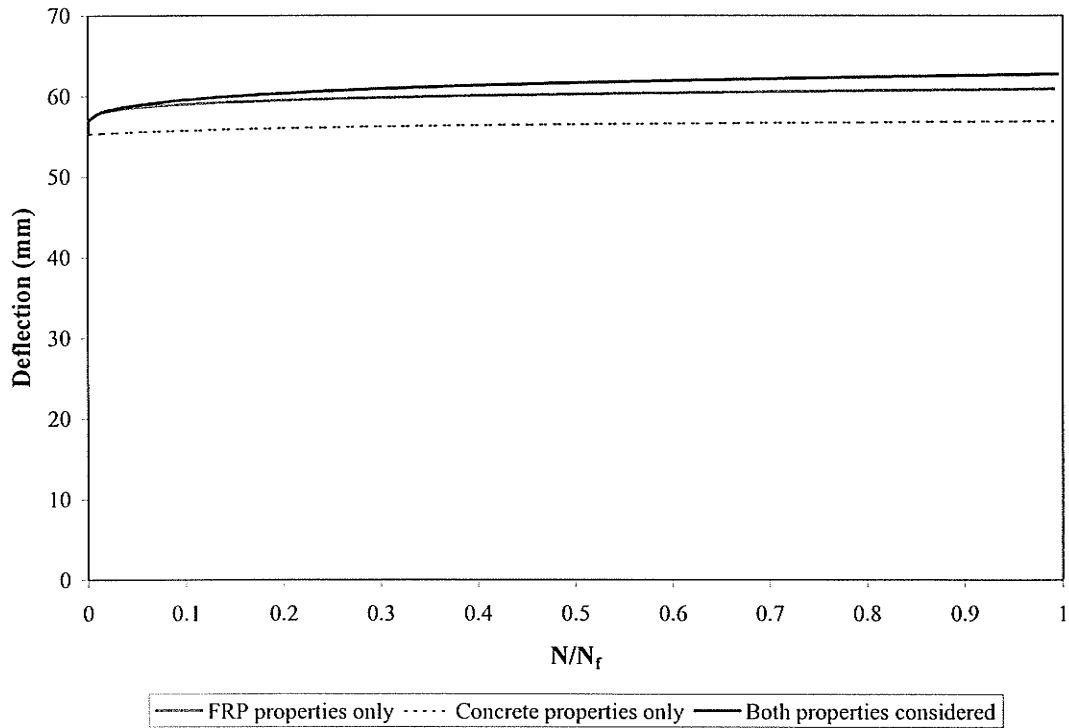


Figure A-3 Effect of the time dependant properties of the materials on the midspan deflection ( $D_t=256 - M_{max}/M_{ult} = 50\% - f = 1\text{Hz}$ )



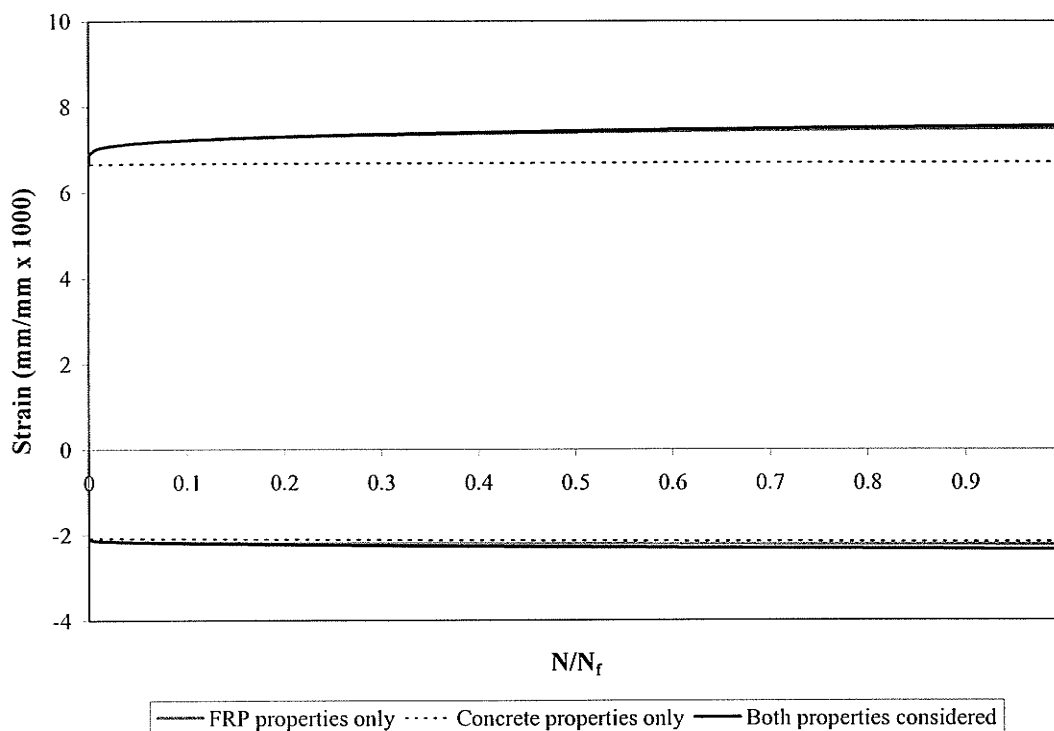


Figure A-4 Effect of the time dependant properties of the materials on the strain behavior ( $D_t=256 - M_{max}/M_{ult} = 50\% - f = 5\text{Hz}$ )

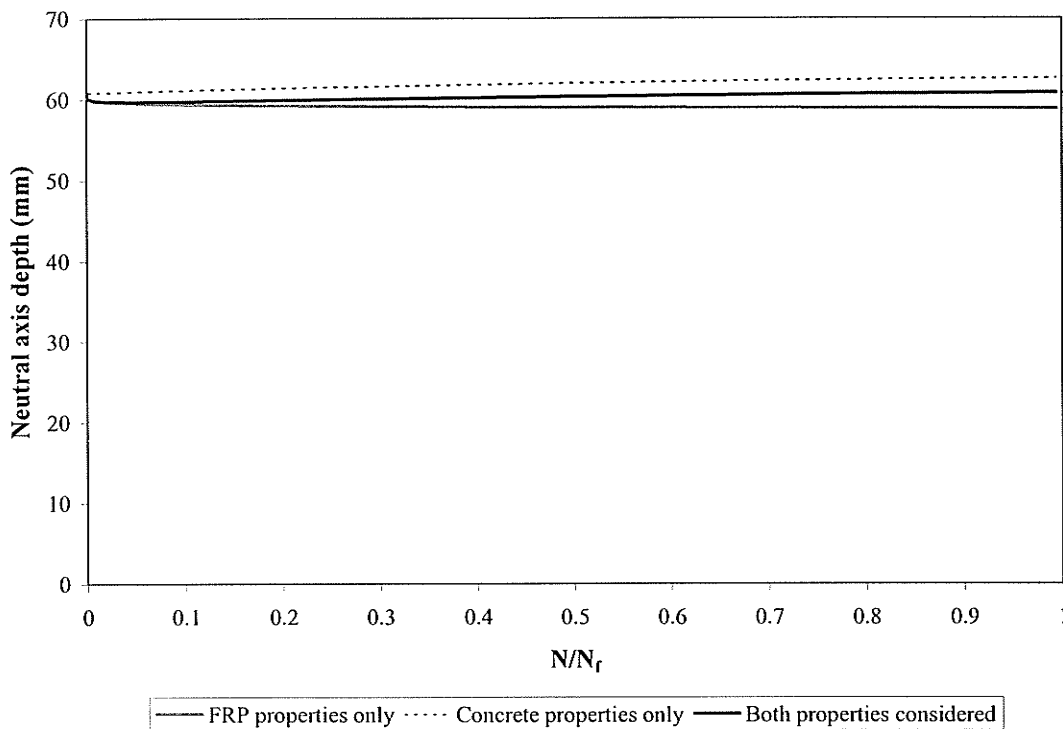


Figure A-5 Effect of the time dependant properties of the materials on the depth of the neutral axis ( $D_t=256 - M_{max}/M_{ult} = 50\% - f = 5\text{Hz}$ )

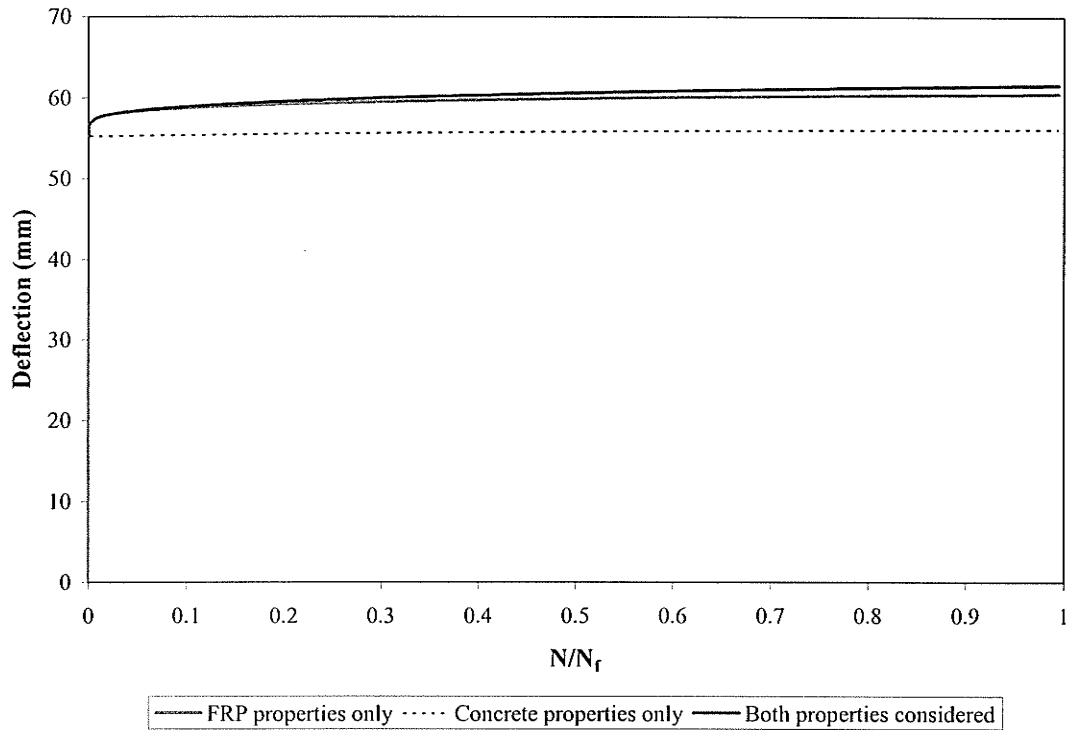


Figure A-6 Effect of the time dependant properties of the materials on the midspan deflection ( $D_t=256 - M_{max}/M_{ult} = 50\% - f = 5\text{Hz}$ )

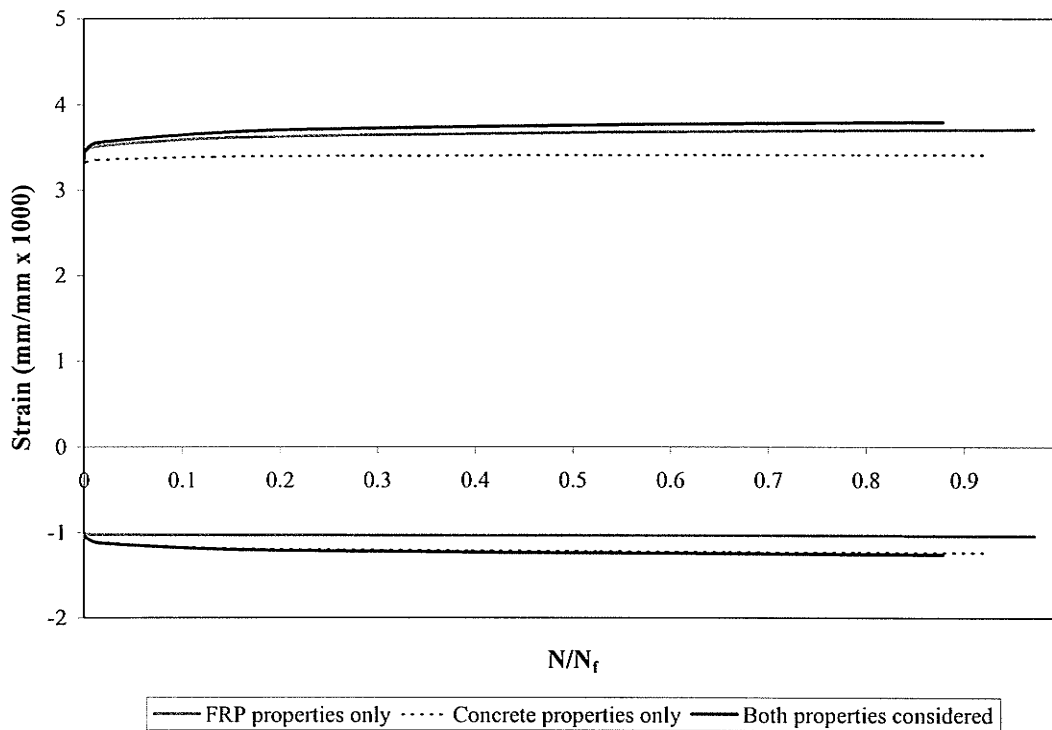


Figure A-7 Effect of the time dependant properties of the materials on the strain behavior ( $D_t=256 - M_{max}/M_{ult} = 25\% - f = 1\text{Hz}$ )

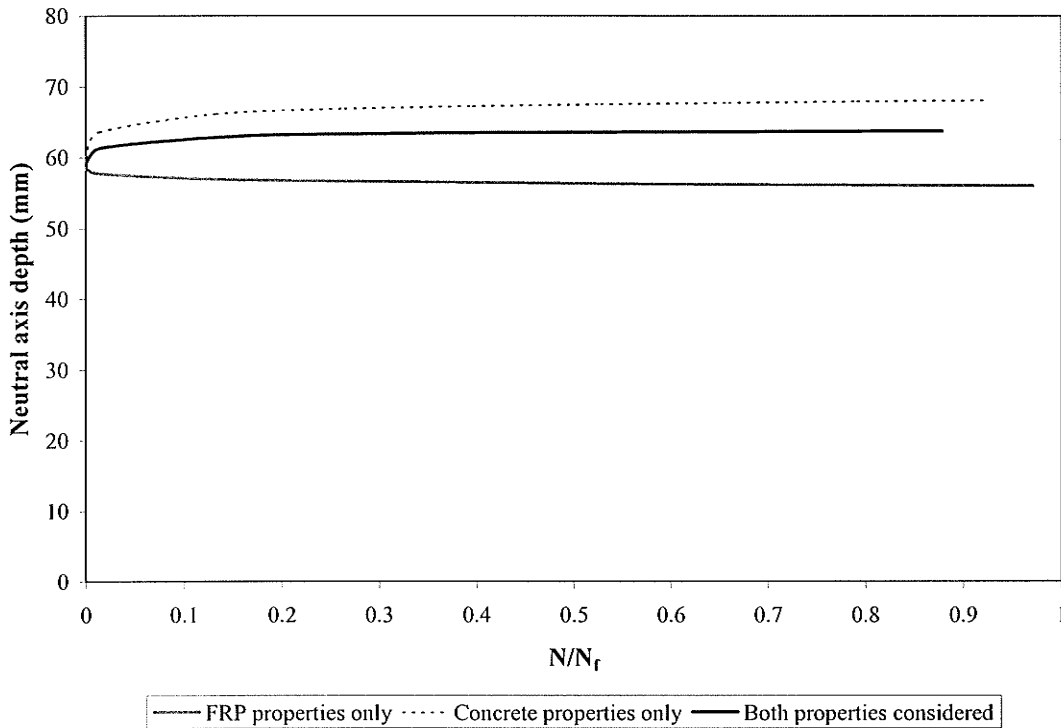


Figure A-8 Effect of the time dependant properties of the materials on the depth of the neutral axis ( $D_t = 256 - M_{max}/M_{ult} = 25\% - f = 1\text{Hz}$ )

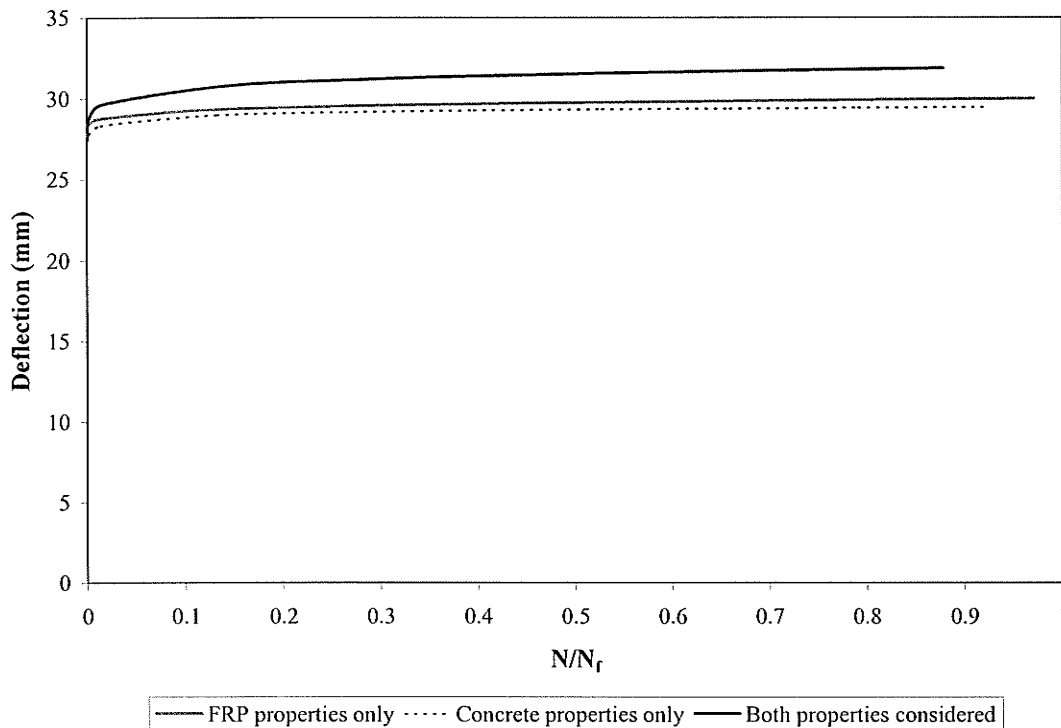


Figure A-9 Effect of the time dependant properties of the materials on the midspan deflection ( $D_t = 256 - M_{max}/M_{ult} = 25\% - f = 1\text{Hz}$ )

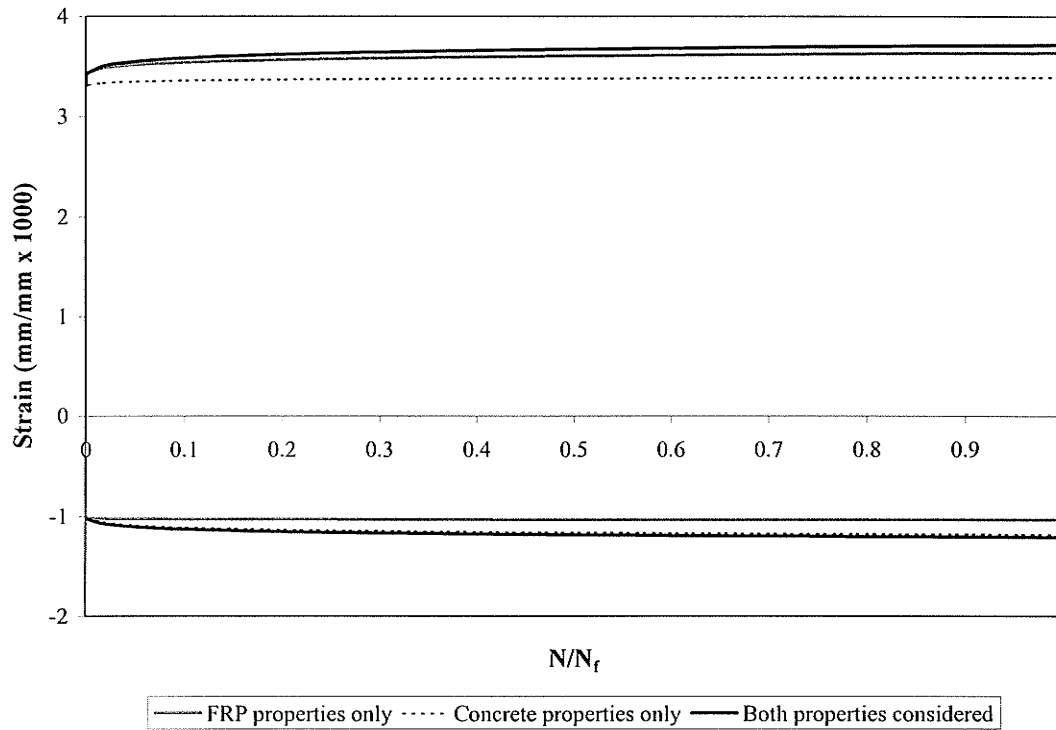


Figure A-10 Effect of the time dependant properties of the materials on the strain behavior ( $D_t=256 - M_{max}/M_{ult} = 25\% - f = 5\text{Hz}$ )

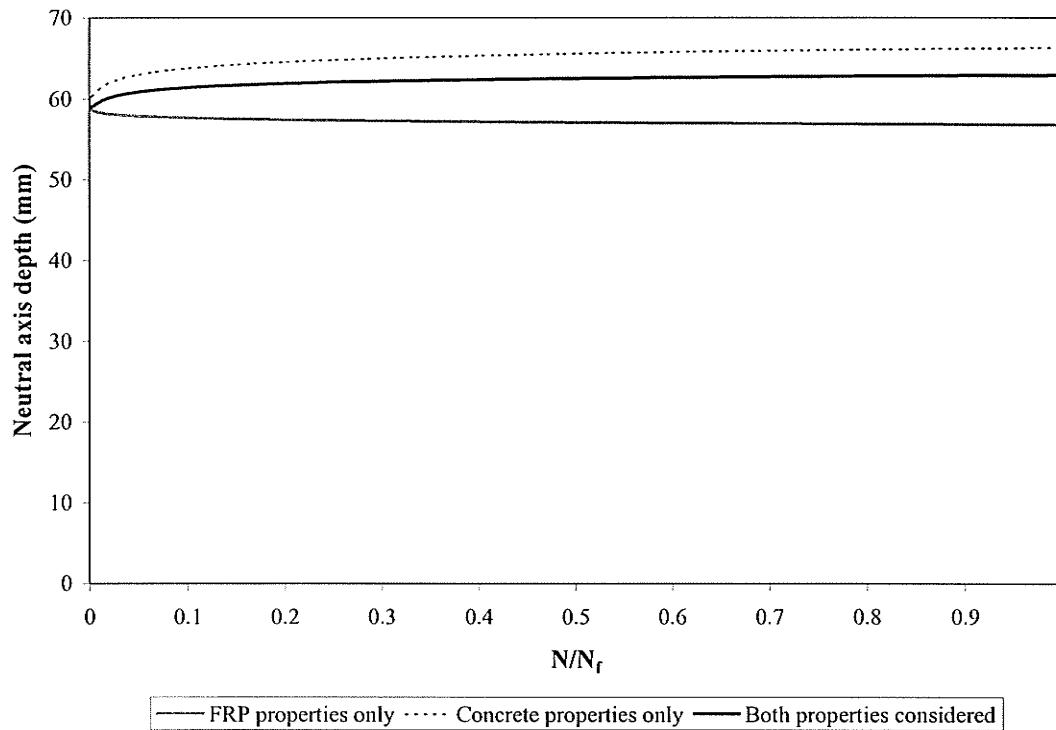


Figure A-11 Effect of the time dependant properties of the materials on the depth of the neutral axis ( $D_t=256 - M_{max}/M_{ult} = 25\% - f = 5\text{Hz}$ )

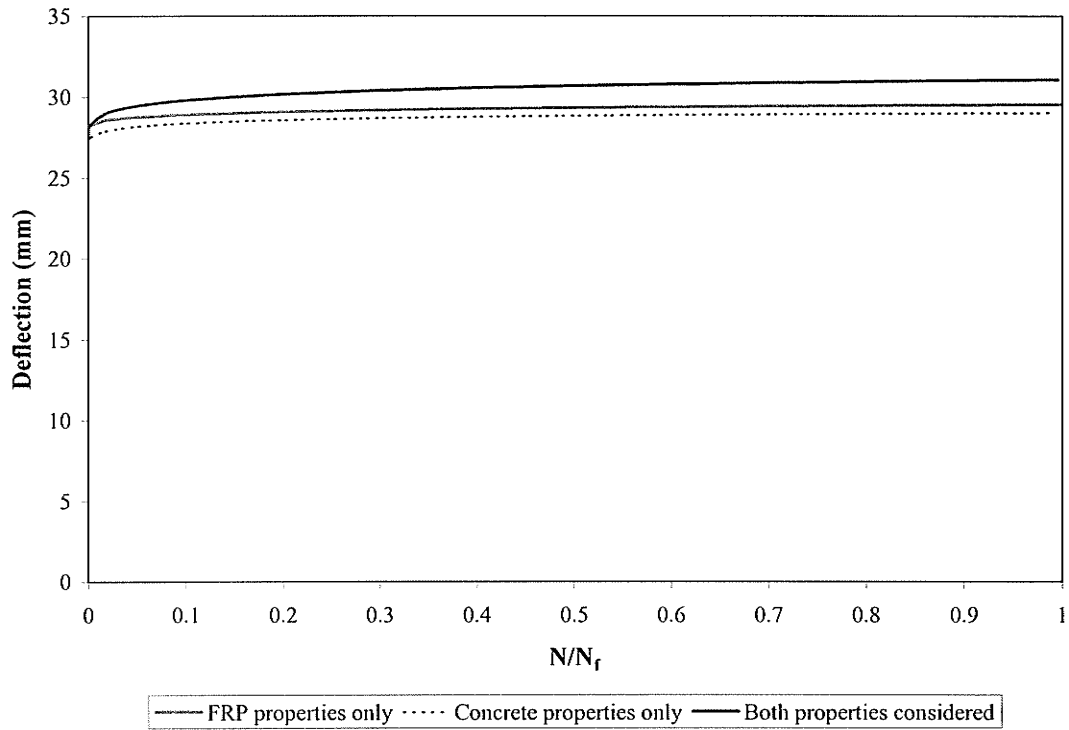


Figure A-12 Effect of the time dependant properties of the materials on the midspan deflection ( $D_t = 256 - M_{max}/M_{ult} = 25\% - f = 5\text{Hz}$ )

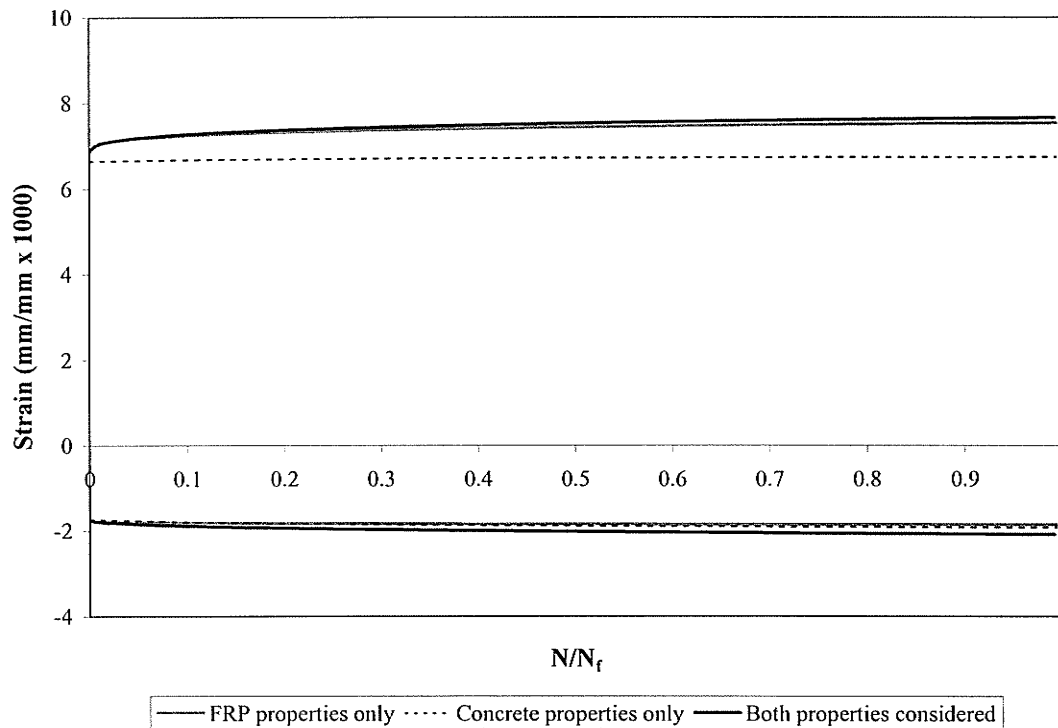


Figure A-13 Effect of the time dependant properties of the materials on the strain behavior ( $D_t = 367 - M_{max}/M_{ult} = 50\% - f = 1\text{Hz}$ )

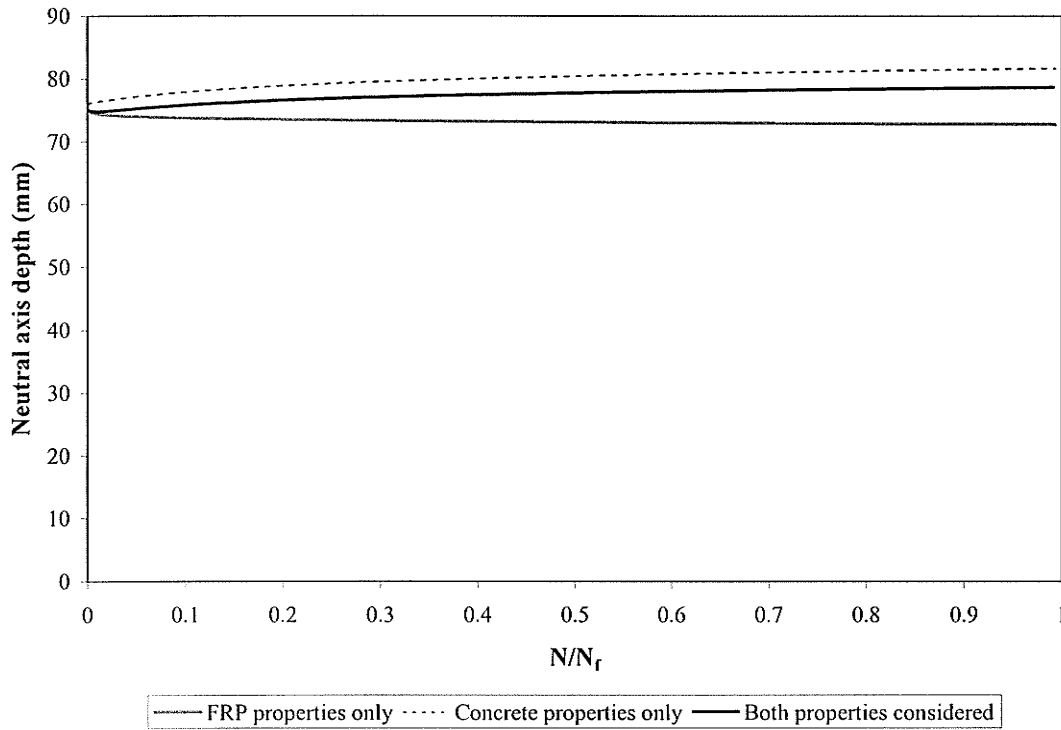


Figure A-14 Effect of the time dependant properties of the materials on the depth of the neutral axis ( $D_t = 367 - M_{max}/M_{ult} = 50\% - f = 1\text{Hz}$ )

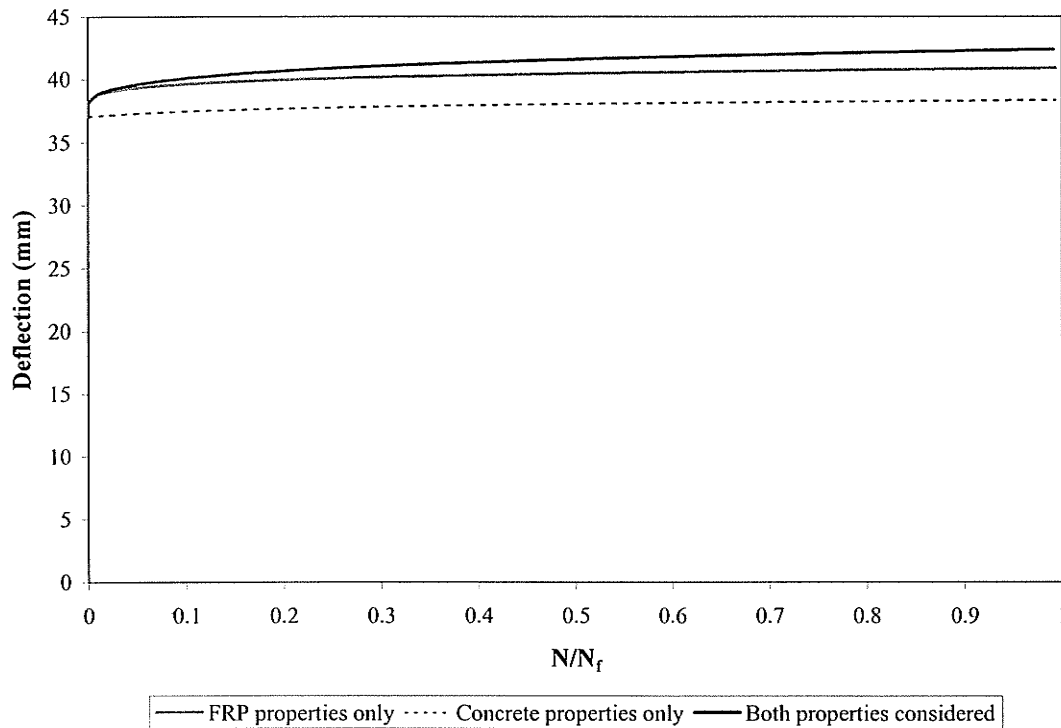


Figure A-15 Effect of the time dependant properties of the materials on the midspan deflection ( $D_t = 367 - M_{max}/M_{ult} = 50\% - f = 1\text{Hz}$ )

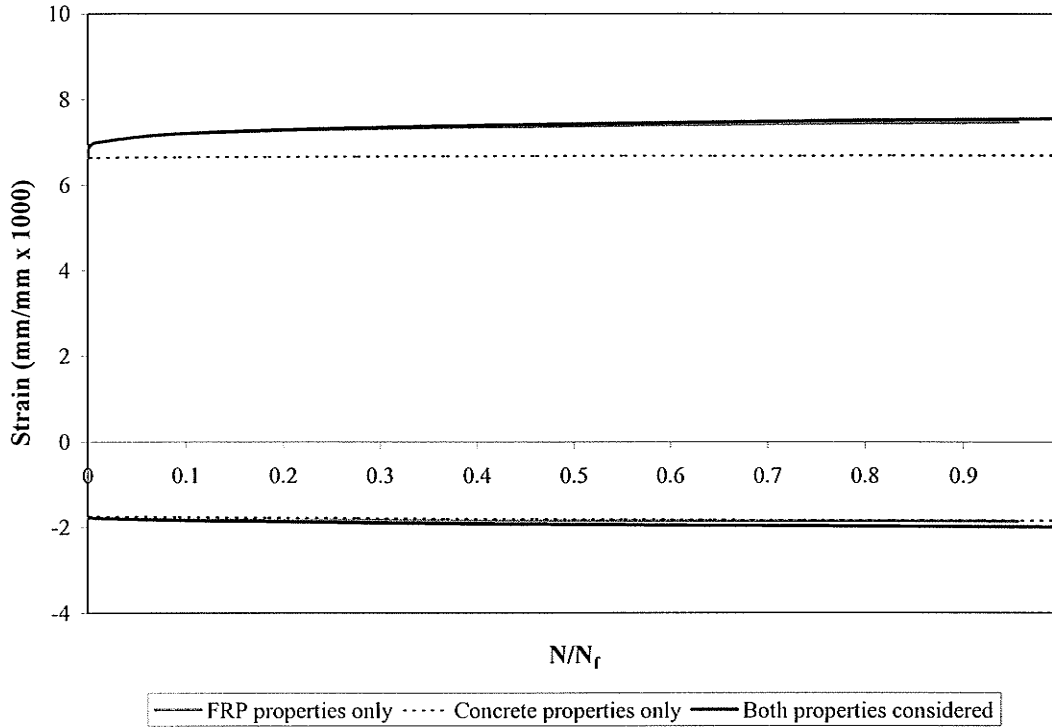


Figure A-16 Effect of the time dependant properties of the materials on the strain behavior ( $D_t = 367 - M_{max}/M_{ult} = 50\% - f = 5\text{Hz}$ )

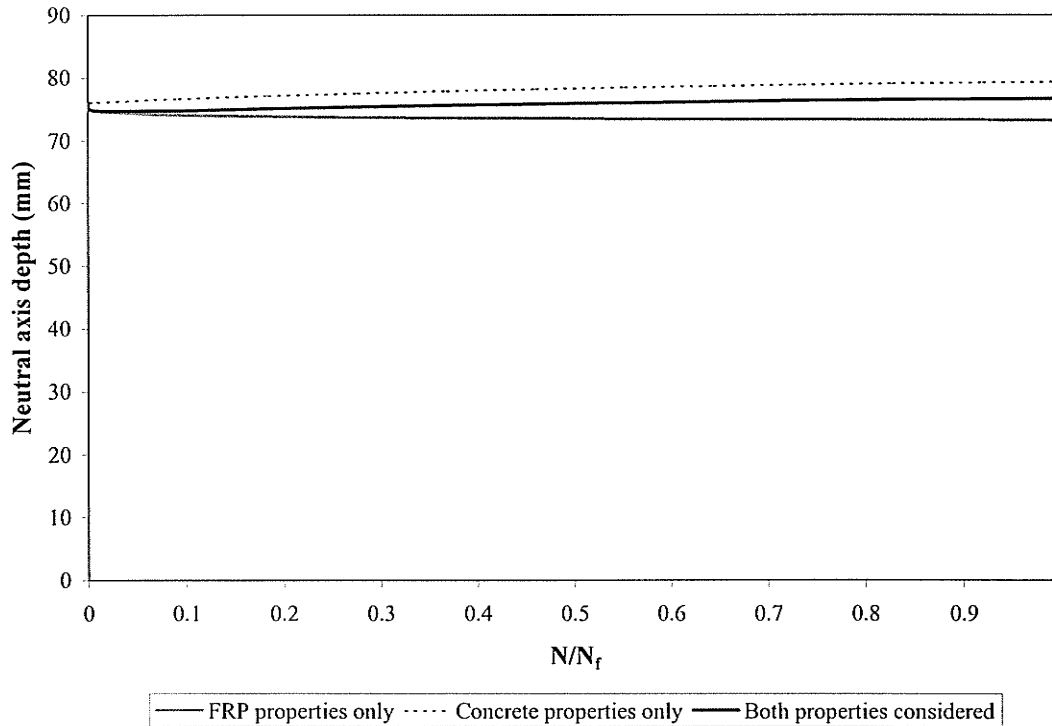


Figure A-17 Effect of the time dependant properties of the materials on the depth of the neutral axis ( $D_t = 367 - M_{max}/M_{ult} = 50\% - f = 5\text{Hz}$ )

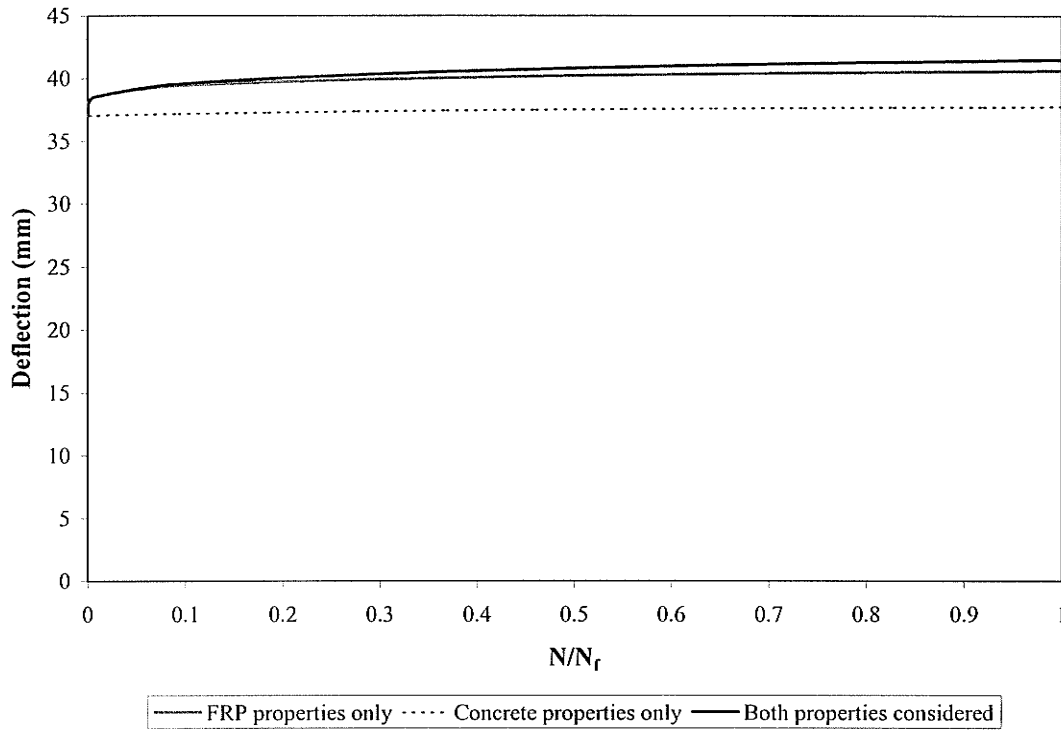


Figure A-18 Effect of the time dependant properties of the materials on the midspan deflection ( $D_t=367 - M_{max}/M_{ult} = 50\% - f = 5\text{Hz}$ )

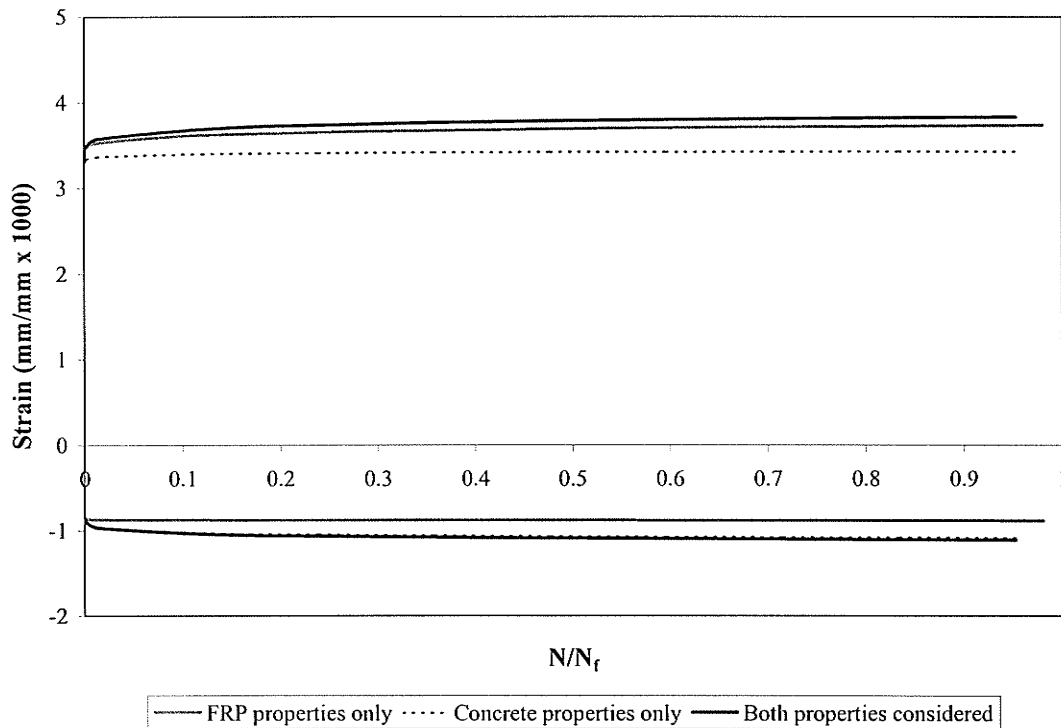


Figure A-19 Effect of the time dependant properties of the materials on the strain behavior ( $D_t=367 - M_{max}/M_{ult} = 25\% - f = 1\text{Hz}$ )



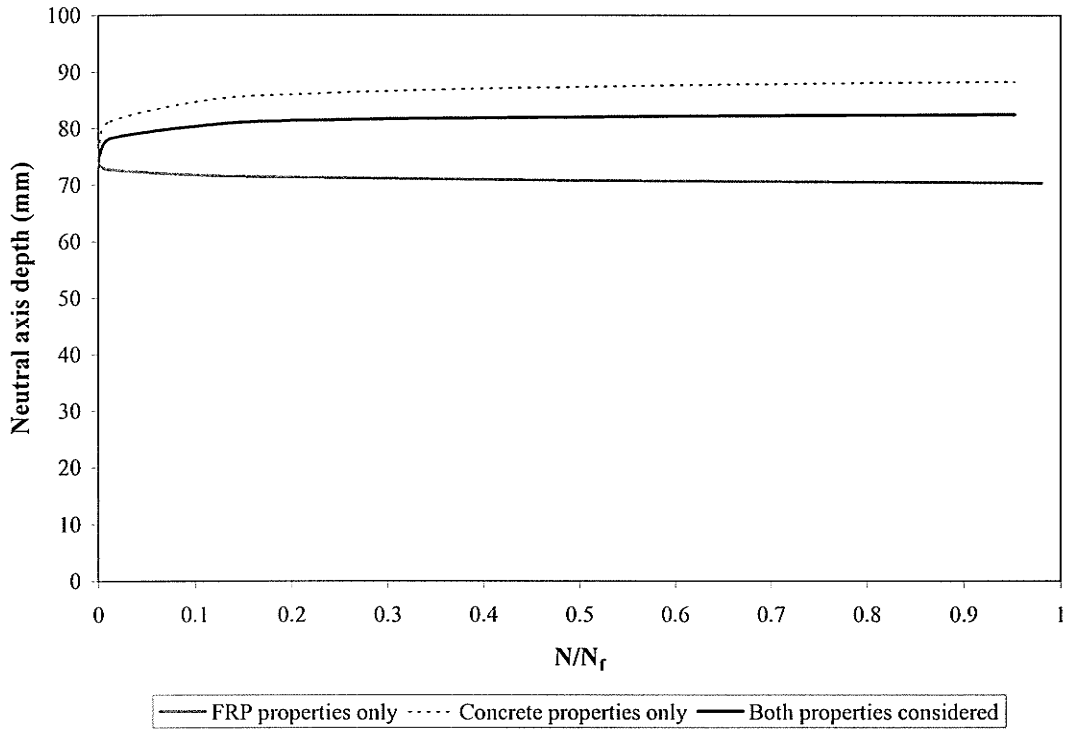


Figure A-20 Effect of the time dependant properties of the materials on the depth of the neutral axis ( $D_t = 367 - M_{max}/M_{ult} = 25\% - f = 1\text{Hz}$ )

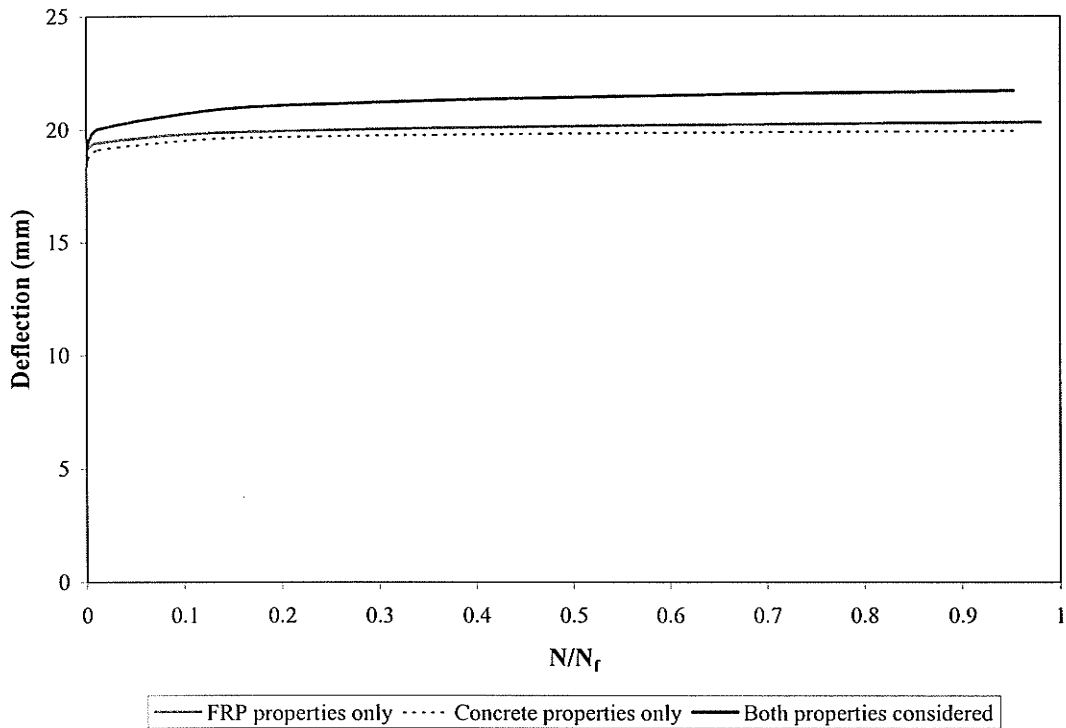


Figure A-21 Effect of the time dependant properties of the materials on the midspan deflection ( $D_t = 367 - M_{max}/M_{ult} = 25\% - f = 1\text{Hz}$ )

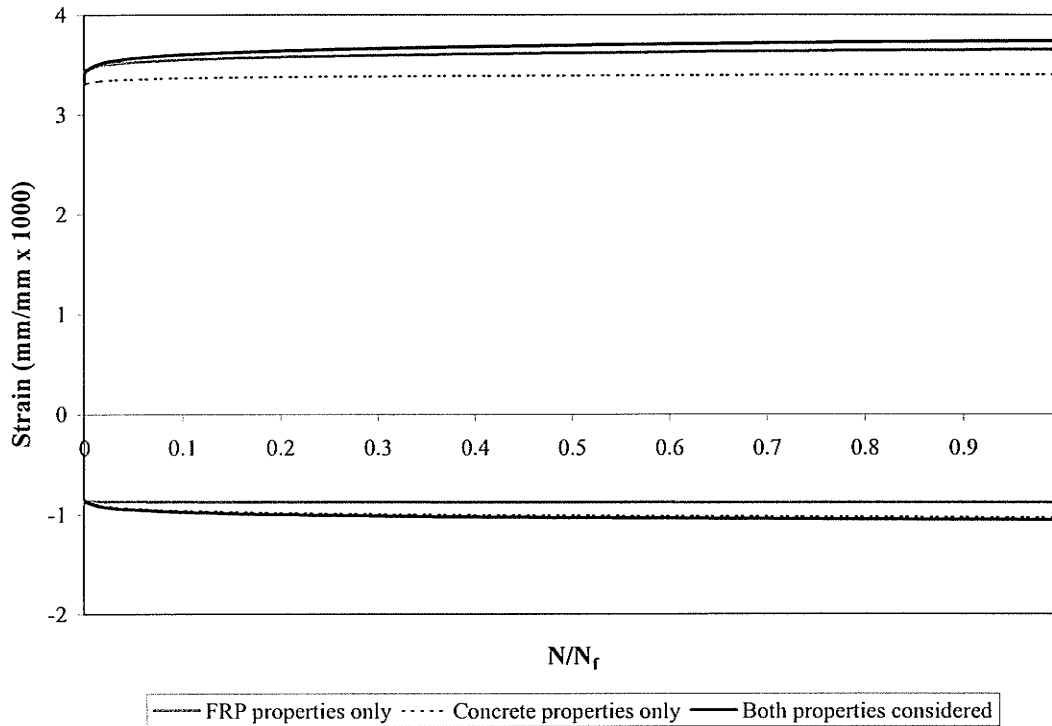


Figure A-22 Effect of the time dependant properties of the materials on the strain behavior ( $D_t = 367 - M_{max}/M_{ult} = 25\% - f = 5\text{Hz}$ )

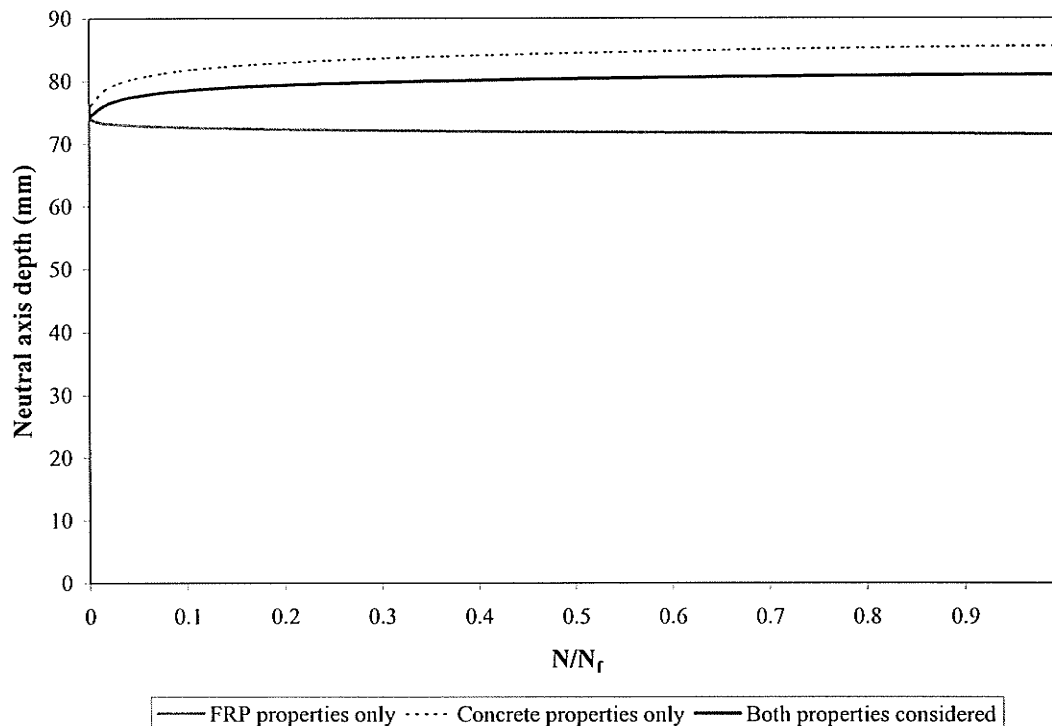


Figure A-23 Effect of the time dependant properties of the materials on the depth of the neutral axis ( $D_t = 367 - M_{max}/M_{ult} = 25\% - f = 1\text{Hz}$ )

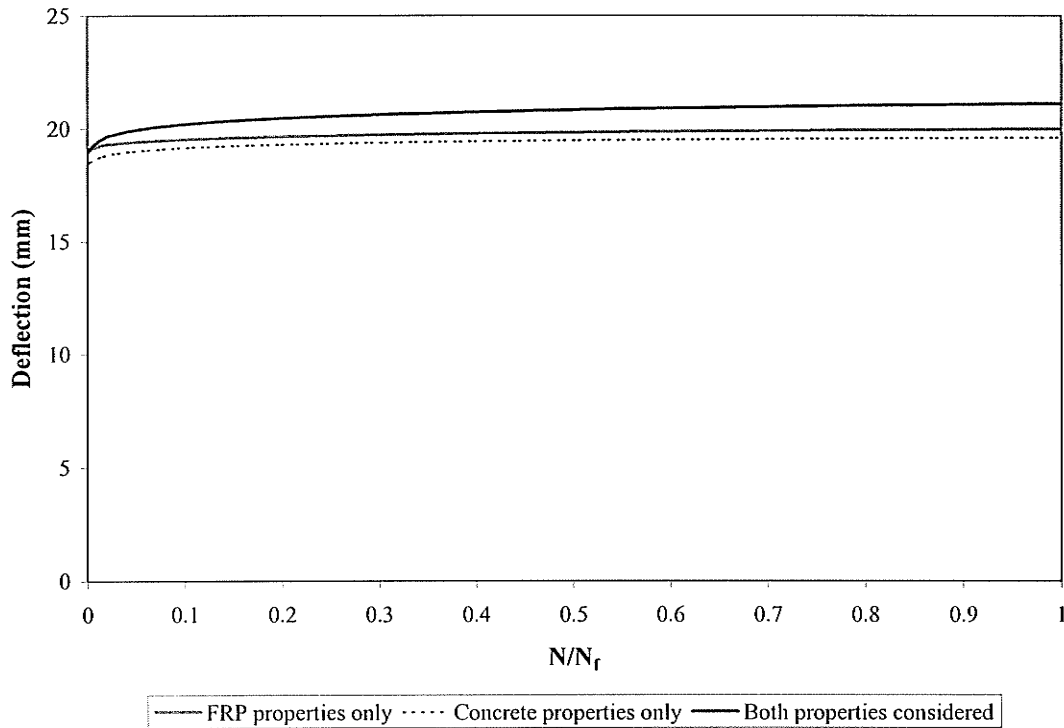


Figure A-24 Effect of the time dependant properties of the materials on the midspan deflection ( $D_t=367 - M_{max}/M_{ult} = 25\% - f = 1\text{Hz}$ )

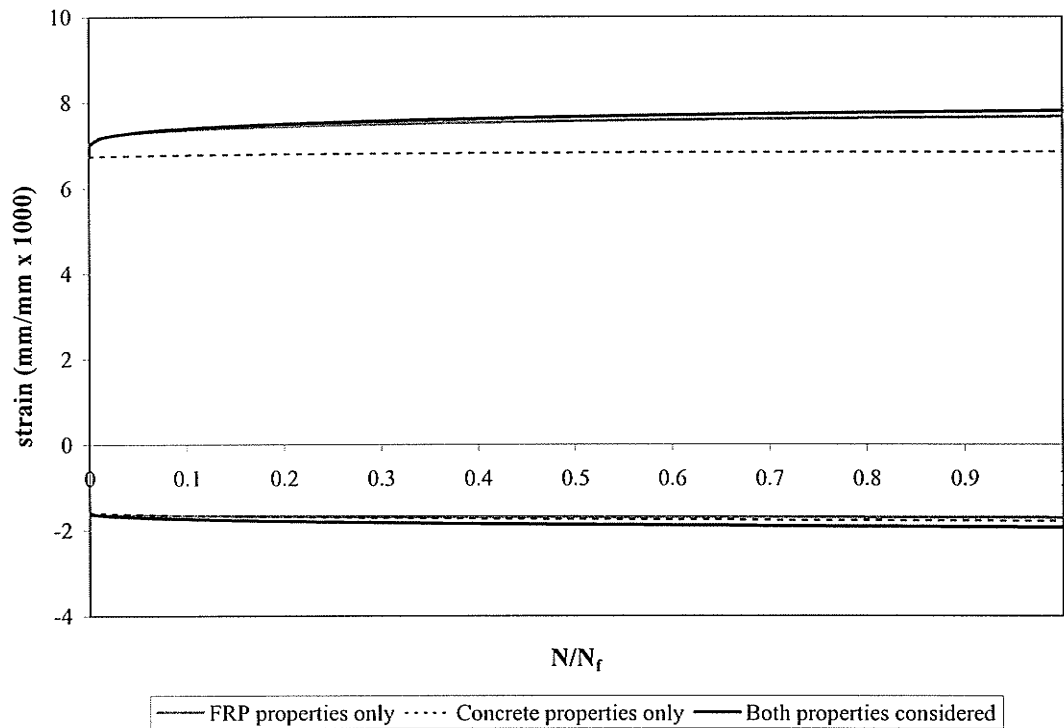


Figure A-25 Effect of the time dependant properties of the materials on the strain behavior ( $D_t=456 - M_{max}/M_{ult} = 50\% - f = 1\text{Hz}$ )

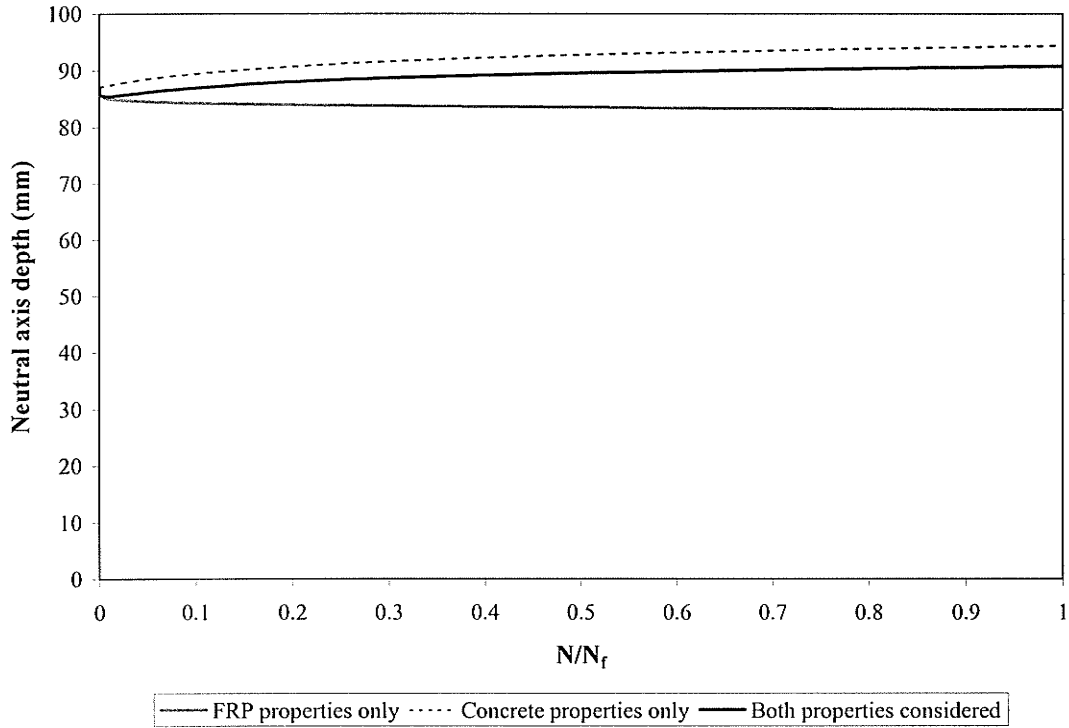


Figure A-26 Effect of the time dependant properties of the materials on the depth of the neutral axis ( $D_t = 456 - M_{max}/M_{ult} = 50\% - f = 1\text{Hz}$ )

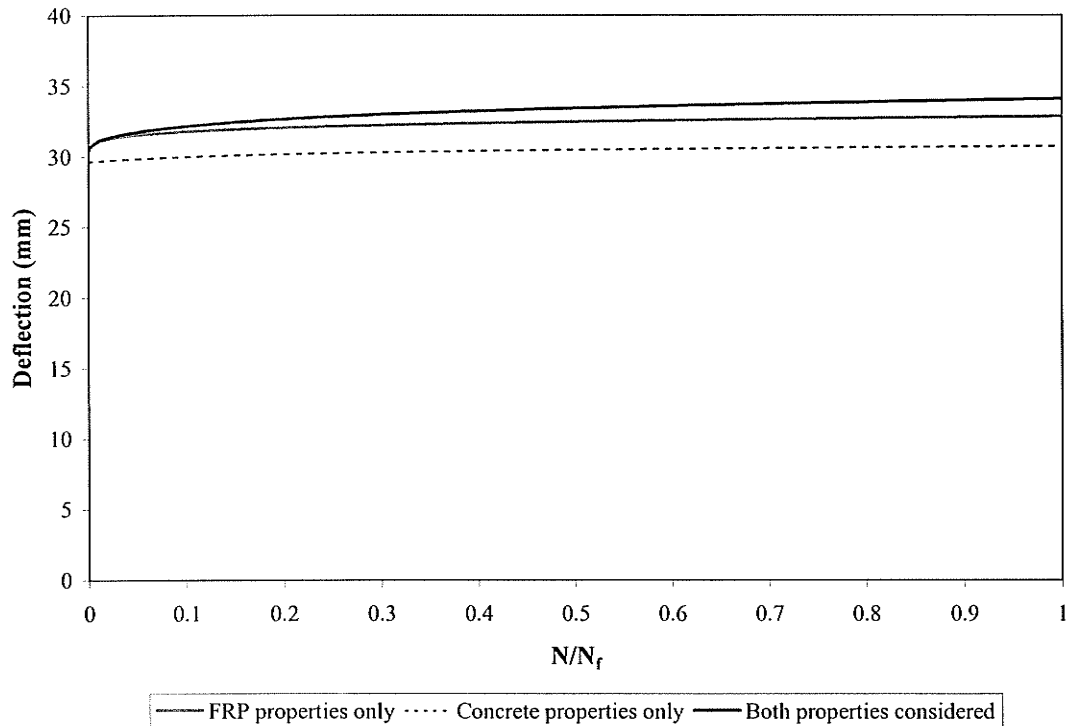


Figure A-27 Effect of the time dependant properties of the materials on the midspan deflection ( $D_t = 456 - M_{max}/M_{ult} = 50\% - f = 1\text{Hz}$ )

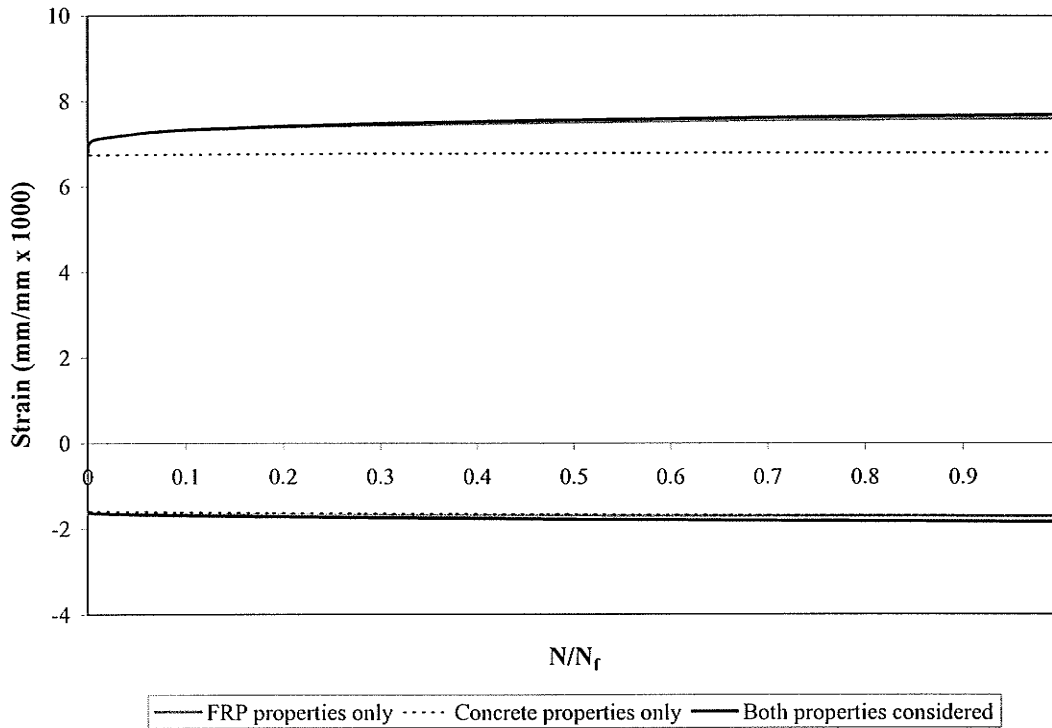


Figure A-28 Effect of the time dependant properties of the materials on the strain behavior ( $D_t = 456 - M_{max}/M_{ult} = 50\% - f = 5\text{Hz}$ )

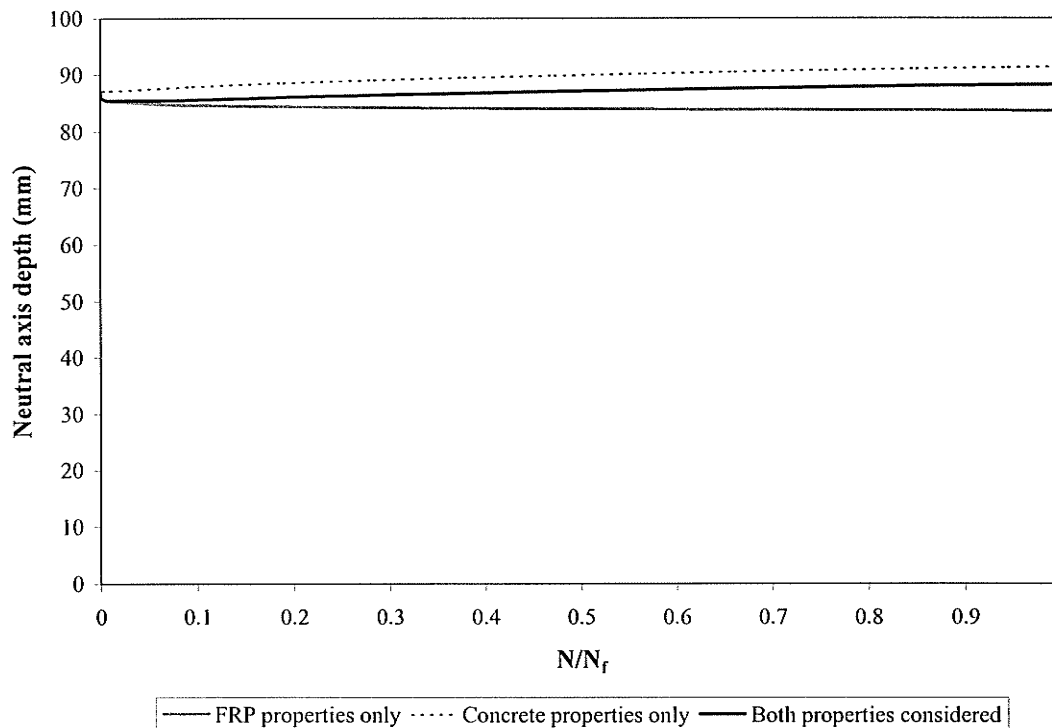


Figure A-29 Effect of the time dependant properties of the materials on the depth of the neutral axis ( $D_t = 456 - M_{max}/M_{ult} = 50\% - f = 5\text{Hz}$ )

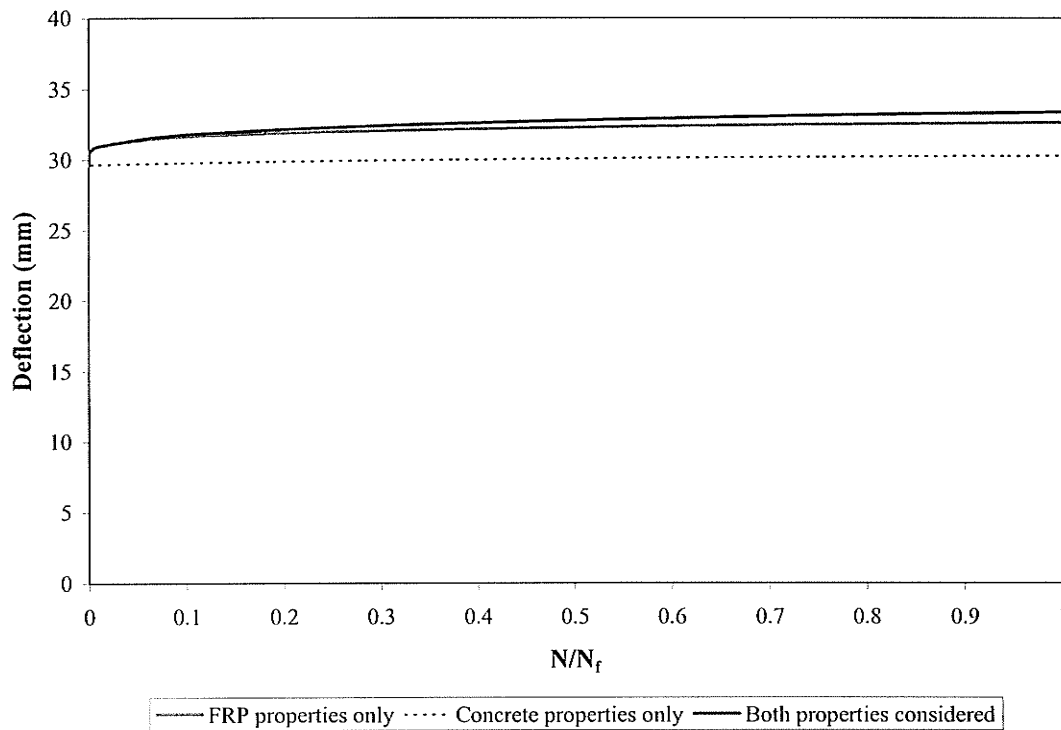


Figure A-30 Effect of the time dependant properties of the materials on the midspan deflection ( $D_t=456 - M_{max}/M_{ult} = 50\% - f = 5\text{Hz}$ )

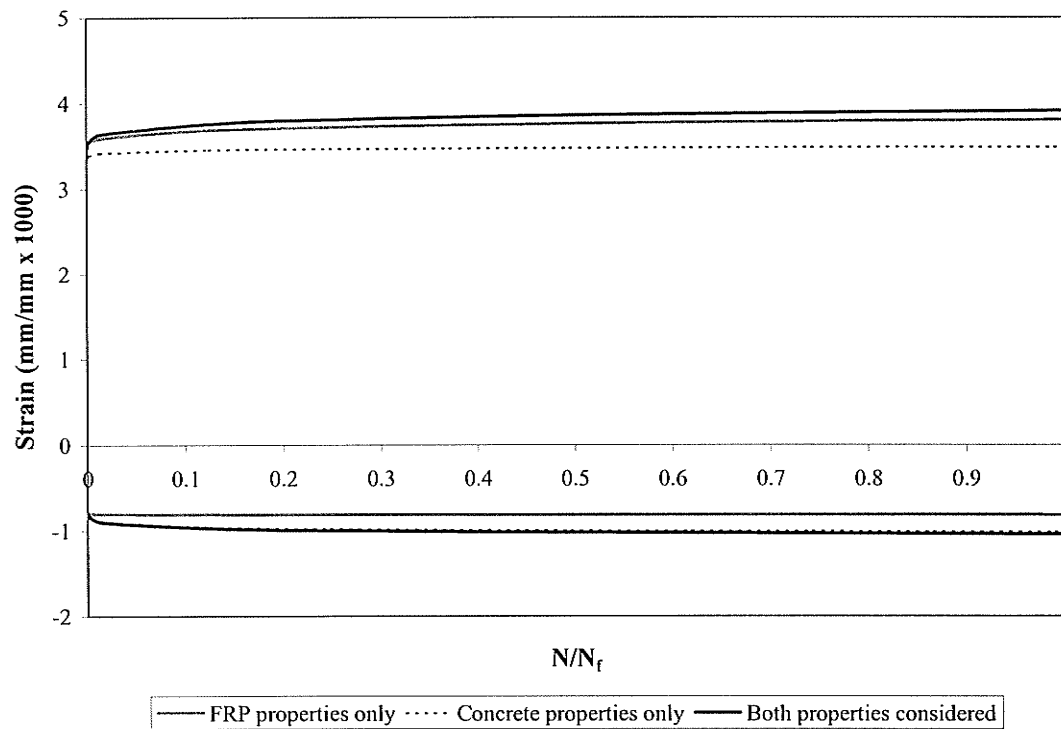


Figure A-31 Effect of the time dependant properties of the materials on the strain behavior ( $D_t=456 - M_{max}/M_{ult} = 25\% - f = 1\text{Hz}$ )

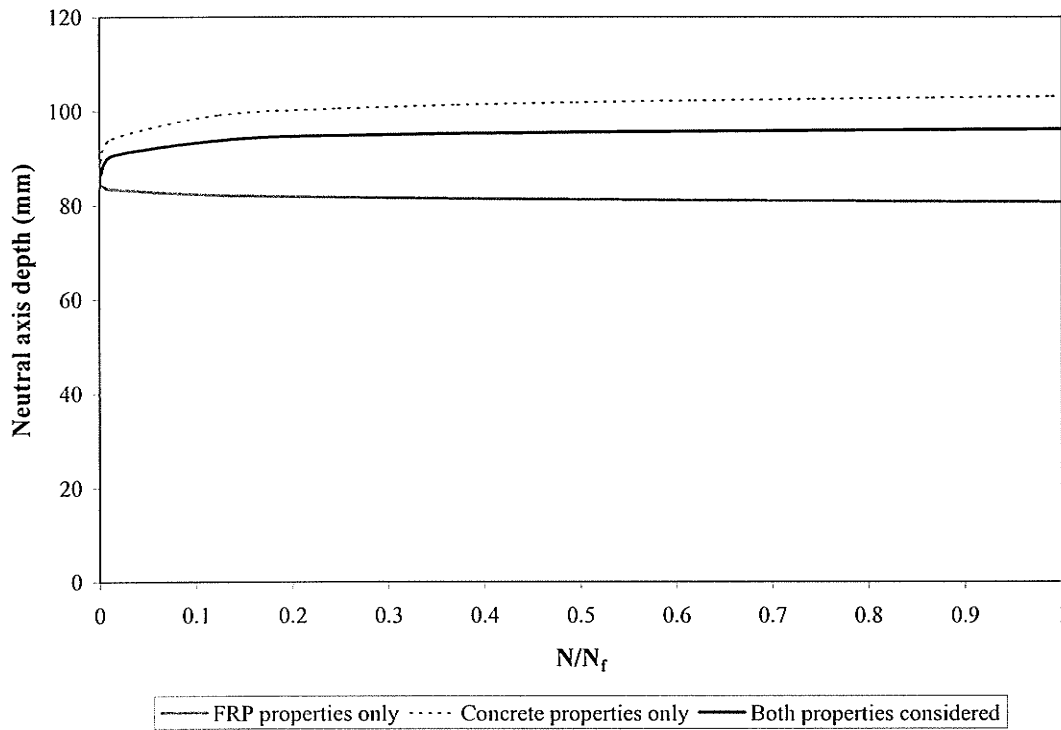


Figure A-32 Effect of the time dependant properties of the materials on the depth of the neutral axis ( $D_t = 456 - M_{max}/M_{ult} = 25\% - f = 1\text{Hz}$ )

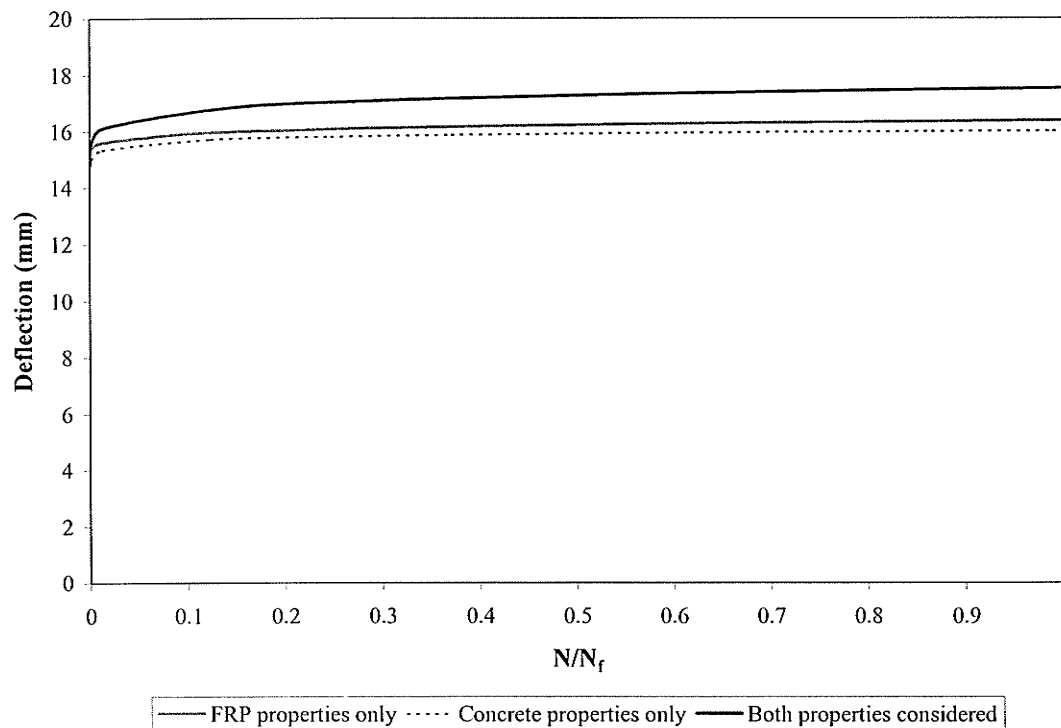


Figure A-33 Effect of the time dependant properties of the materials on the midspan deflection ( $D_t = 456 - M_{max}/M_{ult} = 25\% - f = 1\text{Hz}$ )

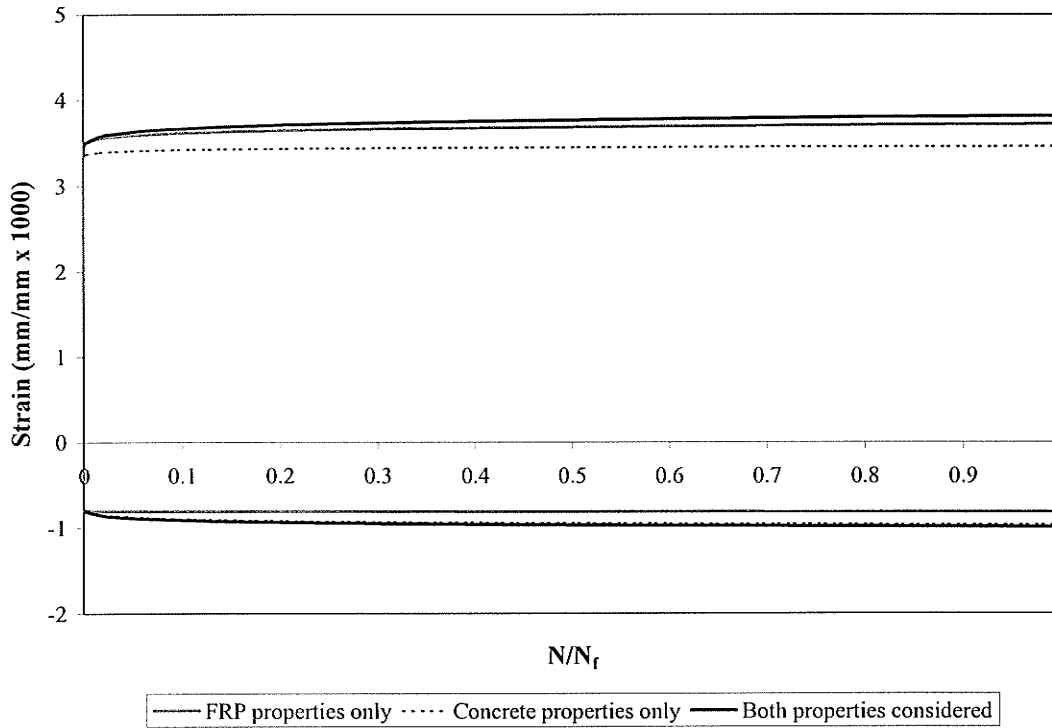


Figure A-34 Effect of the time dependant properties of the materials on the strain behavior ( $D_t=456 - M_{max}/M_{ult} = 25\% - f = 5\text{Hz}$ )

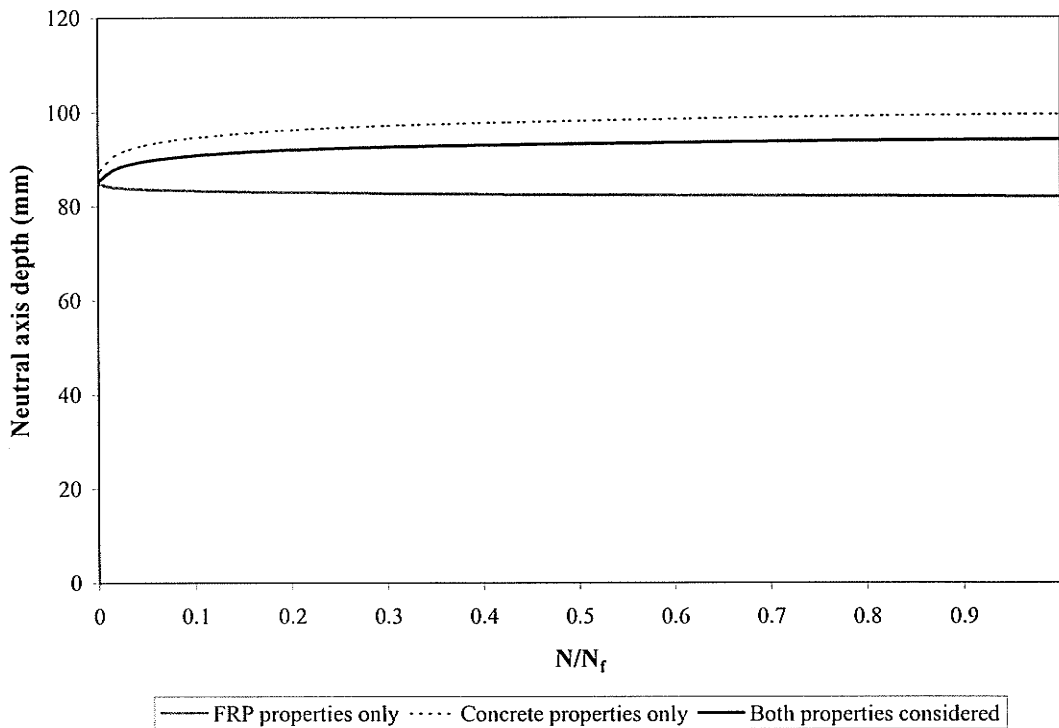


Figure A-35 Effect of the time dependant properties of the materials on the depth of the neutral axis ( $D_t=456 - M_{max}/M_{ult} = 25\% - f = 5\text{Hz}$ )



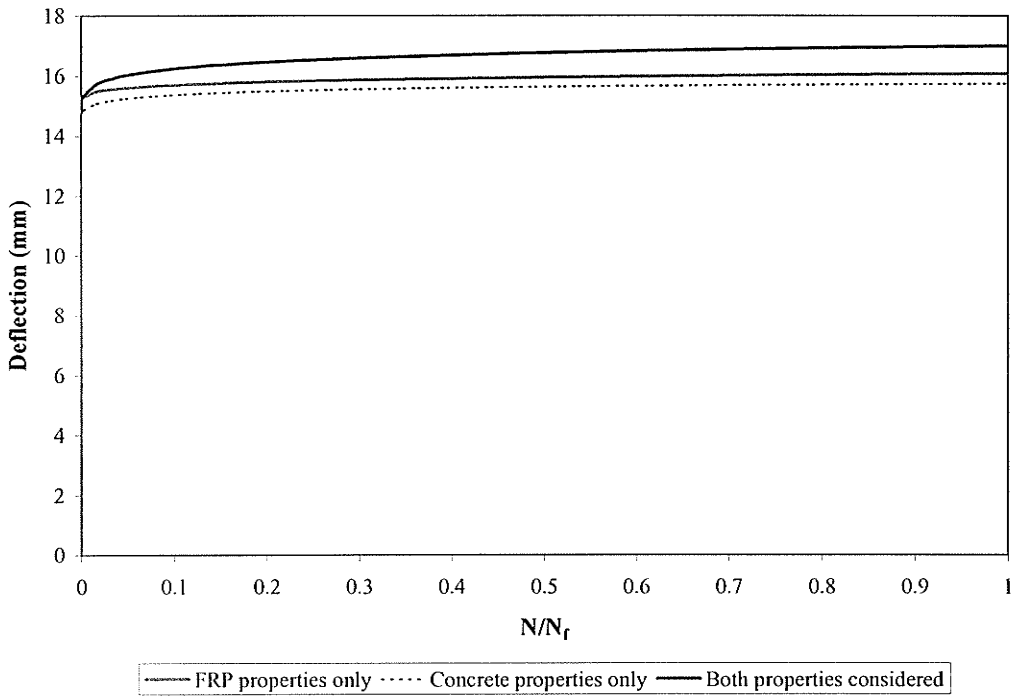


Figure A-36 Effect of the time dependant properties of the materials on the midspan deflection ( $D_t = 456 - M_{max}/M_{ult} = 25\% - f = 5\text{Hz}$ )

**Effect of the loading frequency and load level**

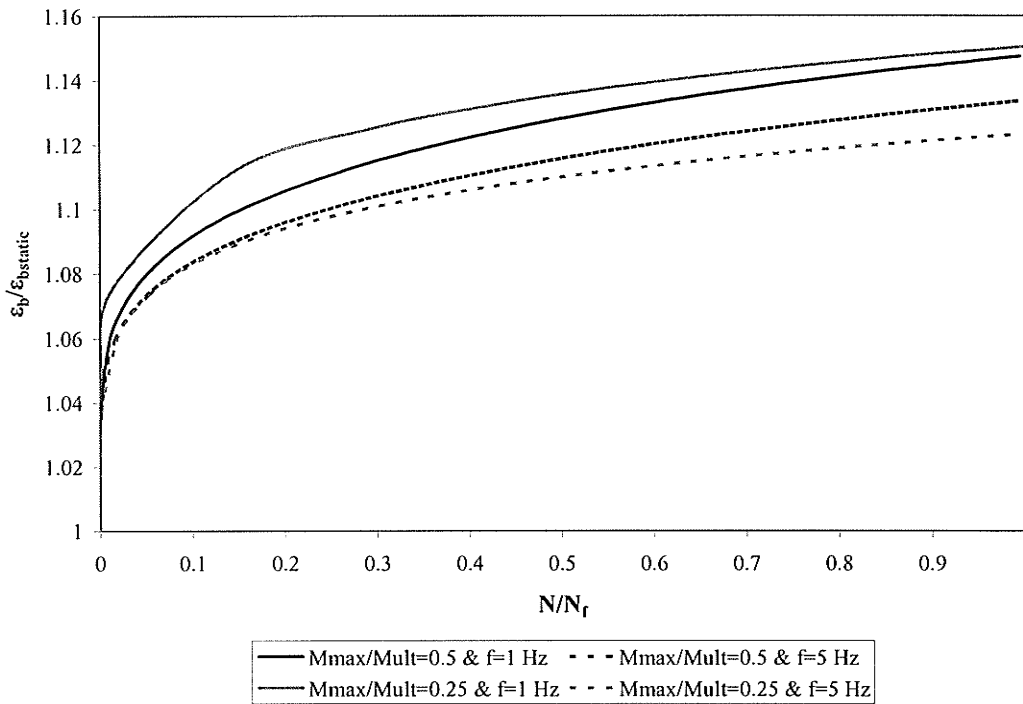


Figure A-37 Effect of the loading frequency and load level on the bottom strain behavior ( $D_t = 256$ )

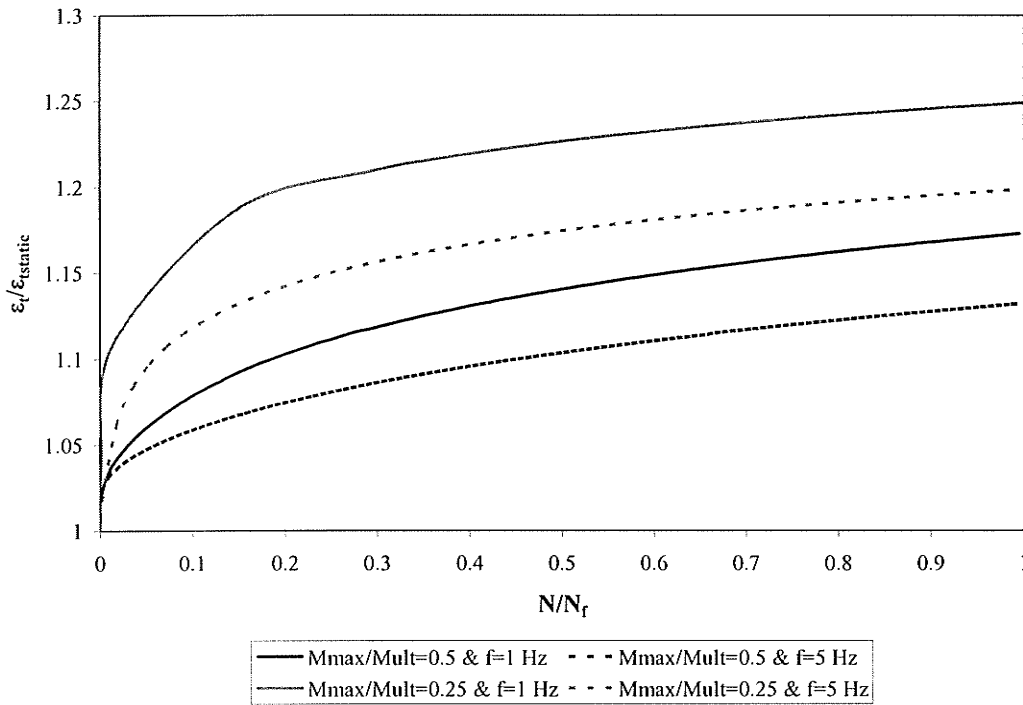


Figure A-38 Effect of the loading frequency and load level on the top strain behavior ( $D_t = 256$ )

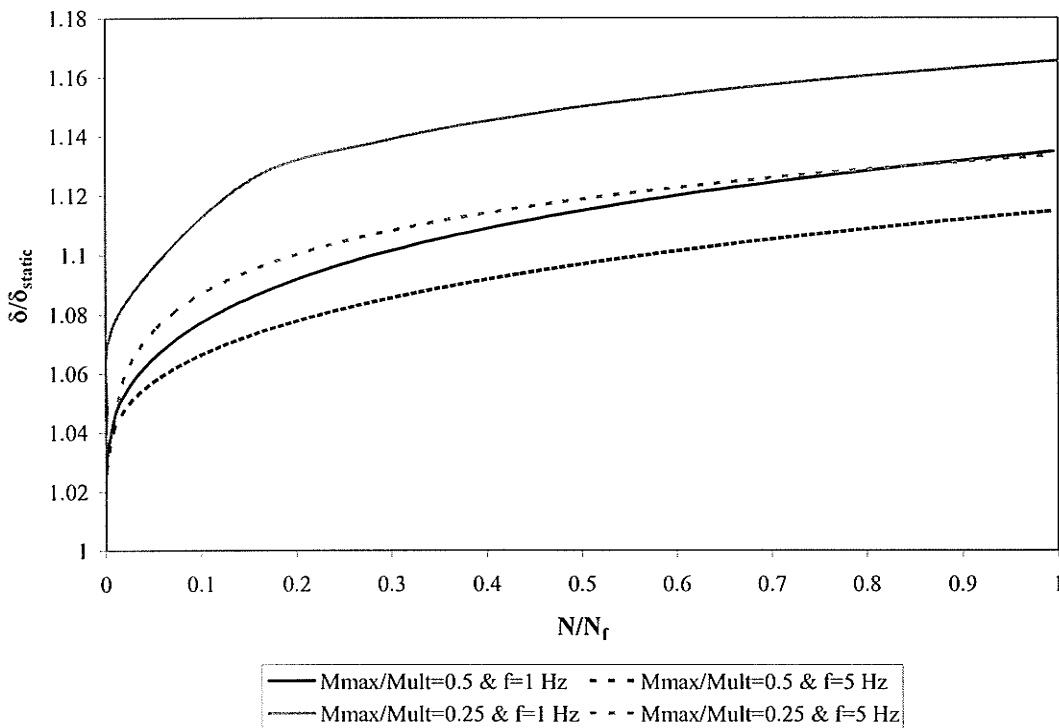


Figure A-39 Effect of the loading frequency and load level on the deflection behavior ( $D_t = 256$ )

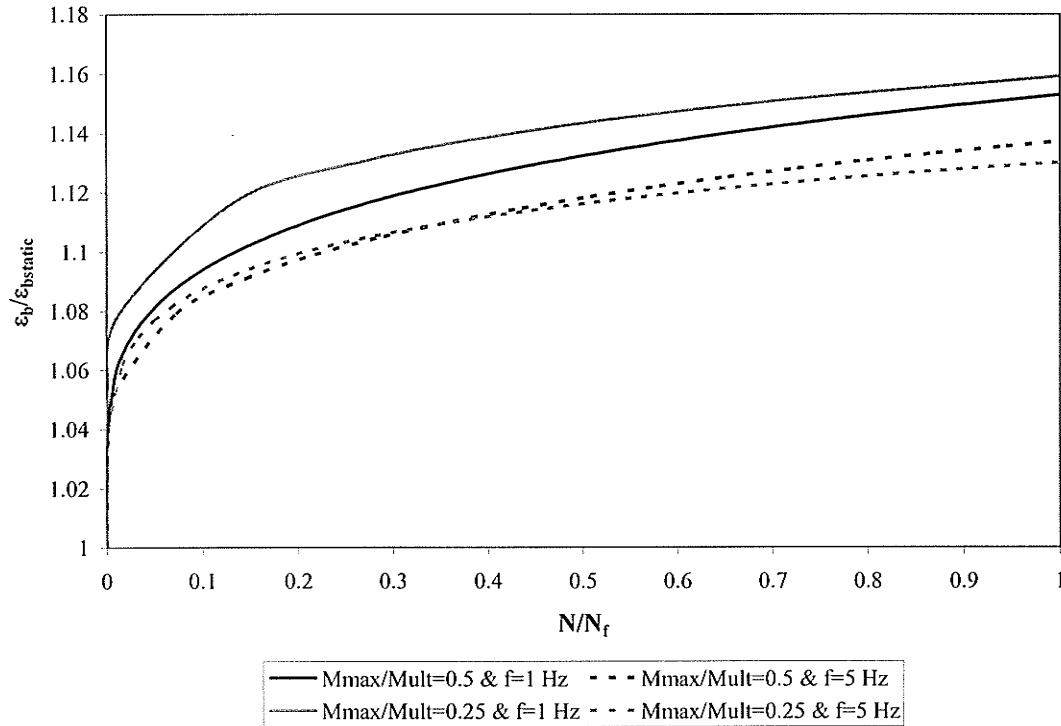


Figure A-40 Effect of the loading frequency and load level on the bottom strain behavior ( $D_t = 367$ )

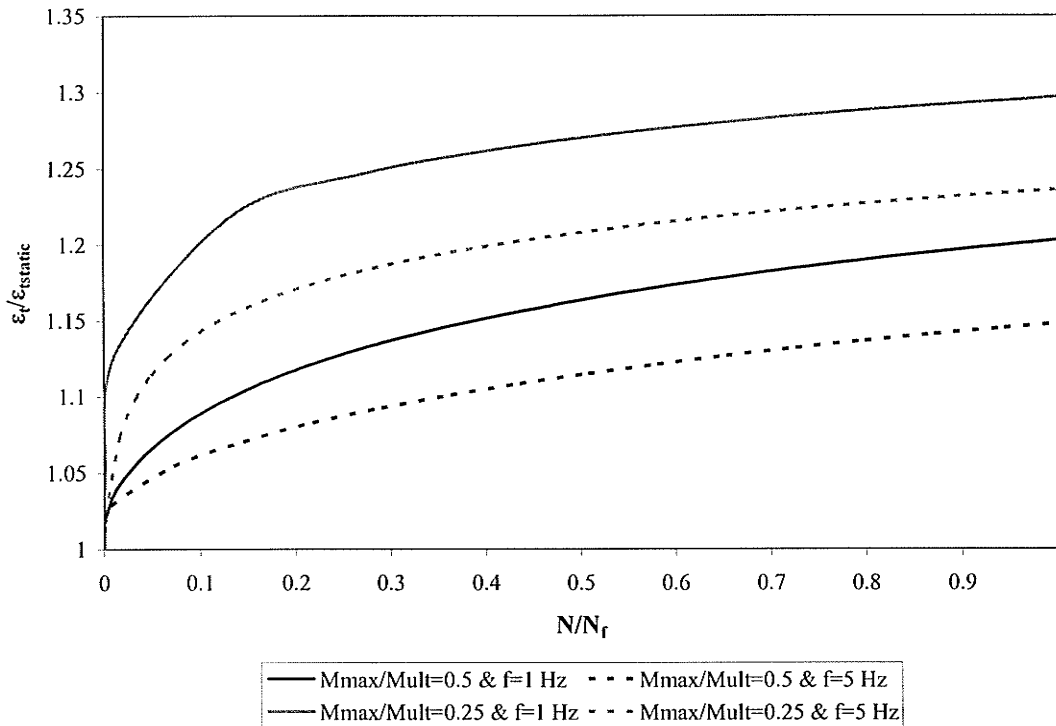


Figure A-41 Effect of the loading frequency and load level on the top strain behavior ( $D_t = 367$ )

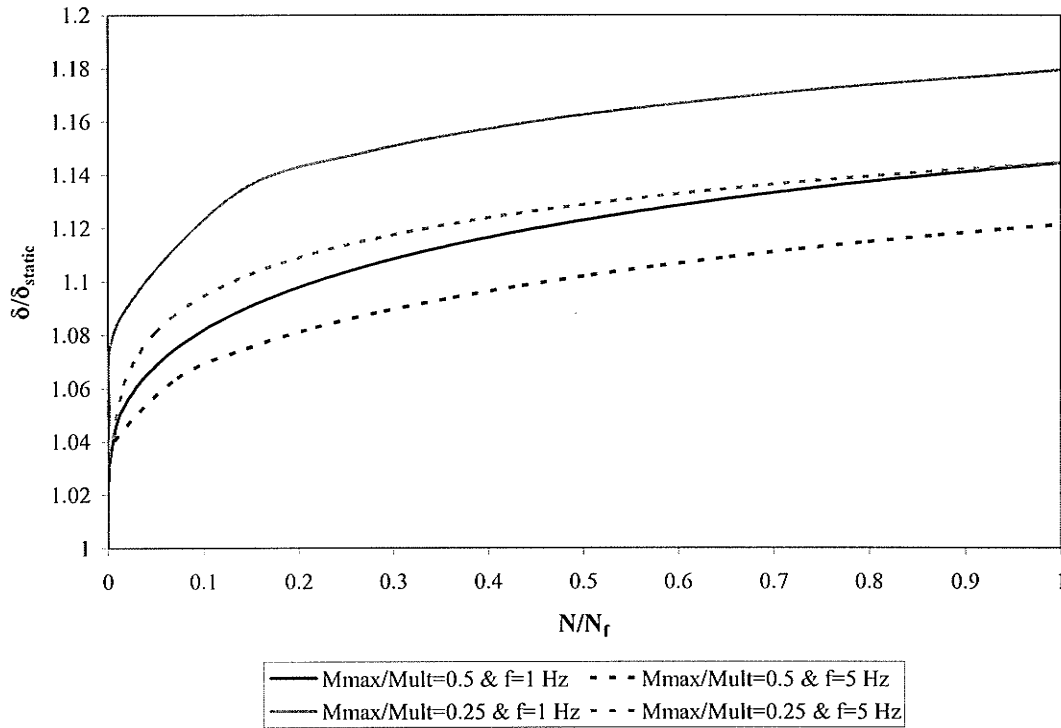


Figure A-42 Effect of the loading frequency and load level on the deflection behavior ( $D_t = 367$ )

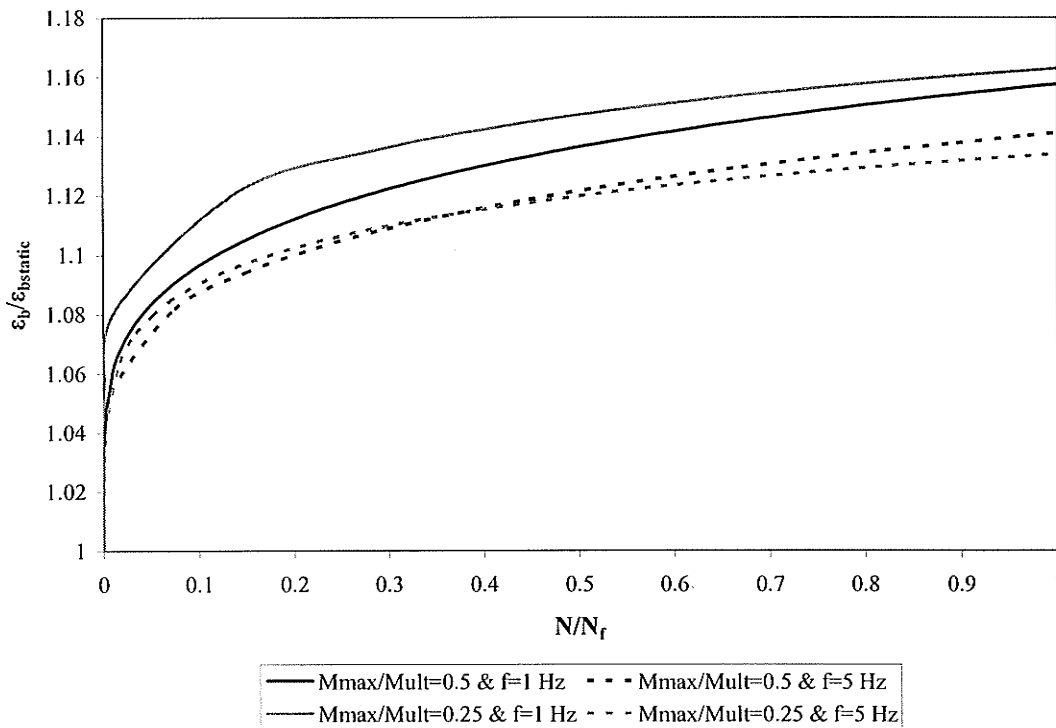


Figure A-43 Effect of the loading frequency and load level on the bottom strain behavior ( $D_t = 456$ )

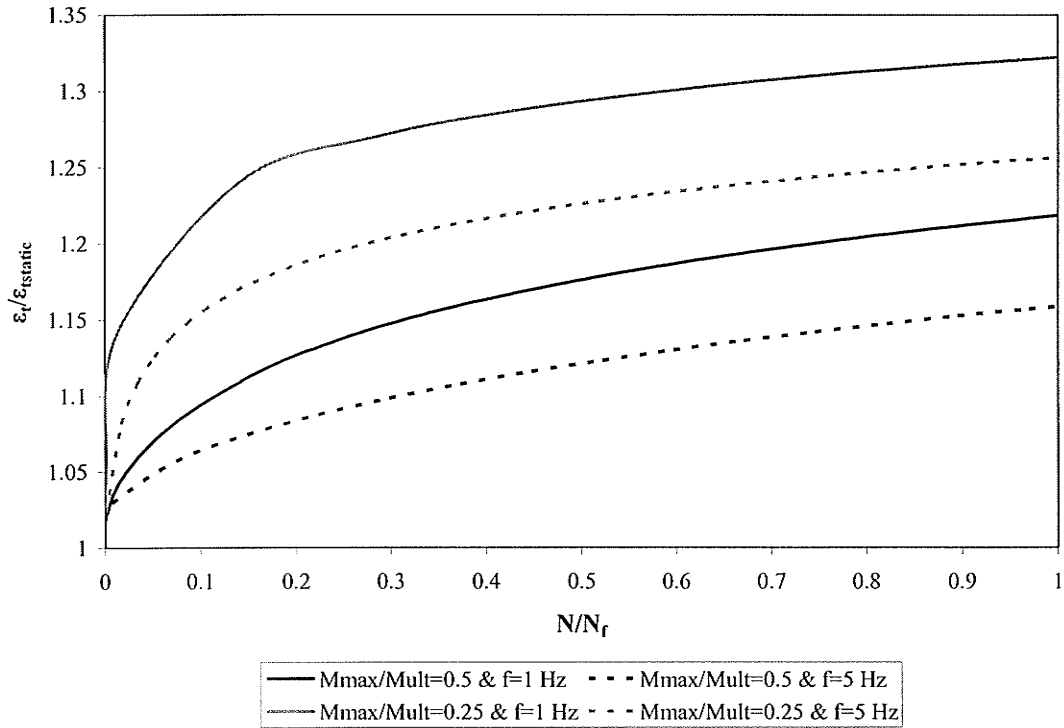


Figure A-44 Effect of the loading frequency and load level on the top strain behavior ( $D_t = 456$ )

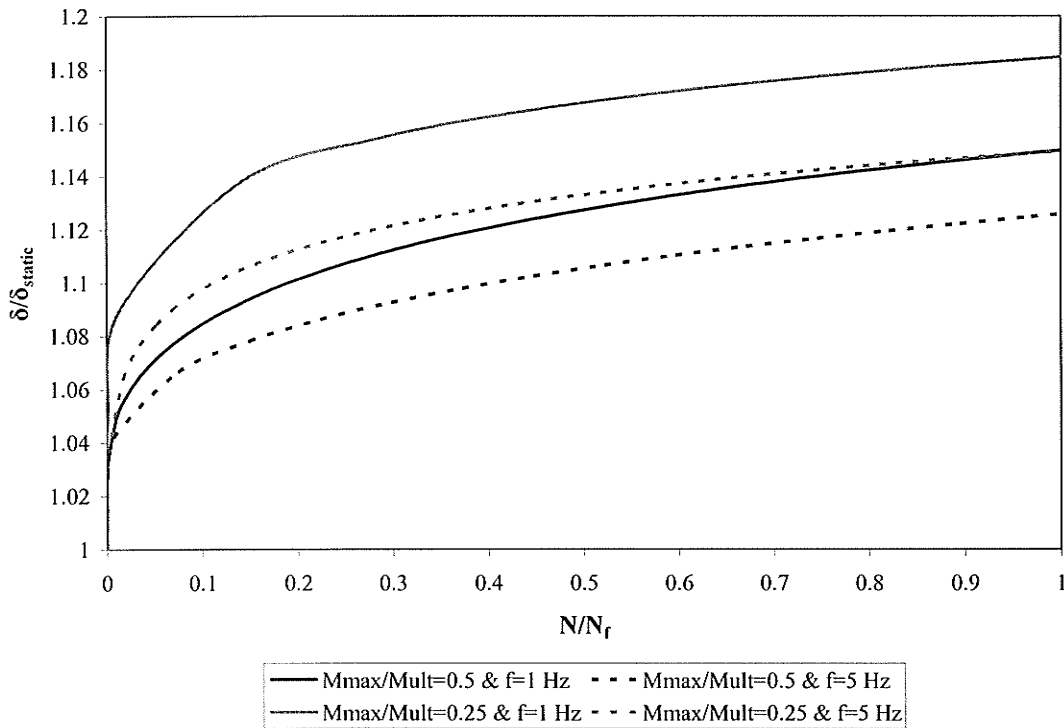


Figure A-45 Effect of the loading frequency and load level on the deflection behavior ( $D_t = 456$ )

Effect of tube size (Reinforcement ratio)

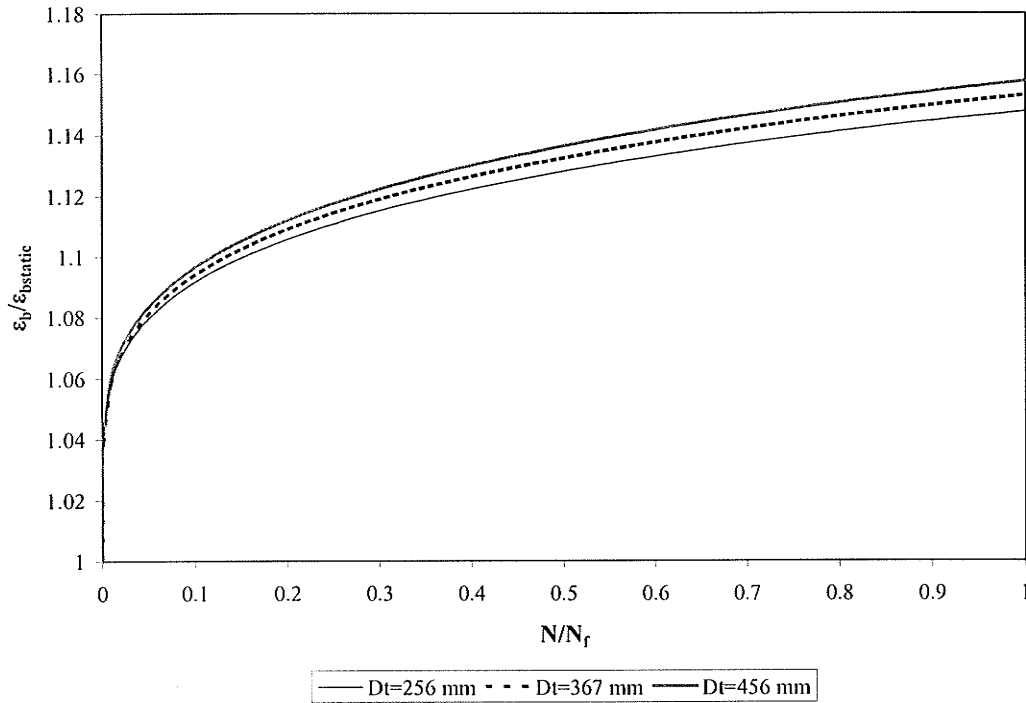


Figure A-46 Effect of the tube diameter on the bottom strain behavior ( $M_{max}/M_{ult} = 50\%$  -  $f = 1\text{Hz}$ )

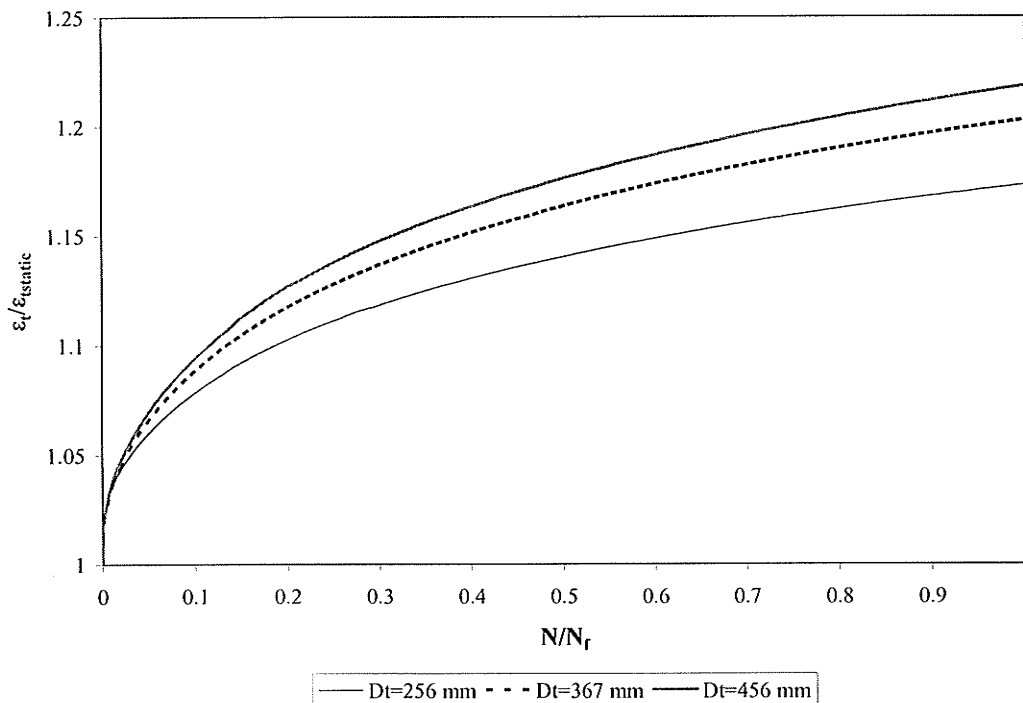


Figure A-47 Effect of the tube diameter on the top strain behavior ( $M_{max}/M_{ult} = 50\%$  -  $f = 1\text{Hz}$ )

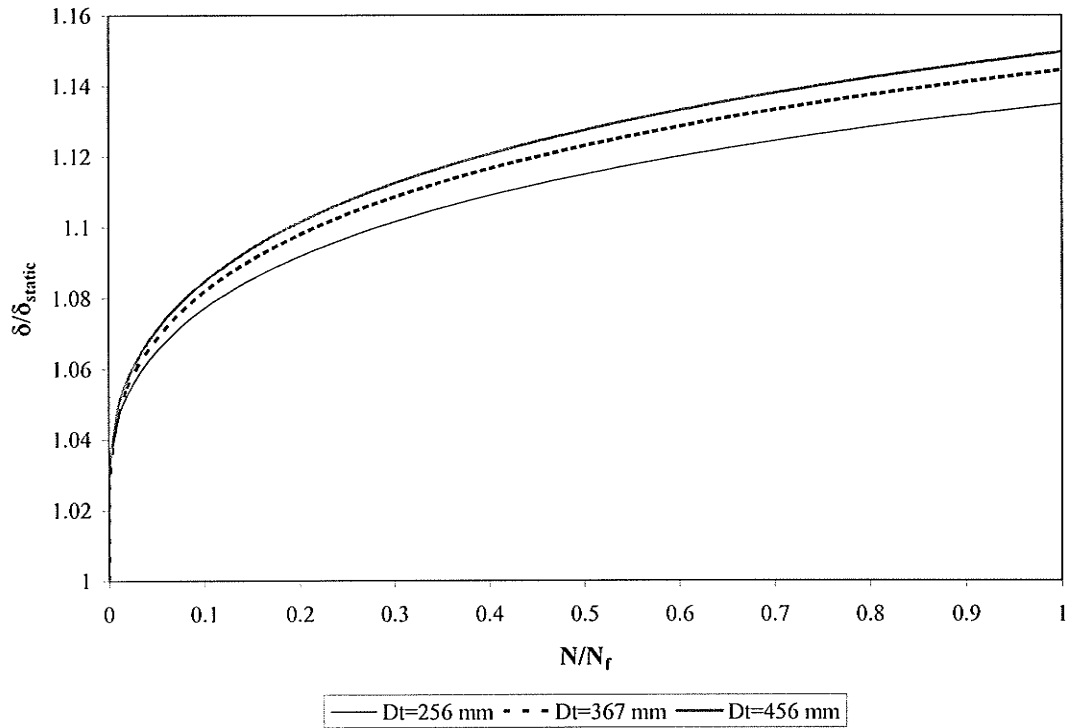


Figure A-48 Effect of the tube diameter on the deflection behavior ( $M_{max}/M_{ult} = 50\%$  -  $f = 1\text{Hz}$ )

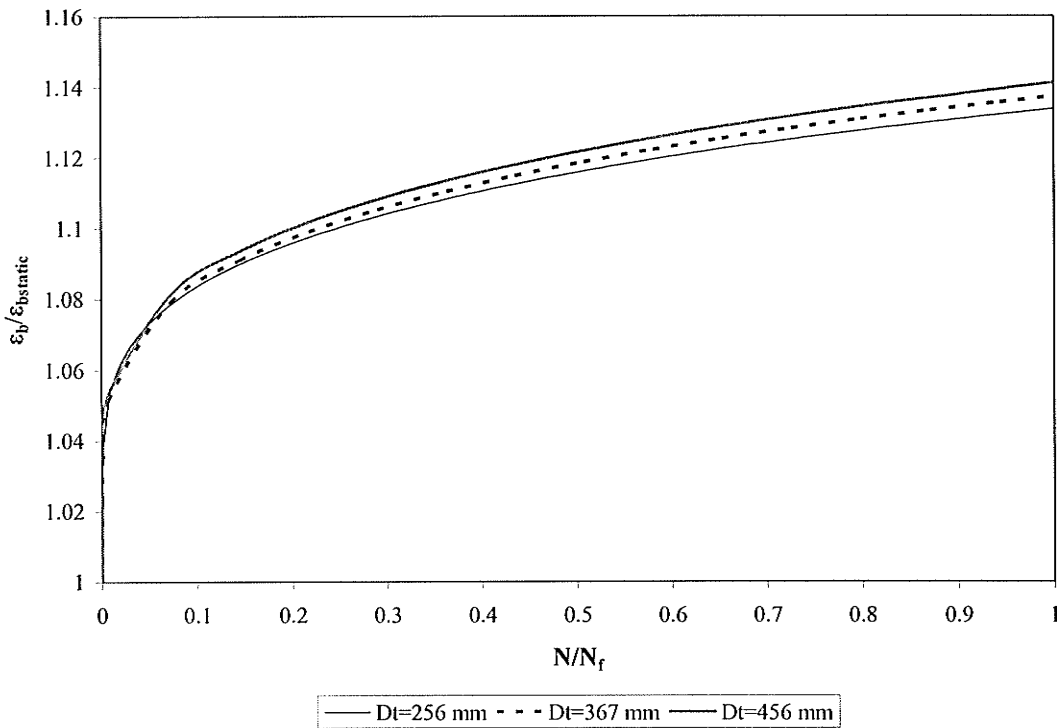


Figure A-49 Effect of the tube diameter on the bottom strain behavior ( $M_{max}/M_{ult} = 50\%$  -  $f = 5\text{Hz}$ )

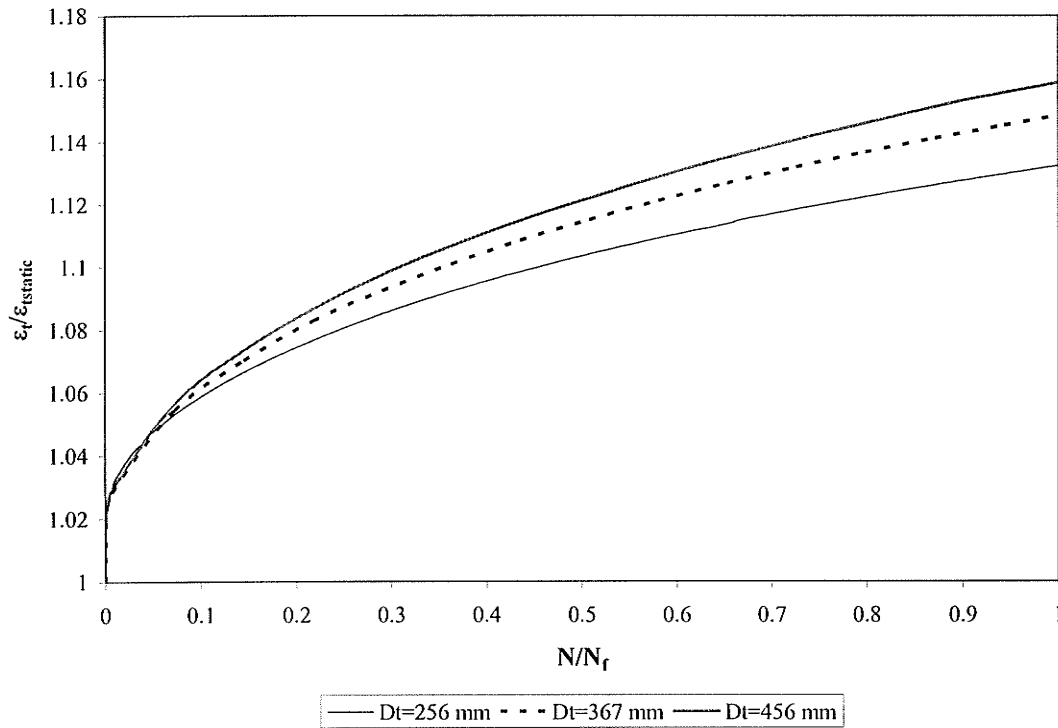


Figure A-50 Effect of the tube diameter on the top strain behavior ( $M_{max}/M_{ult} = 50\%$  -  $f = 5\text{Hz}$ )

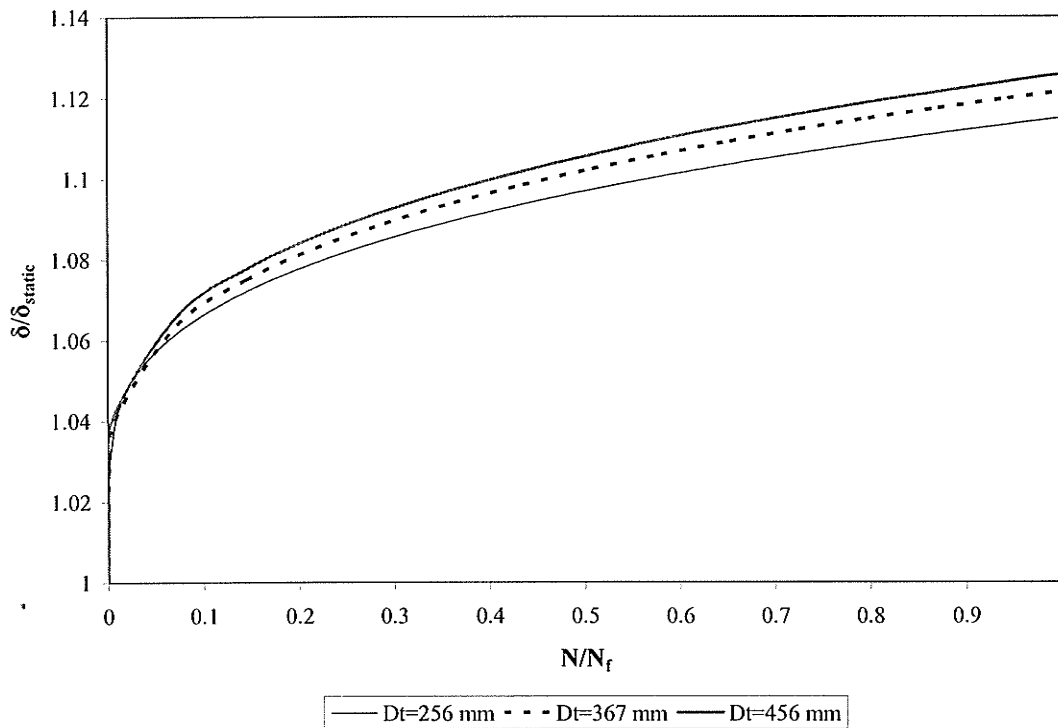


Figure A-51 Effect of the tube diameter on the deflection behavior ( $M_{max}/M_{ult} = 50\%$  -  $f = 5\text{Hz}$ )



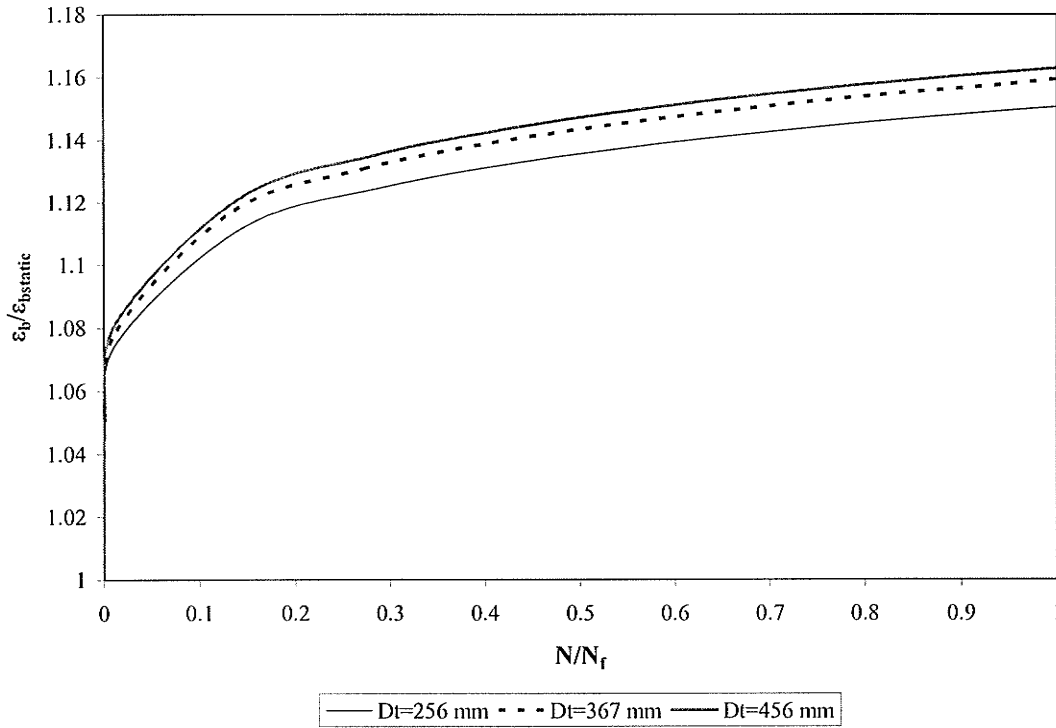


Figure A-52 Effect of the tube diameter on the bottom strain behavior ( $M_{max}/M_{ult} = 25\%$  -  $f = 1\text{Hz}$ )

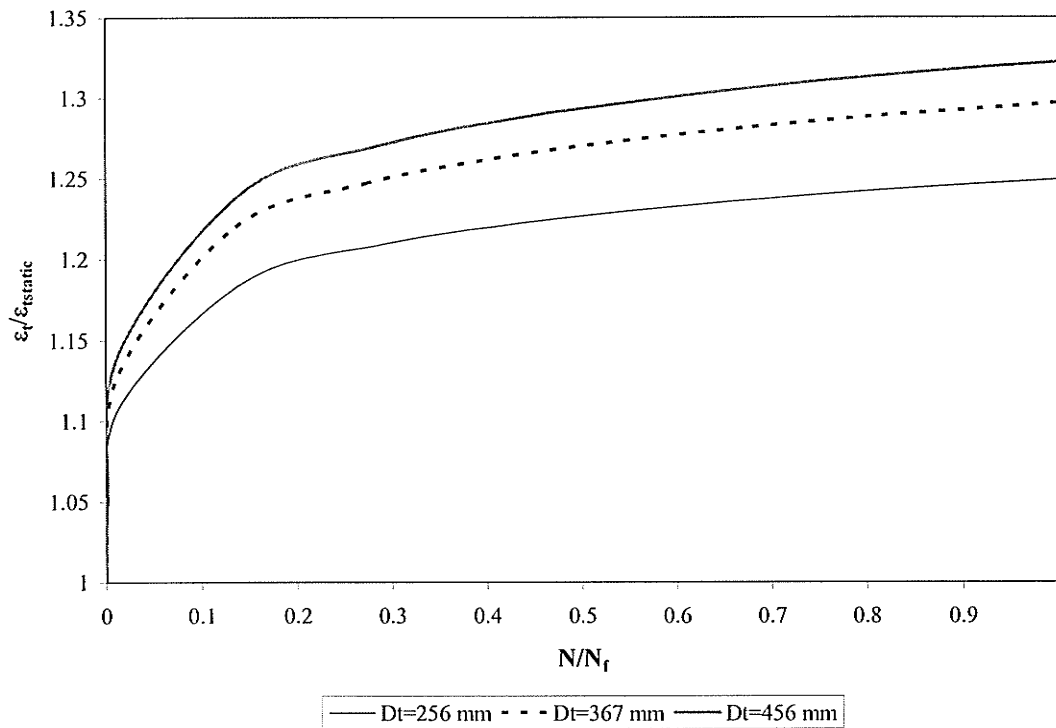


Figure A-53 Effect of the tube diameter on the top strain behavior ( $M_{max}/M_{ult} = 25\%$  -  $f = 1\text{Hz}$ )

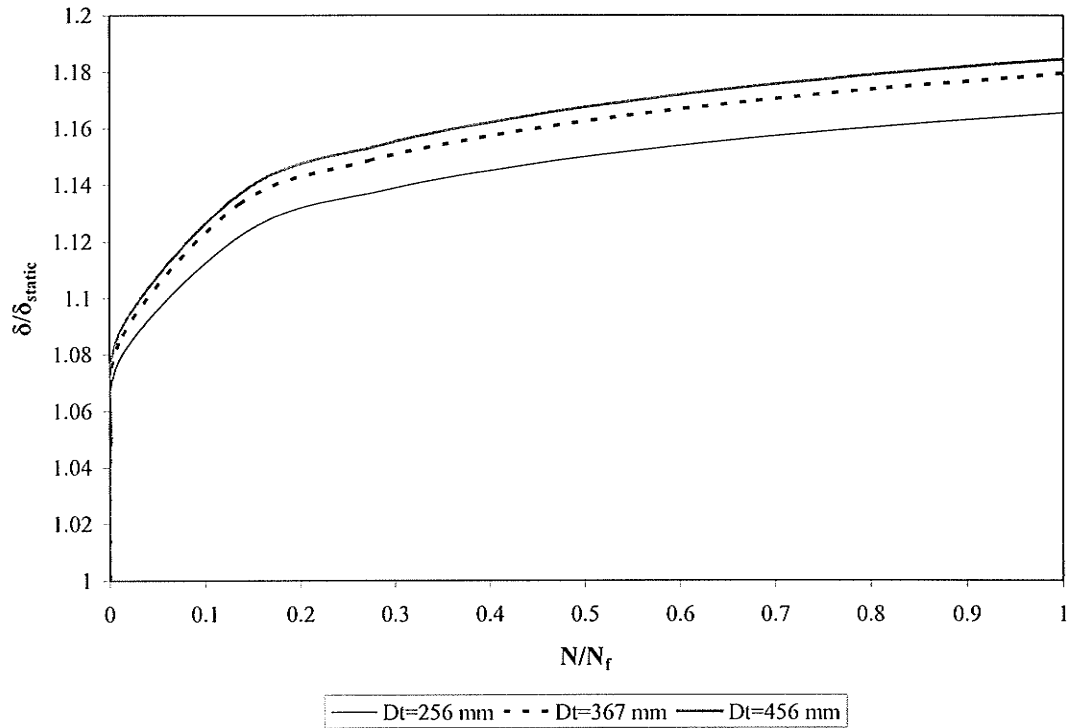


Figure A-54 Effect of the tube diameter on the deflection behavior ( $M_{max}/M_{ult} = 25\%$  -  $f = 1\text{Hz}$ )

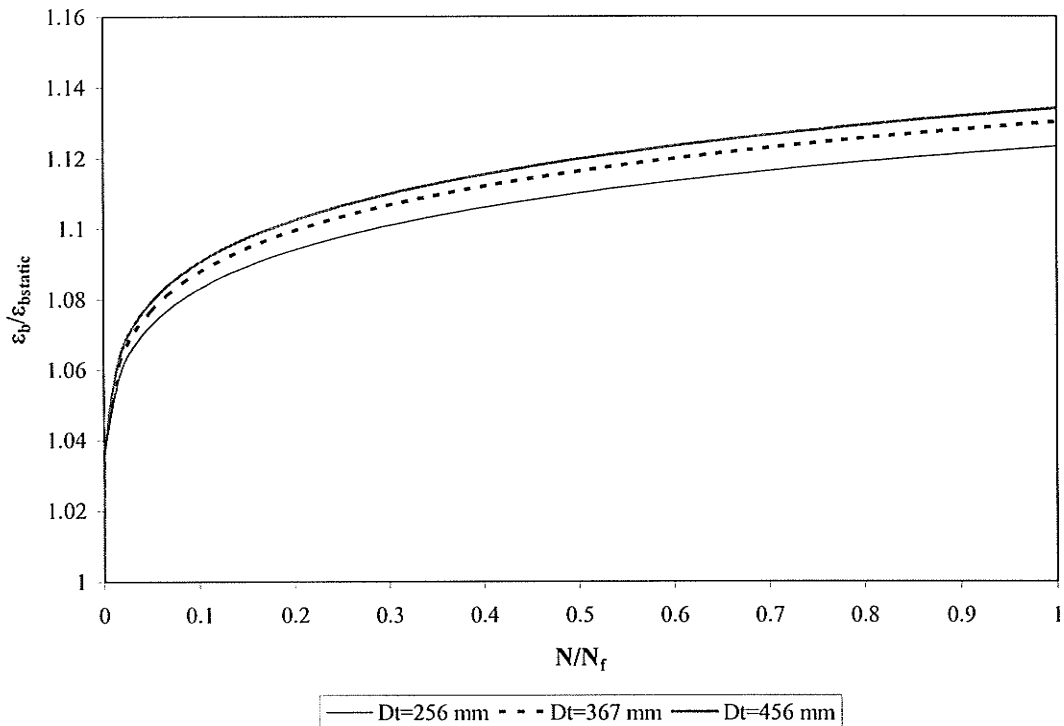


Figure A-55 Effect of the tube diameter on the bottom strain behavior ( $M_{max}/M_{ult} = 25\%$  -  $f = 5\text{Hz}$ )

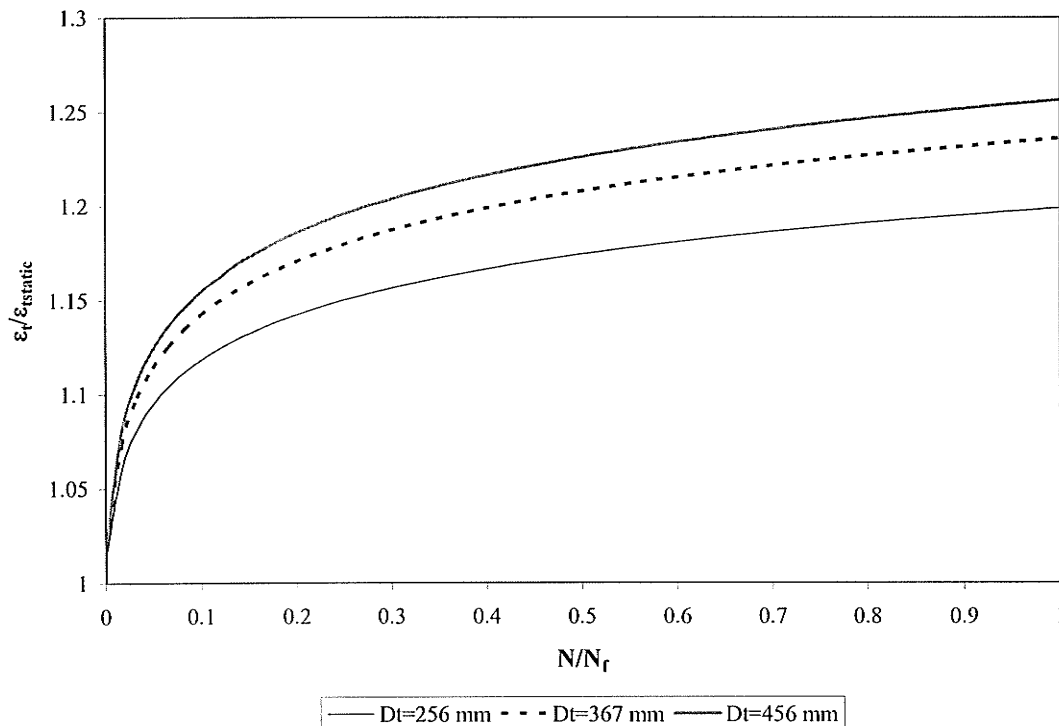


Figure A-56 Effect of the tube diameter on the top strain behavior ( $M_{max}/M_{ult} = 25\%$  -  $f = 5\text{Hz}$ )

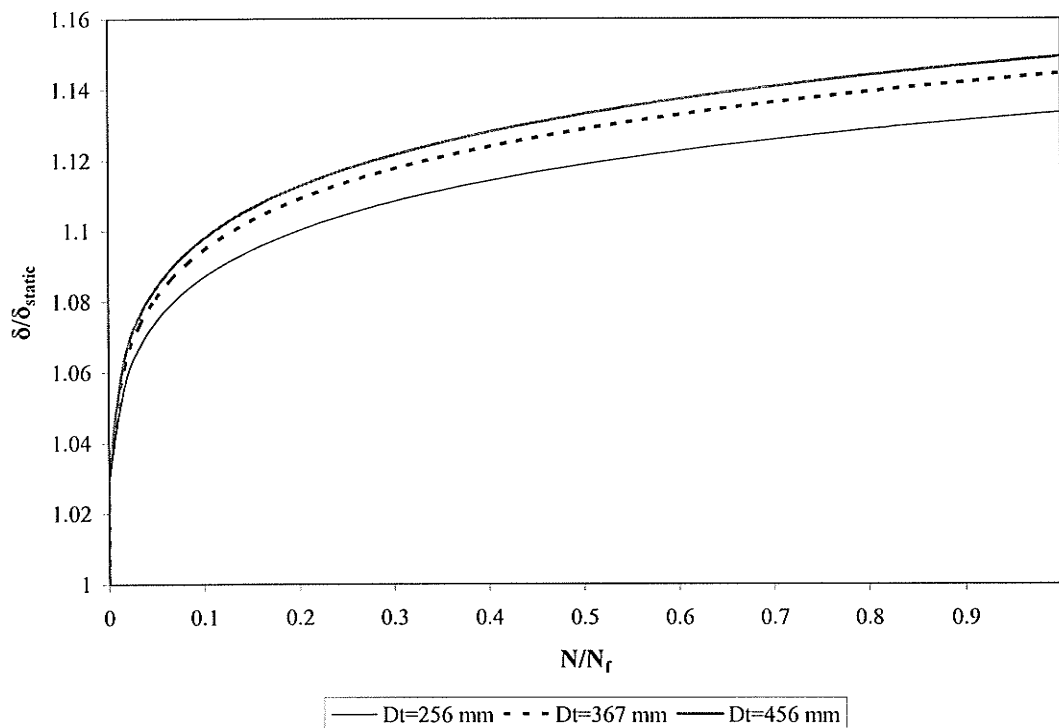


Figure A-57 Effect of the tube diameter on the deflection behavior ( $M_{max}/M_{ult} = 25\%$  -  $f = 5\text{Hz}$ )

## Appendix B

## Computer Program Source Codes

## Static Analysis

```

character*1 ans
  real mt,mcr,ebs(200),ms(200), curs(1000), l1, l2
  common/par/ dt, di, df, fcr, fco, r, Efc, Eft, af, n, hc, Ec,
ecr,
  + eco, fcco, ecco, Ecc, b(4000), ycc(4000), ycf(4000)
  dt=367.0
  t=5.7
  n=100
  fco=58
  Eft=18000
  Efc=18000
  ts=4.8
  pi=4*atan(1.0)
  di=dt-2*t
  df=dt-t
  thn=pi/n
  af=ts*pi*df/n
  fcr=0.5*fco**0.5
  Ec=5000*fco**0.5
  ecr=fcr/Ec
  hc=di/n
  l1=2000.0
  l2=500.0
  do 10 i=1,n
  theta=(i-0.5)*thn
  ycf(i)=df/2*cos(theta)
  ycc(i)=di/2-(i-0.5)*hc
  b(i)=2*((di/2)**2-ycc(i)**2)**0.5
10  continue
  ebcr=dt/di*ecr
  call emcal (ebcr, etcr, c, mcr, curv)
c  write (*,*) ebcr, mcr
  OPEN (UNIT = 1, FILE = 'tml.txt', STATUS = 'unknown')
  write (1,*) 'eb et c def m'
  do 200 mt=10,200,10
  ebs(1)=ebcr/3
  ebs(2)=2*ebcr/3
  ns=20
  x=l1/ns
  def=0
  do 100 j=1,ns
  secm=mt*j/ns
  if (secm.gt.mcr) then
  ebs(1)=0.005
  ebs(2)=0.015
  end if
  l=1

```

```

call emcal (ebs(1), et, c, ms(1),curv)
if (abs(ms(1)-secm)/secm.lt.0.0001) goto 50
l=2
call emcal (ebs(1), et, c, ms(1),curv)
if (abs(ms(1)-secm)/secm.lt.0.0001) goto 50
do 20 l=3,200
ebs(l)=ebs(l-2)+(ebs(l-1)-ebs(l-2))*(secm-ms(l-2))/(ms(l-1)-ms(l-
2
+))
call emcal (ebs(l), et, c, ms(1),curv)
if (abs(ms(1)-secm)/secm.lt.0.0001) goto 50
20 continue
write (*,*) 'no convergance achieved m'
50 curs(j)=curv
if (j.eq.1) then
def=(curs(j)*x**2)/3
else
def=def+curs(j-1)*(j-0.5)*x**2
def=def+(curs(j)-curs(j-1))/2*(j-0.3333)*x**2
endif
c write (*,*) curs(j), def
100 continue
def=def+curs(ns)*l2*(l1+l2/2)
write (*,*) mt, def, ebs(1), et, c
write (1,120) ebs(1), et, c, def , mt
200 continue
close (unit=1)
120 format (5(2x,E12.5))
end
c *****
subroutine emcal (eb,et,cf,m,curv)
c *****
c subroutine for calculatig moment for a given eb
real m,ct(200),eror(200)
common/par/ dt, di, df, fcr, fco, r, Efc, Eft, af, n, hc,Ec, ecr,
+ eco, fcco, ecco, Ecc, b(4000), ycc(4000), ycf(4000)
ct(1)=dt/4
ct(2)=dt/3
k=1
call errcal (eb, ct(k), eror(k), m)
if (abs(eror(k)).lt.100) goto 50
k=2
call errcal (eb, ct(k), eror(k), m)
if (abs(eror(k)).lt.100) goto 50
do 20 k=3,200
ct(k)=ct(k-2)-eror(k-2)*(ct(k-2)-ct(k-1))/(eror(k-2)-eror(k-1))
call errcal (eb, ct(k), eror(k), m)
if (abs(eror(k)).lt.100) goto 50
20 continue
write (*,*) 'no convergance achieved'
50 curv=eb/(dt-ct(k))
et=-1*eb*ct(k)/(dt-ct(k))
cf=ct(k)
end
c *****
subroutine errcal (eb,c,err,m)
c *****

```

```

c  subroutine for section analysis
c  calculating error for a given C and eb
  common/par/ dt, di, df, fcr, fco, r, Efc, Eft, af, n, hc, Ec, ecr,
  + eco, fcco, ecco, Ecc, b(4000), ycc(4000), ycf(4000)
  real mf,mc,mft,mct,m
  z=dt/2-c
  pct=0
  mct=0
  mft=0
  pft=0
  do 10 i= 1,n
  yc=z+ycc(i)
  e=eb*yc/(dt-c)
  if (e.ge.ecr) then
  fc=0.3*fcr/(1+(500*e)**0.5)
  else if (e.ge.0) then
  fc=Ec*e
  else if (e.gt.-0.001) then
  fc=37474*e
  else if (e.gt.-0.0027) then
  fc=8532778.3*e**2+46253.83*e
  else
  fc=-54635*e**2+974.97*e-60.129
  end if
  pc=fc*b(i)*hc
  mc=pc*yc
  pct=pct+pc
  mct=mct+mc
10  continue
  do 20 j=1,n
  yf=z+ycf(j)
  e=eb*yf/(dt-c)
  c  if (e.gt.0.0) then
  c  ff=-188268.0*e**2+25407.0*e
  c  else
  c  ff=630511.0*e**2+26544.0*e
  c  end if
  ff=e*Eft
  if (e.lt.0) ff=e*Efc
  pf=ff*af
  mf=pf*yf
  pft=pft+pf
  mft=mft+mf
20  continue
  err=pft+pct
  m=(mct+mft)*1.0e-6
  end

```

**Cyclic analysis**

```

character*8 fn1
character*12 fn2
common/par/ freq, cnc, dt, icase
real mcy, l1, l2
ns=20
dt=367
l1=1500
l2=500
x=l1/ns
c   freq=0.05
   write (*,*) 'file name'
   read (*,*) fn1
   fn2=fn1//'.txt'
   open (UNIT = 1, FILE = fn2, STATUS = 'unknown')
   write (*,*) 'M='
   read (*,*) mcy
   write (*,*) 'frequency='
   read (*,*) freq
   write (1,*) mcy, freq, dt
c   write (*,*) 'max number of cycles'
c   read (*,*) cnmax
   write (*,*) 'loading case 1=fiber only, 2=concrete only'
   read (*,*) icase
   if (icase.eq.1) then
   write (1,*) 'fiber stiff deg models only considered'
   else if (icase.eq.2) then
   write (1,*) 'concrete stiff deg models only considered'
   else
   write (1,*) 'both fiber & concrete stiff deg models considered'
   end if
   cnc=1.0
   call defcal (mcy, ebt, et, c, def, fmx, ffmn, fcmx, bnf)
   write (*,*) bnf
   write (1,320) cnc, ebt, et, c, def, fmx, ffmn, fcmx, bnf
   cnmax=bnf
   dmg=cnc/bnf
   bnfp=bnf
   cnp=cnc
   ncy=log(cnmax)/log(10.0)-1
   do 200 i=1,6
   if (i.le.ncy) then
   cnc=10.0**i
   else
   cnc=(i-ncy+1)*10.0**ncy
   endif
   write (*,*) cnc
   call defcal (mcy, ebt, et, c, def, fmx, ffmn, fcmx, bnf)
   dmg=dmg+(cnc-cnp)/(bnf+bnfp)*2
   cnp=cnc
   bnfp=bnf
   write (*,*) dmg
   write (1,320) cnc, ebt, et, c, def, fmx, ffmn, fcmx, bnf, dmg
   if (dmg.ge.0.99999) goto 300
200 continue

```

```

300 close (unit=1)
320 format (f12.2,7(2x,f10.4),2x,e14.3e3,2x,f10.4)
end
C*****
*****
      subroutine defcal (mcy, ebt, et, c, def, fmx, fmn, fcmx, bnf)
C*****
*****
c      subroutine for clculating the deflection at a given number of
cycles
      common/par/ freq, cnc, dt, icase
      real ms(1000), mt, mcy, ebs(1000), curv(100), l1, l2
      ns=20
      l1=1500
      l2=500
      x=l1/ns
      do 100 iz=1,ns
      mt=mcy/ns*iz
      ebs(1)=60/1e6*mt
      ebs(2)=80/1e6*mt
      l=1
      call emcal (ebs(1), c, ms(1), fmx, fmn, fcmx, bnf)
      if (abs(ms(1)-mt)/mt.lt.0.0001) goto 50
      l=2
      call emcal (ebs(1), c, ms(1), fmx, fmn, fcmx, bnf)
      if (abs(ms(1)-mt)/mt.lt.0.0001) goto 50
      do 20 l=3,1000
      ebs(1)=ebs(l-2)+(ebs(l-1)-ebs(l-2))*(mt-ms(l-2))/(ms(l-1)-ms(l-
2))
      call emcal (ebs(1), c, ms(1), fmx, fmn, fcmx, bnf)
      if (abs(ms(1)-mt)/mt.lt.0.001) goto 50
20      continue
      write (*,*) 'no convergance achieved m', mt
50      curv(iz)=ebs(1)/(dt-c)
      et=-1000.0*ebs(1)*c/(dt-c)
      ebt=1000.0*ebs(1)
      if (iz.eq.1) then
      def=curv(iz)*x**2/3
      else
      a1=(iz-0.5)*x
      a2=(iz-1.0/3.0)*x
      def=def+curv(iz-1)*a1*x+(curv(iz)-curv(iz-1))/2*a2*x
      endif
100     continue
      def=def+curv(ns)*l2*(l1+l2/2)
      end
C *****
*****
      subroutine emcal (eb,cf,m, fmx, fmn, fcmx, bnf)
C *****
*****
c      subroutine for calculatig moment for a given eb
      common/par/ freq, cnc, dt, icase
      real m,ct(1000),eror(1000)
      ct(1)=0.15*dt
      ct(2)=0.2*dt
      k=1
      call errcal (eb, ct(k), eror(k), m, tole, fmx, fmn, fcmx, bnf)
      if (tole.lt.0.001) goto 50

```



```

k=2
call errcal (eb, ct(k), eror(k), m, tole, fmx, ffmn, fcmx, bnf)
if (tole.lt.0.001) goto 50
do 20 k=3,1000
ct(k)=ct(k-1)-eror(k-1)*(ct(k-1)-ct(k-2))/(eror(k-1)-eror(k-2))
call errcal (eb, ct(k), eror(k), m, tole, fmx, ffmn, fcmx, bnf)
if (tole.lt.0.001) goto 50
20 continue
write (*,*) 'no convergance achieved', eb
50 cf=ct(k)
end
c *****
c      subroutine errcal (eb,c,err,m,tole, fmx, ffmn, fcmx, bnf)
c *****
c      subroutine for section analysis
c      calculating error for a given C and eb
      common/par/ freq, cnc, dt, icase
      real mf,mc,mft,mct,m,rfl
      real b(100), yc(100), yf(100), etc(100), etf(100), fc(100)
      real ff(100)
      parameter (t=5.7, n=100 , Eft=25000, Efc=25000 ,ts=4.8)
      pi=4*atan(1.0)
      di=dt-2*t
      df=dt-t
      thn=pi/n
      af=ts*pi*df/n
      ffu=482.667
      fcu=87.0
      hc=di/n
      gg=log(10.0)
      sint= sind(9.0)
      if (freq.lt.0.5) then
      alpha=0.092
      beta=0.2446
      else if (freq.lt.2.5) then
      alpha=0.1191
      beta=0.275
      else
      alpha=0.1135
      beta=0.3163
      end if
      time=cnc/freq/3600
      ecrc=0.0434*time**0.143
      z=dt/2-c
      pct=0
      mct=0
      mft=0
      pft=0
c      OPEN (UNIT = 1, FILE = 'tcyl.txt', STATUS = 'unknown')
      do 10 i= 1,n
      b(i)=2*((di/2)**2-(di/2-(i-0.5)*hc)**2)**0.5
      yc(i)=z+di/2-(i-0.5)*hc
      etc(i)=eb*yc(i)/(dt-c)
      if (etc(i).ge.0) then
      fc(i)=0
      ncp=i+1
      else if (etc(i).gt.-0.001) then

```

```
if (cnc.lt.1.2) goto 35
if (icase.eq.2) goto 35
sd1=1-393.0*(ff(k)/Eft)**1.608*(cnc/fnf)**0.196
sd2=sd1
if (ff(n-k+1).lt.0) then
sd2=1-1100.0*(ff(k)/Eft)**1.67*(cnc/fnf)**0.167
end if
cf1=1/sd1+scf*ecrc
eol=etf(k)/cf1
ecrp=eol*scf*ecrc
eo2=(etf(n-k+1)-ecrp)*sd2
fmx=eol*Eft
fmn=eo2*Eft
if (eo2.lt.0) fmn=eo2*Efc
tol1=abs((fmx-ff(k))/fmx)
tol2=abs((fmn-ff(n-k+1))/fmn)
ff(k)=(fmx+ff(k))/2
ff(n-k+1)=(fmn+ff(n-k+1))/2
if (tol1.le.0.001 .and. tol2.le.0.001) goto 30
25  continue
   write (*,*) 'number of itterations exceeded fibre', k
30  continue
35  pct=0
   mct=0
   mft=0
   pft=0
   fcmx=fc(n)
   fmx=ff(1)
   fmn=ff(n)
   do 60 ig=1,n
   pc=fc(ig)*b(ig)*hc
   mc=pc*yc(ig)
   pct=pct+pc
   mct=mct+mc
   pf=ff(ig)*af
   mf=pf*yf(ig)
   pft=pft+pf
   mft=mft+mf
60  continue
   err=pft+pct
   tole=abs(err/pct)
   m=(mct+mft)/1e6
   goto 550
500 write (*,*) 'solution not possible n/nf>0.8'
   write (*,*) ib, ic, cnf, cnc, fc(ib), etc(ib)
550 end
```